Physical and dynamical conditions of the molecular gas in the central parsec of the Galaxy

Anna Ciurlo

Université Paris Diderot – Sorbonne Paris Cité

Ecole doctorale 127

Astronomie & Astrophysique d'Île-de-France

Observatoire de Paris – LESIA

THÈSE

Pour obtenir le titre de Docteur en Science

Spécialité Astronomie & Astrophysique

Anna Ciurlo

Physical and dynamical conditions of the molecular gas in the central parsec of the Galaxy

Thèse dirigée par :

Daniel Rouan
Thibaut Paumard
Yann Clénet

Soutenue le 14 décembre 2015, jury :

M. Jacques Le Bourlot	*Président*
M. Andreas Eckart	*Rapporteur*
M. Eric Thiébaut	*Rapporteur*
Mme. Jihane Moultaka	*Examinatrice*
M. Andrea Goldwurm	*Examinateur*
M. Daniel Rouan	*Directeur*
M. Thibaut Paumard	*co-Directeur*
M. Yann Clénet	*co-Directeur*

Acknowledgments

This work would have never been possible without the support, guidance and advise of the many that crossed my path. Given that this text is in English, allow me to thank them all in the everyday language this work was carried out, French, with some of my Italian and a little bit of English.

Merci aux membres du jury, pour avoir pris le temps de lire ce manuscrit et pour la disponibilité ainsi que l'intérêt qu'ils ont montré. Merci à tous pour les remarques et la discussion enrichissante qui en a suivi. Merci en particulier aux rapporteurs qui se sont engagés dans la révision critique du manuscrit même quand le temps était serré. *Thank you for the time you spent on the critical analysis even in the short time available.*

Mes remerciements vont à mes directeurs de thèse, qui ont été complémentaires, présents tout en me laissant mon indépendance. Vous avez cru en moi et vous m'avez toujours soutenue. Au début c'est en vous regardant que j'ai pu apprendre et apprécier l'échange et la discussion scientifique. Merci donc pour vos qualités scientifiques et humaines aussi et pour m'avoir montré le beau la beauté de la recherche. En particulier, merci à Thibaut qui m'a accompagnée dans les premiers pas dans ce monde qui était encore nouveau et qui a cru en moi. J'ai frappé à sa porte bien des fois mais il a toujours su me guider pour que je prenne le relais, m'arrêter quand je commençais à trop me fixer sur un détail. Merci pour m'avoir appris à regarder les choses avec rigueur et fantaisie. Pendant ces années j'ai pu aussi apprécier les nombreuses discussions sur des sujets divers et je suis très contente que tu apprécies le *limoncello*. Merci à Daniel pour ses grandes qualités humaines et scientifiques. Avec les milliers des choses à faire et toutes ses responsabilités, il a toujours trouvé un moment pour discuter, pour me conseiller ou même pour signer un (ou mieux de nombreux) papiers. J'ai pu apprécier durant ces années ton ouverture d'esprit, toujours prêt à la discussion. Tu accueilles avec esprit critique mais cordialité toutes les idées proposées. En ta présence on se sent toujours très créatif et curieux. Merci à Yann, qui a été une présence constante, même au milieu de nombreuses choses à gérer. Tu as toujours été présent et disponible, que ce soit pour corriger un article, trouver une école d'été ou discuter une interprétation. Ton amabilité et tes encouragements m'ont beaucoup aidé dans les moments les plus difficiles.

Merci à Jacques, Franck et Emeric pour la collaboration et les discussions enrichissantes qui ont contribué à améliorer grandement ce travail. Merci à Emeric en particulier pour les graphs et sa grande disponibilité. Merci aussi à tous les collègues de l'Observatoire. Je suis arrivée dans un monde nouveau, dans un pays étranger et votre chaleur a transformé ce monde en quelque chose de beau et de familier. Je me rappelle en particulier d'une épique bataille de boules de neige comme l'un des premières souvenirs. Merci à Gérard, Eric, Damien, Tristan, Marie, Guillaume, Arnaud (sauf pour ses blagues sur la nourriture italienne) et Maxime pour les discussions et les bons moments. Merci à Roderick et Olivier pour les soirées à jouer la guitare et le soutien. Merci à Jonathan pour ses conseils et les inoubliables blagues, il m'a trop fait rigoler. Merci à Vincent, Silvestre, Fréderic, Vincent et Marie, *grazie* à Guy, pour les discussions intéressantes, les conseils et tous les bons moments. Aller au boulot c'était

un plaisir (même si les stores ont été réparés seulement maintenant que je pars..). Merci à Lucien, Luca et Lester, pour les petites et grandes blagues et pour avoir pourri mon bureau plein de fois (merci Jonathan pour l'inspiration). Un merci spécial à Guillaume qui a partagé le bureau avec moi, pas depuis longtemps mais on dirait plus puisqu'il a été extrêmement ennuyant. Au moins cela m'a donné quelque chose sur laquelle décompresser. Mais bon, merci aussi parce qu'il m'a contaminé avec son calme très "vite". Merci Marion, parce que le jour de ma soutenance elle n'a pas stressé et pour le soutien sur lequel je peux compter. Nous avons une approche du monde tant différente que j'aime beaucoup nos discussions. Merci à Nabih, pour être venu à la soutenance et pas au pot seulement. Bon, je rigole ! Merci pour les beaux moments passés ensemble et les histoires drôles à faire pleurer. Merci à Miguel qui a su, lors d'un moment délicat, me dire les bons mots au bon moment. Merci Pierre pour sa bonne humeur et son camion "Never give up, it s a wonderfull world", quand on rédige c'est fondamentale ! Merci aux autres doctorants : Mélodie, Sophie, Clément, Raphael, Aurore, Matthieu, Cateline, Tabatha (et tous celles et ceux que j'oublie) parce que nos chemins ont été parallèles ces années et se sont croisés au club astro, dans l'organisation d'Elbereth, aux journées de thèses, ou simplement dans des moments de convivialité. Un grand merci à Pascal et Guillaume, avec lesquels j'ai partagé l'expérience magnifique du Sénégal, ça n'aurait pas été la même chose sans vous. Merci à JR et Vincent qui en ont fait partie aussi d'une manière. Pour cela je dois aussi remercier Daniel, Didier et Jaques qui l'ont rendu possible. Je tiens aussi à remercier Jacques en tant que directeur de l'ED qui a été fondamental pour la bonne réussite de ma thèse pour le soutien et le suivi des doctorants. On ne se sent jamais abandonnés. Merci aussi à tout le personnel de l'Observatoire qui a rendu ma thèse possible même quand il y avait des problèmes à la dernière minute (merci Jacqueline et Cris !).

Bien sûr je remercie ma famille du fond du coeur pour le soutien fort et toujours renouvelé, parce qu'ils sont tous venus à Paris pour le jour important de la soutenance (en se chargeant du pot aussi). Merci à mes parents pour m'avoir toujours encouragé et m'avoir été d'exemple. Merci à mon Père, pour avoir lu toute la thèse mais surtout pour m'avoir toujours soutenu dans mes choix tout en étant prêt à m'attraper si je tombais. Merci à ma Mère qui est toujours prête à venir à mon secours pour la plus petite jusqu'à la plus grande des choses et le soutien sans faute. Merci à mon frère Giacomo qui est le seul qui trouve jolies mes images du gaz et qui pose toujours des questions philosophiques sur la science et l'Univers. Merci à mon frère Pietro qui m'encourage et me soutient et est toujours fier de moi, je le suis de lui aussi. Son enthousiasme m'est précieux. Merci à ma soeur Agnese qui n'importe quoi je fasse me soutient sans jamais douter et pour la sagesse et la force d'une vraie adulte. Merci à mes grands-parents Orietta e Carlo qui me soutiennent et croient en moi avec grand enthousiasme et confiance. Merci à mon Grand-père Enrico qui m'a fait aimer les sciences, pour nos longues discussions par Skype et son sourire d'approbation qui est une énorme récompense pour moi. Merci à ma Grand-mère Anna pour tout l'amour qui m'a donné force, pour d'être toujours à mes cotés et m'apprendre à sourire à la vie. Merci à mes cousins, cousines, tantes et oncles qui me soutiennent et encouragent.

Merci à mes amis qui ont fait aussi le déplacement pour me soutenir. Merci Mati d'avoir cru la première qu'on allait partagé ces années à Paris. Merci Marci du soutien constant et

présent. Merci Ceci, notre lien et notre support réciproque est sans fin et n'a pas besoin de paroles. Merci aussi aux amis qui ont été proches de loin: Bea et ses paroles qui portent toute la force de son soutien quotidien, Anto pour notre amitié qui ne souffre pas le temps, Pietro compagnon fondamental d'études de physique et grandes discussions, Jack, Gio, Simo et Bruno amis de longue date et de longues discussions philosophiques. Mes remerciements vont aussi à ceux qui ont formé une nouvelle famille pour moi ici à Paris, spécialement: Angelo, Eunjin, Edgard et Andre. Un merci très spécial à Laura et Fany. Vous êtes de la famille pour moi et fondamentales tant dans cette période difficile que pour le futur. Laura avec ta pensée profonde, Fany avec ta force.

Et maintenant, *dulcis* in fundo, merci à Marcello. Depuis longtemps nous marchons ensemble dans cette vie qu'on découvre ensemble. *Non so nulla del futuro se non che voglio passarlo con te.*

Merci encore à toutes et tous ceux que j'ai pu oublier ! *Grazie*!

[...] Così tra questa
Immensità s'annega il pensier mio:
E il naufragar m'è dolce in questo mare.

Giacomo Leopardi, L'Infinito

Contents

Abstract

Physical and dynamical conditions of the molecular gas in the central parsec of the Galaxy

In the central parsec of the Galaxy the environment of the black hole (Sgr A*) presents a very young star cluster, emitting a strong UV radiation, and two main gas structures: the Circumnuclear Disc (CND), composed of dust and neutral gas, and the Minispiral, consisting mainly of dust and ionized gas. The aim of this work is to describe H_2 distribution and properties in the central parsec where the neutral CND encloses the ionized Minispiral, in order to understand the interstellar medium conditions in this ionized environment. This study is carried out through a near-infrared spectro-imaging data cube of the central cavity observed with SPIFFI on the VLT. These observations cover several H_2 lines. The analysis has been done in two parts.

- In the first part of the analysis the gas morphology and dynamics are analyzed. To handle the noise and conserve good angular resolution an original line fitting method is applied: a global regularized 3D-fit, developed by T. Paumard. This method leads to high spatial and spectral resolution maps of the intensity, velocity and width of several H_2 lines. For the first time the extinction map of H_2 is traced directly from the ratio of two H_2 lines, allowing to correct flux maps and to observe the effect of the foreground and local extinction. Molecular gas is detected everywhere. In addition to the known CND, H_2 emission is detected from all over the Central Cavity and in particular in the Northern Arm Cloud, from a region between GCIRS 7 and the Bar and from the border of Minicavity.

- In the second part of the analysis the excitation mechanism of the gas is enquired. A more classical 1D spectroscopic model fitting is applied in order to simultaneously analyze several H_2 lines. The excitation diagrams allowed to estimate gas temperature, mass and density of several zones across the field.

These analyses allowed the detection of H_2 emission from all over the observed field of view. In particular several components of the H_2 emission have distinct physical properties. In the CND the emission comes from a hot, thermalized, thin layer at the surface of the dense clouds. This hot layer contains only a small fraction of the total H_2 mass. In the Central Cavity H_2 is not thermalized. The emission arises from a part of the gas contained in the bulk of the Northern Arm Cloud and also from the more diffuse gas contained in the Central Cavity. A strong deviation from thermal equilibrium is detected near the Minicavity and can be interpreted as coming from H_2 constantly formed and destroyed in steady state, out of equilibrium.

Keywords: Galactic Center – Interstellar medium: molecules – Techniques: imaging spectroscopy – Infrared: Interstellar Medium

List of acronyms

ADU	Analog to Digital Unit
AGN	Active Galactic Nucleus
CND	Circumnuclear Disk
CMZ	Central Molecular Zone
(F)UV	(Far) Ultraviolet
IFS	Integral field spectroscopy
ISM	Interstellar medium
ISRF	Interstellar radiation field
LTE	Local thermodynamic equilibrium
(N)IR	(Near) Infrared
OPR	Ortho-to-para ratio
PDR	Photon dominated region
PSF	Point spread function
(SM)BH	(Supermassive) black hole
S/U	Signal-to-uncertainty ratio

Structure of the central parsecs of the Galaxy

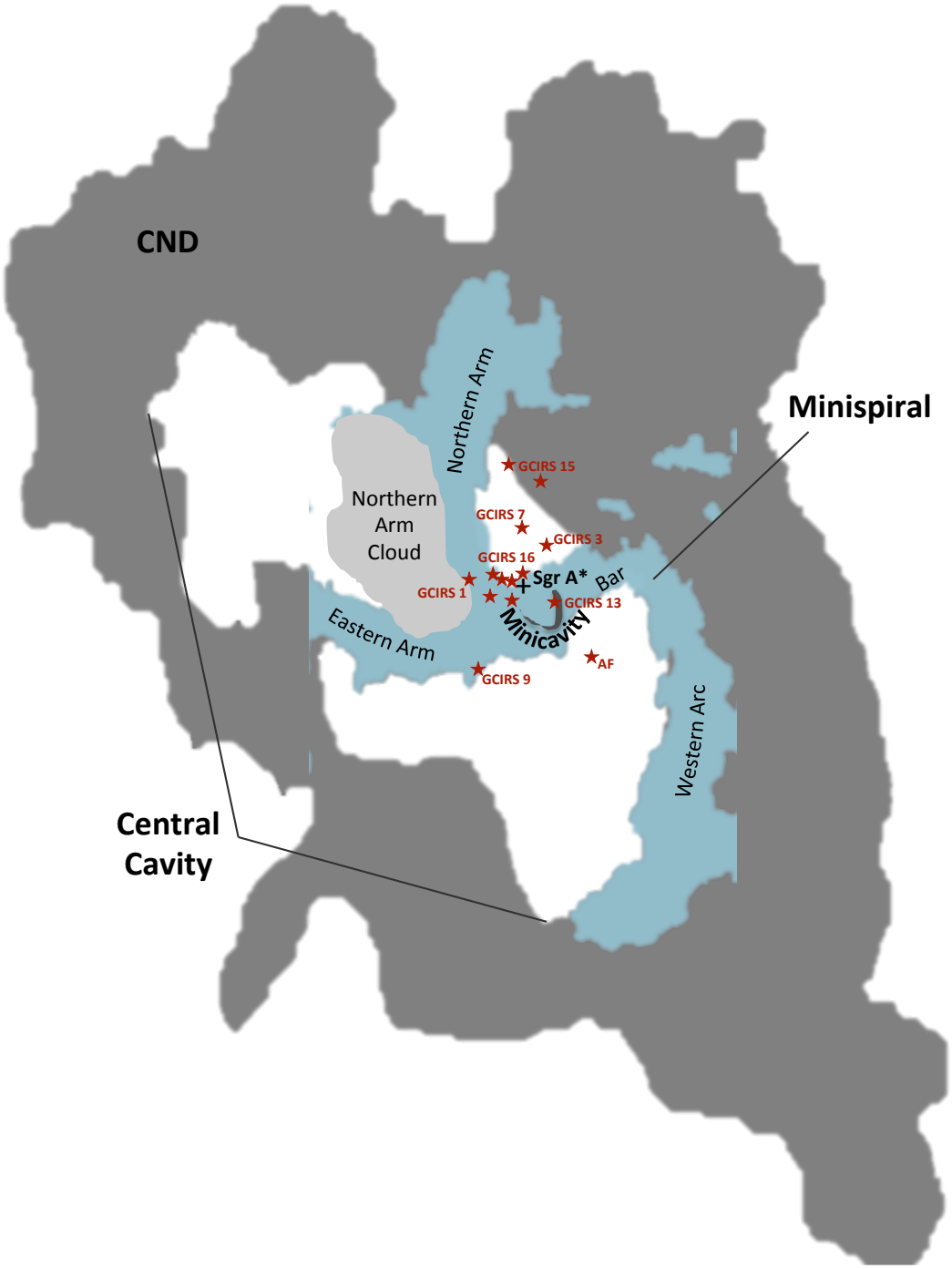

Chapter 1

Introduction

Contents

1.1 Context

Phenomena taking place at the center of galaxies have proved to be of great importance to characterize galaxy formation and evolution. The proximity of the Galactic Center of the Milky Way makes it an exclusive object for the investigation of phenomena related to the activity in galactic nuclei.

There is strong evidence that most galaxies contain supermassive compact objects. The hypothesis proposed by Lynden-Bell & Rees (1971) is that most – if not all – normal galaxies have massive, but dormant, supermassive black holes (SMBHs) at their centers. The center of the Galaxy encloses a mass of 4 10^6 $M_\odot$ as evidenced by measurements of stellar orbits (Schödel et al. 2002; Ghez et al. 2005) contained within 0.1 pc. Firstly observed as a strong radio source, identified as Sgr A*, the Galactic Center indeed seems to host a SMBH which

is accreting and radiating. For instance flares observed in the IR (Genzel et al. 2003a) or in X-rays (Baganoff et al. 2003) are clearly related to the presence of the SMBH and accretion events. However, given its mass, it does not shine as brightly as it could. The Eddington luminosity (the maximum luminosity) of a BH of that mass is $L_{Edd} \sim 10^{11} L_{\odot}$ while the Milky Ways SMBH radiates $\sim 10^{-7} L_{Edd}$ (Narayan et al. 1998; Baganoff et al. 2003). The Galactic Center is thus not considered as an Active Galactic Nucleus (AGN).

AGNs correspond to the small fraction of those galaxies where the SMBH is responsible of very energetic phenomena. An accretion disk supplies the material that is fed to the SMBH (Lynden-Bell 1969); the conversion of gravitational energy in thermal energy through friction is responsible of the very large luminosity. The most powerful AGNs (Quasars) are also the farthest away, while Seyfert galaxies – closer to Earth than Quasars – are less powerful but with brighter nuclei than those of normal galaxies. Changes in luminosity and number of AGNs over time may be a key element to interpret galaxy formation and evolution but also to understand the origin of their central SMBHs.

Even though there are similarities with Seyfert galaxies, (Woltjer 1959 and Lo & Claussen 1983 pointed out that it seems to be closely related to these active galaxies) the Galactic Center would seem to be in a non-active state. However, cycles of higher activity might have taken place in the past and might take place in the future, given the current conditions of matter and star activity (Morris & Serabyn 1996). The Galactic Center is thus an unique laboratory to study SMBHs and explore their impact on stellar and interstellar environment without being dazzled by the extreme luminosity of an AGN.

The Galactic Center is only 8.5 kpc far away, while the nearest normal spiral galaxy (M31) is located at a distance of 700 kpc and the nearest Seyfert galaxy (NGC 1068) is located at a distance of 25 Mpc. Therefore in our Galaxy we have a unique chance to observe in detail the environment of a galactic nucleus harboring a SMBH. The Milky Way can be described as a barred spiral (von Linden et al. 1996) and looks very standard. Therefore the results obtained from its study are presumably applicable to other galaxies as well.

The interstellar medium (ISM), and particularly its molecular phase, plays an important role as it fuels galaxy evolution through star formation and SMBHs growth. The study of the structure and physical conditions of molecular gas helps putting constraints on the mass inflow to the center, and allow to study the evolution and nature of the driving force. Molecules may also play a role in regulating the activation/deactivation of starburst and AGNs phases as they have been detected in large galactic outflows.

The Galactic Center is obscured, at optical wavelengths, by an extinction of $A_V \sim 30$ magnitudes because of diffuse dust along the line of sight. Radio, infrared (IR) and sub-millimeter wavelengths can penetrate these obscured regions. In particular the IR molecular emission can be observed from very inner regions of galaxies with deeply obscured nuclei.

In the Galactic Center, temperatures, densities, and internal velocity dispersions are higher than elsewhere in the Galaxy (Güsten 1989). Powerful large-scale shocks are involved in the ISM excitation, as underlined by high velocity bulk gas motions and velocity discontinuities. The very different nature of the dense ISM in the inner Galaxy makes it useful not only for proving theories about the interaction with stars in the nuclei of other galaxies, but also as a laboratory for studying physical effects on the ISM in some extreme conditions of UV field and shocks.

The goal of the present work is to study the molecular phase of ISM in the central parsec of the Galaxy to characterize its physical conditions. In the following sections a brief introduction of the Galactic Center environment – focusing on the central parsecs of the Galaxy – and a short description of the ISM physics and properties will be given. For a more complete review on the Galactic Center see Morris & Serabyn (1996); Genzel et al. (1994); Mezger et al. (1996). A review of the Central parsec has been published by Genzel et al. (2010). For a detailed review on Sgr A* see Morris et al. (2012). Latest results are provided by the conference proceedings of the IAU 303 Symposium (Sjouwerman et al. 2014).

1.2 The Galactic Center environment

The whole Galaxy contains a mass of around 10^{11} $M_\odot$ and extends for 14 kpc. The Solar system is located at ∼8.5 kpc from the Galactic Center, between two spiral arms.

The Galactic Center notion refers to a wide range of sizes: from several thousands of parsecs to the very immediate surroundings of the BH. In the following sections, a short description of the various gas and stellar structures of the Galactic Center shall be provided. These are ordered according to scales from few thousand parsecs to the geometrical center.

1.2.1 The Bulge and the Bar

Within 3 kpc from the center, the stars are arranged in an ellipsoidal bulge: the Galactic Bulge, extending down to 0.3 kpc. The stars here are of a late type and any present-day star formation seems to be lacking (Frogel 1988).

At the same distance scale, stars are distributed along a stellar Bar extending out to 2 kpc, with an axis ratio of 3 : 4. This Bar plays a role in matter inflow towards the inner few hundred parsecs (Morris & Serabyn 1996). Indeed, the Bar has the effect of deviating the gas from circular motion to elongated orbits because of cloud collisions. Shocks in these orbits compress the gas into molecular form. The orbiting gas loses angular momentum and it is driven inward at around 0.1–1 $M_\odot$ yr^{-1}. The gas can then end up forming stars (dominating processes 0.3–0.6 $M_\odot$ yr^{-1}; Güsten 1989), it can be lost as a thermally driven galactic wind (0.03–0.1 $M_\odot$ yr^{-1}) or it can accrete into the much smaller-scale Circumnuclear Disk (0.03–0.05 $M_\odot$ yr^{-1}; Sect. 1.2.5).

1.2.2 The Central Molecular Zone

At around 200 pc, gas density increases and the gas is mainly in molecular form. This region is usually referred to as the Central Molecular Zone (CMZ).

Here, there are many massive, high-temperature (30–200 K) and dense (10^4 cm^{-3};Ginsburg et al. 2015) molecular clouds with broad line width (10–30 km s^{-1}). Such densities are typical of clouds cores with a low filling factor, but they are required for the clouds to resist tidal shearing (Guesten & Downes 1980). The orbits of these clouds are not completely stable.

As previously discussed the gas which is not consumed in star formation is swept away through galactic winds – after entering a hot X-ray emitting halo – or it moves inwards towards the center. In the central parsec only a tiny fraction of the inflow material is currently accreted

by the compact source Sgr A*. The Limit Cycle hypothesis (Sect. 1.2.8) states that this inflow of material provokes stars formation, which temporarily turns off the inflow opposing strong winds to the incoming material (Morris & Serabyn 1996).

The CMZ is divided in two main structures:

- A high-velocity (130–200 km s^{-1}) component that appears as a continuous ring (the 180-pc molecular ring). This structure traces a H I/H_2 transition (Binney et al. 1991).
- A low-velocity ($<$ 100 km s^{-1}) component of massive and dense molecular clouds moving in the same plane as the Galactic plane (the Galactic Disk population). There are also filament-like clouds which are predominantly stretched arcs and gaseous arms (Bally et al. 1988).

The ionized gas in the same area is more uniformly distributed than the neutral one, indicating a more even distribution of heating sources.

Dust temperature decreases rapidly with increasing distance reaching 23 K at 200 pc. Hot dust (50 K) is located mainly in the inner few parsecs.

The X-ray spectrum of the inner 150 pc indicates the presence of many point sources as well as of a high-T plasma (1–15 keV; among others, Nottingham et al. 1993; Markevitch et al. 1993). Koyama et al. (1996) also note that the X-ray spectrum of the central 150 pc of our Galaxy is very similar to that of the Seyfert 2 galaxy NGC 1068. This diffuse emission could be the result of the explosion of a great number of supernovae ($\sim 10^3$). This scenario implies that the Galactic Center in the past released a greater amount of energy with respect to the activity we are observing today. Such past energy release is compatible with the idea of some past starburst episode.

An intense magnetic field pervades the central hundreds parsecs. It is perpendicular to the Galactic plane in the inter-cloud space while it is predominantly parallel in dense clouds (Ferrière 2009).

1.2.3 Sgr A

The central 30 pc are occupied by the compact Sgr A radio complex. This source was discovered by Piddington & Minnett 1951 and it was associated with the Galactic Center by McGee & Bolton (1954). Downes & Martin (1971) resolved the Sgr A into the extended synchrotron source Sgr A East and the compact, three-armed spiral-shaped, H II region Sgr A West (the Minispiral). Harvey et al. (1976) detected a double-peaked far-infrared dust surface brightness; later it was interpreted by Becklin et al. 1982 as emission from a dust torus surrounding the Galactic Center. Today, this feature is referred to as the Circumnuclear Disk (CND). At, or close to, the dynamical center of the Galaxy there is the compact source Sgr A* where most of the radio emission comes from.

1.2.4 Sgr A East

The Sgr A East structure is an extended (7 pc x 9 pc) synchrotron, shell-like source located at a projected distance of 2.1 pc from Sgr A*. In projection, Sgr A East encloses the ring formed by the CND which, in turn, encircles the Minispiral (Fig. 1.1).

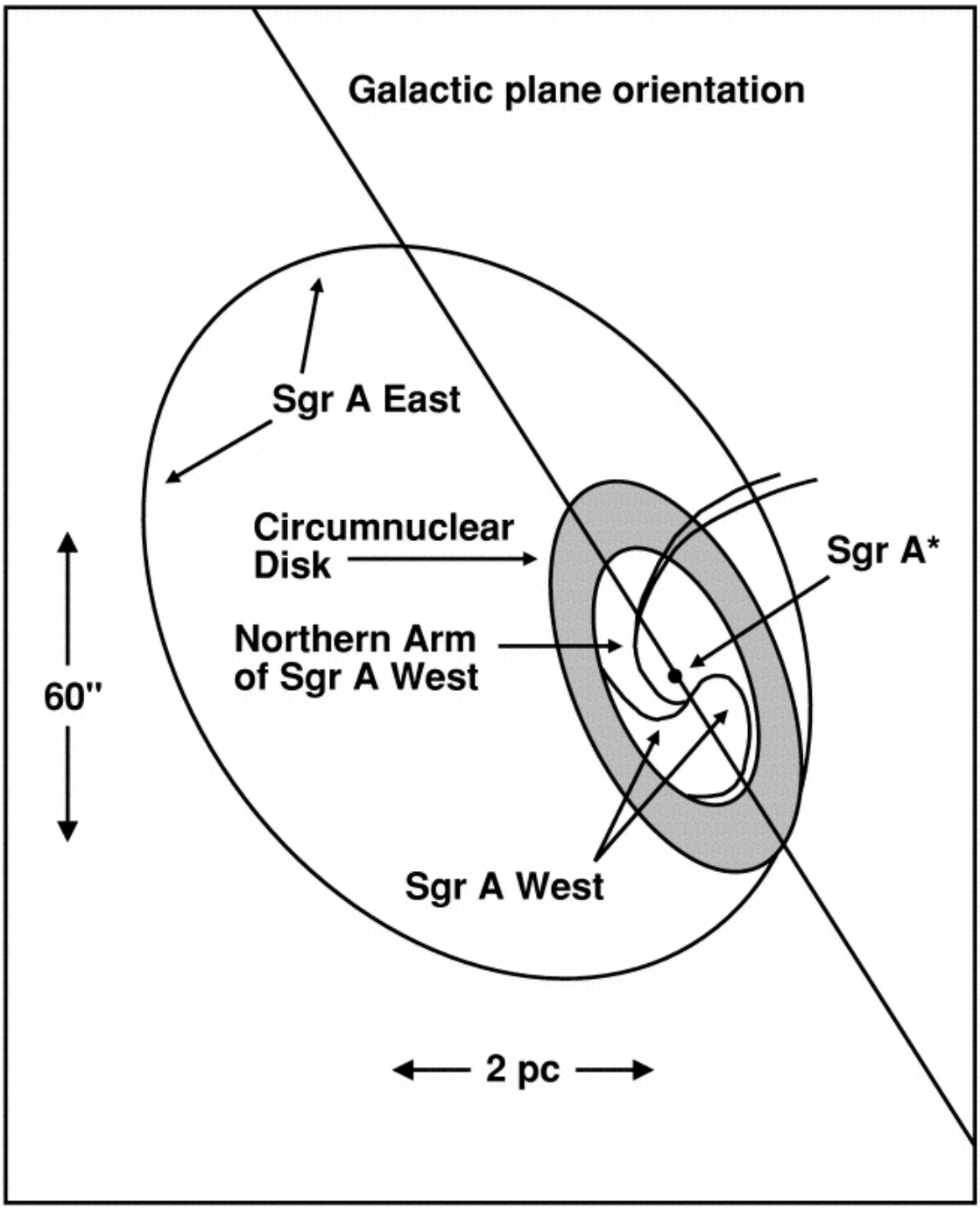

Figure 1.1: Schematic structure of the central few arcseconds (Baganoff et al. 2003).

The prevailing hypothesis is that Sgr A East has been created by an explosive event inside a dense Giant Molecular Cloud 5 10^4 years ago (Mezger et al. 1989; Zylka et al. 1990). This explosion may have also strongly affected the structure of the CND. At 80 pc around the Galactic Center the X-ray pervasive hot plasma has a similar expansion age. Both structures may come from the same event.

1.2.5 The Circumnuclear Disk

The CND is a compact, asymmetrical, torus of dust (Becklin et al. 1982) and molecular gas (HCN, Guesten et al. 1987; Christopher et al. 2005, CO, Guesten et al. 1987 and H_2, Yusef-Zadeh et al. 2001) which rotates around Sgr A* at 110 km s^{-1}, in the same direction as the general galactic rotation (Jackson et al. 1993). It is inclined with respect to the galactic plane.

The CND is fragmented in many clumps that have large velocity dispersions ($\sim$17 km s^{-1}) and are very dense ($\sim 10^{6-8}$ cm^{-3}; Christopher et al. 2005; Smith & Wardle 2014). The filling factor is around 10%. Due to this clumpiness, the UV radiation penetrates efficiently. The line width is large ($\sim$ 40 km s^{-1}) and implies a large inter-clump velocity dispersion caused by collisions and shocks. Outside of the CND there are several massive molecular clouds (Mezger et al. 1996).

The gas and dust temperatures are high (50–200 K for the gas and 50–70 K for dust, Becklin et al. 1982; Christopher et al. 2005, among others). The inner rim is hotter (few 100 K) and denser (10^{4-7} cm^{-3}) than the outer part. This rim is a Photon Dominated Region (Genzel et al. 1994, see Sect.1.3.5). The well-defined, sharp border is ionized by radiation supplied by the central star cluster.

Beyond its inner rim the CND distribution is highly asymmetrical: 7 pc at negative galactic longitudes while it extends to only 3 pc at positive galactic longitudes. The higher symmetry of the inner rim with respect to the outer part could be explained by the naturally shorter orbital time-scale. Despite its clumpy structure, the CND is usually modeled as a rotating ring. The CND has an inner radius of $\sim$1–1.7 pc and an outer radius of 3 –7 pc. The region it encloses is referred to as the Central Cavity.

The mass contained in the CND is around 10^6 $M_\odot$(Christopher et al. 2005), its density is in the range of 10^4–10^6 cm^{-3}. Most estimates of the mass and density are below the critical density required for stability against tidal disruption, implying that this structure is short-lived. However Christopher et al. (2005) have found higher densities and propose a longer lifetime for this feature. The present irregular appearance suggests a short lifetime as well since asymmetry suggests time-dependence. Its dynamical age is estimated to be around 10^5 yr (Guesten et al. 1987), i.e. around the same age as Sgr A East and the thermal plasma. Notwithstanding the above, there is presently no conclusive evidence to confirm either the stable scenario or the transient scenario. But, if the CND is a permanent feature, it must have a strong impact on the inner stellar cluster and it probably is a preferential star formation site.

In both scenarios the sharp inner edge and the large density drop in the Central Cavity have to be interpreted as transient features. This cavity is probably the result of the interaction between the inflow gas and the radiation provided by central star cluster (Guesten et al. 1987). The stars of this cluster are in a windy phase which pushes the gas away from the center. Once the source of this wind disappears, the gas accretion towards the central parsec may increase

again and lead to another star formation episode, coherent with the continuous but episodic Limit Cycle scenario (Morris & Serabyn 1996).

There are two main hypotheses about the origin of the CND:

- capture and subsequent tidal disruption of a passing giant molecular cloud;
- energetic disruption of a stable pre-existing disk.

Whatever its origin is, it might be connected to the expansion of Sgr A East. It is likely that the shell-like radio feature either compressed and pushed gas towards the center or disrupted a pre-existing disk. The Minispiral is also deeply connected to the CND as, for instance, the Western Arc of this H II region traces the inner edge of the CND. The interaction among all these structures is still unclear but they may interact or have interacted.

Mass inflow from the CND towards the Central Cavity is few 10^{-2} $M_\odot$ yr^{-1} (Guesten et al. 1987; Jackson et al. 1993). The magnetic field is high (0.5–2 mG) and may play a role in the disk dynamics and in angular momentum loss (Guesten et al. 1987; Morris & Serabyn 1996).

On the CND inner border, an emission from vibrationally excited H_2 has been detected. There are two main competing heating mechanisms for the CND (Gatley et al. 1986; Yusef-Zadeh et al. 2001):

- shocks, both dissipating the local turbulence and from winds of the Central Cavity;
- UV radiation, provided by the central star cluster.

The northeastern lobe of the CND is shielded from the UV field by the Northern Arm of the Minispiral. Therefore, at least in this region, cloud-cloud collisions are more likely to heat the gas. For the rest of the CND the observed emission can be due to UV fluorescence (Pak et al. 1996) or it might be a consequence of a strong shock caused by the central wind (Gatley et al. 1984, 1986). The central star cluster is likely the source of this wind (Yusef-Zadeh 1994). For instance GCIRS 16NW and 16SE2 are the sources of a 600 km s^{-1} and a 2 500 km s^{-1} wind respectively (Martins et al. 2007). This interpretation is supported by the fact that it would explain the large line width and the sharp transition observed at the CND inner border where gas is in a quasi-steady equilibrium between the wind and the turbulent disk.

1.2.6 Sgr A West and the Central Cavity

Inside this Central Cavity, at 1.7 pc the gas density drops by an order of magnitude or two with respect to the CND (from 10^{21} cm^{-2} at the center of the Central Cavity to 10^{23} cm^{-2} at the inner edge).

This cavity contains hot ($\sim 10^6$ K) X-ray emitting gas (Baganoff et al. 2003; Muno et al. 2004). X-rays maps also exhibit a number of point-like sources including a counterpart to the Sgr A* radio source. The Central Cavity contains 300 $M_\odot$ of neutral gas and few $M_\odot$ of dust (Davidson et al. 1992) in addition to the ionized gas (Jackson et al. 1993; Davidson et al. 1992). Within the Central Cavity the dust temperature rises as high as 300–400 K (Gezari, D. and Dwek, E. and Varosi F. 2003). This very hot dust is locally heated by the stars embedded into it, while warm dust (170 K) is heated from outside by luminous, hot He I stars. The innermost $10''$ contains a TeV source whose origin is not yet clear. As previously pointed out, this cavity

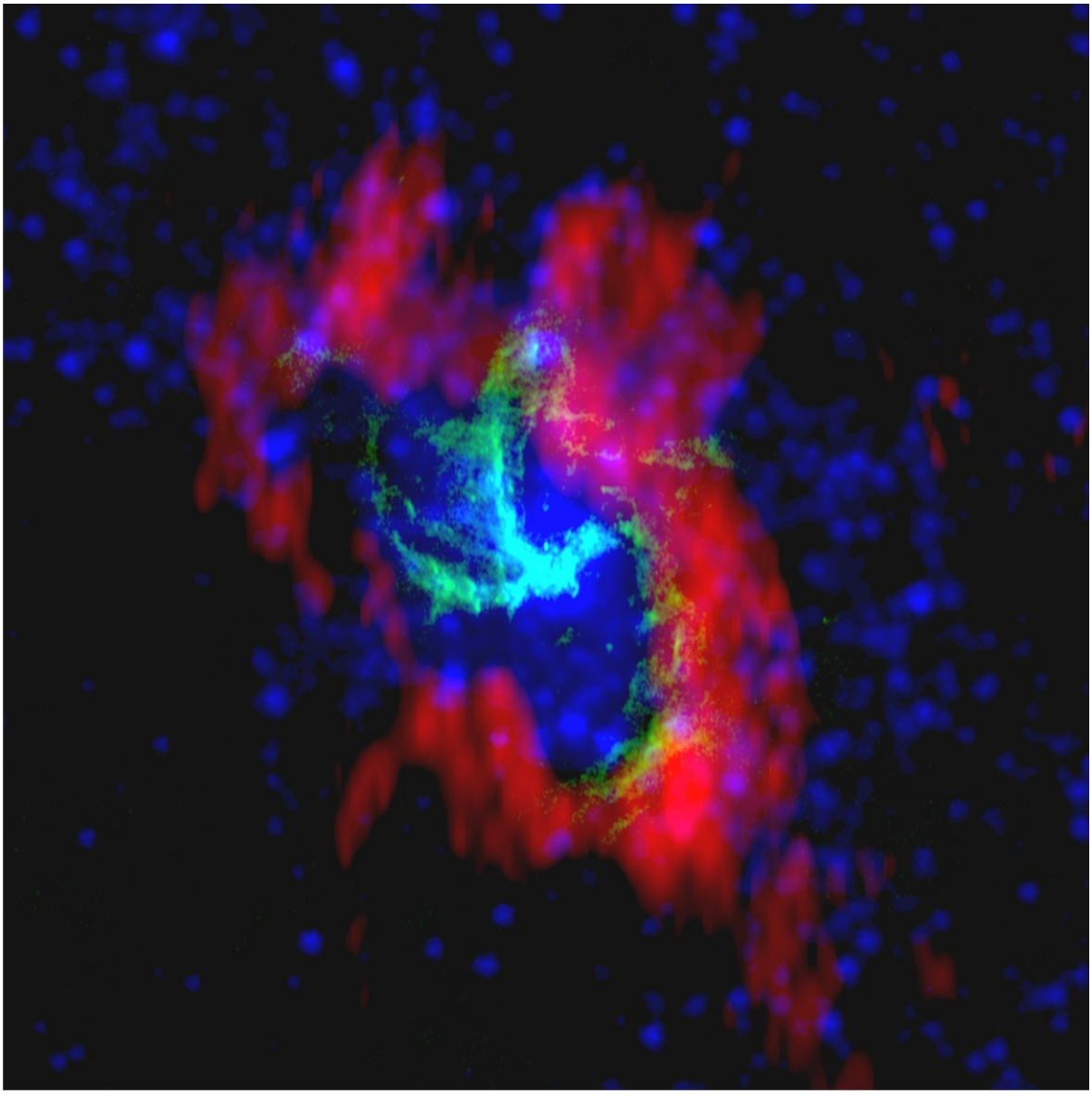

Figure 1.2: Combination of a radio image of the Minispiral (NRAO Very Large Array, green), HCN emission of the CND (BIMA, red) and infrared stars emission (NASA Spitzer Space Telescope, blue). Credits: F. Yusef-Zadeh (http://images.nrao.edu/667).

may be the result of the action of the wind produced by the young massive star being in a windy phase (Genzel et al. 1994; Morris & Serabyn 1996).

In the Central Cavity lies Sgr A West, an 2.1 pc × 2.9 pc ionized structure of density 10^3 cm^{-3} and H II mass of $\sim$ 250 M$_\odot$. It has been discovered thanks to the high angular resolution of the VLA (Lo & Claussen 1983; Ekers et al. 1983; Brown & Johnston 1983). This is an optically thin H II region, more filamentary than the surrounding CND.

The ionized gas appears, in projection, as a spiral feature (as showed by the 2 cm emission) and it therefore is referred to as the Minispiral (Lo & Claussen 1983). However, individual features of the Minispiral appear not to be confined to a single plane and the spiral shape is a projection effect (Paumard et al. 2004). The streamers of the Minispiral are photo-ionized by UV radiation provided by the massive young stars (see for instance Martins et al. 2007). The peculiar motions of the Minispiral arms may be the result of the interaction with stellar winds or of cloud-cloud collisions. The spiral features contain 15 M$_\odot$ and they are relatively smooth (Ekers et al. 1983).

The Minispiral is composed by a Northern and an Eastern Arm, a Bar and a Western Arc (Fig. 1.3). The Western Arc is the inner ionized border of the CND. The Northern Arm is the photoionized layer at the surface of a neutral cloud, referred to as the Tongue (here referred to as the Northern Arm Cloud), falling towards the center (Davidson et al. 1992; Telesco et al. 1996). Zhao et al. (2009) suggested that the Northern Arm and Eastern Arm may collide in the region of the Bar. The Northern Arm contains the Minicavity radio features: a nearly circular 2″ hole in the ionized streamers of the Minispiral, 3.5 ″ southwest of Sgr A* (Lutz et al. 1993).

The temperature inside the Minicavity are of 1–2 10^4 K as estimated from near-infrared (NIR) Fe III lines by Eckart et al. 1992). The CND eastern border is not ionized as it happens for the Western Arc. The reason can be the presence of the dense ($\sim 10^{22}$ cm^{-2}) Tongue which blocks the radiation. In the Northern Arm of the Minispiral, emission from a small amount of UV-pumped H_2 has been detected (Depoy et al. 1989; Lutz et al. 1996) as well as Fe II emission (Depoy 1992; Burton & Allen 1993). Fe II is detected in the Minicavity as well (Depoy 1992).

The origin of the Minispiral streamers is likely the infall of passing molecular clouds which are then stretched by tidal distortion (Ekers et al. 1983). The surface of these clouds would then be ionized by UV radiation and lead to the observed features (Paumard et al. 2004).

To summarize there is a cascade between scales: the massive molecular clouds orbiting in the CMZ are in a non-circular motion because of the presence of the stellar star Bar, hence neutral gas can spiral inwards and fuel the CND. In turn, it drops material into the Central Cavity, which, being illuminated by the UV field, is the origin of the observed Minispiral (Güsten 1989; Morris & Serabyn 1996; Paumard et al. 2004).

1.2.6.1 Stars of the Central parsecs

Stars located within the central parsec are responsible for the ionization of the gas and for the heating of dust within the Central Cavity.

The stellar density increases towards the center, from a few tenths of parsecs to the Central Cavity (Becklin & Neugebauer 1968; Catchpole et al. 1990). In particular, the central parsec

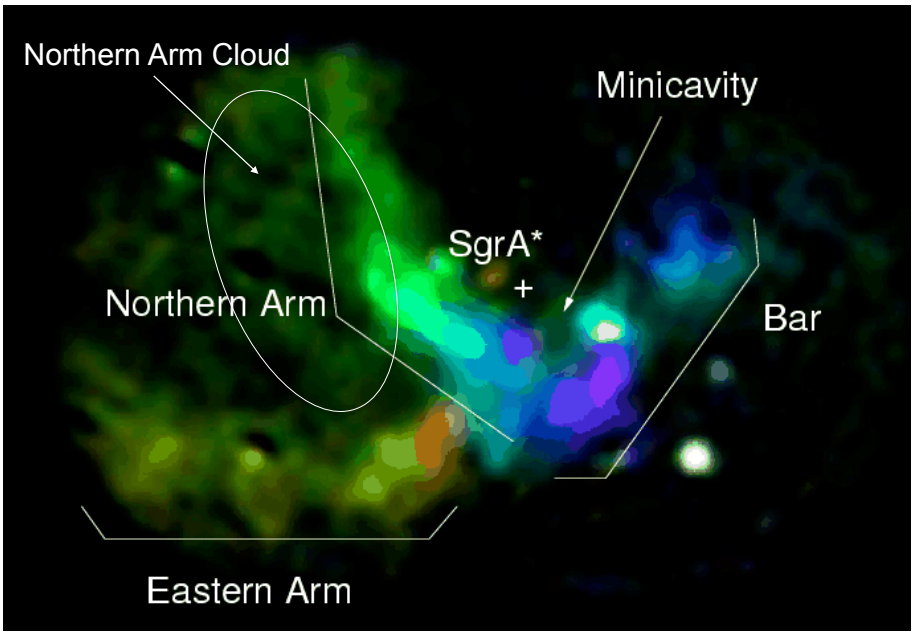

Figure 1.3: Image of the Brγ emission of Sgr A West. The velocity scales ranges between -350 (purple) and +350 km s-1 (red). Credits: Paumard et al. (2004).

contains a high number of hot early-type stars (Krabbe et al. 1995; Blum et al. 2003; Paumard et al. 2006; Bartko et al. 2009), making the Galactic Center one of the richest concentrations of such stars in the Galaxy. Star formation is recent in the central parsec (Rieke & Lebofsky 1982, for instance) and the young stars, mixed with old ones, dominate the luminosity. These stars are indicated as the cause of the windy phase which takes place in the central parsec. The early type stars are concentrated in the central 12″. GCIRS 16 is the brightest central condensation of this cluster of early type stars. The brightest star in the Galactic Center, GCIRS 7, is a red supergiant (late type star, Becklin & Neugebauer 1968), associated with the star formation event of the early type stars (Paumard et al. 2014b). Of the young (4–8 Myr) nuclear cluster more than 100 stars have been identified as Wolf-Rayet or OB stars (Allen et al. 1990; Ghez et al. 2003; Paumard et al. 2006; Bartko et al. 2009, among others).

There are at least two distinct dynamic populations. The first one is distributed on a clockwise disk and composed of very massive stars. These stars have formed because of fragmentation and instabilities in a massive gaseous disk 4–6 Myr ago (Genzel et al. 2000; Levin & Beloborodov 2003; Paumard et al. 2006; Lu et al. 2009). The second population is more isotropically distributed and there is an on-going discussion on a possible second disk (Genzel et al. 2003b; Bartko et al. 2009).

Stars contained within one arcsecond of the SMBH are referred to as S-stars. How these stars are formed that close of the SMBH is still unclear. The tidal forces of the BH should indeed strongly disfavor star formation. This problem is referred to as the "paradox of youth" (Ghez et al. 1998).

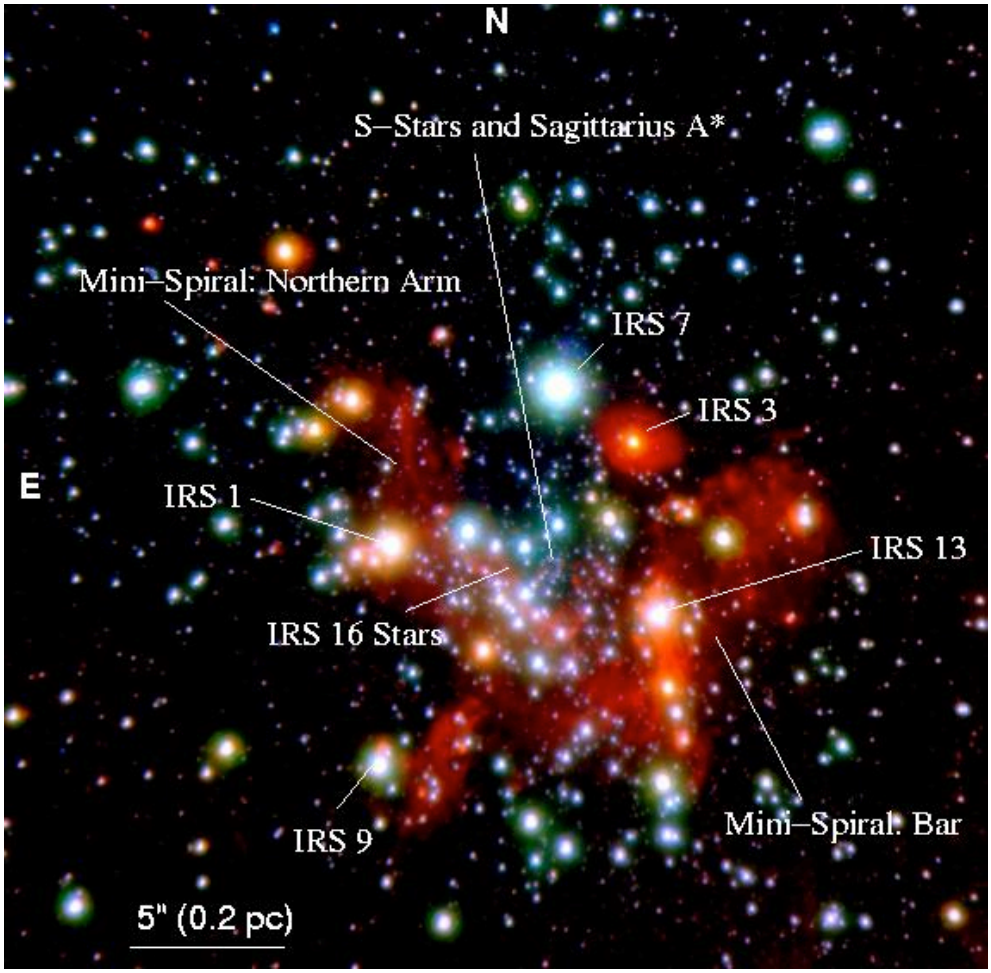

Figure 1.4: Stars of the central parsec imaged in the NIR by NACO at the ESO VLT. The red extended emission is due to gas and dust in the Minispiral or to circumstellar material of individual stars. Credits: Galactic Center webpage of the Physikalisches Institut, University of Cologne (https://www.astro.uni-koeln.de/node/235).

1.2.7 Sgr A*

The existence of a strong compact radio source at the Galactic Center has been at first observed by Lynden-Bell & Rees (1971). Sgr A* is located at the dynamical center of the Galaxy, embedded in the center of the extended components of Sgr A West, in front of the Bar of the Minispiral (Beckert et al. 1996).

The apparent size of Sgr A* depends on the wavelength but it is in the milli-arcsecond domain. This compact radio source (Balick & Brown 1974; Lo 1985; Yusef-Zadeh et al. 1986) is the most likely candidate for a central SMBH, even though it is much fainter than it could be given its mass.

Studies of the proper motion of the central stellar cluster suggested a mass of 2.6 10^6 $M_\odot$ confined within 0.015 pc (Eckart & Genzel 1997; Ghez et al. 1998). Schödel et al. (2002), Ghez et al. (2000) and Eckart et al. (2002) localized the mass within 30 mas,

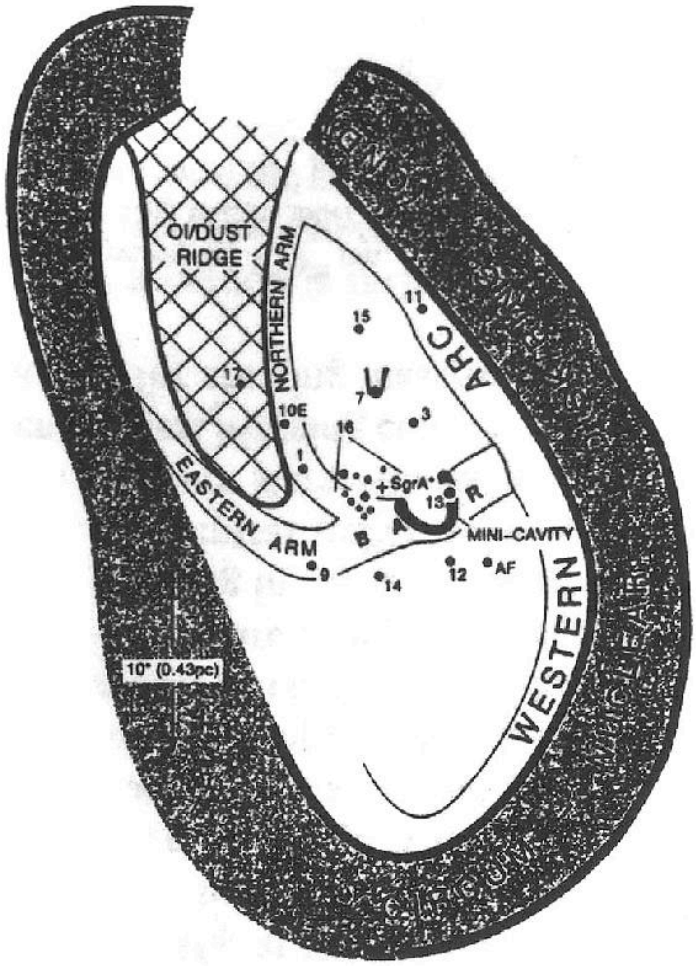

Figure 1.5: Scheme of the structure of the central parsec (Genzel et al. 1994).

strongly supporting the BH interpretation for Sgr A*. The inferred mass for the Galactic Center BH is considerably less than that inferred for BHs in most AGNs, but well in the range of Seyfert and normal galaxies.

If the Galaxy shows indeed a core activity too low to be an AGN on the other hand, the CND seems to be comparable to the obscuring tori that are responsible for differences in the various AGN classes. The formation of such tori appears to be a direct consequence of the presence of massive central BHs. Notwithstanding the above, there is no direct evidence for the presence of a standard accretion disk in the Galactic Center. While the present-day accretion into the BH seems to be rather low, there is plenty of gas and dust supply available in the inner 200 pc suggesting that different phases or activity might take place or have taken place.

1.2.8 Limit Cycle

In the Limit Cycle scenario, exposed by Morris & Serabyn (1996), the Galactic Center activity begins when a cloud passes close enough to be captured and starts the accreting processes. This cloud is disrupted and it forms an asymmetrical disk, like the observed CND. Instabilities

or inter-clump collisions could, in a relatively short period (10^4 yr), transfer gas into the central potential well defined by the central star cluster (0.2<r<1.2 pc). This inflow would then be accreted by the central compact object or would contribute to the star formation. The following phase would be a windy period with radially propagating winds, radiation and energy. Such an outward movement would reverse the flow through winds (from O and Wolf-Rayet) and high mass outflow. Gas clouds would be pushed away and be mixed with the orbitally moving gas preventing it from falling inwards. As stars evolve (few 10^6 yr) they would explode in Supernovae. At this point a fraction of the gas would be able to start falling inward again, pushing against the central stars wind.

According to the described situation, the windy phase is the phase in which the Galactic Center is observed now. Since the gas is not smoothly distributed it could be the sign that there are recurrent periods of the SMBH accretion. The possible scenario to describe the Galaxy is thus an oscillation between Seyfert and starburst periods, separated by a quiet period.

1.3 Interstellar medium

While on one hand star formation is considered to be the motor of galaxy evolution, on the other hand the space amid stars is filled with very structured and varied gas and dust. The interstellar medium (ISM) plays a fundamental role in every phase of star formation as well as in all the processes taking place in galaxies (Dalgarno 2000). The center of the Milky Way galaxy is no exception in that respect. A very complete description of ISM properties and physics is provided by R. Pogge notes[1] and Tielens (2010). A very complete review on molecular hydrogen is provided by Habart et al. (2005).

Having R. Pogge notes as basis, in the following sections, a brief summary of the ISM main features will be given, focusing on its most abundant molecule: H_2.

1.3.1 Studying the ISM

The first evidence of the existence of a gas pervading the space amid stars has been inferred in the 19th century thanks to the observations of nebulae where the clouds cannot be resolved in individuals stars (for example the diffuse nebula of Orion).

The bright and diffuse nebulae are, in fact, regions where the gas surrounding a hot star is photoionized by its radiation. It is the case of H II regions where the interstellar gas is ionized and heated by the UV radiation produced by O and B stars. In planetary nebulae the excitation mechanism is similar but the origin of the UV radiation is a white dwarf illuminating the ejected stellar envelopes in a dying star. In the case of Supernova remnants, the gas is ionized by the passage of the shock wave expanding into the ISM of Supernova type I or II; in this case the heating is mechanical. However 90% of the H^+ is located outside H II regions, in the warm ionized medium.

H_2 is the most abundant, but also the most elusive molecule in the ISM. First observations of interstellar H_2 were made in the 70s as absorption UV lines towards hot stars. Later

[1] http://www.astronomy.ohio-state.edu/~pogge/Ast871/Notes

H_2 rotational-vibrational collisionally-excited lines were observed in the NIR. However most of the cold (10 K) H_2 remains invisible.

The satellite IRAS, ISO, SPITZER, HERSCHEL, WMAP and COBE have observed the ISM in the infrared and in the far-infrared providing maps of dust and molecular emission of the Galaxy and of other galaxies.

1.3.2 Physics of the ISM

In general the ISM is far from being at thermal equilibrium and it is characterized by different thermal phases. Even though there is no thermal equilibrium, other equilibriums may apply: kinetic equilibrium in cold neutral clouds, excitation equilibrium for population that follows a Boltzmann distribution, ionization equilibrium when the photoionization equilibrates recombination and pressure equilibrium between cold and warm components. The gas is generally at pressure equilibrium, at least at large scales, especially for the atomic medium.

The ISM gas phase is composed for 90% of hydrogen, 10% helium, 0.1% of metals and is present in different phases (Molecular clouds, H I absorption/emission, H II emission). Molecular clouds are primarily composed of H_2, at 10–20 K with a density of 10^3 cm^{-3} on average but they are mainly traced by CO emission lines. Warm ionized medium of H II regions have temperatures between 6 000 K and 12 000 K with a density of 0.1 cm^{-3} in 25% of the volume. This gas can be traced by recombination lines such as Hα and radio Bremsstrahlung emission.

Dust is mixed in all these phases (except the hottest) and plays a fundamental role in each. It is the cause of interstellar extinction and the site of interstellar chemistry, especially of H_2 formation. Dust grains are produced by stars in their post-AGB phase while expelling their envelope. The composition of grains and their size distribution are rather well known thanks to various observational constraints. It consists of a mixture of carbonaceous and silicate grains with a wide range of sizes (from 1Å to few microns). Wavelength-dependent extinction by dust grains through scattering and absorption results in the obscuration and reddening of objects.

1.3.3 Molecular clouds structure and properties

Most of the knowledge on clouds has been acquired through CO observations which showed that the clouds are very clumpy. They have dense cores of typical size $<$1 pc and a density of $>10^6$ cm^{-3}. The clouds have a size in the range 3–20 pc and a mean density of 10^{3-4} cm^{-3}. Clouds are generally organized in larger complexes of 20 –100 pc with masses up to 10^{4-6}M$_\odot$.

1.3.4 Molecular hydrogen

Molecular hydrogen is the stable form of H at low temperatures and it dominates the ISM. It plays an important role in processes regulating star formation and the evolution of galaxies since:

- It represents the earliest stage of condensation of ISM matter to form stars;
- Formation of H_2 on grains initiates the chemistry of interstellar gas;

Moreover many competing mechanisms could contribute to its excitation and thus it can probe a wide range of distinct environments.

H_2 forms on dust grains starting at 10 K and can be destroyed by UV. For H_2 to exists there has to be a sufficiently large regions shielding it from UV photons (A_V ∼0.01–0.1 mag).

Being a highly symmetric molecule, it has no permanent dipole moment and only electric quadrupole transitions may occur with small transition probabilities (A-values) and high excitation energies. Therefore H_2 is excited only at high temperature or in strong UV radiation fields. H_2 lines are thus generally of negligible intensity except in unusually warm regions (500–1000K), like near hot stars and active star forming regions.

According to Combes & Pineau Des Forets (2000), most of H_2 may hide in cool, shielded regions where the excitation is too low to be detected through emission lines. These peculiarities make H_2 detectable only in particular environments, as studied in the present work, while the bulk molecular gas is generally studied through CO. The formation of this molecule occurs under specific conditions, which are favorable for H_2 formation too. H_2 is thus estimated from observed quantity of CO, in particular the CO J=1-0 line at 2.6 mm.

Otherwise H_2 is directly observable in two cases. The first case is the absorption at far-UV wavelengths in the diffuse ISM. This is the only direct proof of the cold H_2 which represents most of the ISM. The second case is the NIR emission of rotational-vibrational lines in warm regions (500–2000 K) where H_2 is excited by shocks or UV-fluorescence. H_2 have been mostly studied in the 2.12 μm rotational-vibration line 1-0 S(1). This line has been mainly detected in shock regions and PDRs.

The detection and study of NIR H_2 emission in the central parsec is the main subject of this thesis. A brief introduction on its physical properties is given in the following sections. A more detailed discussion on its excitation mechanisms will be provided in Chapter 4.

1.3.4.1 NIR vibrational rotational emission lines

Each electronic state has a set of rotation-vibration levels which are characterized by a vibrational quantum number, v, and a rotational quantum number, J. Permitted transitions are listed in Table 1.1.

name	ΔJ
O	-2
Q	0
S	+2

Table 1.1: Rotational-vibrational transitions notation is $v_{upper} - v_{lower}$ X(J_l) where X = O, Q, S of table above and $\Delta J = J_{upper} - J_{lower}$. The first is 0-0 S(0) at 28.2 μm, the others are at shorter wavelength and higher energies. Pure rotational transitions are found down to 3.4 μm followed by vibrational-rotational lines in the range 1–4 μm, clustering around 2 μm.

The H_2 molecule has two spin states: the ortho (triplet) state, with parallel nuclear spins, and the para (singlet) state, with anti-parallel nuclear spins. Odd-numbered transition lines correspond to ortho states while even-numbered transitions match para states. For thermalized

populations the ortho-para ratio (OPR) is 3, following the spin statistics. There are several observations which report OPR different from 3 (Fuente et al. 1999, for instance). Deviations from this ratio can appear for radiative de-excitation from the Lyman-Werner bands which are the sign for UV excitation (fluorescence). Sternberg & Neufeld (1999) pointed out that, in the case of fluorescence, a OPR smaller than 3 is the result of different optical depth, in the UV-pumping, for ortho- and para-H_2. Nevertheless OPR could be actually smaller than 3 as the result of dynamical processes bringing colder gas into the PDR, or to fast conversion from ortho- to para-H_2 during the molecule formation on grains surface (Le Bourlot 2000).

1.3.4.2 Excitation

For excited H_2 to be detectable, the excitation temperature has to be >1000 K. Excitation can be probed by excitation diagrams, where the column density of a state is plotted against the corresponding upper state energy (see Chapter 4, Sect. 4.2).

The possible excitation mechanisms are the following:

Collisional excitation: in this case the gas is heated by shocks. It affects low-J levels, exciting the molecule in a bottom-to-the top way. It happens for shocks at a speed greater than 6 km s^{-1} but lower than 25 km s^{-1}; above such speed the shock would dissociate the molecule. The typical resulting temperature is around 1000 K but lower than 4000–5000 K. Little emissions is produced from transitions with $v \geq 3$. Fe II often traces shock regions as well; thus a correlation between the spatial distribution of the two species should be an indication of this excitation mechanism. For high density the population is thermalized and the kinetic temperature approaches the physical excitation temperature of the gas. A range of temperatures is also possible while integrating on the line of sight. Below a certain (critical) density, the population levels starts to deviate from thermal equilibrium. This density depends on the colliders: for H_2–H_2 collisions it is 10^{5-6} cm^{-3}, for H^0 it is 10^3 cm^{-3}.

UV fluorescence: this excitation happens in the neighborhood of stars emitting mainly UV and it depends strongly on the UV intensity. A UV photon is firstly absorbed in the Lyman/Werner bands. Then this excitation is followed by a radiative de-excitation into the ground state. Some of this de-excitation (∼12%) will go into the dissociation band while the rest will go to bound levels, resulting in a pumping of the population. The excitation temperature of rotational states, within a given vibrational level, is different from the temperatures among different vibrational levels, given a rotational state. The excitation diagram can thus be split in distinct diagrams with separate curves by vibrational state, as the result of the different effects on different v-levels. On the contrary, in collisional shocks, these temperatures are the same. Another signature of this kind of excitation is a significant populations level for lines with v>4. However sometimes it is difficult to distinguish between collisional excitation and fluorescence because under certain conditions they can give similar diagrams.

Formation excitation: when a H_2 molecule is formed, the resulting binding energy has to be redistributed between heating of the dust grain, kinetic energy ejecting the molecule,

and excitation of the newly formed H_2 (see Sect. 1.3.4.3). This can result in the excitation of rotational-vibrational states.

1.3.4.3 Formation and destruction

The most common formation process is grain surface catalysis. This process implies a H colliding on a dust grain, where it sticks. This requires that the grain is not too hot, as high temperatures would lower the atom adherence to the grain. The H atom migrates on the grain until it reaches a site where it is more strongly bounded (by chemisorption or physisorption). Here, it more likely sticks long enough to encounter another H atom and reacts to create H_2 releasing a 4.5 eV energy. This energy heats the grain (resulting in a IR emission from dust later), ejects the molecule and/or gives vibrational energy to the molecule which is later radiated away as NIR emission.

The most efficient H_2 destruction is via the absorption of UV-photons. However, the photon absorption leads to dissociations only in 12% of the cases while in most of the cases it produces fluorescence excitation.

Starting from column densities of N=10^{14} cm^{-2} and then scaling as the $N^{3/4}$, Lyman and Werner bands start to become optically thick. All photons that could photodissociate the molecule are absorbed in the outer layer of the cloud, shielding the H_2 material within it. Dust also plays a role in shielding the molecular hydrogen from absorbing photons. Self-shielding allows H_2 to survive in the UV radiation field of the diffuse ISM. This effect happens in diffuse clouds exposed to the interstellar radiation field (ISRF) and in dense clouds, close to UV sources (e.g. H II regions, reflection nebulae around early type stars).

1.3.5 Photon dominated regions

In a photon dominated region (PDR), the UV radiation field illuminates the warm and partially ionized surface of molecular clouds. Therefore, PDRs separate the cold gas of the molecular clouds from warm, ionized gas. Here H_2 is dissociated into H I. This transition region contains atomic H as well as H_2. Because of the strong relationship between dust and H_2, PDRs show far-infrared emission from hot dust as well.

The two main parameters regulating the PDR properties are the UV-radiation intensity and the gas density. The UV field can be provided by discrete sources, like early O and B stars. In this case one will observe H II regions, separated from H_2 by an H I/H II thin interface. On the other hand if late type stars, or the ISRF, provide the radiation field, there is little or no H II and a sharp H I/H_2 interface, because of self-shielding. Dust limits UV penetration and it is the dominating effect at $A_V > 2$. CO is dissociated at the surface of the clouds, again, because of self-shielding. The temperature peaks at the H/H_2 interface where the high-energy photons heat the gas. After this boundary the temperature decreases to 10–100 K.

PDRs are the most important source of H_2 emission. At sufficiently high densities (>10^4 cm^{-3}) H_2 is maintained in thermal equilibrium and low levels are consistent with a Boltzmann distribution. For a complete review see Hollenbach & Tielens (1999).

1.3.6 Shock regions

Shock regions are sources of H_2 emission as well. Among the causes of shocks, one can find outflows and jets, supernovae and expanding H II regions (Draine & McKee 1993; Hollenbach & Tielens 1997). The mechanical energy of the shock heats the gas. If the shock does not dissociate the molecules, they can become warm enough to be collisionally excited. Typical temperatures are 2000–3000 K. Orion OMC-1 (Rosenthal et al. 2000) is an example of shock-excited H_2 emission.

1.4 Aims of the thesis's work

Observing the ISM in the Galactic Centre is a challenge due to the large interstellar extinction and the large number of bright, emission line stars. High spectral and spatial resolutions are necessary to disentangle the stellar and interstellar components. Moreover, because of the high extinction due to 8 kpc of dust, the Galactic Center is observable only at longer (infrared and radio) or at shorter (hard X-rays and γ-rays) wavelengths than the visible domain. The development of new instruments and techniques at all wavelengths, over the past decades, has permitted outstanding progresses in the knowledge of the Galactic Center.

The Galactic Center presents many unanswered issues, such as the "paradox of youth" of the S-star cluster. Star formation in this extreme environment should be inhibited by the intense magnetic field and by gravity. Yet many young stars are observed in this region. For what concerns the central parsec scale, the stars were formed in a massive disk. However the question of the formation of S-stars in the central arcsecond remains unanswered.

The low accretion rate of the central BH is not explained either. At present there are no observations of the BH accretion disk. However, the observed emission (NIR and X-ray flares) comes from the close surroundings of the BH. This is the indications that there must exist an accretion structure. New instruments and experiments such as the EHT (Ricarte & Dexter 2015) and GRAVITY (Eisenhauer et al. 2008; Gillessen et al. 2010) will make the most inner region of the Galactic Center accessible.

Another open issue is the motion of the gas from one scale to the other. The problem is to understand the mechanism that causes angular momentum loss and, consequently, provokes the inward fall of the gas.

Even though the stability of the CND is still a matter of debate, if its clumps are unstable, the great velocity differences can easily result in an infall of a cloud into the Central Cavity. In this case the Minispiral would be the result of this infall when the stretched clouds, teared off from the CND – or alternatively swept away by Sgr A East – are illuminated by the strong radiation field. In this inflow process the Northern Arm will probably accrete onto the BH, unless it is eventually swept away by an energetic event, such as the Supernova explosion of one of the evolved stars of the central parsec.

In this picture, the role of the ISM in interaction with the extreme environment of the central parsec, is important to characterize this complex area. The aim of the present work is to study the ISM molecular phase (H_2) in an area where the neutral CND leaves space to the ionized Minispiral. H_2 is expected to be destroyed in the Central Cavity because of the strong UV radiation. However, it is observed almost everywhere.

More importantly, Gatley et al. (1986) indeed detected molecular gas emission inside the Central Cavity of the CND. The analysis of HCN and O I by Jackson et al. (1993) led to the detection of a large amount of neutral gas associated with the streamers of the Minispiral and several dense and distinct streamers at the edge of the CND. Yusef-Zadeh et al. (2001) detected molecular hydrogen (H_2) in the inner edge of the CND.

The purpose of this work is to make a step further and extend the search and study of H_2 in the central parsec, characterizing the gas distribution, dynamics and excitation with the best angular resolution. In particular, spectro-imaging data in the NIR, taken with integral-field spectrograph SPIFFI (VLT/SINFONI without the adaptive optic) has been analyzed. The observations are seeing-limited (FWHM 0.75″), and at a spectral resolution R = 1 300. In this dataset we detect half-a-dozen of rotation-vibrational H_2 line which allow us to separate the gas emission from discrete sources and to study spatial distribution, dynamics and excitation of the molecular gas.

In Chapter 2 we present the observations, the applied calibration and the analysis methods applied, in particular the original regularized 3D-fitting method. In Chapter 3 this method is applied on some of the detected H_2 lines to study the distribution and dynamics of the gas. Maps of the line flux, radial velocity and line width are provided. In this same Chapter the extinction is computed through the ratio of two of the observed lines and a model to describe its local and foreground effect is proposed. In Chapter 4 all detected lines are simultaneously analyzed through a more classical 1D fit to characterize the gas excitation, temperature and mass on several zones across the field and investigate the CND and Central Cavity physical conditions. In Chapter 5 we give a summary of the findings of this work to draw the conclusions and perspectives.

Chapter 2

Dataset and Analysis method

Contents

This chapter is devoted to the description of the dataset that we have used and the methods that we have applied.

The present work consists in the analysis of one specific NIR spectro-imaging dataset. Spatially and spectrally resolved observations are of great interest for the understanding of the Galactic Center region. The combination of spatial and spectral resolution is required to disentangle separate contributions from distinct sources which are often spatially overlapping in this crowded environment. A spectro-imaging dataset is thus well suited for the study of ISM: it allows to access detailed spectral information of a spatially extended source (such as the ISM).

In the previous Chapter it has been discussed that the observation of H_2 emissions lines is possible only in a particularly warm environment. The Galactic Centre is an example of such an environment: a quick look at the dataset, before any treatment, shows that some of these H_2 lines are clearly detectable in the central parsec.

The dataset spectral range covers several H_2 lines but sometimes the emission has a very low signal-to-noise ratio. To overcome this problem, a new method is applied: the regularized

3D-fit (Paumard et al. 2014b). It consists in a global fit of an observed line over the field of view, taking into account the fact that neighboring pixels must be correlated.

In additions to this method a more classical fitting analysis is applied on some selected regions for lines that do not present a signal-to-noise high enough in the whole field.

2.1 Dataset

The dataset was acquired during the first observing runs of the integral field spectrograph SPIFFI (Eisenhauer et al. 2000) as a guest instrument at the VLT in March and April 2003.

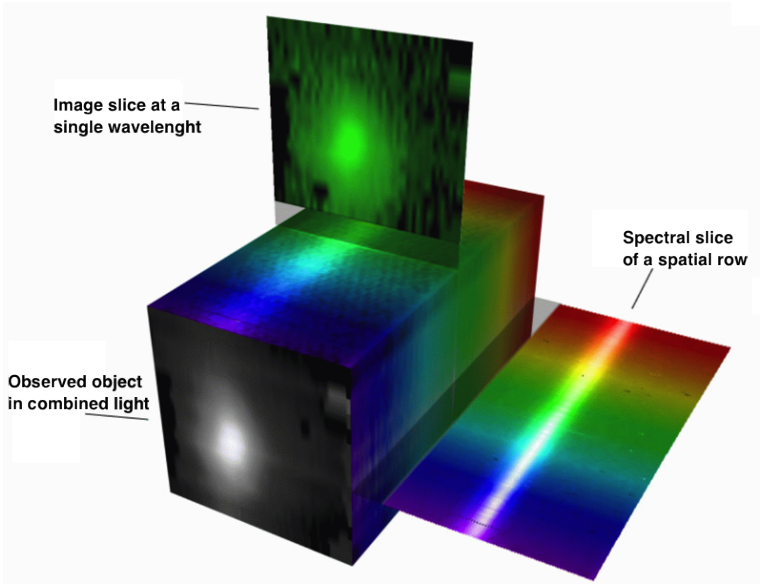

Figure 2.1: Illustration of a typical integral field spectroscopy data cube. There are two spatial-dimensions and one spectral-dimension, i.e. a spectrum corresponds to every pixel of the field of vied. Credits: Stephen Todd (ROE) and Douglas Pierce-Price (JAC), http://ifs.wikidot.com/what-is-ifs.

2.1.1 Integral field spectroscopy

Integral field spectroscopy (IFS) allows gathering spectra of a two-dimensional field of view. The dataset final format is that of a data cube, with two spatial dimensions and one spectral dimension (c.f. Fig. 2.1). It means that a spectrum corresponds to each spatial pixel of the 2D observed field.

The classical imaging spectroscopy uses scanning techniques. Wavelength scanning techniques are used to observe a large field of view, obtaining restricted wavelength ranges. Slit scanning instead allows to obtain a larger spectral range, but only for a small field of view. The main problem of these techniques is that data has to be taken in a temporal sequence. In the NIR, especially for the study of extended sources, this causes many difficulties because of

the variability of the atmosphere background, which affects each sequence in a different way. For compact sources scanning techniques are not optimal either since most of the information is concentrated just on a small part of dataset. Moreover, scanning is time-consuming.

IFS alleviates the disadvantages of traditional imaging spectroscopy since the spectra of all the pixels of a 2D-field can be obtained simultaneously. All spectra taken with an ISF are equally affected by the atmosphere, resulting in a much improved relative calibration. There is also a much reduced integration time. The disadvantage is that both spatial and spectral resolutions have to be compromised for the combination of the two types of data. IFS instruments are very well optimized in the NIR. For instance slicers – which have the role of decomposing the 2D image in a 1D slit – can be easily cooled making them well adapted to IR observations.

Various spectral and spatial features of a single object (or multiple objects) in the field of view can be studied efficiently. IFS is thus very well suited to study the gas morphology and dynamics. For instance, simultaneous study of several spectral lines and their relative variations across a wide field of view can be studied. Concerning the ISM, much of the information resides in the relative intensities of lines to derive temperature and excitation mechanism. Also extinction correction can be derived from the comparison of lines of the gas itself. When comparing lines of different chemical species, IFS allows minimizing the error linked to the compatibility of distinct observations while keeping the observed field of view sufficiently wide to observe the spatially extended features.

IFS is thus a very versatile technique. The same dataset can be used for many different analysis. For instance, the dataset analysed in this work has been taken with the prime objective of studying the star population of the central parsec. Among others, Horrobin et al. (2004) published the observation of two rotating stellar rings in this region obtained with this same dataset. Even though the dataset primary objective was the study of stars, because of the wide spectral range and the richness of sources in the Central parsec, it is perfectly suited for the study of ISM, in particular H_2.

In the following section a brief description of the SPIFFI instrument will be provided along with the applied calibration. The detailed description of SPIFFI is provided by Eisenhauer et al. (2000); Tecza et al. (2000).

2.1.2 SPIFFI instrument

SPIFFI (Spectrometer for Infrared Faint Field Imaging) is the integral field spectrograph of the SINFONI instrument at the VLT. SINFONI is the combination of SPIFFI with the adaptive optics system MACAO. With SINFONI, adaptive optics was offered for the first time to NIR IFS at an 8-meters telescope.

SPIFFI has been assembled at the Max-Planck-Institute for Extraterrestrial Physics (MPE, Eisenhauer et al. 2000). It consists of an image slicer that decomposes the 2D observed field of view into a 1D pseudo-slit that feeds a grating spectrometer equipped with an array-detector. The SPIFFI image slicer was under development before the complete project of SINFONI started and thus it was ready before the adaptive optics module. The instrument was then installed at the VLT as guest instrument for seeing-limited observation in 2003.

SPIFFI has been constructed with the aim of gathering medium-resolution spectra in a

2D-field in a single exposure covering J (1.1 – 1.4 μm), H (1.45 – 1.85 μm) or K (1.95 – 2.45 μm) spectral bands. H and K bands can be observed together in a combined mode at a lower spectral resolution. At the time of design of the instrument, the largest IR detector was of size 1024×1024. In order to maximize its exploitation, 1024 pixels (i.e. 32×32 pixels in a 2D field) can be dispersed simultaneously to obtain spectra of 1024-channels each. SPIFFI has three pixels scales: 250, 100, 25 mas/pixel. The observations used here have a 0.25″ pixel scale which leads to a field of view of $\sim 8'' \times 8''$.

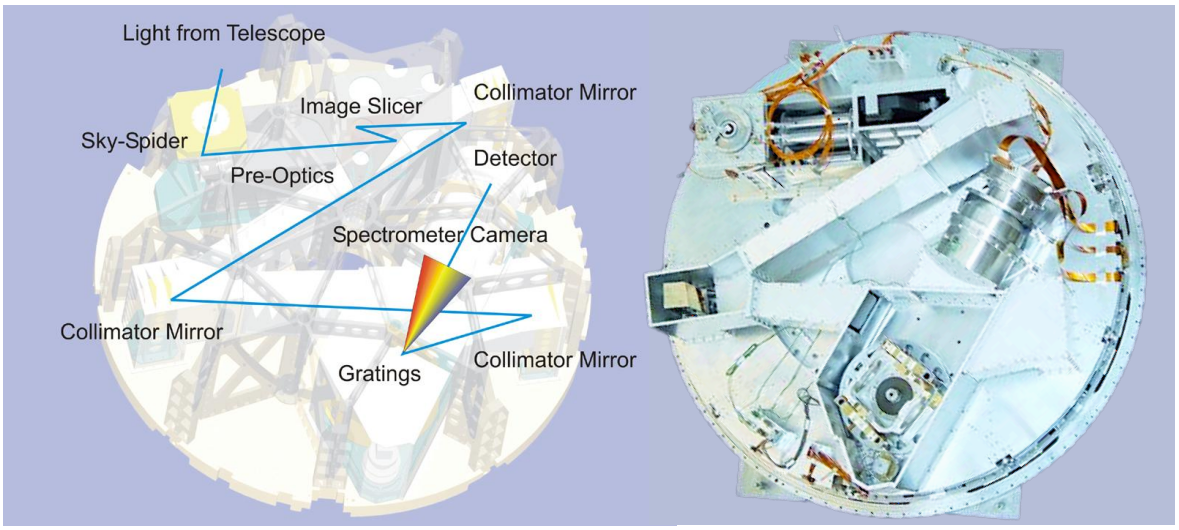

Figure 2.2: *Left:* Illustration of light path inside the instrument from MPE Annual Report http://www2011.mpe.mpg.de/JB2001/kapitel3-2.html *Right:* Picture of SPIFFI from ESO VLT SPIFFI webpage http://www.eso.org/sci/facilities/paranal/instruments/sinfoni/inst/instrument.html.

The design of SPIFFI is illustrated in Fig. 2.2. The light coming from the telescope (and from the adaptive optics in the case of SINFONI) first passes through a "sky-spider", which has the function of reflecting the light up to 45″ away from the object, allowing the simultaneous observation of the sky background. The light then arrives onto the image slicer where the 2D-field is decomposed and rearranged as a pseudo 1D slit, which then feeds the spectrometer.

The SPIFFI image slicer consists of two parts: a small and a large slicer. The small slicer is a stack of 32 mirrors tilted at different angles. It is placed at the telescope focal plane. The observed field of view, received from the telescope, is separated into 32 slitlets. The principle is displayed in Fig. 2.3. The 32 slitlets reflect the light on the large slicer which consists of two layers of mirrors arranged in a brick-wall pattern. These mirrors rearrange the strips to form a contiguous pseudo-slit.

The light of the pseudo-slit is collimated on the gratings which disperses every pixel before the camera optics focuses the spectra on an HAWAII detector of 1024×1024 pixels.

The image slicer is completely made of zero-expansion-glass to avoid differential thermal contractions. All parts are optically contacted, i.e. all surfaces are held together by intermolecular forces only. Optics and detectors are cooled to 77 K in a liquid nitrogen cryostat.

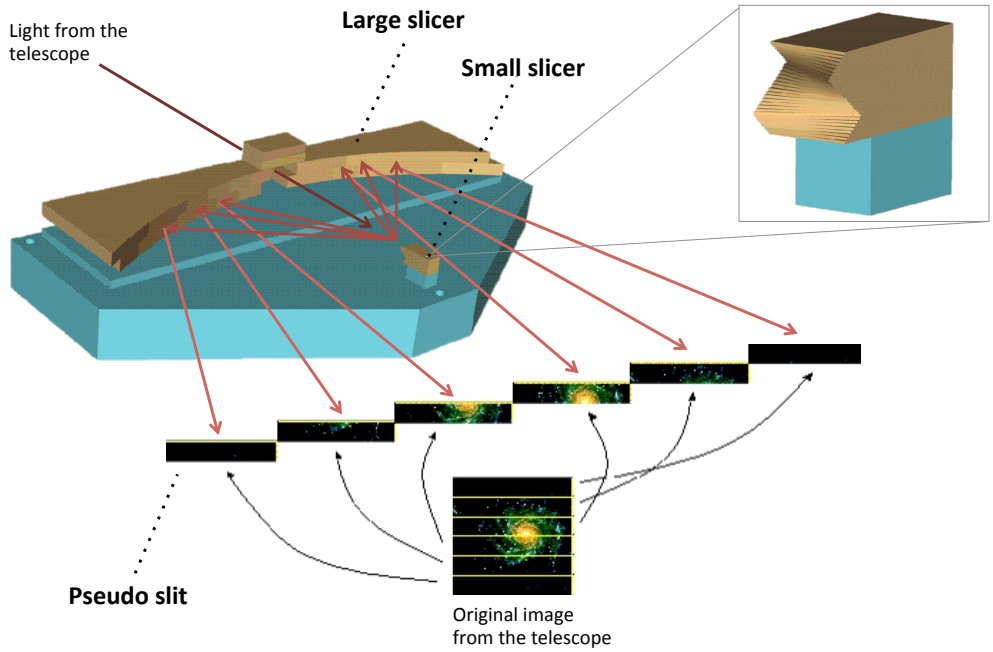

Figure 2.3: Simplified illustration of SPIFFI image slicer (only 6 slices are shown instead of 32). The 2D field of view of the telescope is separated in several slitlets by the small slicer. The large slicer rearranges the slitlets to form a pseudo-slit that feeds the spectrograph. Adapted from Tecza et al. (2000) slicers images and pseudo-slit illustration from ESO VLT SPIFFI webpage http://www.eso.org/sci/facilities/paranal/instruments/sinfoni/inst/instrument.html.

The spectral resolution is about 3 500 in K-band, 2 500 in H-band, 2 000 in J-band and 1 300 in H+K mode.

The raw data consist of a frame of 1024 spatial pixels in the x-direction and 1024 spectral pixels in the y-direction. Because of their particular format, SPIFFI dataset requires its own data reduction software, described in Schreiber et al. (2004). The pipeline software resamples the raw data on a linearized wavelength scale and composes the final datacube: 32×32 spatial pixels and 2560 spectral pixels. At a specific wavelength the datacube yields the corresponding monochromatic image. The pipeline also applies the standard processing such as sky subtraction, flat-fielding and bad pixel interpolation.

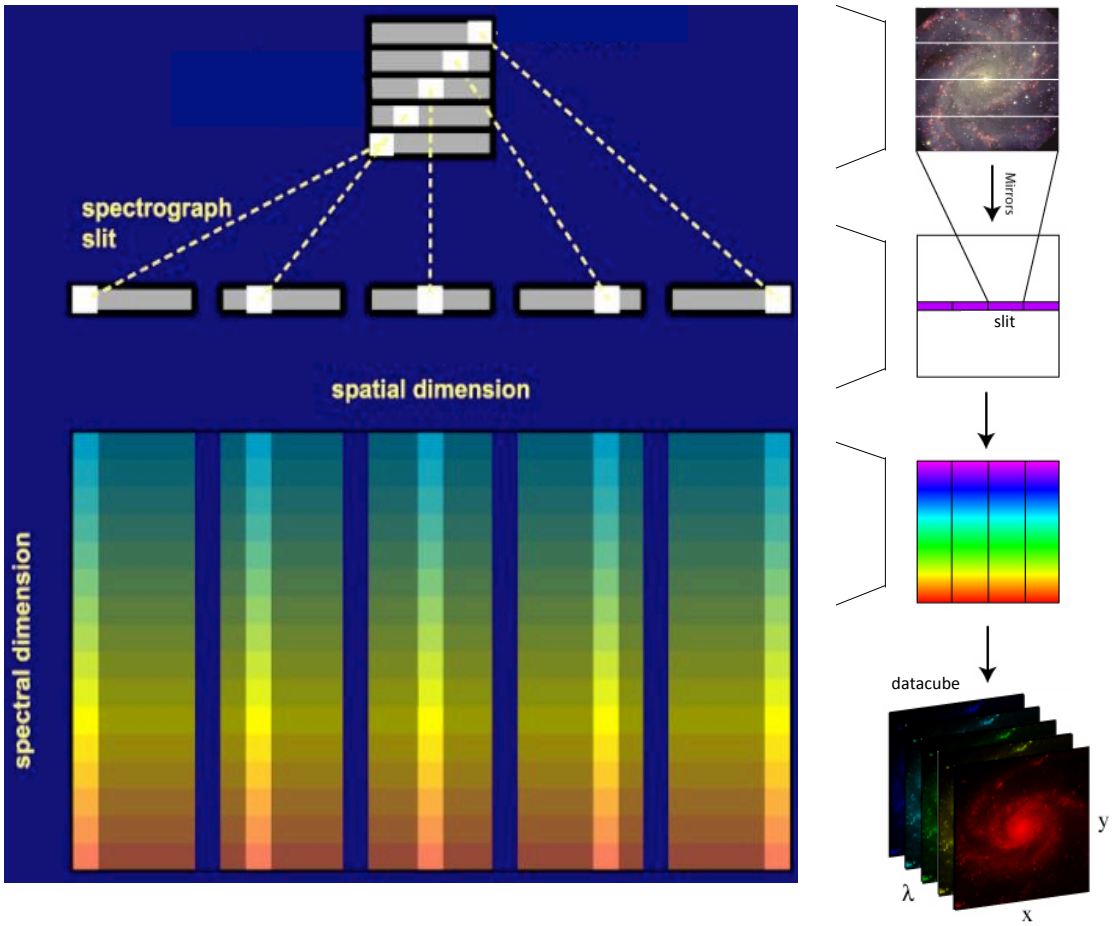

Figure 2.4: Illustration of the IFS procedure. The image is separated in slices which are then rearranged on a contiguous slit. Afterwards every pixel is spectrally dispersed. The dataset is then rearranged to obtain a data cube (c.f. Fig. 2.1) with two spatial dimensions and one spectral dimension. Adapted from Westmoquette et al. (2009) (illustration of datacube creation) and ESA PACS documentation `http://herschel.esac.esa.int/Docs/PACS/html/ch02s04.html`.

2.1.3 Observations

SPIFFI has been installed at the UT2 (Kueyen) telescope of the VLT (Horrobin et al. 2004). The central parsec of the Galaxy has been observed for one hour leading to the construction of a $\sim 35'' \times 35''$ mosaic. A sky datacube of $8'' \times 8''$ has been registered as well. The observations produced several publications about stellar He population (Eisenhauer et al. 2003; Horrobin et al. 2004; Paumard et al. 2006; Fritz et al. 2011, among others).

The observations are seeing-limited (FWHM $0.75''$) with a $0.25''$ pixel sampling and a spectral resolution $R = 1\,300$ in the combined H+K mode. The observations were treated by the SPIFFI pipeline (Schreiber et al. 2004), the reduced datacube is the same as in Eisenhauer et al. (2003) and Horrobin et al. (2004). The final datacube is atmosphere background-corrected but no absolute flux calibration is applied to the intensities which are left in pixel values (Analog

to Digital Unit, ADU).

Because of the wide spectral range covered, the dataset includes many H_2 lines. The lines detectable in SPIFFI dataset are reported in Table 2.1.

v_u	v_l	J_u	J_l	Transition name	Wavelength [μm]	avg S/N	max S/N
1	0	5	3	1-0 S(3)	1.9575	2.6	9.1
1	0	4	2	1-0 S(2)	2.0337	1.1	6.4
1	0	3	1	1-0 S(1)	2.1217	5.3	30.8
1	0	2	0	1-0 S(0)	2.2232	1.9	8.0
2	1	3	1	2-1 S(1)	2.2476	1.0	3.2
1	0	1	1	1-0 Q(1)	2.4065	3.9	23.9
1	0	2	2	1-0 Q(2)	2.4133	0.9	4.9
1	0	3	3	1-0 Q(3)	2.4236	4.4	22.3

Table 2.1: Table of transition name, wavelength, average and maximum signal-to-noise ratio (S/N) over the field, for H_2 lines covered by the SPIFFI spectral range.

The average spectrum of the SPIFFI field of view is displayed in Fig. 2.5.

The 1-0 S(1) line has been detected before in the central parsec by Yusef-Zadeh et al. (2001) and is clearly visible also in SPIFFI dataset. This is the line with the best signal-to-noise ratio on the average spectrum of the datacube, followed by 1-0 Q(3) and 1-0 Q(1) lines. 1-0 S(3) and 1-0 S(0) have a lower signal-to-noise ratio but they still stand out of the noise fairly well in the average spectrum. On the other hand 1-0 S(2) and 1-0 Q(2) are quite indistinguishable from the noise on the average spectrum. However all these lines show a strong maximum in the top-right corner of the SPIFFI field of view (Fig. 2.6). Here all signal-to-noise ratios are higher and 1-0 S(2) and 1-0 Q(3) are clearly detected. 1-0 S(0), unlike all the others detectable lines, shows a maximum also few arcseconds South of the center of the field (c.f. Fig. 2.6).

The analysis of these lines – both in the entire field and in some chosen areas for lines not detectable everywhere – constitutes the main part of this work and will be done in more details in Chapters 3 and 4. This analysis is also the object of a paper submitted to A&A (Ciurlo et al., accepted, Appendix D).

The spectrum also contains recombination lines. Of special interest for this analysis are: Brγ, Fe III and Fe II (c.f. Table 2.2).

Name	Wavelength [μm]
Fe II	1.643
Fe III	2.2178
Brγ	2.166

Table 2.2: Names and wavelengths of the recombination lines included in the analysis.

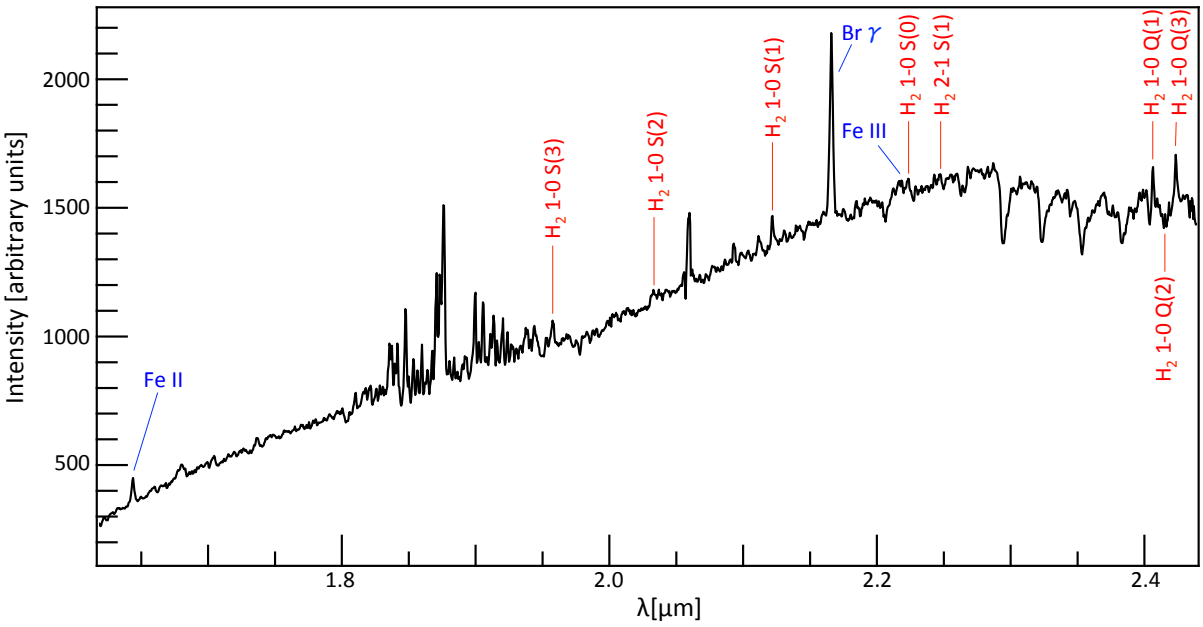

Figure 2.5: Average spectrum on the whole SPIFFI datacube. No flux calibration is applied yet. All the lines studied in this work are marked on the graph: molecular H_2 lines in red, recombination lines in blue.

These lines are particularly relevant since:

- Brγ is the most intense line of the spectrum and traces the Minispiral.
- The Fe III line, identified by Lutz et al. (1993), traces the Minicavity and it is located very close to the 1-0 S(0) line in the spectrum.
- The Fe II line is located at a shorter wavelength than the other lines, but it interestingly presents a maximum in the same region as 1-0 S(0) (Fig. 2.6). The Fe II line at this wavelength has been observed by Depoy (1992). These authors located its emission peak $\sim 10''$ South of GCIRS 7. This position is indeed compatible with maximum observed in SPIFFI dataset.

The in-depth analysis of these lines will be the object of a further study. However, a first step of analysis is approached in Appendix B.

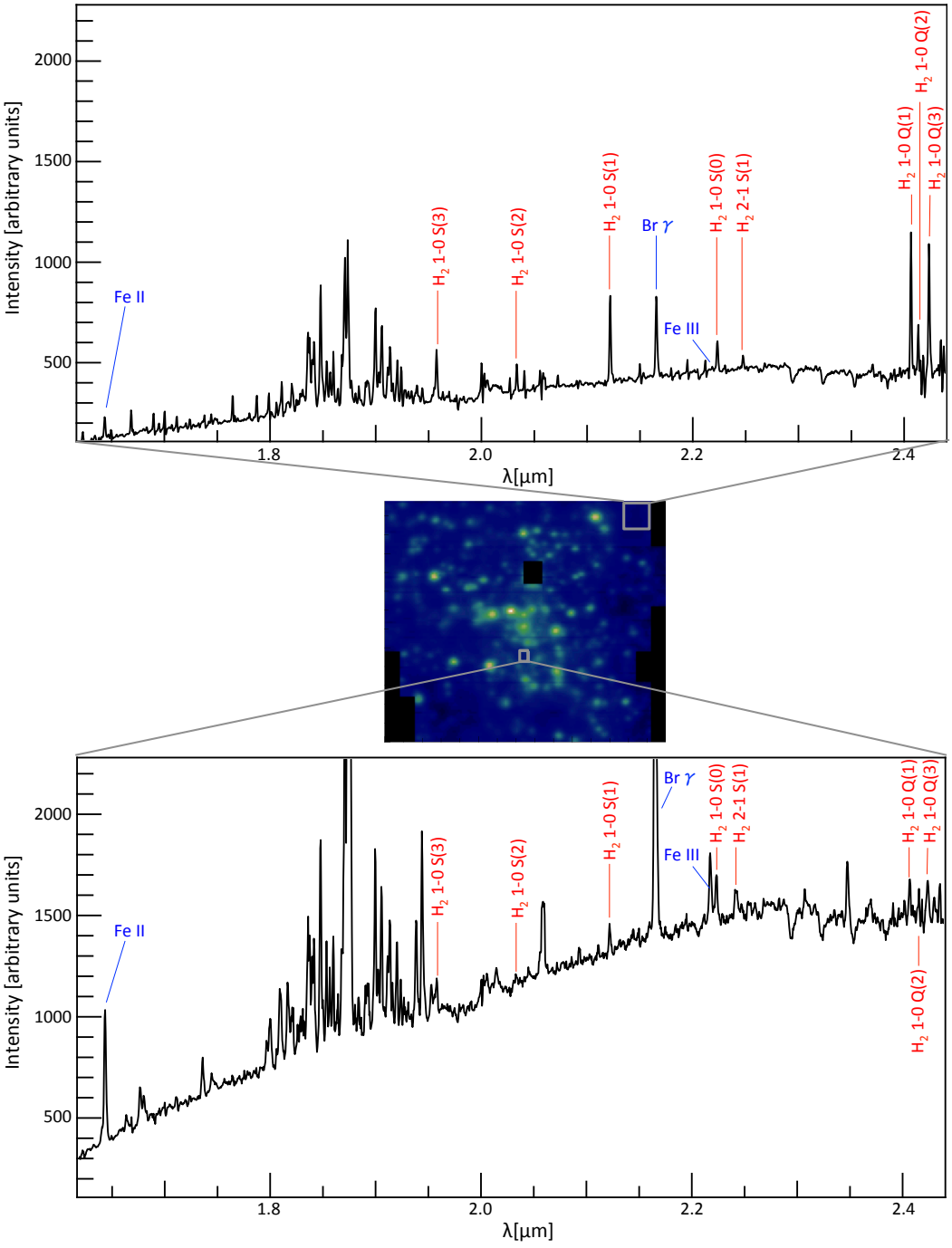

Figure 2.6: Image of the integrated flux of SPIFFI bandpass and the average spectrum of two zones: the H_2 lines peak and the 1-0 S(0) and Fe II peak.

2.2 Calibration

All the calibration and analysis has been carried out with the interpreted language `Yorick` with the addition of few computations in `IDL`. All the fits in the analysis have been done through the `lmfit`[1] method of `Yorick`: an Implement Levenberg-Marquardt method for non-linear least squares fit to a function of an arbitrary number of parameters.

The datacube can be easily displayed through `cubeview`[2] for Yorick (Paumard 2003). The `cubeview` interface allows to simultaneously display the spectral and spatial information. An area can be selected on the spatial field of view to display the corresponding average spectrum. A portion of the spectrum can be selected as well, to show the integrated flux, 2D-image, of the field of view. This tool is very useful to set parameters and visually analyze specific features.

The observations we used were already reduced and partially calibrated to remove the atmospheric absorption features. However the dataset is not calibrated in flux and a photometric calibration is needed.

To complete the calibration and control all its steps, stars in the field are selected from Paumard et al. (2006), Blum et al. (2003) and Bartko et al. (2009) catalogs. The stars shall have the characteristics of being well known and isolated as much as possible. The spectrum of these calibrators is extracted by summing pixels within a diamond-shaped aperture. Since the aperture is centered on the integrated flux map, the Point Spread Function (PSF) should not vary in width and position with the wavelength. To verify that the PSF remains constant in the whole spectrum, an isolated AGB star is considered for a test. A 2D-Gaussian profile is fitted on the AGB star image for each monochromatic image, i.e. for the 2D-field corresponding to each spectral channel. In Fig. 2.7 (top) the width along the two spatial axes of the PSF, for every wavelength, is plotted. Indeed the PSF remains rather constant along the spectrum. Similarly Fig. 2.7 (bottom) shows the centroid position for each spectral channel. The centroid remains stable at wavelengths beyond 1.9 μm but shifts up to 0.5 pixels at shorter wavelengths. All H_2 lines are at wavelengths longer than 1.9 μm where the shift does not introduce a significant bias. It could become more important for Fe II at 1.643 μm. However for the first stage analysis intended for this line this bias does not represent a strong limitation. In practice the range of interests is 1.94 – 2.45 μm.

The calibration has been done in two steps: the first step is to correct the slope of all spectra (relative calibration, Sect. 2.2.1), the second step is to convert the ADU in physical flux units (photometric calibration, Sect. 2.2.2).

2.2.1 Relative calibration

The relative calibration consists in dividing the datacube by the observed spectrum of a standard spectrometric calibrator and multiplying by the intrinsic – or expected – reddened spectrum of this calibrator.

Three bright stars from the GCIRS 16 complex are considered as standard stars. At this stage, only the continuum shape of the spectra is taken into account, while the absolute flux calibration comes at a later stage. To extract the observed spectrum of each calibrator,

[1] https://github.com/frigaut/yorick-yutils/blob/master/lmfit.i
[2] http://manpages.ubuntu.com/manpages/natty/man1/cubeview.1.html

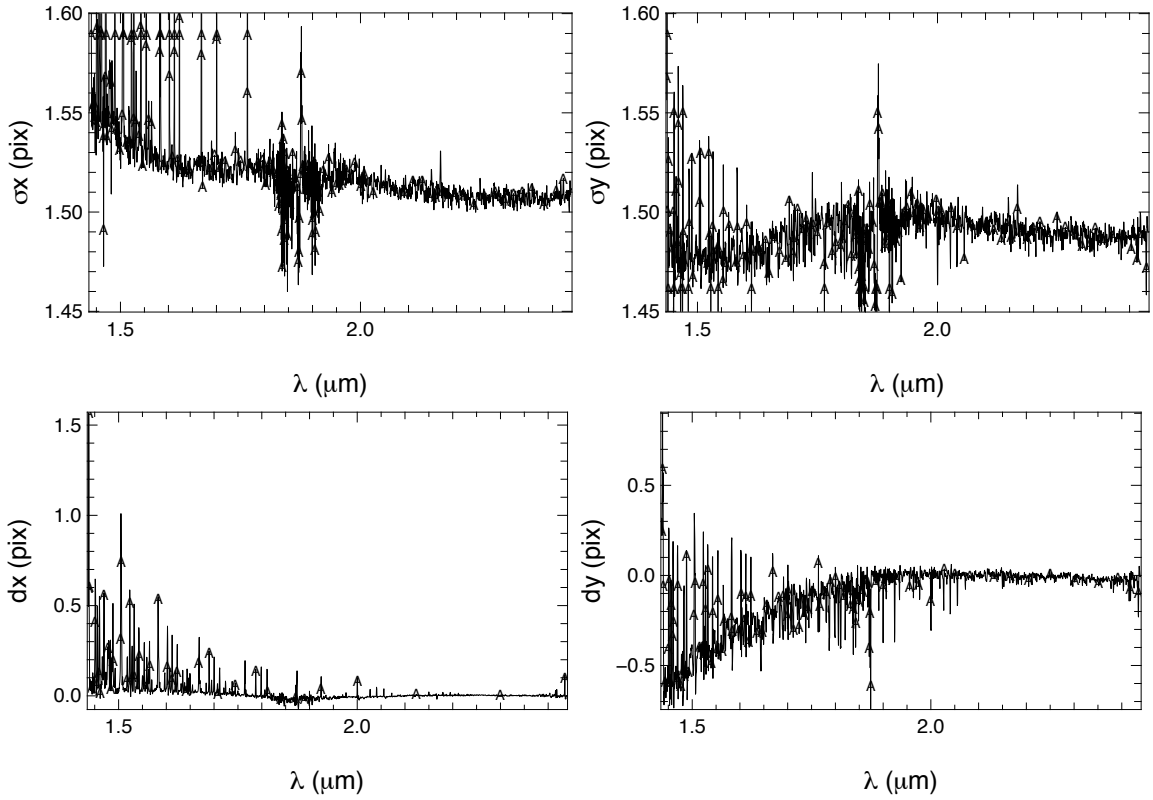

Figure 2.7: PSF width (*top*) and centroid position (*bottom*) along x-axe (*left*) and y-axe (*right*) for a 2D-Gaussian fit of an isolated AGB star.

a diamond-shaped aperture of 5-pixel width and height (13 spatial pixels, white pixels in Fig. 2.8) is considered at the location of the star. For a given calibrator, we compute the average spectrum over this aperture.

The background contribution has to be subtracted from the observed spectrum. To do so an easy choice is to use a 5-pixel wide square aperture, minus the circular aperture used to estimate the star's spectrum itself (12 pixels, black pixels in Fig. 2.8).

This whole procedure is done through the following steps:

1) the star spectrum is extracted summing up spectra of all spatial pixels contained in the diamond-shaped aperture.

2) The flux in the corners of the square circumscribing this aperture is used to perform background subtraction.

3) The continuum of this background-subtracted spectrum is modeled via a polynomial function (Fig. 2.9).

5) The expected spectral shape of every star is estimated using a blackbody curve. The spectral type of all calibrator is the same: Ofpe/WN9, which corresponds to an effective

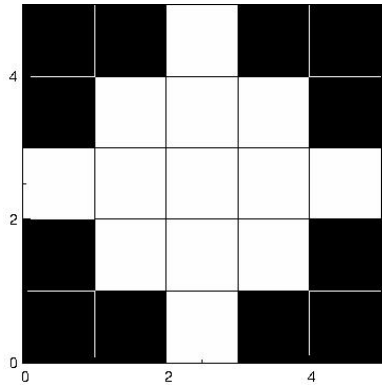

Figure 2.8: Structure of the 5 × 5 pixel size aperture used for calibration. Spectra corresponding to white pixels are summed up to measure the star spectrum, black pixels are used to perform background subtraction.

temperature of 30 000–39 000 K (Pasquali et al. 1996). For such high temperatures the emission is in the Rayleigh-Jeans tail of the black body, where the shape of the curve doesn't change much for temperatures which differ of few thousand K. Therefore an intermediate value of 35 000 K is considered for every calibrator star. The extinction law applied to the black body emission is $A_\lambda \sim \lambda^{-\alpha}$, where $\alpha \sim 2.07$ (Fritz et al. 2011). The local extinction, different for each star, is taken from the Schödel et al. (2010) extinction map.

6) Every spectrum in the SPIFFI cube has to be divided by the continuum-subtracted calibrator spectrum (step 3) and multiplied by this theoretical spectrum (step 5).

In practice we computed a calibration factor for each wavelength.
This procedure has been repeated for each of the three selected calibrators.

2.2.2 Photometric calibration

Photometric calibration is performed through the spectrum of cool stars of known magnitude taken from Blum et al. 2003 and Bartko et al. 2009 catalogs. The spectrum is extracted and calibrated as in the previous section.

A synthetic PSF of same width as the real one, but oversampled, has been used to calculate the energy actually enclosed in the backgroud-subtracted diamond-shaped aperture considered. A synthetic effective PSF is employed because there are almost no isolated stars in the field. The enclosed energy is estimated to be ∼25% of the total.

The flux for each star is computed from the known magnitude m_k as $F_{th} = F_0 \cdot 10^{-m_K/2.5}$ where $F_0 = 1.697\ 10^7$ erg s^{-1} cm^{-2} is the flux of Vega in the K band. For each photometric calibrator:

a) The observed K-band flux is computed integrating the measured spectrum over the K band pass 1.77 – 2.59 μm.

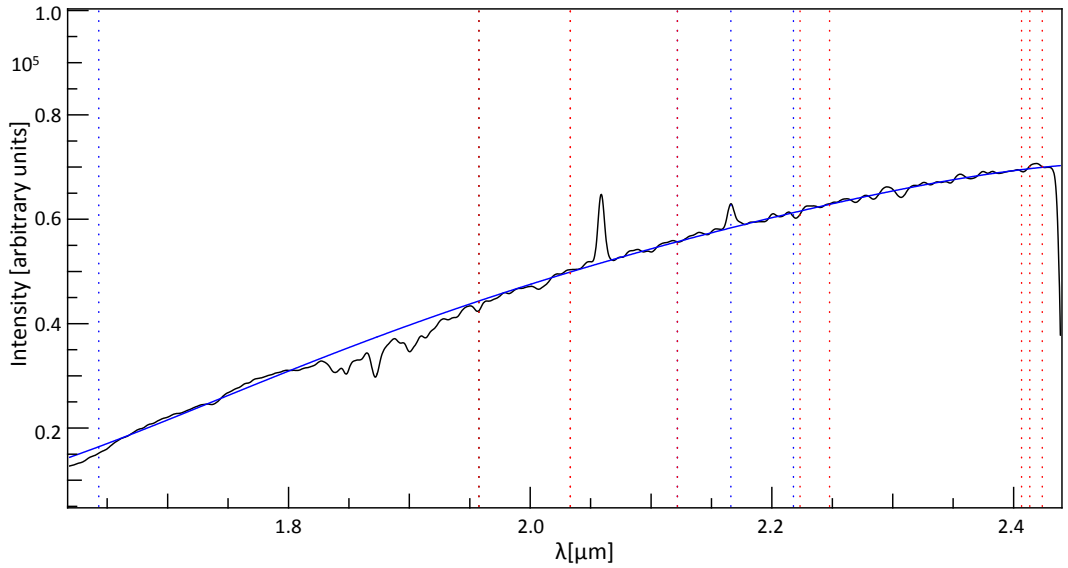

Figure 2.9: The spectrum of GCIRS 16NE has been smoothed (*black* line) and modeled with a polynomial function (*blue* line).

b) Knowing that the observed flux represents ∼25% of the total it is compared to the expected flux, computed from the star magnitude, to obtain the ADU-flux units conversion factor.

The procedure is repeated for different photometric reference stars.

2.2.3 Final calibration factor and uncertainty

Three stars are used for the relative calibration (hereafter A calibrators): GCIRS 16NW, GCIRS 16C and GCIRS 16NE from Paumard et al. (2006). Seven stars are used as photometric calibrators (hereafter B calibrator): stars 19, 28, 84, 91, 102, 105 from Blum et al. 2003 and star 68 from Bartko et al. 2009.

Stars for relative calibration (A)		
label	name	type
E19	GCIRS 16 NW	Ofpe/WN9
E20	GCIRS 16 C	Ofpe/WN9
E39	GCIRS 16 NE	Ofpe/WN9

Table 2.3: Original paper label, standard designation and spectral type of stars used as calibrator for relative calibration, from Paumard et al. (2006) catalog.

To summarize, the calibration is given by the factor:

$$CF(\lambda) = \frac{BB_r(\lambda)}{C_A(\lambda)} \cdot \frac{F_{th,B}}{F_{obs,B}} \tag{2.1}$$

Stars for photometric calibration (B)		
label	name	K-magnitude
19	–	10.14 ± 0.03
28	GCIRS 11	9.17 ± 0.07
84	–	9.88 ± 0.04
91	GCIRS 9	8.61 ± 0.03
102	GCIRS 28	9.36 ± 0.03
105	–	8.91 ± 0.03
68	–	10.67 ± 0.01

Table 2.4: Original paper label, standard designation (where available) and K-magnitude for stars used as calibrator for photometric calibration, from Blum et al. 2003 and Bartko et al. 2009.

Where BB_r is the theoretical emission of the calibrator star, i.e. a black body emission, reddened by the Galactic extinction. C_A is the continuum of the calibrator star A. $F_{th,B}$ is the expected flux of photometric calibrator star B, computed from its known magnitude. $F_{obs,B}$ is the observed total flux of photometric calibrator star B.

The final calibration factor at each wavelength, for each combination of A and B stars, is displayed in Fig. 2.11. Each curve gives the factor by which the flux in ADU, obtained from the original dataset, must be multiplied, in order to obtain a photometrically calibrated result. The average value of the eighteen curves is considered as the final relative correction (green curve on Fig. 2.11). The main sources of uncertainty are:

- uncertainty on the photometric calibrators magnitude (5–10%)
- uncertainty on the actual flux contained in the aperture due to inexact centering of the star PSF-centroid within the aperture (up to 15% for a shift of the centroid of 0.5 pixels on both axis as estimated from a simulation on the synthetic PSF).

Since the propagation of uncertainty combining these errors is not easy to manage the uncertainty is evaluated as the dispersion of the curves of the different calibrators, with respect to the average value: ∼35%.

When considering the ratio of two spectral lines the uncertainty due to the photometric calibration (i.e. the imperfect knowledge of the calibrator star magnitude and inexact centering) is not relevant any more since this error is common to all lines. In this case the uncertainty is only due to the dispersion of the A calibrators curves. For every star B there is a "pack" of curves with slightly different slopes. The maximum dispersion is taken as the estimated uncertainty. This leads to an uncertainty of 8% in the range 1.9 – 2.45 μm and of 10% at 1.64 μm and is more or less the same for each B calibrator.

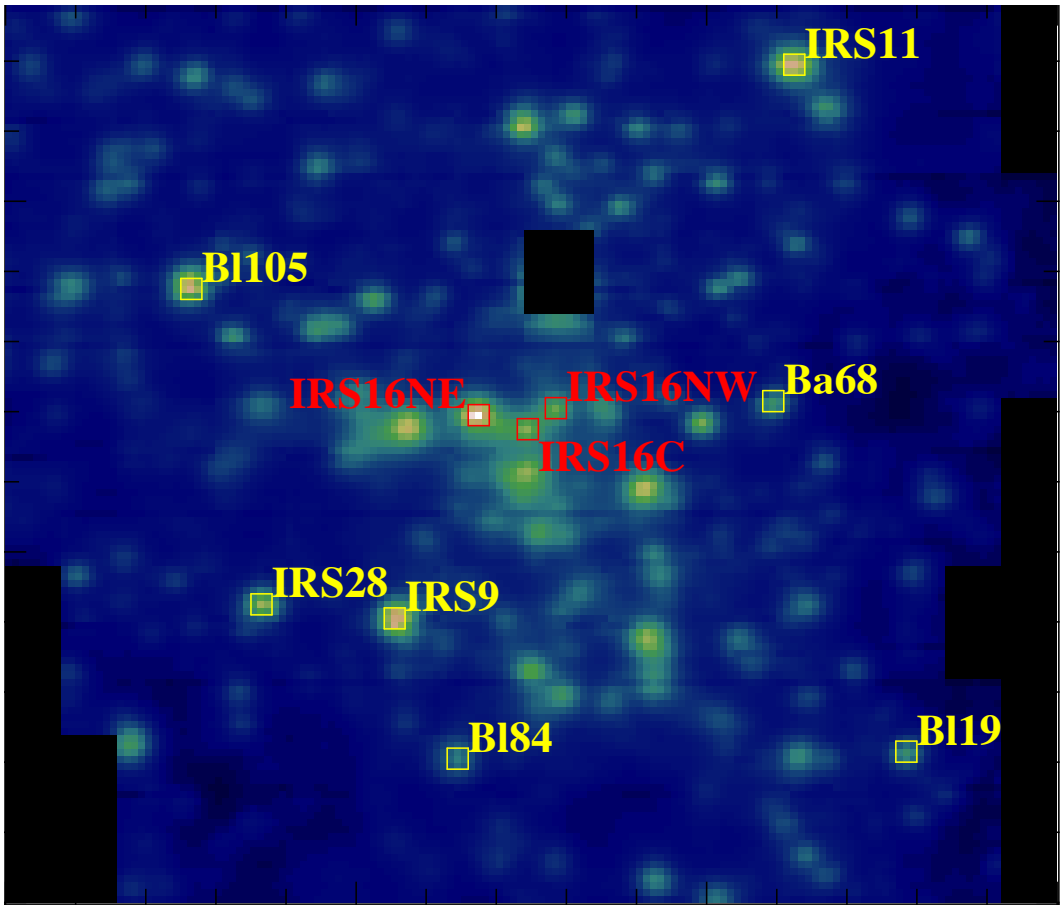

Figure 2.10: Collapsed mosaic of SPIFFI datacube showing the stars used as calibrators for relative (*red*, Paumard et al. 2006) and photometric (*yellow*; "Bl" label for Blum et al. 2003 stars and "Ba" label for Bartko et al. 2009 stars) calibration.

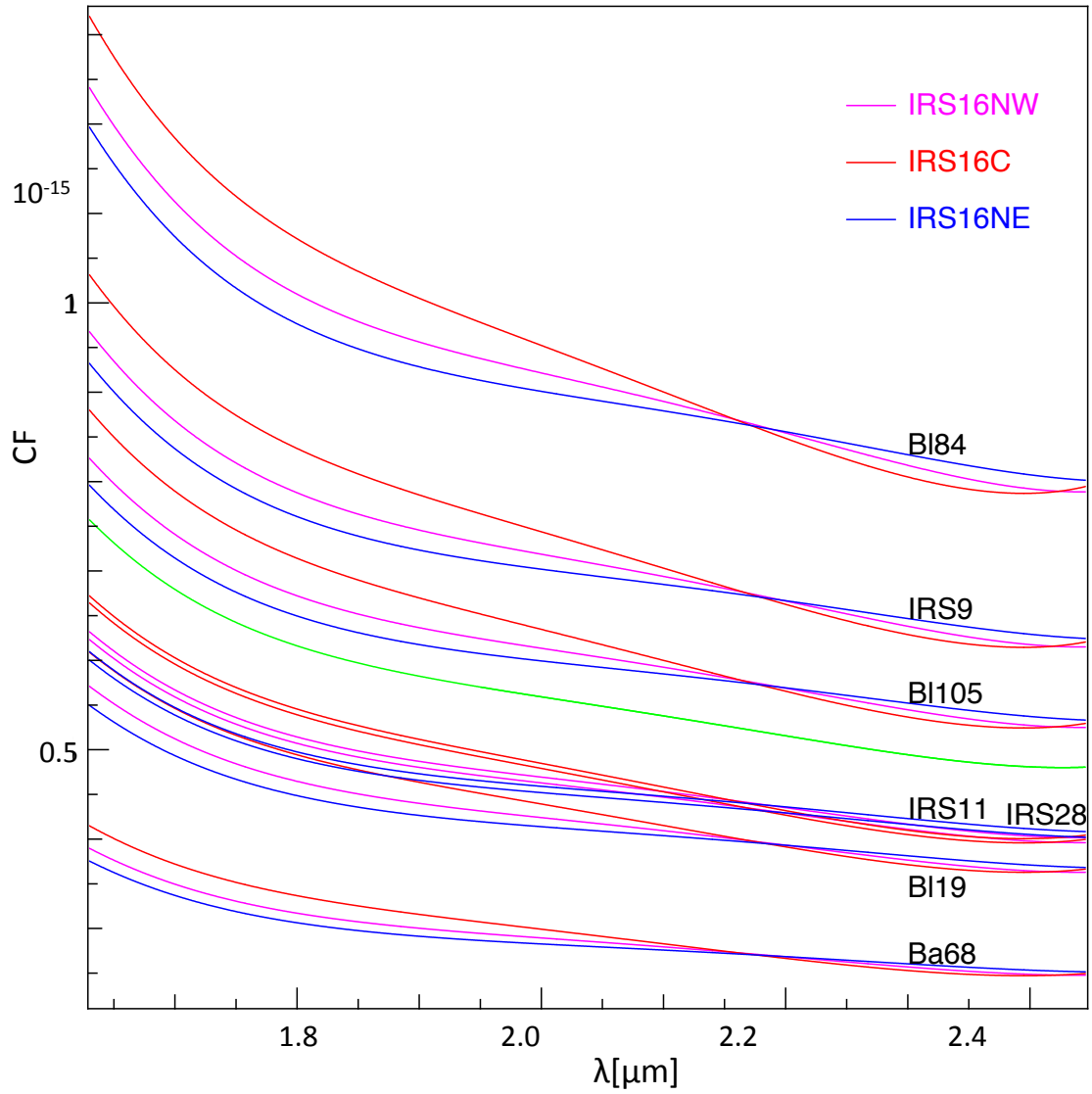

Figure 2.11: Final calibration factor (c.f. Equation 2.1) for every combination of A (Paumard et al. 2006) displayed in *red*, *magenta* and *blue*) and B stars ("Bl" label for Blum et al. 2003 stars and "Ba" label for Bartko et al. 2009 stars). Stars are labelled as in Tables 2.3 and 2.4. The *green* line traces the average of all curves.

2.2.4 Continuum subtraction

In order to measure the intensity of each detected H_2 line, the contribution of the underlying continuum must be subtracted. The continuum could be modeled over the entire spectral range. However, in practice, it is very delicate to obtain an accurate fit over the entire spectrum and in addition, not all lines of the spectrum are of interest for this work. It is therefore safer and more efficient to consider a sub-cube where the spectral range is restricted to few thousands km s^{-1} around the line of interest. For instance, for 1-0 S(1) one can consider a window of

$\sim$7 000 km s^{-1}, centered on S(1) wavelength (Fig. 2.12).

Since the spectrum is rich in gaseous and stellar lines and, sometimes, artifacts, only some portions of the sub-spectrum are actually chosen to evaluate the continuum. `Cubeview` helps choosing these ranges as it allows visualizing spectra everywhere in the field. In this way one can select manually spectral zones free of lines and artifacts. The average value (in the spectral dimension) over each of these ranges is computed, and the points obtained are fitted with a polynomial function of fifth degree (Fig. 2.12). This allows to obtain a as precise as possible estimate of the local continuum around each line, at each pixel.

Once the continuum subtraction is applied, the resulting spectrum can be fitted with a Gaussian model. However not the entire spectrum can feed the fit procedure. The spectral ranges to be fitted by the Gaussian must be identified in order avoid pollution by any other spectral feature which is not related to the H_2 line under study. This spectral range is selected by trying to keep it as wide as possible while avoiding all nearby lines and artifacts. Unfortunately this often leads to a very narrow range around the H_2 line. Therefore, two or more additional ranges, on both sides of the central line, are chosen in regions free of artifacts, but yet as close as possible to the line, to complete the Gaussian "tales". An example of this selection for 1-0 S(1) is given in Fig. 2.12.

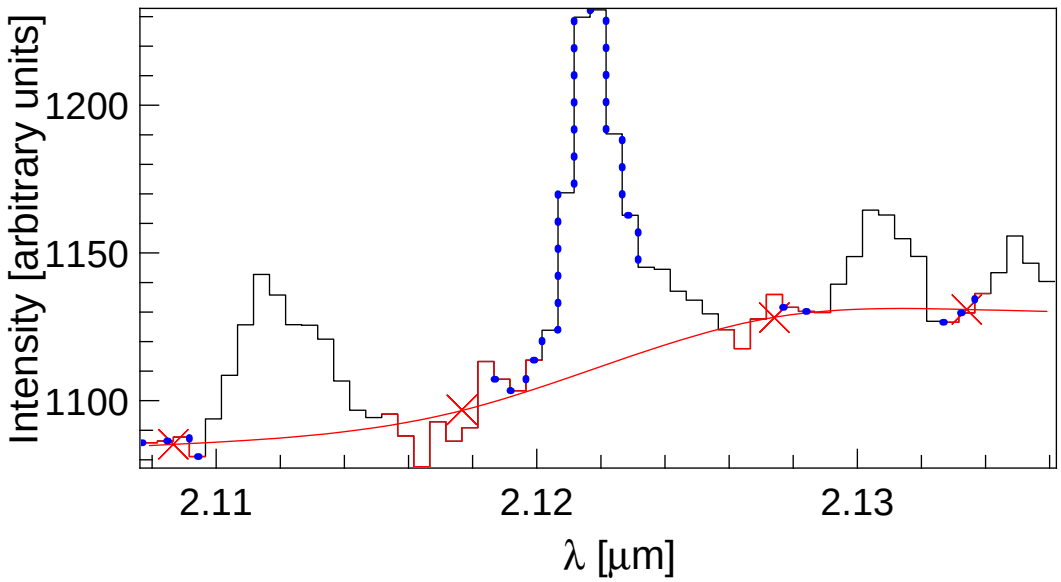

Figure 2.12: Example of continuum evaluation for 1-0 S(1). The spectral ranges chosen to evaluate the continuum are colored in red. The average on each range is marked by cross symbols. The red solid line shows the final evaluation of the continuum. The blue dotted points identify the spectral range to be given to the fitting procedure.

2.3 Analysis methods: regularized 3D-fitting of spectroscopic data

H_2 emission lines can be modeled with a Gaussian profile leading to the determination of intensity, velocity and width.

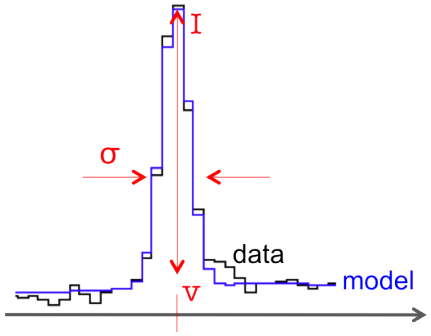

Figure 2.13: Example of emission line fitted with a Gaussian.

The velocity v is calculated from Doppler effect: $\Delta\lambda/\lambda = v(\lambda)/c$ where λ is the wavelength of the emission line peak and c the light speed.

The measured line width, in practice, does not corresponds to the intrinsic line width because it is affected by the instrumental width. Intrinsic width can be calculated from measured and instrumental width. However the instrumental width is a function of the wavelength. We will show in Sect. 2.4 that, given the uncertainties on the measured and the instrumental width, the uncertainty on the intrinsic width is very large. We will therefore only consider the measured width hereafter. For this reason it is better to consider the line flux instead of the intensity: the flux does not depend on the choice of the width – either measured on intrinsic – and it is therefore a more stable quantity.

The model for a H_2 line spectrum, corresponding to a given spatial pixel $[x, y]$ is:

$$G_{x,y}(\lambda) = F_{x,y}\ e^{\left(\frac{v(\lambda)-v_{0,\alpha,\delta}}{2\ \sigma_{v,\alpha,\delta}}\right)^2} \tag{2.2}$$

Where $F_{x,y}$ is the line flux, $\sigma_{v,x,y}$ the line width in km s^{-1} and $v_{0,x,y}$ the radial velocity.

The SPIFFI datacube contains the spectra of all spatial pixels of the $\sim$35″ field. Each spectrum in the field of view can be fitted with the one-dimensional model of Equation 2.2 yielding values of flux, velocity and width for each pixel. It is then possible to build two-dimensional maps of physical parameters (in this case flux, velocity and width) for a given H_2 line. The outcome of this analysis is thus one map for the line flux, one for the line velocity and one for the line width.

The classical approach for this kind of analysis is to consider each spectrum individually, pixel by pixel, and fit it with a Gaussian profile to gather the values of the three parameters. The maps resulting of this approach are noisy. If the dataset has a sufficiently high signal-to-noise ratio and noise is mainly statistical, one can safely apply a spatial smoothing to obtain a good compromise between signal-to-noise and spatial resolution.

However, in the SPIFFI dataset the signal-to-noise ratio of H_2 lines in not good everywhere in the field of view, especially at the location of stars, where there is additional photon noise. In this case spatial smoothing has the effect of degrading the spatial resolution everywhere. Uniform smoothing across the field would increase the signal-to-noise ratio where it is low, but lower it where it is already reasonable. Moreover this operation increases the correlation between neighboring pixels and introduces edge effects on the border of the field of view and in zones with missing data.

2.3.1 Regularized 3D-fitting

To overcome the above problems a new approach is used, developed by Paumard et al. (2014a): the regularized 3D-fitting. This method, instead of fitting each spectrum individually, performs a global fit over the 3D cube. In this section we give a brief description of this method, more details will be given in Paumard et al. 2016 (in prep.).

The regularized 3D-fitting takes inspiration from the deconvolution context and consists in minimizing an estimator, ε, which is the weighted sum of a χ^2 and a regularization term:

$$\varepsilon(F, v, \sigma) = \sum_{x,y,\lambda} [(D - M) \cdot W]^2 + \sum_{a_i=F,v,\sigma} R_i(a_i) \tag{2.3}$$

where the first term is the χ^2-term: difference between 3D-dataset D and the model M. The points of the cube are indicated by spatial coordinates $[x, y]$ and wavelength channel λ. W is a weighting function that takes into account the signal-to-noise ratio. $R_i(a_i)$ is the regularization term for the a_i-fitting parameter (flux F, velocity v and width σ).

The regularization has the role of injecting as much *a priori* information as possible. For this purpose a quadratic-linear regularization is used. This regularization is called L1–L2 and it is borrowed from the deconvolution context. The principle has been developed in Green (1990), S. Brette (1996), Mugnier et al. (2001), generalized in Mugnier et al. (2004) and coded in the Yoda software by D. Gratadour[3]. The expression of this regularization for every parameter map a_i is:

$$R_i(a_i) = \mu_i \sum_{u=x,y} \left[\frac{\Delta O(u)_{a_i}}{\delta_i} - ln\left(1 + \frac{\Delta O(u)_{a_i}}{\delta_i}\right)\right] \tag{2.4}$$

where $\Delta O(u)_{a_i}$ is the spatial gradient of the a_i-parameter and $u = x, y$.

For weak gradients (small $\Delta O(u)$) the logarithmic term of L1–L2 dominates and the term become a quadratic criteria which penalizes gradients and smooths the map. On the contrary, when $\Delta O(u)$ is large, strong gradients are restored. The transition from one regime to the other is adjusted through two hyper-parameters δ_i and μ_i.

This algorithm is very well suited to treat objects with strong, spatially correlated, gradients such as sharp edges (e.g. planetary surfaces) or, in our case, ridges and streamers. Indeed the algorithm disfavors random variations on the maps – strong gradients between pixels, which are noise – but still allows quick and coherent variations.

[3] https://github.com/dgratadour/Yoda

Thanks to this approach, data with low signal-to-noise ratio weigh less, spatial resolution is conserved and edge effects are minimized. The fit over pixels with low signal-to noise is highly improved since the procedure uses neighboring points to adjust the solution. This prevents over-fitting noise spikes. If data are missing in some portions of the field, the regularized 3D-fitting acts as an interpolating function. This is the case, for instance, of spatial pixels corresponding to the location of stars. Stars present in the field could locally bias results near the studied transition lines, due to increased photon noise and because of spectral features. Here, the photon noise can be very high and it is best to just mask out these areas and to not consider them in the fitting procedure. Bad pixels should always be masked out when known, and the corresponding region shall be interpolated over.

However there is one major inconvenient in this 3D method: the necessary tuning of the hyper-parameters δ_i and μ_i, for each parameter map (flux, velocity and width). Six hyper-parameters have therefore to be chosen. They are in fact not independent from each other and this complicates the finding of a good solution. Increasing δ_i would allow the criterion to approach the quadratic form, smoothing the image. However, it also has the effect of lowering the overall weight of the regularization with respect to the χ^2-term. In the same way the weight of the regularization can be augmented rising the value of μ_i but also lowering the value of δ_i.

The method procedure is iterative and it adds more details at every step. The search for all three Gaussian parameters – flux, velocity and width – has to evolve in similar ways, in order to allow the procedure to search far enough to find acceptable values for all. This means the three maps should be equally "evolved", i.e. with the same degree on details covering the ranges of variation of the parameters.

The solution that we have chosen is to rescale each initial parameter map according to a factor, in order to make all parameters of the same order. For instance, for a normalized Gaussian profile, the flux values would be of the order of 1, while line velocity and width would be of the order of 100 (when expressed in km s^{-1}). The scale factor would thus bring all parameters to vary around 1. Relative values of this factor are very important to achieve the solution where the criterion is minimized for all parameters. It would seem that there are 9 hyper-parameters to tune (six hyper-parameters plus three scale factors). In fact the scale factor has also the effect of lowering or raising the overall weight of the regularization term and the smoothness of the final maps. It has just the same behavior as the δ_i hyper-parameter. Therefore only six hyper-parameters are necessary (δ_i and μ_i for each of the three Gaussian parameter). In the next section the effect of these six hyper-parameters are discussed, as well as the strategy to chose them.

The fitting method used is the limited memory variable metric algorithm (VMLM-B) of OptimPack[4], described in Thiebaut (2002).

2.3.2 Hyper-parameters tuning

The aim of the hyper-parameters tuning is to lead the minimization procedure towards the absolute minimum of the criterion ε. To reach this minimum requires the fine tuning of each of the six hyper-parameters. The aims is to obtain maps which appear smooth at a scale as close as possible to the spatial resolution. The final result should be appropriate everywhere,

[4] http://cral.univ-lyon1.fr/labo/perso/eric.thiebaut/?Software/OptimPack#Nocedal1980

i.e. the obtained 3D model should be equivalent to what one would obtain with a classical 1D fit over any aperture.

The main difficulty is that these hyper-parameters are not independent. μ_i regulates the smoothness of each parameter map. An increase of μ_i has the immediate effect of smoothing the image, but it also has the secondary effect of limiting the search of the estimator's minimum. Relative values of $1/\delta_i$ rescale each parameter, in order to make them vary around the same numerical order of magnitude. A decrease of $1/\delta_i$ leads to more "evolved" maps, but it also has the effect of lowering the width of the regularizing term and to amplify the noise.

The challenge is to balance the six hyper-parameters in order to have sufficiently smooth maps, while conserving fine spatial structures. The procedure was run several times with different combinations of hyper-parameters, to find the best strategy to identify the good hyper-parameters combination.

After multiple trials what we identified as the best strategy is the following:

- Set a proper initial guess: the initial guess is important to achieve a good fit. It has to be close to the final average solution, in order to allow the procedure to converge towards an absolute minimum. Only three values are chosen for each hyper-parameter (one for each Gaussian parameter, i.e. three flat maps); it means that the initial guess should reflect the average value of each parameter across the entire field of view. These values can be evaluated directly from raw data with the help of the visualizer `cubeview`. This often gives a sufficiently precise initial guess. However, if the the obtained maps are too smooth, too noisy or not enough "evolved", it might then be a good idea to change the initial guess, to help the procedure to converge. The ranges of variation of each Gaussian parameter must be injected in the method as well. It defines the minimum and maximum of flux, velocity and width. These limits are set once more by looking directly the dataset and estimating the range of variation for each parameter.

- Set the scale factor hyper-parameter: each scale factor should be chosen in order to make all three parameters vary in the same range. The starting values of these hyper-parameters would simply be the order of magnitude of each parameter (for instance 100 for line width which should be around 120 km/s). These hyper-parameters are then more finely tuned, trying to allow each map to cover as much as possible of the selected range of variations (i.e. "evolved" map). Once these ranges are well covered, the resulting maps are often noisy, since they are under-regularized.

- Set the smoothing scale: the natural following step is to enhance the smoothing to avoid the noise amplification obtained in the previous step. The smoothing scale can often be the same for each Gaussian parameter. Sometimes, when the ranges of variations are not quite of the same amplitude, it can be useful to enhance the smoothing for just one parameter in order to obtain the same visual smoothing for each map corresponding to the input data spatial resolution.

An example of the hyper-parameters tuning is given in Fig 2.15. The equilibrium between the six hyper-parameters is delicate and needs several iterations.

Three major tools help understanding how good a fit is, at every step:

- Evolution of the maps: all three maps should range between the minimum and maximum values and thus present sufficiently detailed maps. Otherwise the value of one or more of the Gaussian parameter would remain too close to its average initial value and the 3D-model would be either underestimated or overestimated.

- Smoothness of the maps: the good degree of smoothing is the one that gives structures more or less of the same size as the spatial PSF of the dataset. This allows seeking for the degree of smoothness that conserves enough details.

- Comparison of the 3D model to raw data: thanks to `cubeview` the 3D-model obtained with regularized 3D-fit can be easily compared to the raw data, to get an idea of how far from the solution one is, over the entire field of view.

We cannot, at the moment, provide an objective, absolute and automatic criterion to find the best hyper-parameters combination. The reduced χ^2 of the fit gives some indication. However, different combinations of hyper-parameters often lead to very close values of the reduced χ^2. This quantity is thus useful in the first steps of the hyper-parameters tuning, to find the right direction when far from minimum conditions. Once one starts to approach the solution, the χ^2 values became very close. It is always more efficient to look at the parameter maps and choose manually the fine tuning, and further discriminate among results that could have very close values of reduced χ^2. For instance in Fig. 2.15 the third and the fourths cases presented would seem both good models, with close values of the χ^2. However the third case shows less details than the fourth case. Therefore the final solution is reached manually adjusting the hyper-parameters tuning at each step with the above tools. These are objective criteria that allow one to judge the result *a posteriori*.

A strong objective *a posteriori* criterion to assess the method is given by the comparison of the 3D model obtained with a classical 1D model. Individual spectra in several zones (Fig. 2.16) are extracted. These average spectra are fitted with a classical 1D-model. The regularized 3D-fit model is averaged over the same zones in order to compare the two models. Fig. 2.18 shows that the two fit are highly consistent one with another and with data. Indeed when comparing the two models of Fig. 2.15 to a 1D-fit and to raw data (Fig. 2.18) the fourth 3D model can hardly ever be distinguished from data and the 1D model, while the third case 3D model often overestimates the line width.

One final, stronger, *a posteriori* criterion is to look at the regularized 3D-fit results for distinct H_2 lines. It will be shown in Chapter 3 that 1-0 S(1), S(3), Q(1) and Q(3) all show the same large-scale structures in each parameter map. The regularized 3D-fit procedure is applied independently on these lines for which the spectral environment and the signal-to-noise ratio can be very different. Nevertheless all the maps produced show the same structure, at least at large scale. This is a confirmation that the observed features are not artifacts due to the fitting procedure.

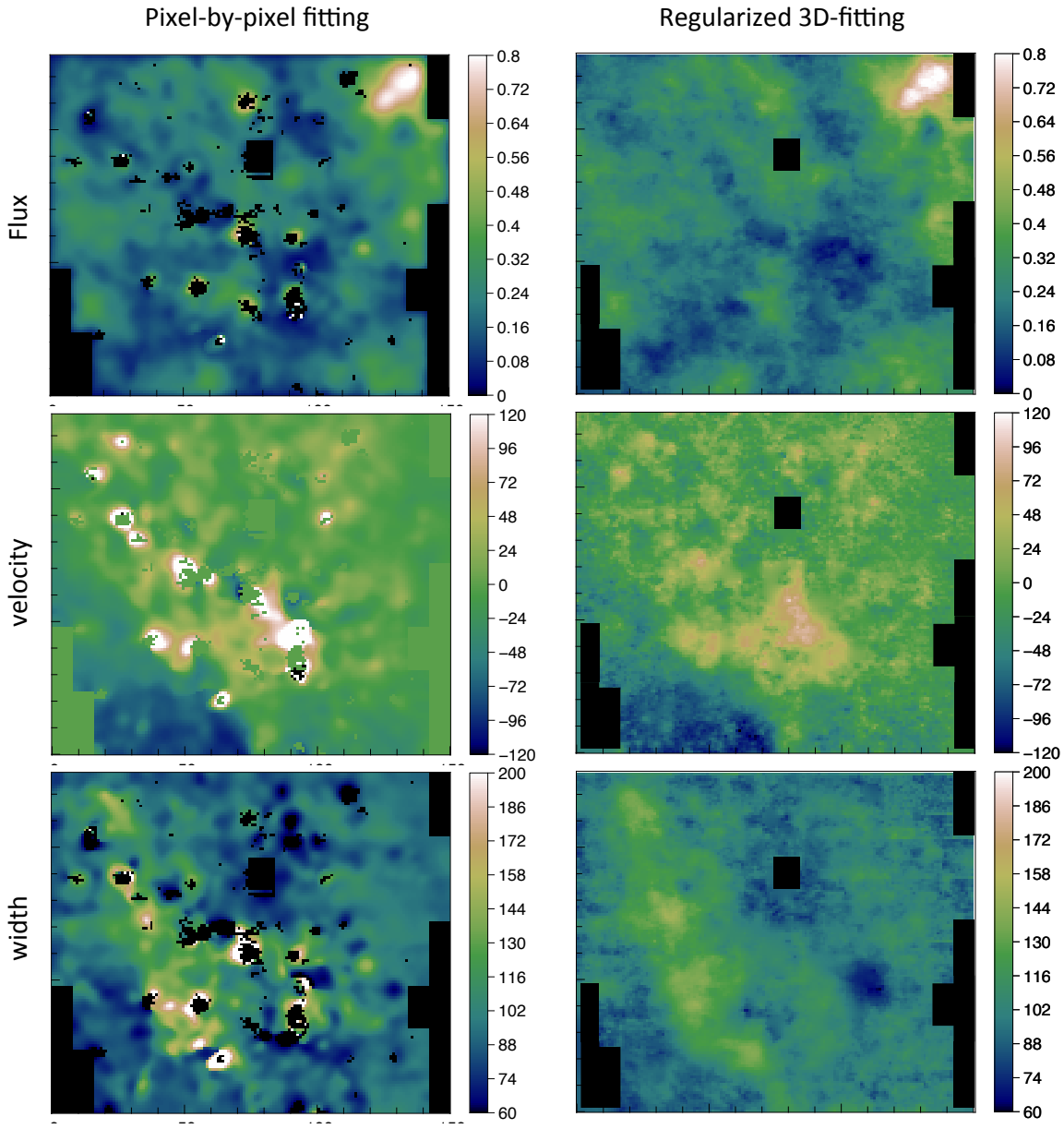

Figure 2.14: *Left* : flux, velocity and width maps obtained with a pixel-by-pixel fit on previously smoothed data with a constant aperture of 2 pixels. *Right* : flux, velocity and width maps obtained with regularized 3D-fit. With this procedure the final maps are much less affected by noise and structures are more easily identified, as it can be easily seen for the width maps.

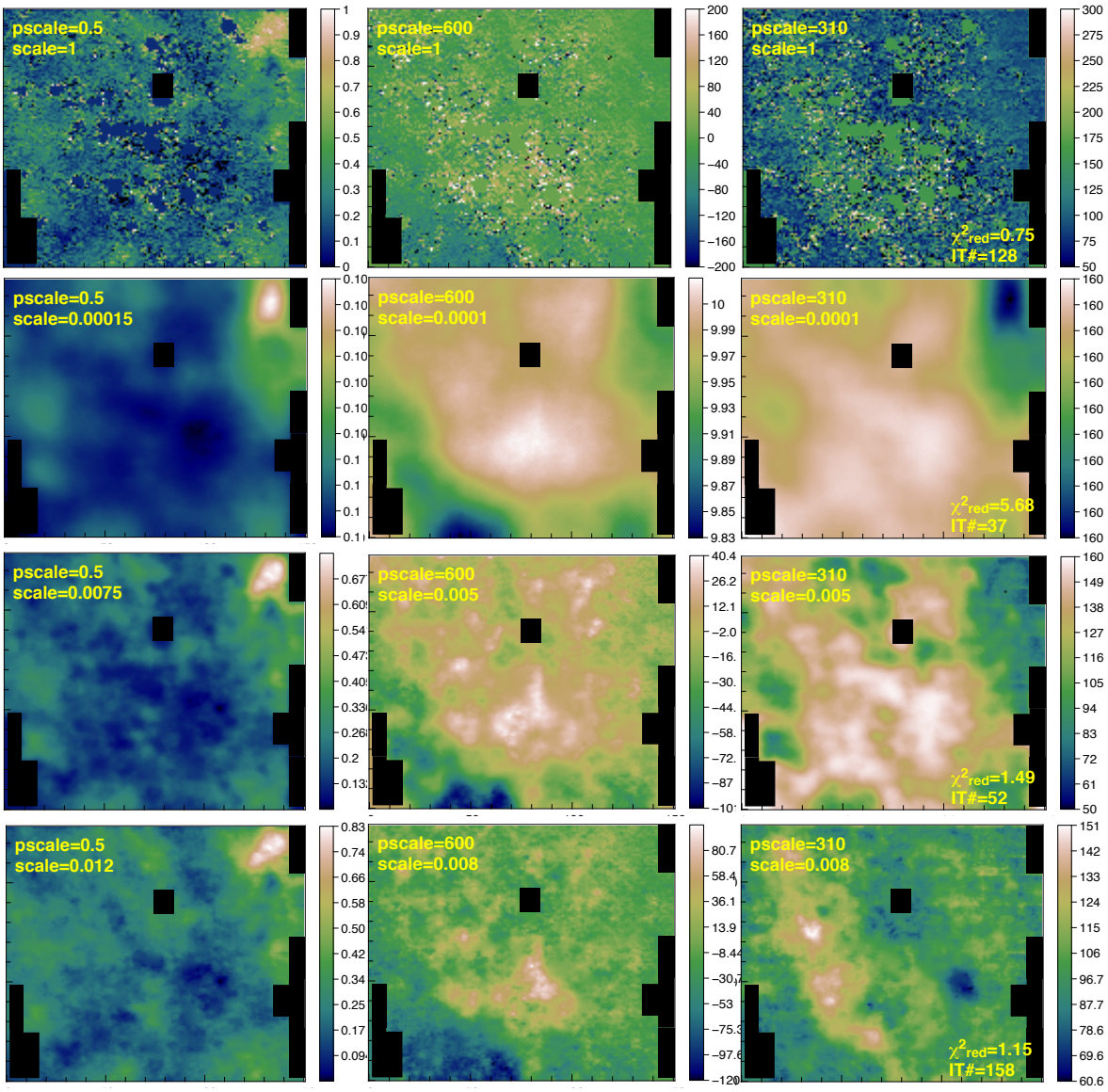

Figure 2.15: Example of maps obtained for different combinations of hyper-parameters. Here $scale \sim 1/\mu^2$ and $pscale \sim 1/\delta$. In the first case, maps cover well the range of variation of each parameter but are too noisy and no interpolation over missing data is provided. In the second case, maps are too smooth and the procedure does not allow to search the solution far enough (maps not "evolved" enough). In the third case, there are enough variations within each map but the width map does not show yet the fine structures that one can observe in the fourth case, which is the best solution. For each example the final reduced χ^2 is given, along with the number of iterations the procedure needs to converge. Both quantities are useful to check the goodness of the fit, i.e χ^2 close to 1 and a sufficiently high number of iterations.

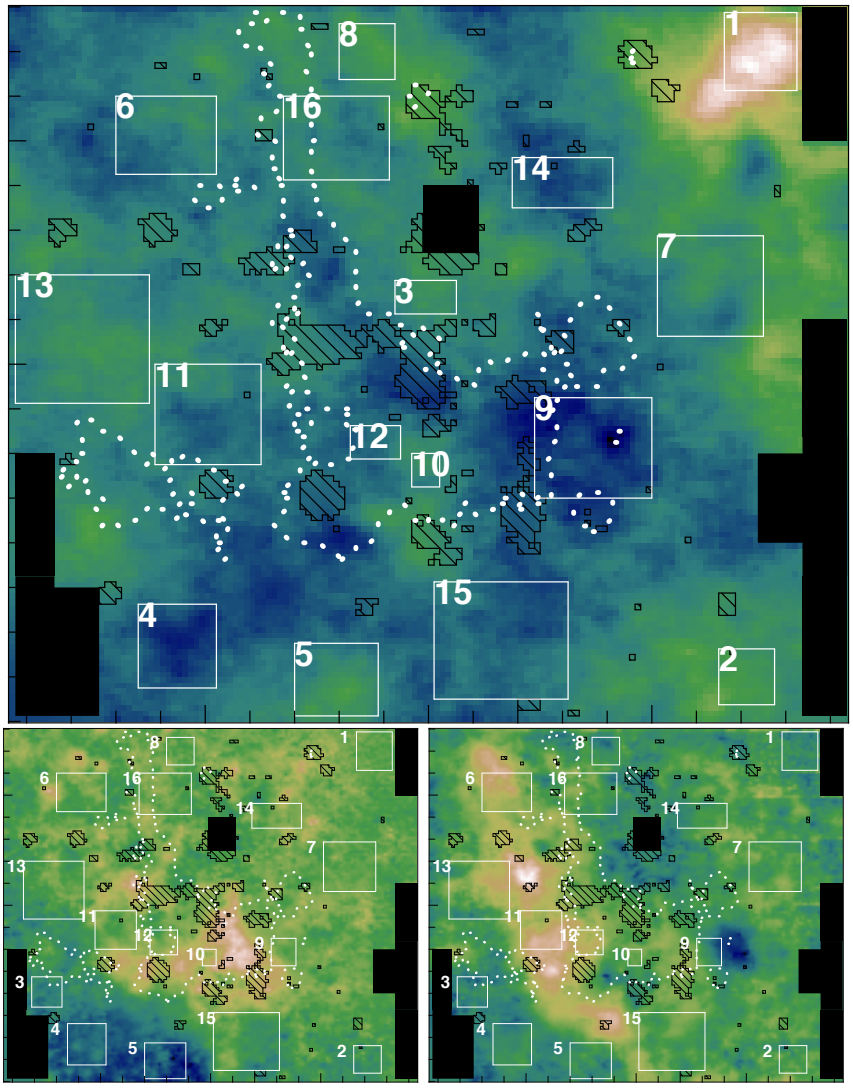

Figure 2.16: Zones where individual spectra of S(1) line, have been extracted, superimposed on parameters maps.

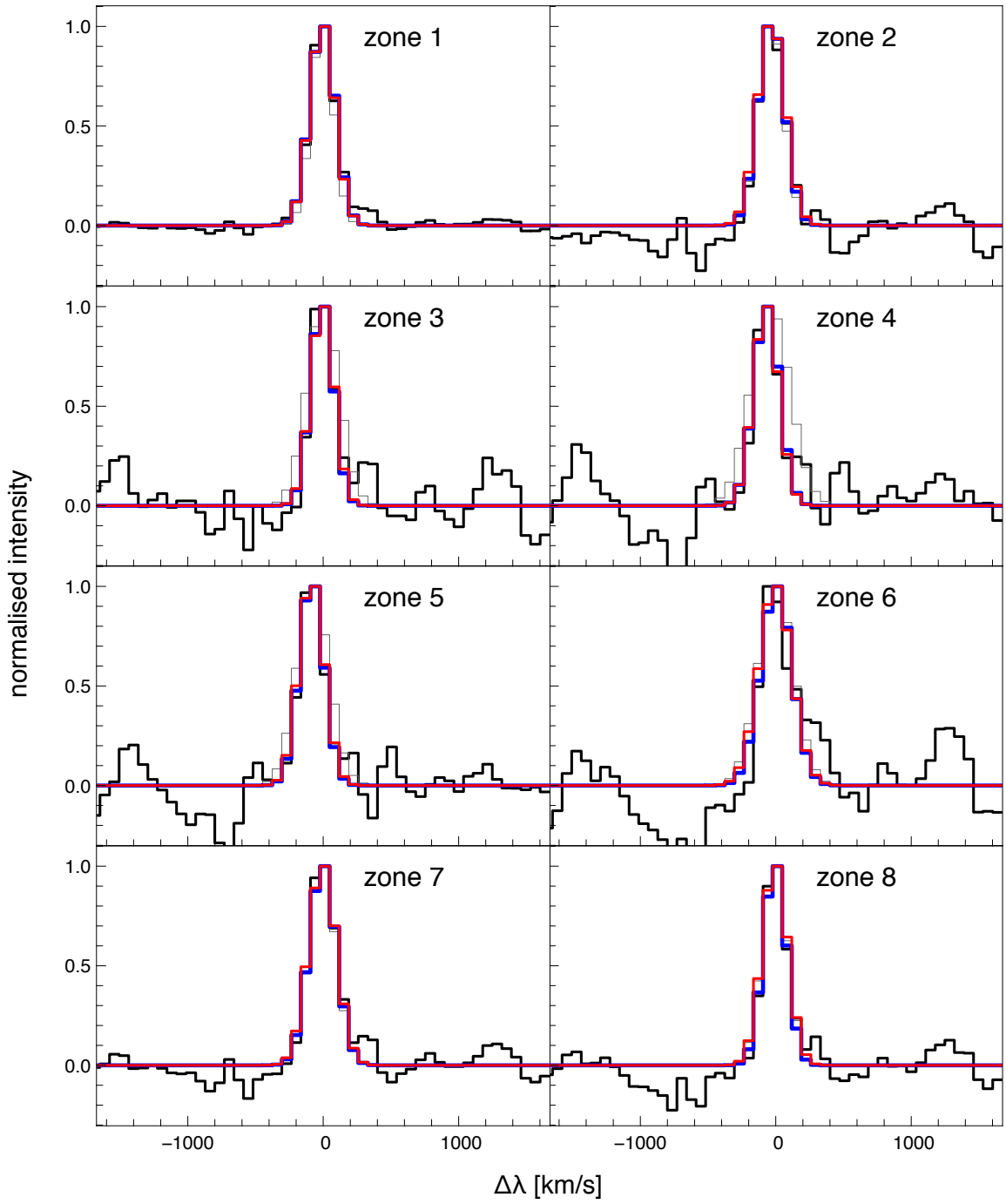

Figure 2.17: For each zone, normalized average spectrum (black) superimposed with the respective 1D-model (solid *blue*) and regularized 3D-fit model (dashed red). The two models can hardly ever be distinguished; when integrating over an aperture, our 3D method is equivalent to classical data analysis. The *gray* line reproduces the 3D model obtained for the third case showed in Fig. 2.15. Comparing this model with raw data and with the 1D fit shows that, even though this model is not far from the solution, it generally overestimates the width. Our best model (fourth case of Fig. 2.15, *red* line on the plot) reproduces much better the observations. X-axis is in km s^{-1}, y-axis is in ADU.

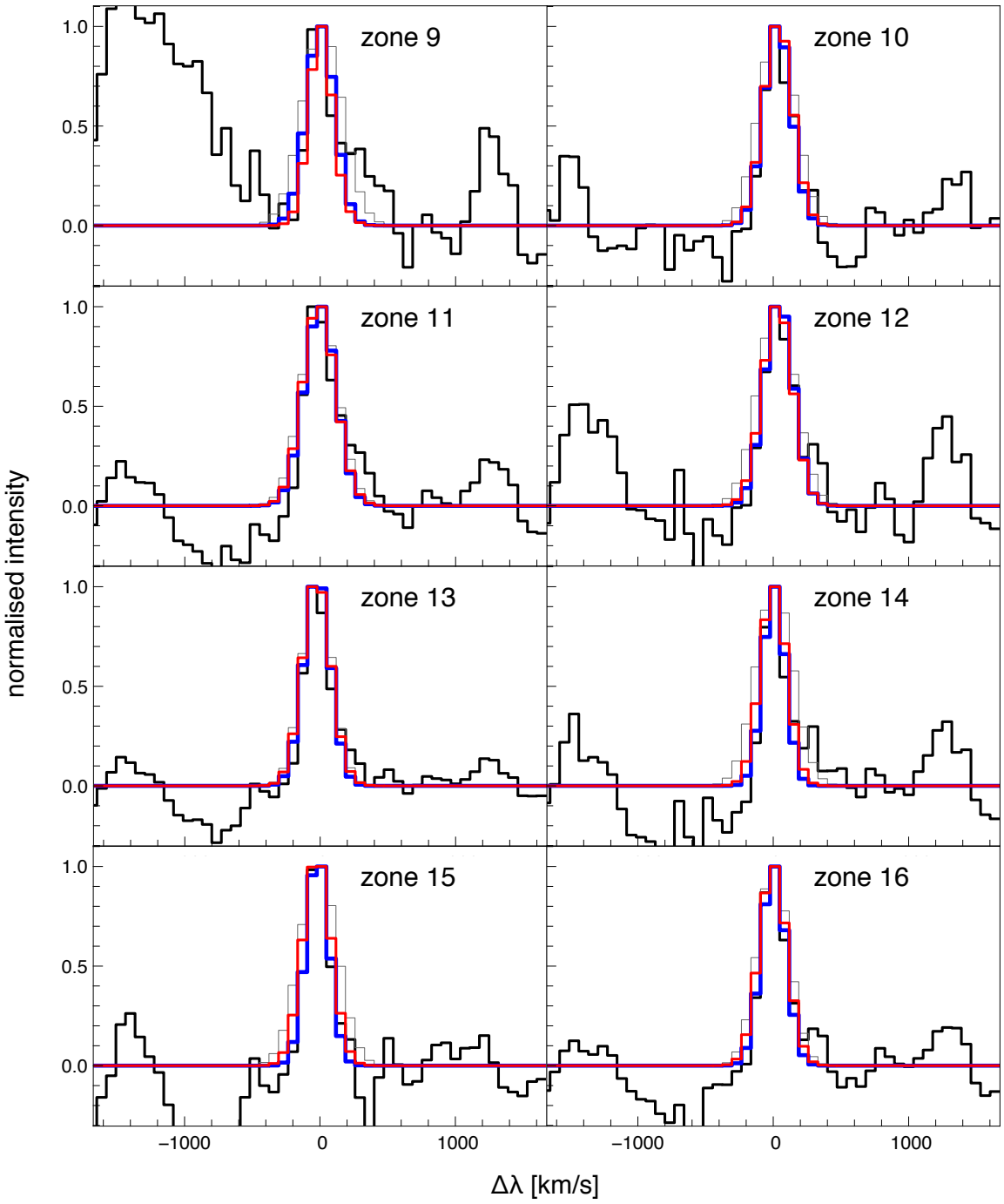

Figure 2.18: Follows from Fig. 2.16.

2.3.3 Uncertainties

The method does not provide a direct estimate of the related statistical uncertainties. We developed a separate technique to evaluate them.

The SPIFFI cube is split into four sub-cubes by keeping in the cube only the odd columns and odd rows, then only the odd columns and even rows etc. Therefore, just one spatial pixel, out of four on a 2 × 2 square and its corresponding spectrum are considered each time (Fig. 2.19). A new, complete, datacube is built interpolating among the chosen points. Since this procedure can be done four times it provides four data cubes, with independent realization of the photon noise.

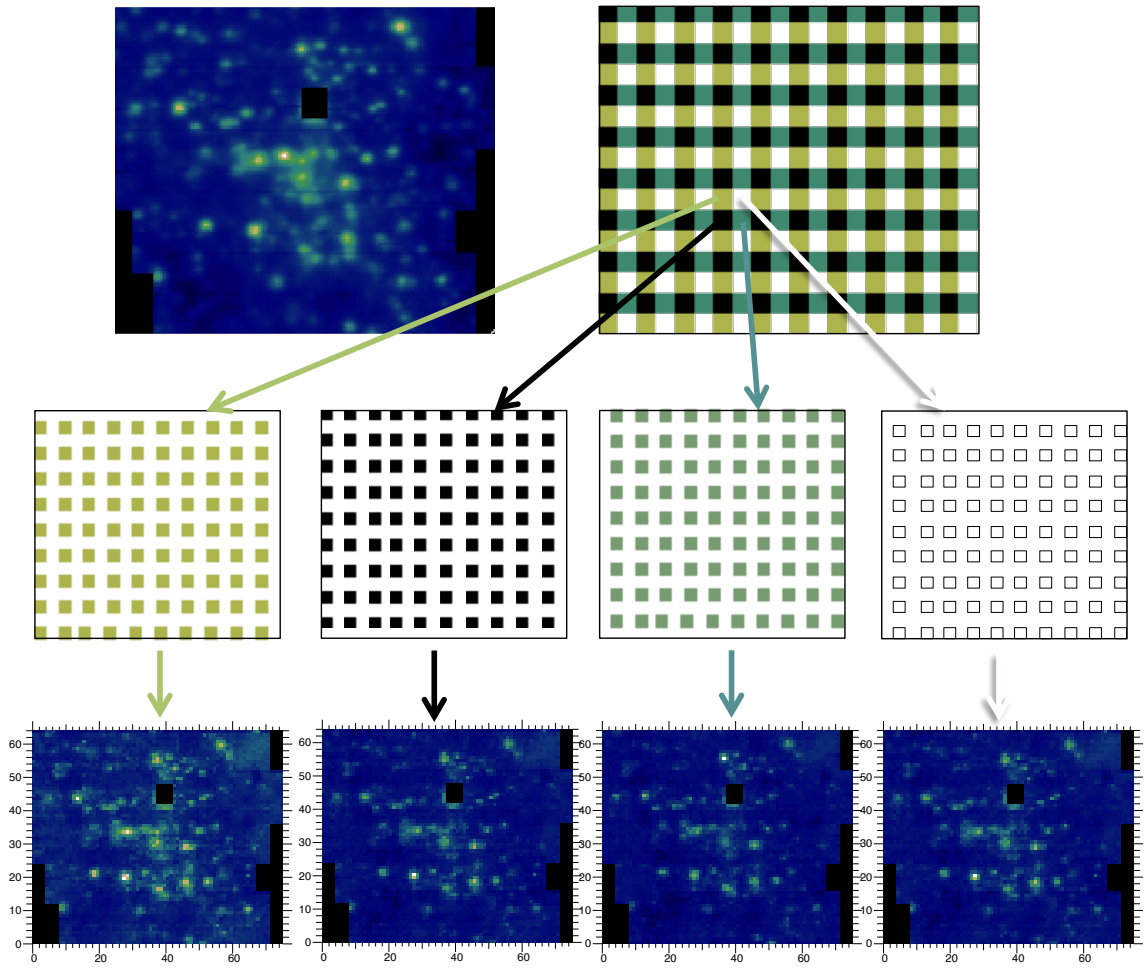

Figure 2.19: Four data cubes are created from the original dataset, taking one pixel over four and interpolating over the holes.

Each cube feeds the regularized 3D-fitting procedure with the same initial guess and hyper-parameters tuning. The regularized 3D-fit uncertainties, for each parameter map, corresponds to the standard deviation of the four obtained solutions. Every uncertainty has to be divided

by 2 because there has been four times less significant information (only one pixel out of four comes from the original cube). The result is a map of uncertainty for each Gaussian fit parameter.

2.3.3.1 Systematic uncertainties

In addition to the above described statistical errors we investigate below three sources of systematic errors.

The choice of hyper-parameters to inject into the algorithm The chosen hyper-parameters – as well as the initial guess for the fitting procedure – influences the resulting maps, especially where the signal-to-noise ratio is poor. When the method works properly, parameter maps are smooth and show significant spatial variations (Fig. 2.15). It means that the model resembles the observations. In this case small variations of hyper-parameters lead to variations in the parameter maps, which in generally remain within the previously discussed error bars. This source of error is therefore not significant compared to the statistical uncertainties.

Continuum estimation Continuum subtraction is estimated by polynomial fit, before applying the regularized 3D-fitting algorithm. Continuum is evaluated on some portions of the spectrum that are free of any gaseous or stellar line. However some H_2 lines happen to be very close to stellar lines. Because of the poor signal-to-noise, it is sometimes difficult to determine where the continuum is standing, and changes in the choses ranges could lead to some changes in the parameter map values. Such changes are generally smaller than the error bars and the shape of parameter maps remains very stable .

Calibration Absolute flux map has one additional source of error which comes from the relative and photometric calibration (see Sect. 2.2.2 for the estimation of this error).

2.4 Instrumental line width

In order to compute the intrinsic line width σ_r, the observed width σ_m has to be corrected for the instrumental width σ_i:

$$\sigma_r = \sqrt{\sigma_m^2 - \sigma_i^2} \tag{2.5}$$

The SPIFFI spectral resolution for these observations is $R \sim 1\,300$. However the SINFONI user's manual[5] shows that the instrumental width varies with the wavelength. In particular it shows the profiles of arc lamp lines, at three wavelengths. The width of these lines is measured here with a Gaussian fit. The three widths obtained are modeled with a quadratic law to estimate the variation of the instrumental width with wavelength. The profiles and the resulting model are shown in Fig. 2.20.

The plot shows that indeed the width varies with wavelength. The values obtained with the model of arc lines (hereafter referred to as "lab-lines") cannot be directly applied since on-sky

[5] https://www.eso.org/sci/facilities/paranal/instruments/sinfoni/doc.html

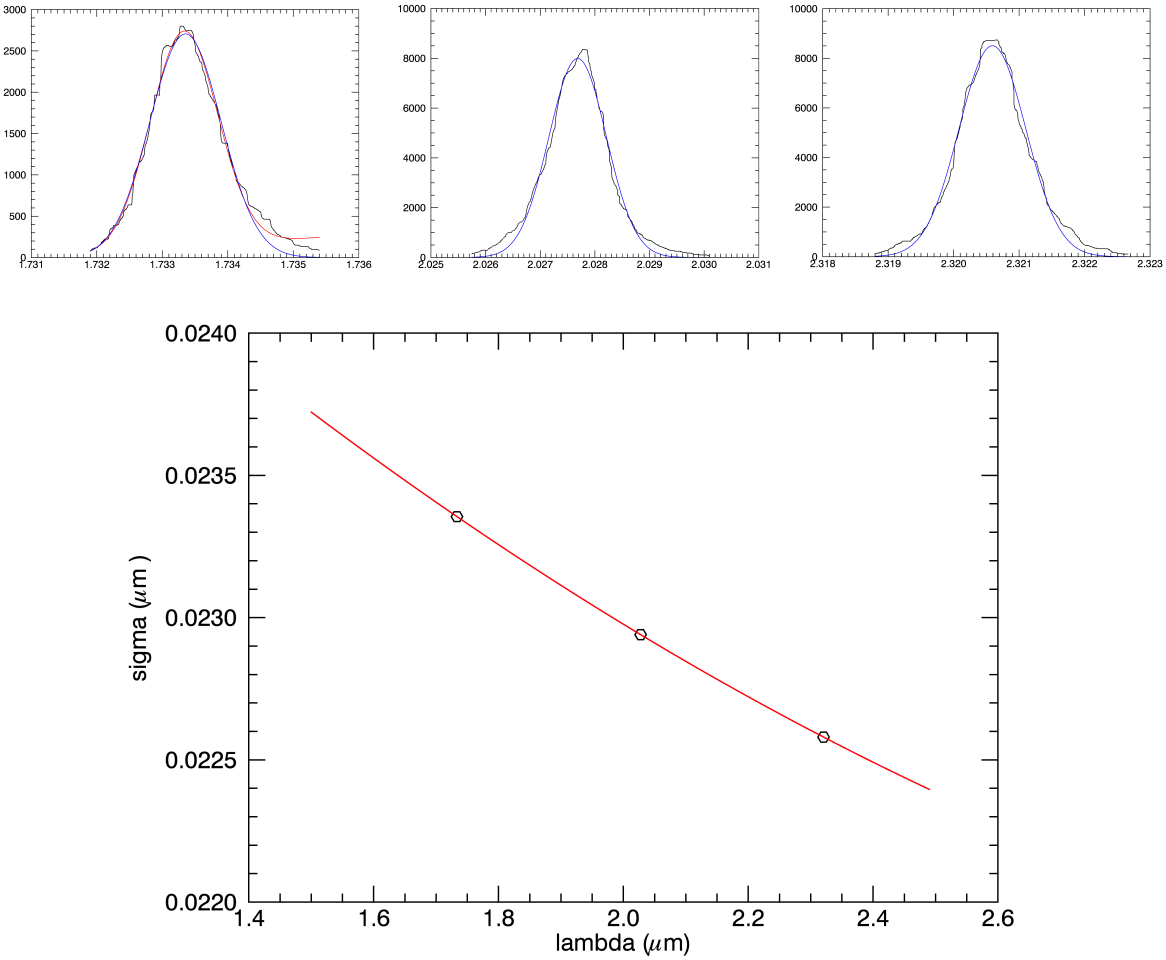

Figure 2.20: *Top:* arc line profiles (from SINFONI user manual), fitted with a Gaussian. *Bottom:* Model of the variation of PSF width with wavelength obtained fitting arc lines.

conditions might be different. To evaluate the resolution relative to these observations, the sky cube was used. Here, many OH atmospheric lines can be seen. Given the very narrow intrinsic width of these lines, they are, in principle, a very good tool for measuring the instrumental width. The average spectrum of the sky datacube is shown in Fig. 2.21.

The easiest choice would be to select OH lines close to the H_2 lines under study and interpolate the value of instrumental width values. However, no intense OH line is present beyond ∼2.3 μm and thus for the 1-0 Q transitions, no interpolation can be done. Moreover, OH lines should be rather isolated in order to be well fitted and, for most H_2 lines, the closest OH line is not the best choice.

This problem can be overcome by modeling the variation of the instrumental width over the whole 1.9 – 2.45 μm range. For this purpose we selected ten lines using two criteria: the lines have to be rather isolated and as close as possible to one of the H_2 lines under study. Each of the selected OH lines has been fitted by a Gaussian and a continuum to measure its

width (Fig. 2.22). The curve of the width as a function of λ is then fitted with a quadratic

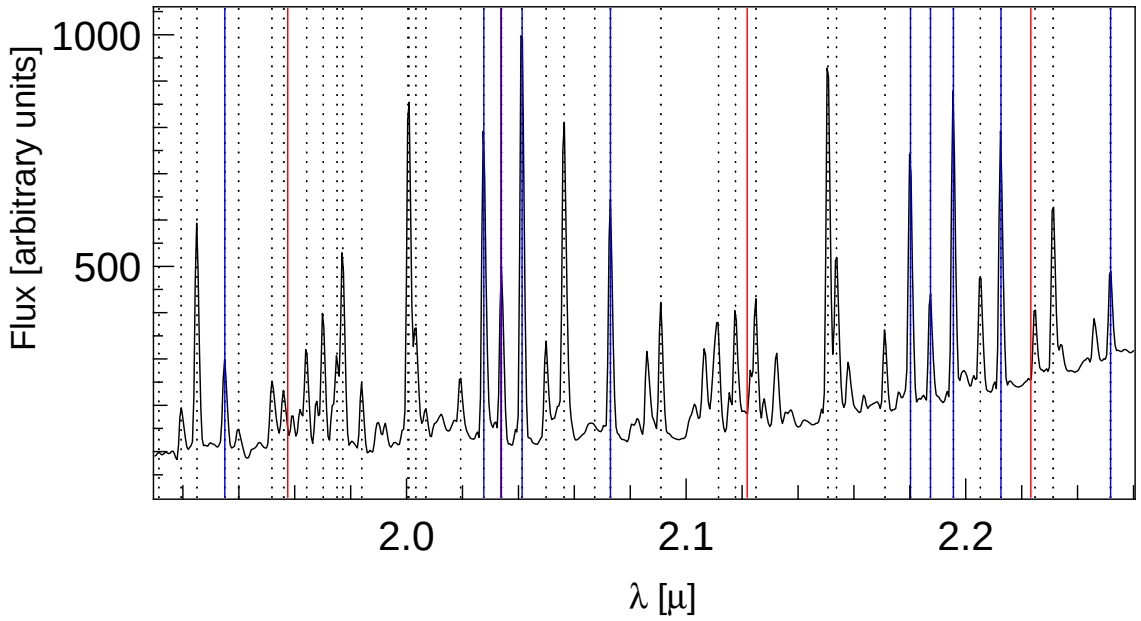

Figure 2.21: Average spectrum of the sky datacube. OH lines with significant intensities are marked by the dotted lines. Blue lines make the OH lines used to measure the instrumental width. The red line marks the wavelength of H_2 1-0 lines. .

law. The maximum variation of the fitted parameters within the error bars is used to trace the maximum and minimum curves which represent the uncertainty of the model. Fig. 2.23 shows the measured instrumental width for the ten selected OH lines – with the relative uncertainties issued from the Gaussian fit – and the corresponding quadratic model. The slope of the curve is similar to what was obtained with the lab-lines, but the values of the instrumental width are significantly higher. These values are of the same order of magnitude as the measured width of the H_2 lines.

The intrinsic width could indeed be tiny but with the present model and uncertainty it is impossible to derive it in a significant way. This is why only measured widths are considered for the purpose of this work. The observed variations on the width map are significant and remain valid though.

Limits can be put on the intrinsic width values, from the lab-lines model – which represents an upper limit – and the OH lines model –which represents a lower limit. Three zones in the width map are considered to calculate intrinsic width values reported in Table 2.5.

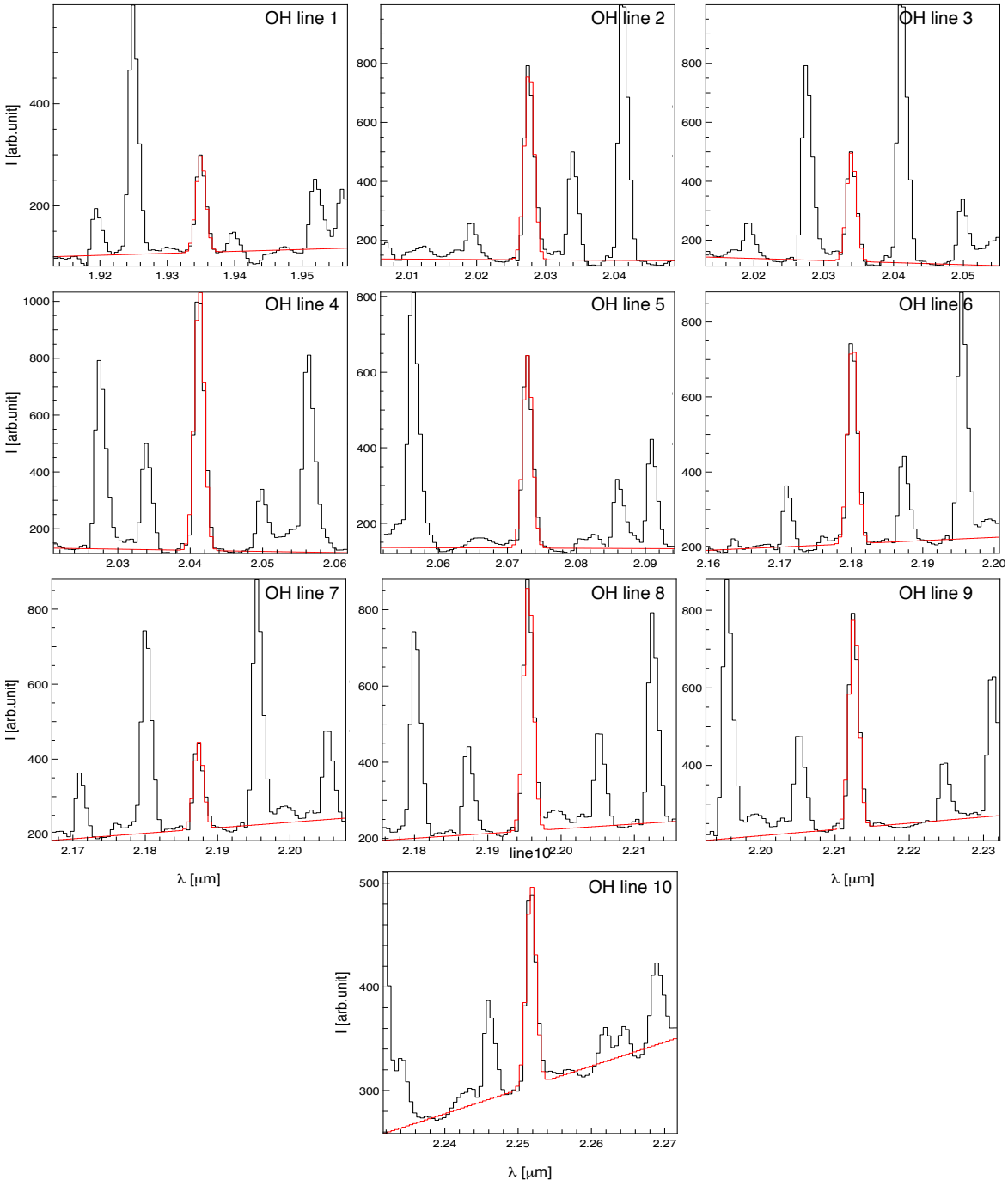

Figure 2.22: Gaussian fit of well-isolated OH lines on the average spectrum of the sky datacube.

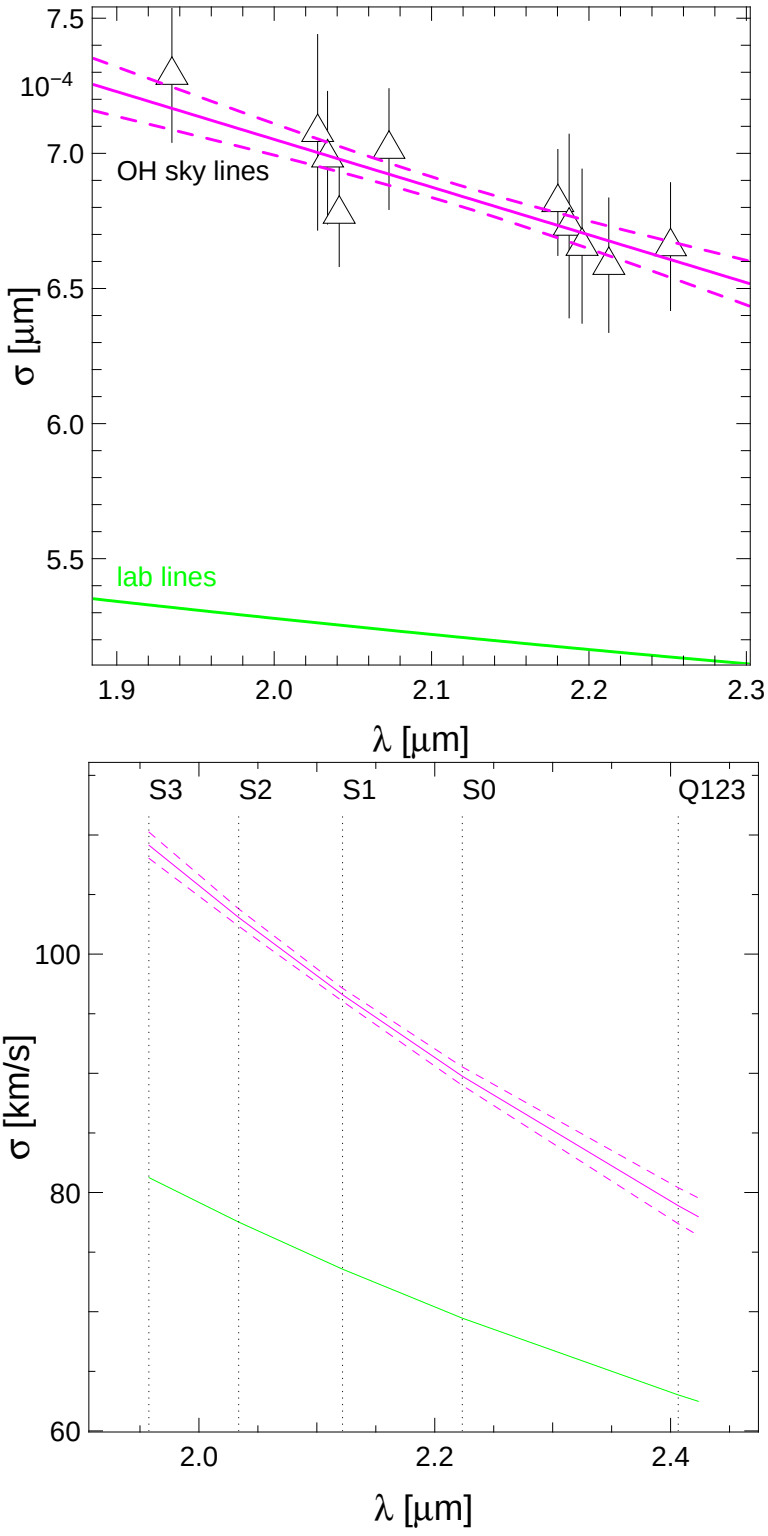

Figure 2.23: *Top:* triangles show the width (in μm) measured on OH-lines. The *magenta* line shows OH-lines model and its uncertainties. The *green* lines show the lab–lines model. *Bottom:* the same as the top graph but in km s^{-1} scale.

zone	σ_m	σ_r	
		lab lines	OH lines
A	97	4	58
B	102	32	66
C	117	66	88

Table 2.5: Measured line width averaged on three zones of Fig. 2.24 and correspondent intrinsic width limits calculated from OH and lab lines models.

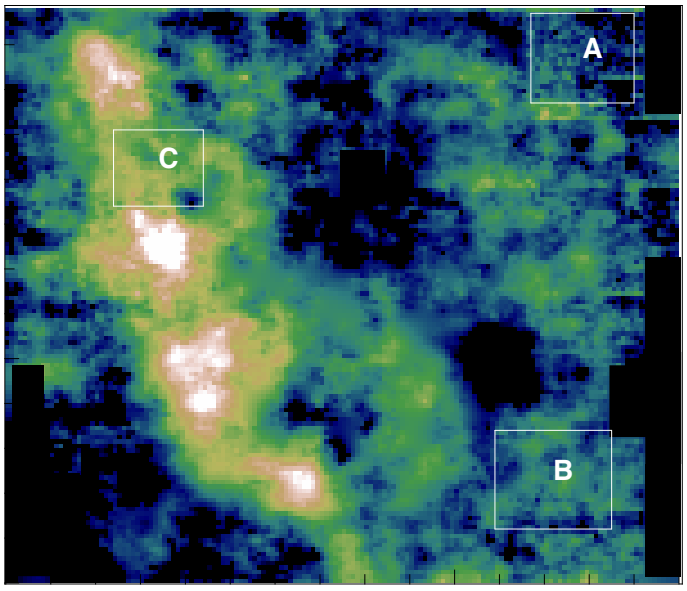

Figure 2.24: Zones where upper and lower limits on the instrumental width are computed. The zones are superimposed on a measured width map.

2.5 Analysis methods: multiline analysis

As previously discussed, not all the lines have sufficiently high signal-to-noise ratio to be treated through the regularized 3D-fitting method. However some lines have a sufficiently high signal-to-noise ratio in some portions of the field. In these regions the study of H_2 can be extended to others lines such as 1-0 S(2), 1-0 Q(2) and 2-1 S(1). Even though no complete parameters maps can be achieved for these lines, the comparison of a wide number of lines is very useful when analyzing the physical properties of the gas in some areas.

2.5.1 Simultaneous fit of spectral lines

The best choice to correctly compare intensities is to simultaneously fit all the H_2 line under study. This allows all lines to have the same velocity and width and avoids propagating uncertainties

In this context the main problem is the continuum evaluation. As previously discussed it is not easy to find a uniform continuum for the wide spectral range of SPIFFI. It is better to subtract the continuum around each line separately and then reconstruct a global spectrum. To do so a spectral window of 10 000 km s^{-1} is considered around each detectable line. A sub-datacube is created and continuum is subtracted as in Sect. 2.2.4. The continuum-subtracted sub-cubes are then put together to build a unique spectrum (Fig. 2.25). From this continuum-subtracted new datacube, we consider the average spectra computed over zones few pixels wide. The selected zones are the same as in Fig. 2.16. These zones have been selected with the objective of having as much H_2 lines as possible. However, not all the same H_2 lines are detectable in every region. Therefore, not all zones present the same number of H_2 lines finally included in the analysis.

For each zone the average spectrum is fitted with a multiple Gaussian profile function. The parameters of this function are: the principal line flux (here 1-0 S(1) since it has the best signal-to-noise ratio), fluxes of every other line with respect to the principal line, velocity and width.

In this way we simultaneously measure the flux for each line (all-lines model). This approach implies that all lines have the same width and velocity. This hypothesis is discussed in Chapter 3. Fig. 2.25 shows an example of the resulting fit.

2.5.2 Uncertainties

The statistical errors given by the multiline fit are small (few per cent) and do not reflect the true uncertainties. The main source of error is the continuum evaluation. The main effect of this evaluation is to overestimate or underestimate the intensity of a given line. This can affect the relative strength of lines and thus the quantities the multiline analysis aims to estimate. For this part of the analysis it is particularly delicate to obtain an accurate estimate of relative intensities.

Therefore, the final uncertainties for this analysis must take this effect into account. The line width is not much affected by bad continuum estimate. Moreover, thanks to the simultaneous fit, it is evaluated through many lines at the same time. This gives it a much higher stability. The line velocity is not affected at all. Hence one can make the assumption that the continuum evaluation affects only the intensity. To evaluate this effect, for each spectral window, we consider the difference between the model and the continuum-subtracted spectrum and compute the interquartile range of this difference. Half of the interquartile range provides the estimation of the error on the chosen continuum, thus on the intensity.

The actual Gaussian parameter considered is the flux, which is related to intensity I and width σ through $F = I \cdot \sigma \cdot \sqrt{2\pi}$. Therefore the final uncertainty on flux is $\sqrt{2\pi} \cdot (I \cdot \Delta_\sigma + \sigma \cdot \Delta_I)$. Where Δ_σ is the statistical uncertainty on the width and Δ_I the uncertainty on intensity, estimated through interquartile range.

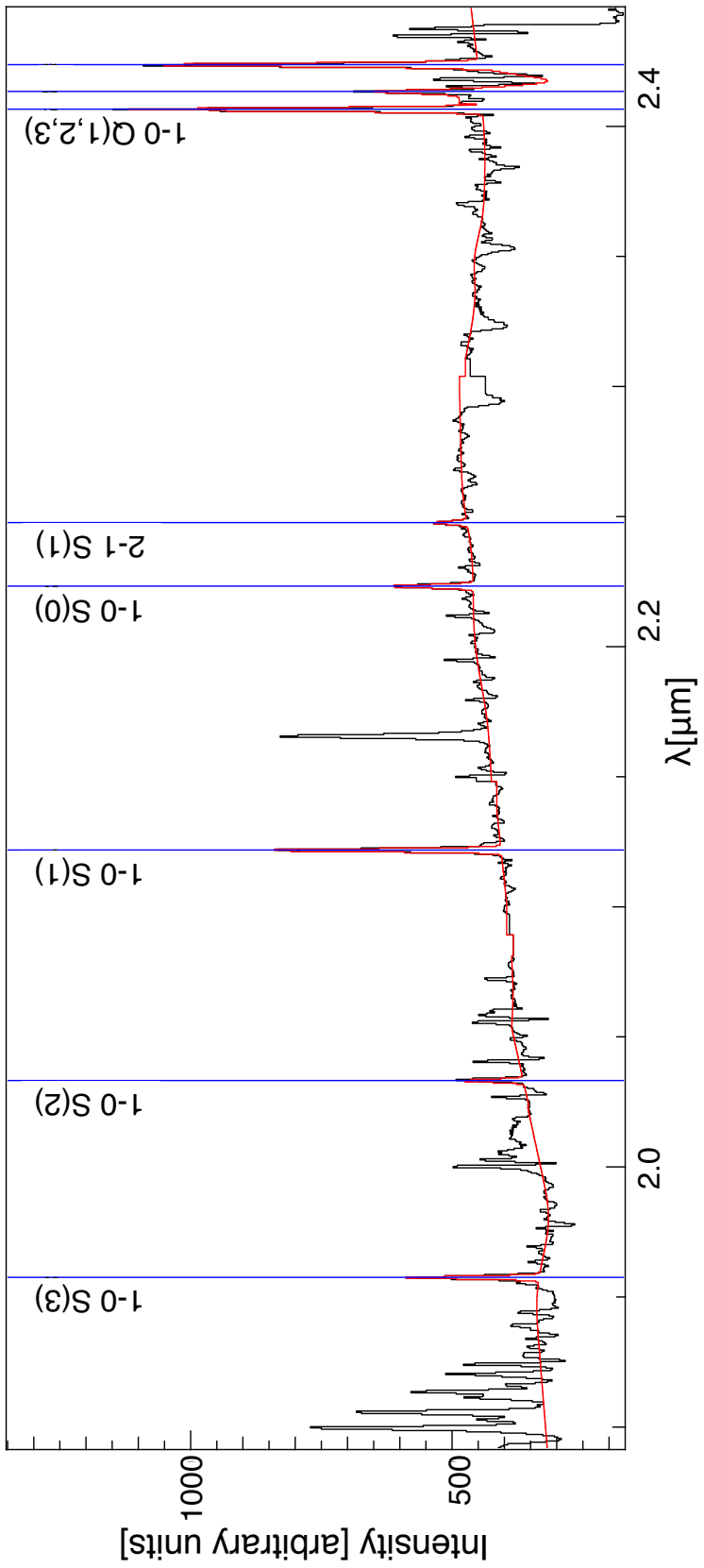

Figure 2.25: The average spectrum of zone 1 of Fig. 2.16 (*black* line) is compared to the result of the multiline-fit (*red* line).

Chapter 3

H_2 morphology and dynamics

Contents

This chapter is devoted to the results on H_2 spatial distribution and dynamics.

The analysis of emission lines is useful to study not only the gas distribution, but also its radial velocity and line width across the field. The regularized 3D-fitting, presented in Chapter 2, is very well suited for this purpose since it allows the simultaneous determination of these three parameters, giving a more comprehensive picture of the gas location and properties.

In the NIR there are many H_2 lines, especially around 2.2 μm. As previously discussed in Chapter 1 the emission of H_2 is undetectable in the average galactic ISM, excepted for unusually warm regions as the central parsec of the Galactic Center. Molecular gas in the central parsec has been previously studied through CO lines, which is the main tracer of cold dense molecular clouds. These analysis trace the CND clouds, however they miss molecular gas which could be located within the CND's Central Cavity. However a quick look at the SPIFFI datacube indicates that H_2 seems to be present in the region. Even though the strong

UV field is likely to dissociate the H_2 molecules, they can survive if shielded. The shielding can be provided either by PDR region, dust or self shielding, provided that the column density is high enough. The UV photons, attenuated by the shielding, can then provide the necessary excitation for H_2 lines to become detectable.

H_2 emission has indeed been detected in the Central Cavity. Yusef-Zadeh et al. (2001) provided a good resolution map of the distribution of H_2, in particular of the 1-0 S(1) line, in the central few parsecs. The maps show that the emission is strong in the CND and it extends also into the Central Cavity.

Yusef-Zadeh et al. (2001) concentrated on the 1-0 S(1) transition line at 2.1218 μm. Other H_2 lines are observable around 2 μm, however they are less intense or close to strong stellar or interstellar spectral features, which makes it difficult to measure them accurately. The regularized 3D-fitting method can overcome some of these problems, even in regions with low signal-to-noise that would not have been accessible with classical techniques. Four H_2 lines, in addition to 1-0 S(1), were accessible to the regularized 3D-fit: the ortho 1-0 S(3), 1-0 Q(1) and 1-0 Q(3) lines and the para 1-0 S(0) line. We present high-resolution maps of the flux, velocity and width variations across the field for each of the four lines.

The map by Yusef-Zadeh et al. (2001) is not corrected for the extinction. Extinction varies widely over the central parsec: of the A_K ~2.5–3.5 magnitudes of extinction on the line of sight, up to 1 mag is due to local extinction (Paumard et al. 2004). Therefore, the knowledge of local extinction is crucial to separate the gradient of the the extinction from those due to intrinsic brightness fluctuations. This work aims at separating these two contributions and show the intrinsic variations of H_2 emission in the central parsec. 1-0 S(1) and 1-0 Q(3) are transitions from the same level of the H_2 molecule. Hence, the apparent ratio of fluxes of Q(3) and S(1) lines gives a direct estimate of the local extinction and therefore gives access to the intrinsic source variations of H_2 emission in the central parsec.

In the next sections the analysis firstly concentrates on the 1-0 S(1) line, then it is extended to the others four lines. Afterwards we investigate the extinction correction and present the first dereddened map of H_2 in the central parsec. This analysis is mostly found in the article Ciurlo et al. 2016 (submitted to A&A, accepted). The last section of this Chapter presents the study of the correlation between the extinction and the dereddened flux which will be the subject of another article (Ciurlo et al. 2016, in prep.).

3.1 Regularized 3D-fit of 1-0 S(1)

The 1-0 S(1) transition line at 2.1218 μm is the H_2 line with the best signal-to-noise in the dataset. Therefore it is the natural starting point of the analysis.

The aim is to obtain maps of each parameter of the Gaussian fit to the line (flux, velocity and width), i.e. obtain the best estimate of each of the three parameters for each pixel. In Chapter 2 it has been shown that this method is more efficient for this task than classical pixel-by-pixel fitting (Chapter 2, Sect. 2.3.1). Therefore, the regularized 3D-fitting has been applied to the 1-0 S(1) line on SPIFFI data cube (3D-fit, see Chapter 2 for details on the regularized 3D-fitting application).

A pixel-by-pixel fit (1D-fit; Chapter 2) has also been performed on a few selected zones of

the field and compared with the results of the regularized 3D-fitting to verify the consistency of the method.

The uncertainties have been estimated with the 4-cubes techniques exposed in the previous chapter. Relative and photometric calibration have been applied to the flux map as described in the previous chapter as well.

In the following sections we present the analysis of the parameter maps.

3.1.1 Flux map

The calibrated 1-0 S(1) flux map, together with the corresponding uncertainty map is reported in Fig. 3.1.

The map shows that the H_2 emission is detected everywhere in the SPIFFI field of view, even in the ionized Central Cavity, as indicated by the signal-to-uncertainty ratio (S/U) which almost everywhere is larger than 10.

The SPIFFI field of view covers part of the western and eastern borders of the CND. In the southeastern and northwestern corners there are, respectively, a weak and a strong emission, most probably dominated by CND molecular gas which is located there. Because of the inclination of the CND with respect to the plane of the sky (Liszt 2003), in the western border – in particular in the North of the SPIFFI field – the CND is closer to the observer and then presumably less extinct. The weak southeastern emission corresponds to the most remote – i.e. presumably more attenuated – CND side. This is coherent with a stronger emission coming from the closest, and thus less extinct, side (the northwestern corner).

3.1.1.1 Comparison to previous works

In Fig. 3.2 the flux map is compared to the one obtained by Yusef-Zadeh et al. (2001). The global pattern is the same, showing, for instance, a stronger emission at the borders of the SPIFFI field of view.

In particular, we find several common features:

- The bright emission coming from the northwestern corner: the observed maximum is slightly shifted to the East with respect to the maximum of the Yusef-Zadeh et al. (2001) map. This peak of emission spatially corresponds to, and is most probably associated with, the CND.

- In the southeastern corner the weak emission located between two stronger peaks of emission: this feature is also associated with the CND.

- The "plume" feature located in the north, near GCIRS 7: as pointed out by Yusef-Zadeh et al. (2001) this plume-like feature does not appear to be associated neither with any the Minispiral's ionized streamers nor with the CND.

The absolute values of the flux are compared in Fig. 3.3. The contours trace very similar shapes. There seems to be an offset of around 5 10^{-16} erg s^{-1} cm^{-2} $arcsec^{-2}$ between the two maps. Knowing that the error bars are around 10% on average (plus the 30% uncertainty of the absolute values) for the map derived here and 30% for Yusef-Zadeh et al. (2001), the two results

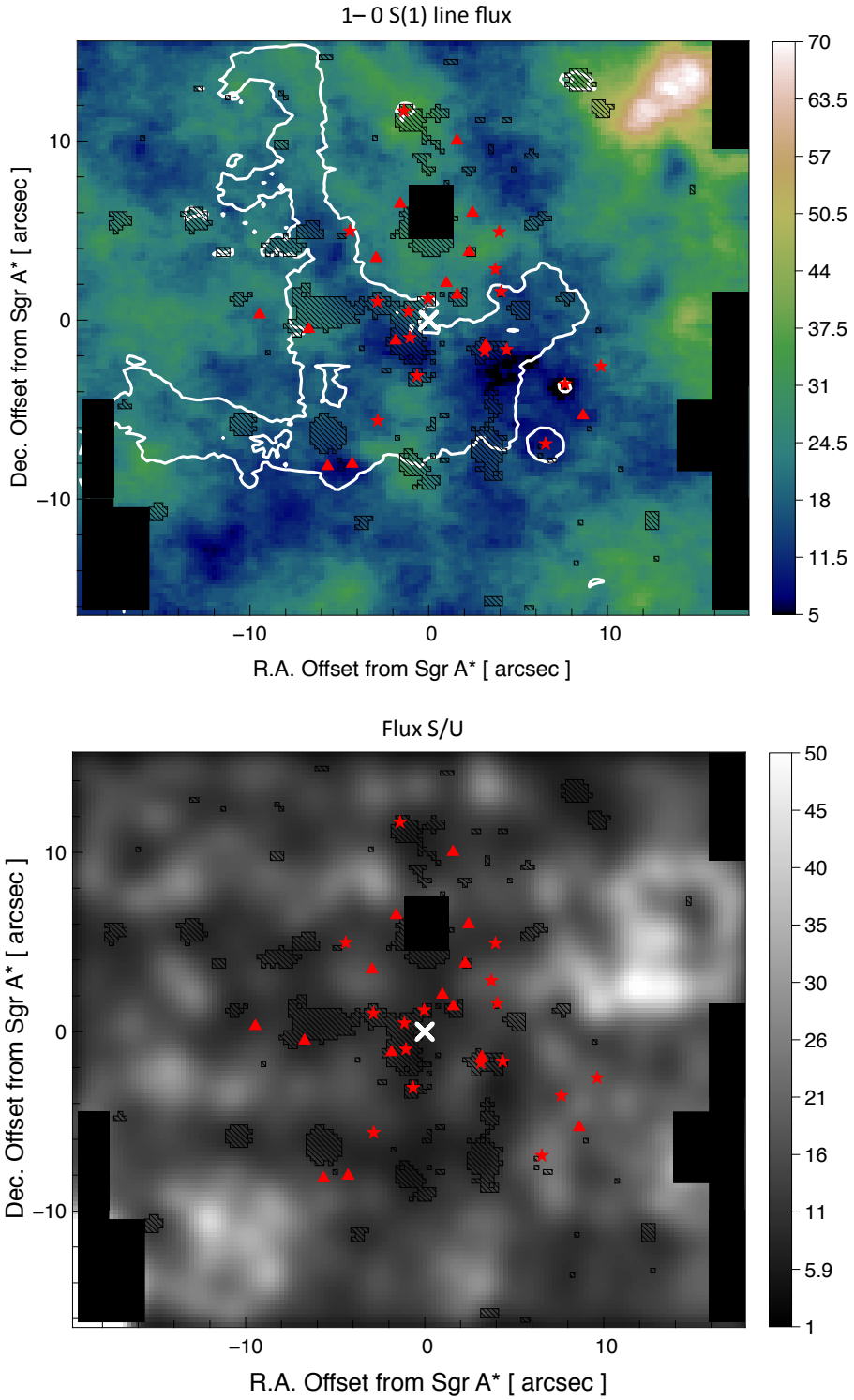

Figure 3.1: *Top:* Flux map of the 1-0 S(1) line. Line flux is in 10^{-19} W m^{-2} arcsec^{-2}. Sgr A* position is marked by the cross. White contour traces Brγ emission of the Minispiral at $2 \cdot 10^{-16}$ W m^{-2} arcsec^{-2}. Dashed areas cover zones that have been interpolated. Red symbols indicate the position of Wolf-Rayet stars: star for type WN and triangle for type WC (Paumard et al. 2006 catalog). Solid black areas covers not observed areas, the black square in the center covers GCIRS 7. *Bottom:* signal-to-uncertainty ratio map (S/U).

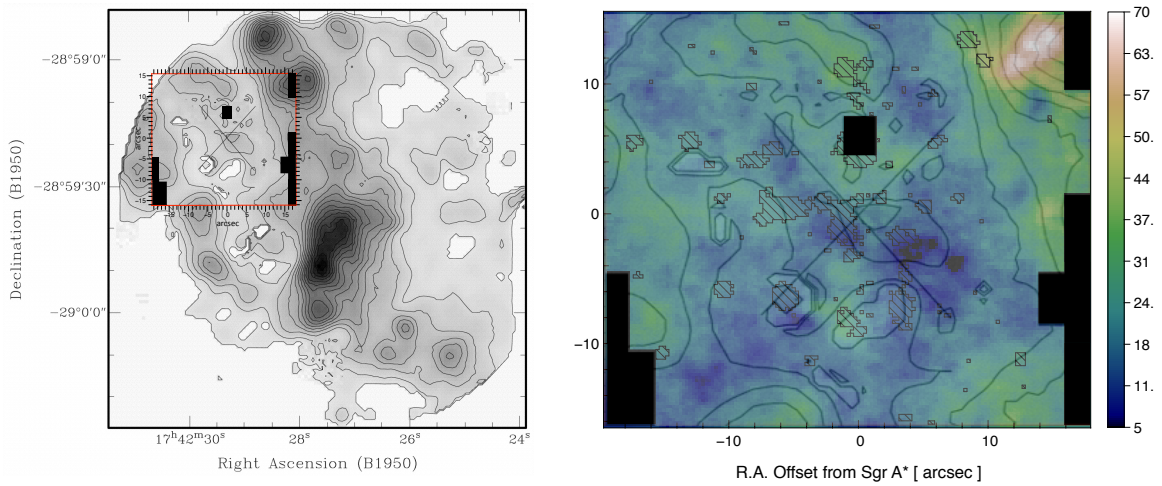

Figure 3.2: *Left:* Integrated H_2 1-0 S(1) line emission by Yusef-Zadeh et al. (2001). Contours are overlaid on a gray-scale representation of the same data. Contour start at (and are in increments of) $5 \cdot 10^{-16}$ erg s^{-1} cm^{-2} arcsec^{-2}. The SPIFFI field of view is represented into the red square. *Right:* Flux map of the 1-0 S(1) line obtained through regularized 3D-fit superimposed on the contour maps obtained by Yusef-Zadeh et al. (2001). Sgr A* is marked by the cross. Line flux color-bar is in the same units as the left image.

are nicely compatible. Since the two analysis use very different techniques and are completely independent (both the flux measurement technique and the absolute flux calibration), this agreement is a good confirmation of the validity of both results.

It is also interesting to compare these results to the distribution of HCN, often used to trace the CND. A very detailed map of HCN in this region has been provided by Christopher et al. (2005). This HCN distribution clearly traces the CND clumps. In Fig. 3.4 it is compared to SPIFFI and Yusef-Zadeh et al. (2001) H_2 maps. In the southeastern corner of the SPIFFI field the H_2 emission is very close to the HCN feature referred to as the Southern Extention by Christopher et al. (2005). The northwestern corner and western border H_2 emissions coincide with the HCN distribution as well.

The H_2 emission (both in Yusef-Zadeh et al. 2001 and SPIFFI map), in contrast with HCN, remains fairly significant inside the CND borders. This emission could arise from the background of the Minispiral. This idea is suggested by the fact that the shape of the Minispiral seems to stand out where the H_2 emission is weaker. In particular there is a well-defined emitting area West of the Brγ emission of the Northern Arm. Indeed, material in this region of the Central Cavity is less dense than in the Minispiral arms or in the CND and would not stop the background emission as much. However the most tantalizing interpretation is that the H_2 emission comes from the Central Cavity itself, close to the center. This interpretation seems more natural because, for these lines to be observed, the gas has to be quite warm. Indeed in the central parsec the molecular gas is exposed to the intense UV radiation that can pump the molecules in excited states. On the other hand, in such hostile environment H_2 could be efficiently photo-dissociated. There must be some shielding mechanism or active reformation of molecules to support this idea. This question will be addressed in more details

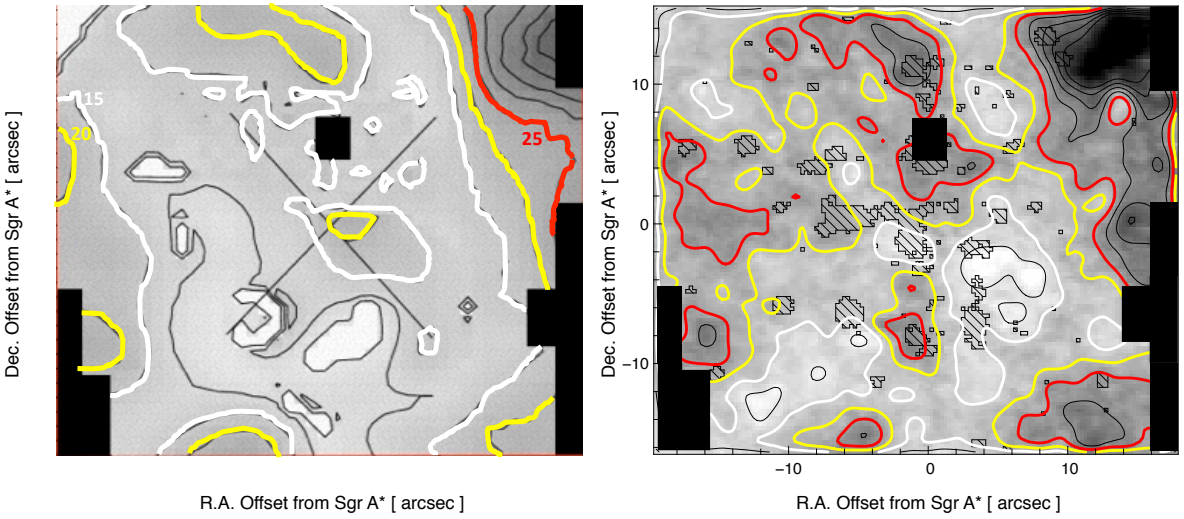

Figure 3.3: *Left:* zoom of the integrated H_2 1-0 S(1) line emission by Yusef-Zadeh et al. (2001) on the SPIFFI field of view. Contours start at (and are in increments of) $5 \cdot 10^{-16}$ erg s^{-1} cm^{-2} arcsec^{-2}. White, yellow and red contours marks 10, 20 and 25 10^{-16} erg s^{-1} cm^{-2} arcsec^{-2} respectively. *Right:* Contours of the 1-0 S(1) line flux obtained through regularized 3D-fit. Contour colors and levels are in the same units as the left image. Sgr A* is marked by the cross

in Chapter 4. In the next chapter the simultaneous analysis of several H_2 lines will provide indications that this emission is indeed in the central parsec.

Nevertheless the flux map indicates that there are, at least, two distinct components of the emission: one associated with the CND (mainly in the southern, western ad eastern borders of the SPIFFI field of view) and one inside the Central Cavity, mainly East and North of Sgr A*. However, a more precise interpretation on H_2 distribution has to take extinction into account, as it will be done in Sect. 3.3.1.

3.1.2 Velocity map

The 1-0 S(1) velocity map and the corresponding error map are shown in Fig. 3.5. The southeastern corner presents a well-pronounced blueshift. The motions of all objects in the central parsec have been depicted in Paumard et al. 2006, as reproduced in Fig. 3.6. The CND rotates in anti-clockwise direction and it is inclined with the top-right corner closer to the observer. The gradient in this portion of the field is consistent with a motion towards the observer from the top-left to the bottom-right of this corner. The H_2 velocity map is thus consistent with the CND inclination and rotation at this location.

The velocity at the borders corresponds also well to the CND motion when compared with the HCN velocity (Christopher et al. 2005). Fig. 3.7 shows the comparison between the HCN and H_2 velocity maps. The velocity gradient observed in the southeastern corner follows fairly well the HCN velocity field. For instance the velocity corresponding to the Southern Extension is around -40 km s^{-1} while Christopher et al. (2005) found $\sim$ -50 km s^{-1}. These authors found

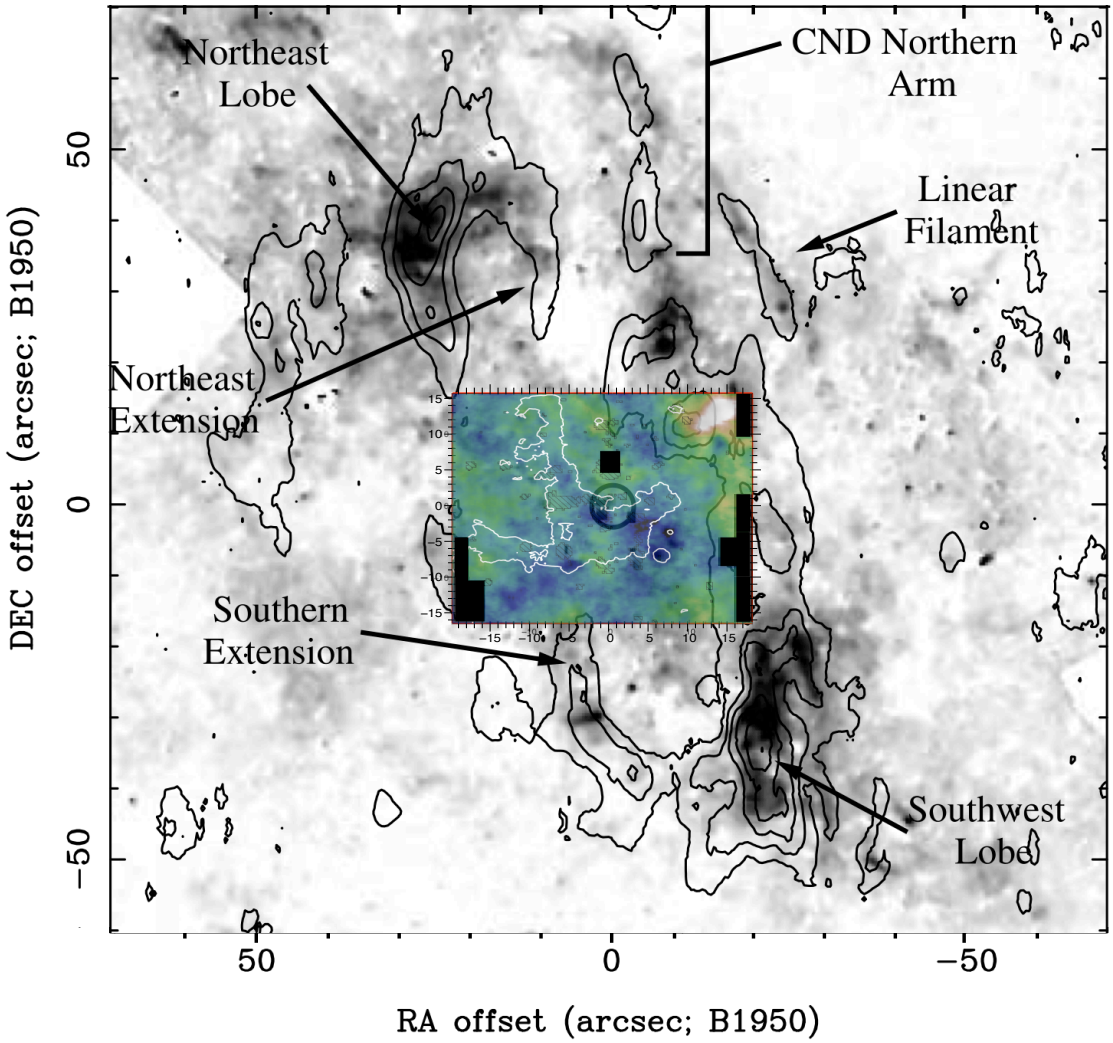

Figure 3.4: Christopher et al. (2005) HCN distribution contours are superimposed on H_2 map of Yusef-Zadeh et al. (2001). H_2 flux map obtain with the regularized 3D-fit is traced in colors, units are the same as in Fig. 3.1.

50–60 km s^{-1} for the northwest corner and western border of the CND, in agreement with what we found here: ∼30–50 km s^{-1}.

Apart from the blue-shifted corner, most of the field covered by SPIFFI shows a relatively uniform motion at around 30–50 km s^{-1}. There is no evident gradient in the north.

In the field there are also several features at higher positive velocities. Most of the time these peaks correspond to the location of stars. Some of these peaks may be artifacts of the model due to unrelated stellar features or photon noise. If indeed these features were real, a very tentative explanation would be that they correspond to actual H_2 emission in the gas ejected by the stars themselves. The western part of the field – corresponding to the CND border – looks smoother in velocity than the Central Cavity. This can be interpreted as the result of the more complex structure and dynamics of the Central Cavity with respect to the CND and an additional evidence that the H_2 emission is not coming from a remote background.

The velocity measurement at the center of the map is strongly affected by artifacts due to

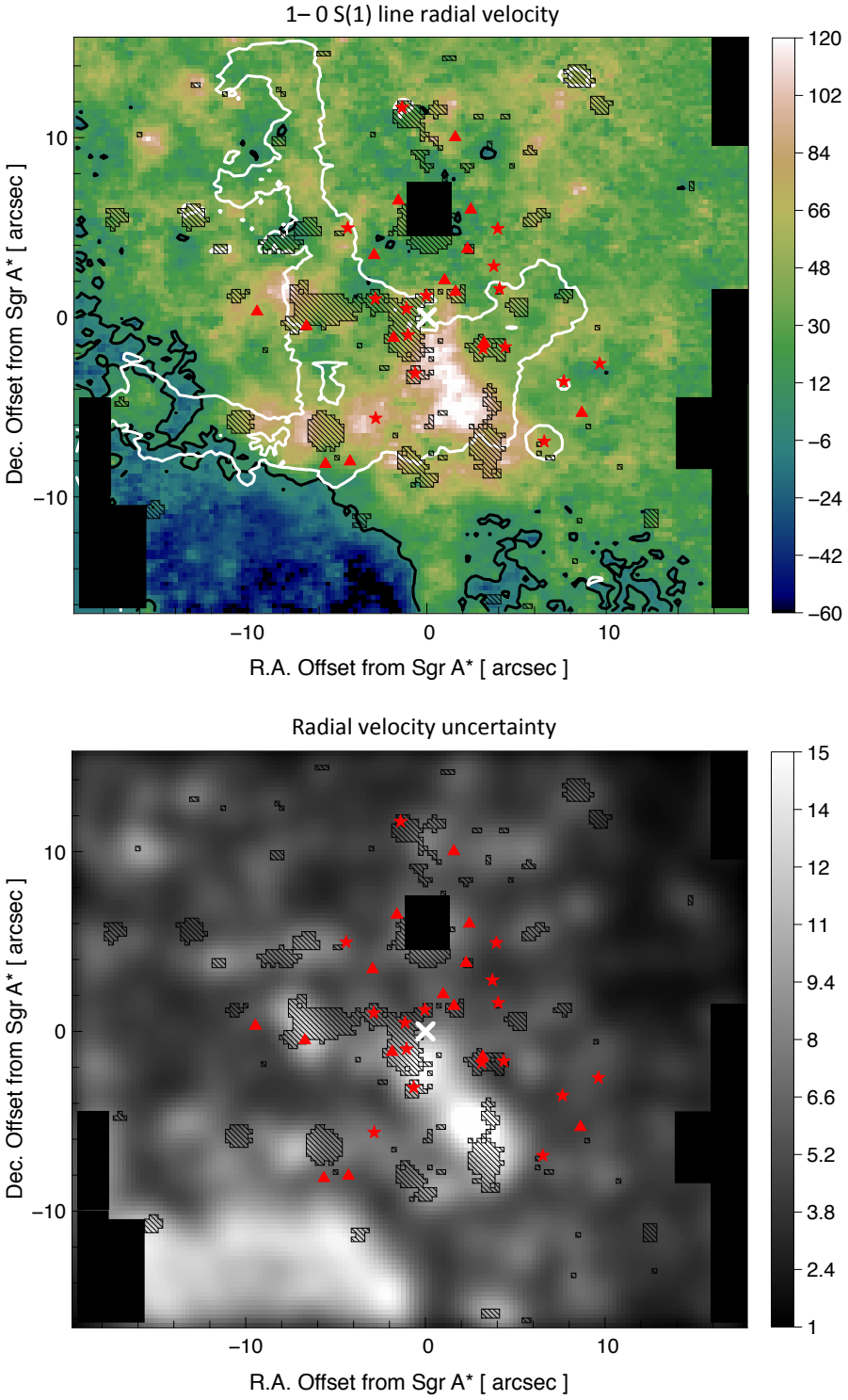

Figure 3.5: *Top:* Velocity map of the 1-0 S(1) line. Velocity is in km s^{-1}. Negative velocities (*blue*) correspond to approaching emission. The solid black line indicates points at zero velocity. *Bottom:* uncertainty map. Symbols as in Fig. 3.1.

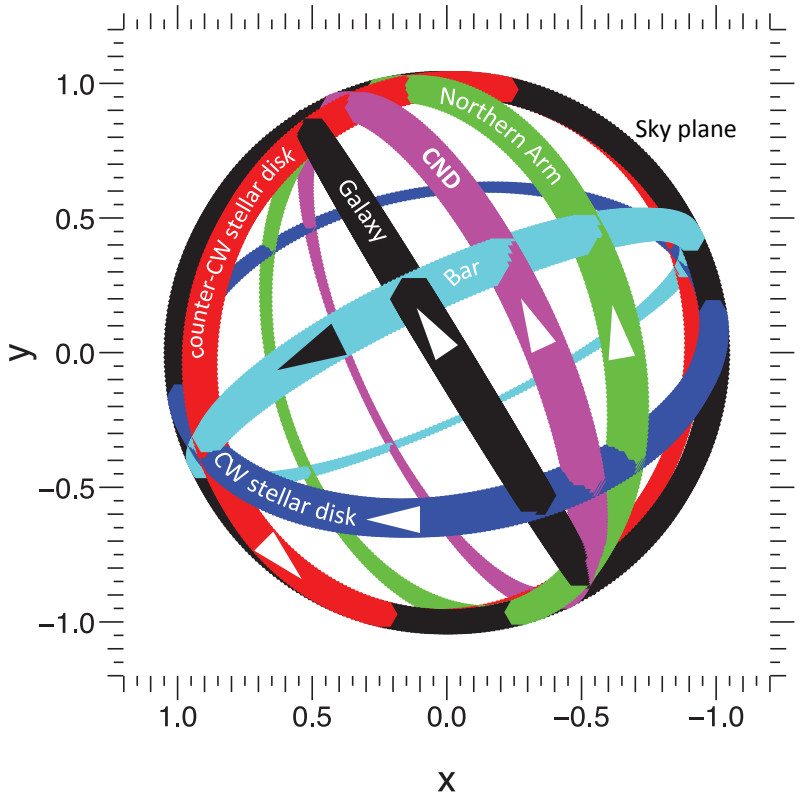

Figure 3.6: Planar structures of the central parsec from Paumard et al. (2006). Each plane is represented by one ring. The thickness of the ring figures the proximity to the observer. Arrows indicate the direction of rotation. *Magenta:* the CND. *Black:* the Galaxy and sky. *Green:* the Northern Arm of the Minispiral. *Cyan:* the Bar of the Minispiral. *Blue and red:* the clockwise (CW) and counterclockwise stellar systems respectively (Chapter 1, Section 1.2.6.1).

nearby stars. This region is very close to the Minicavity, a shell of $\sim 5''$ (Yusef-Zadeh et al. 1989; Eckart et al. 1992), probably created by the interaction between the stellar wind and the ISM (Lutz et al. 1993) or by a jet from Sgr A* (Eckart et al. 1992). It is thus a region of shock and the high velocity observed here may be related to this shock. However the bad signal-to-noise ratio prevents any strong conclusion in this region.

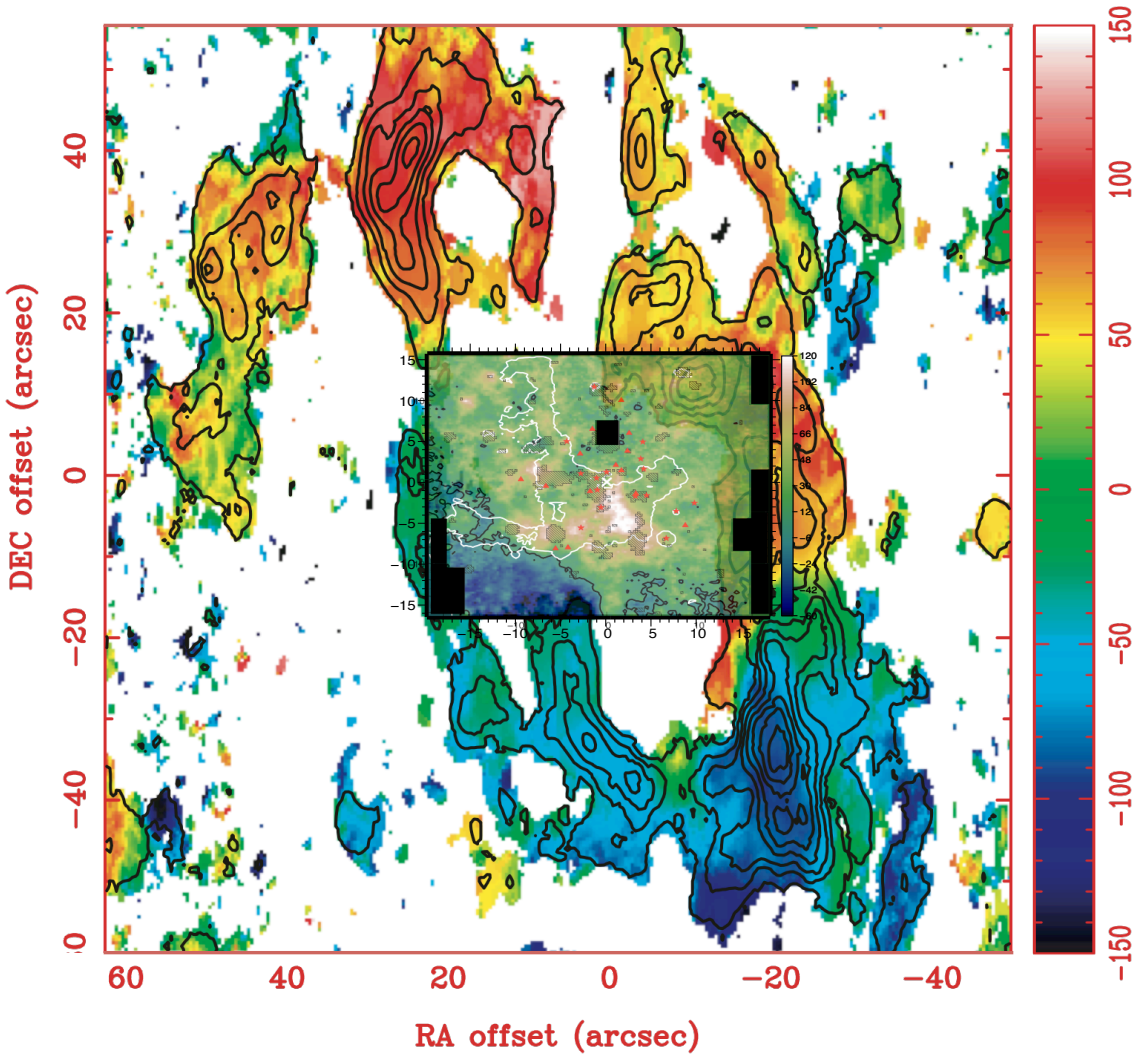

Figure 3.7: The 1-0 S(1) velocity map is superimposed on Christopher et al. (2005) map of HCN flux (contours) and its flux-weighted average velocity (colors).

3.1.3 Width map

The width map and the corresponding error map are reported in Fig. 3.8.

The H_2 1-0 S(1) line looks narrower in the southeastern and northwestern corners than in the rest of the field. These two regions undoubtedly corresponds to the CND. The CND is, by definition, denser than its Central Cavity. The Central Cavity is thus more transparent than the CND to both the UV radiation, which excites H_2, and the IR photons of H_2 lines. In the CND, a high optical thickness is reached over a short geometrical length, whereas in the Central Cavity, the same optical thickness is reached only by integrating over a longer path, over which the velocity dispersion can be larger. In the CND the emission more likely comes from the surface of its dense clouds, illuminated by the UV. On the other hand, in the Central Cavity, the observed larger width might be the consequence of the integration over a longer line of sight.

There are two exceptions to this dual behavior: the first is around GCIRS 7, on the "plume" feature, the second is between the Bar and the Western Arc, around 8″ West and 4–6 ″ South of Sgr A*. The first case might be an indicator of conditions similar to those observed on the CND (i.e. a thinner emitting layer of material). The second case refers to an area where the spectrum suffers from the spectral pollution by a strong absorption feature. Imperfect subtraction of this stellar feature explains the apparent narrowness of the interstellar line.

There are some strong enhancements (i.e. large width) along a ridge slightly shifted to the East with respect to the Northern Arm of the Minispiral. This area corresponds to a thick cloud whose western boundary is ionized and traced by the North-South Brγ emission (Jackson et al. 1993; Paumard et al. 2004), hereafter referred to as the Northern Arm Cloud. The width map enhancements correspond, in projection, to part of this cloud, suggesting that the H_2 inside is more turbulent.

Combining these observations with the previous discussion on the flux and velocity map, different features of the emission seem to characterize different conditions and environments of H_2 (c.f. Fig. 3.9):

- One component of the emission comes from the CND. There, the flux is stronger in the closest side of the CND (the northwest corner) and weaker in the most remote side (southeast corner). In both corners the line is narrower with respect to the majority of the field because of the higher density of the CND itself which does not allow to integrate deep into it. Another emission characterized by a narrow H_2 line comes from around GCIRS 7, in projection.

- The other component comes from the Central Cavity (at least in projection). Here the gas is less dense and it is possible to penetrate on a longer distance so that the observed widening of the line traces the dispersion in velocity along this line of sight. This effect is particularly strong inside the thick Northern Arm Cloud. Here the emitting material might extend more deeply and it is probably turbulent, implying a velocity gradient along the line of sight.

The spatial appearance of the width map is very different from the flux map. They even might look slightly anti correlated. Fig. 3.10 shows that in fact there is no statistically significant correlation or anti-correlation between the two maps.

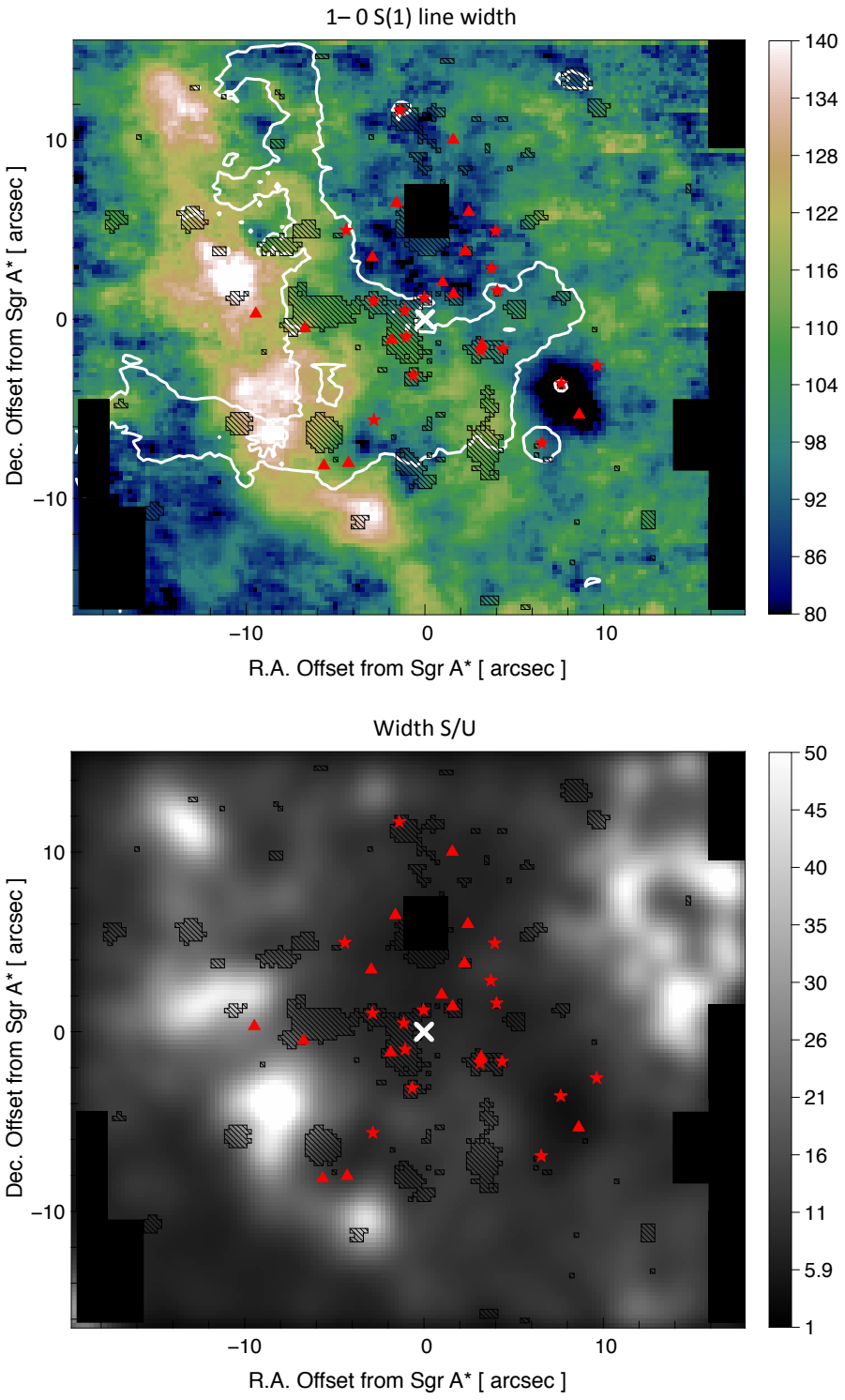

Figure 3.8: *Top:* Width map of the 1-0 S(1) line. Width is in km s^{-1}. *Bottom:* signal-to-uncertainty ratio (S/U) map. Symbols as in Fig. 3.1.

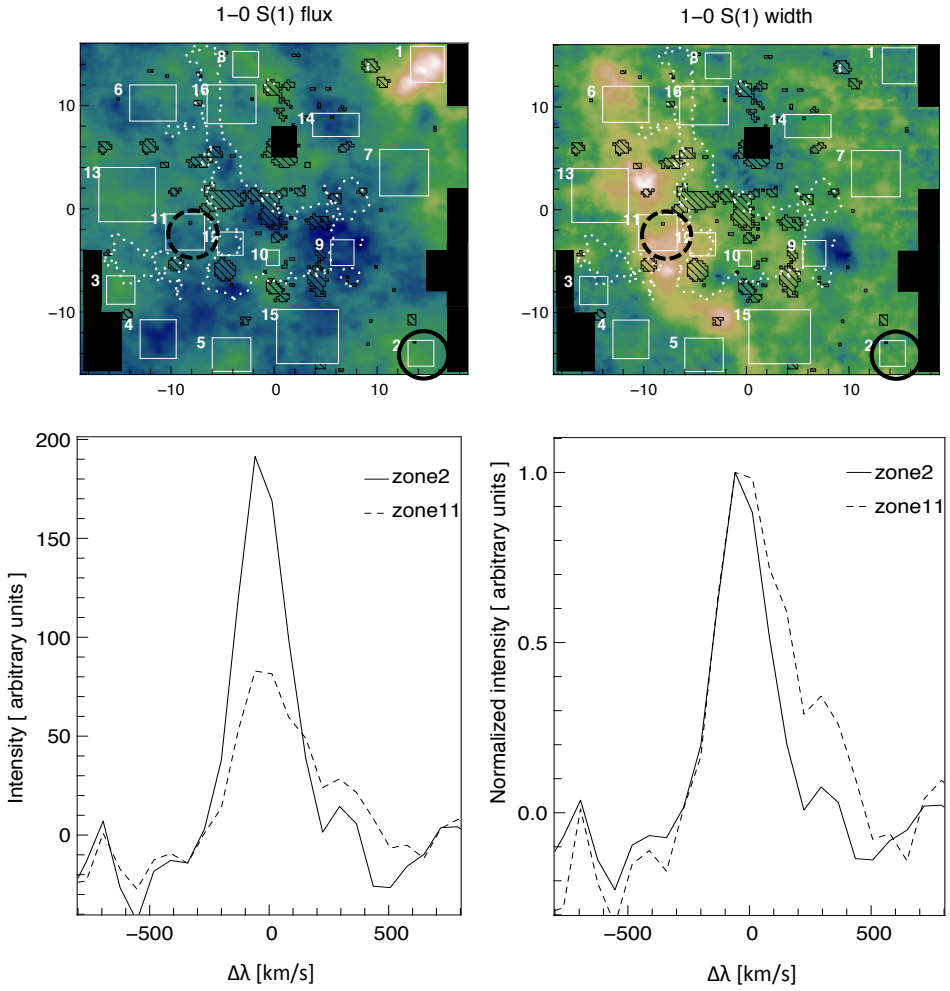

Figure 3.9: *Top:* Flux (*left*) and width (*right*) maps of 1-0 S(1) line. *Bottom:* Average spectra around S(1) line, of zone 11 (wider line and weaker emission) and 2 (stronger emission and narrower line) comparison (*left*) and normalized spectra comparison (*right*).

The line width parameter represents the fitted measured width, which is the quadratic sum of intrinsic and instrumental width. As previously discussed in Chapter 2, an estimation of the instrumental width from the OH sky lines has been attempted, but the reached precision is too poor to obtain a trustful intrinsic width map: the intrinsic width is too small compared to this instrumental resolution to estimate it properly. However variations of the intrinsic width translate into detectable variations in the observed width.

3.2 Regularized 3D-fitting of other lines

To complement the results obtained for the 1-0 S(1) line, the regularized 3D-fit has been applied to others H_2 lines which are covered by the SPIFFI spectral range. There are three lines which are well suited for this purpose: 1-0 S(3), 1-0 Q(1) and 1-0 Q(3) at 1.9575 μm, 2.4066 μm and

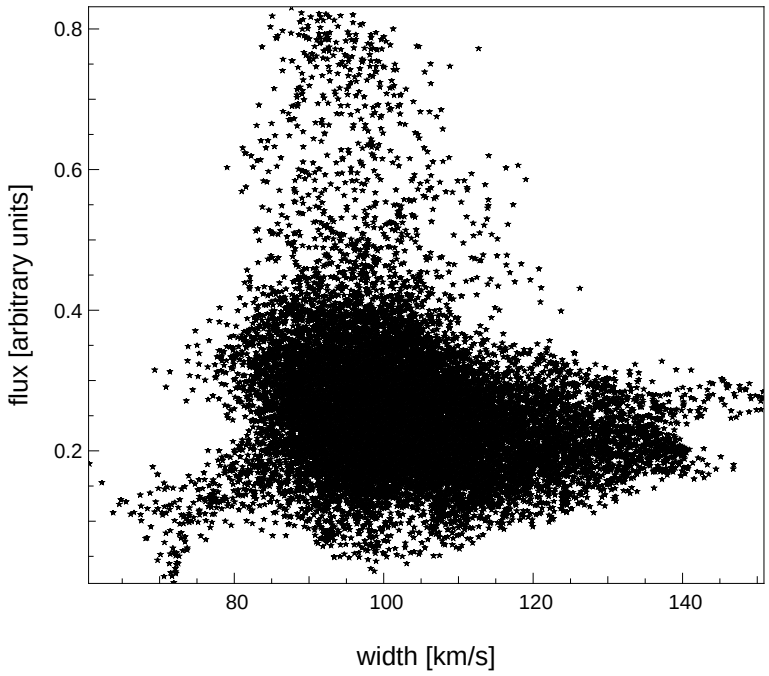

Figure 3.10: The flux of 1-0 S(1) is plotted against the corresponding width. No strong correlation between the two quantities can be inferred

2.4237 μm respectively. These lines have a sufficient signal-to-noise ratio to be studied through the regularized 3D-fitting across the field. Moreover they have the advantage of being lines of the ortho hydrogen, like 1-0 S(1). For this reason they are more suited at confirming the results obtained for 1-0 S(1). The 1-0 S(0) line is analyzed with the regularized 3D-fit method as well, allowing to include para hydrogen in the analysis.

3.2.1 Ortho 1-0 lines

Even though these lines are among the H_2 lines with the best signal-to-noise ratio – after S(1) – in the SPIFFI spectral range, they are in a more complex spectral environment than the S(1) line. S(3) is near the atmospherically absorbed range between the H and K bands. Q(1) and Q(3) are close to CO stellar photospheric absorption features. These strong absorption features affect the observed parameters, sometimes making H_2 lines appear narrower or weaker than they actually are. To alleviate these difficulties, a particularly careful choice of the wavelength domain where the continuum level is evaluated has been done (Chapter 2, Sect. 2.2.4). The retrieved maps from the regularized 3D-fit for each of these lines are displayed in Fig. 3.12.

Even though the fitting procedure is more challenging than for 1-0 S(1) maps, the three ortho lines maps shows features similar to those of 1-0 S(1).

Flux maps: besides the obviously difference in absolute values, all maps show the same patterns as S(1). In particular on each map we recognize the strong CND-emission in the northwestern corner, the weaker emission in the opposite corner, the Plume feature and the

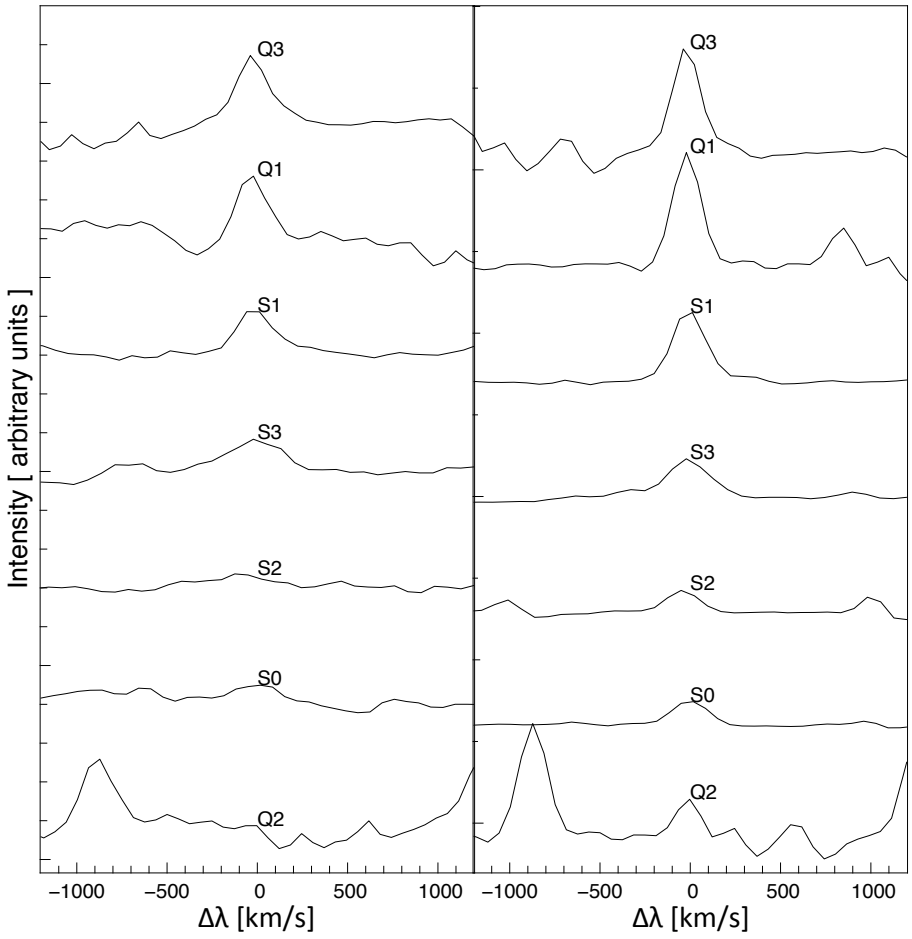

Figure 3.11: Detectable H_2 lines uncalibrated spectra, arbitrarily shifted along the y-axis for the sake of comparison, averaged over the whole field (*left*) and only over the northwestern corner of the CND (*right*).

emission on SPIFFI field of view sides corresponding to the CND. The relative differences of line fluxes is studied in more details in the next chapter, where H_2 excitation is investigated.

Velocity maps: for all lines the velocity maps show a gradient in the southeastern corner, as observed for S(1). S(3) shows a strong negative velocity few arcseconds South and East of Sgr A*. This feature is due to the spectral pollution by a nearby atmospheric line which is difficult to separate from the contribution of S(3). It has the effect of introducing a false blueshift of the line in this area. Q(1) and Q(3) seems to be less affected by the stellar artifacts in the center of the field than S(1). For these two lines we do not observe the strong positive velocities observed for S(1). This is an indication of the fact that the observed high-speed feature might indeed be a consequence of pollution by stellar lines. These stellar lines are closer to S(1) wavelength and thus naturally affect more this line than the others.

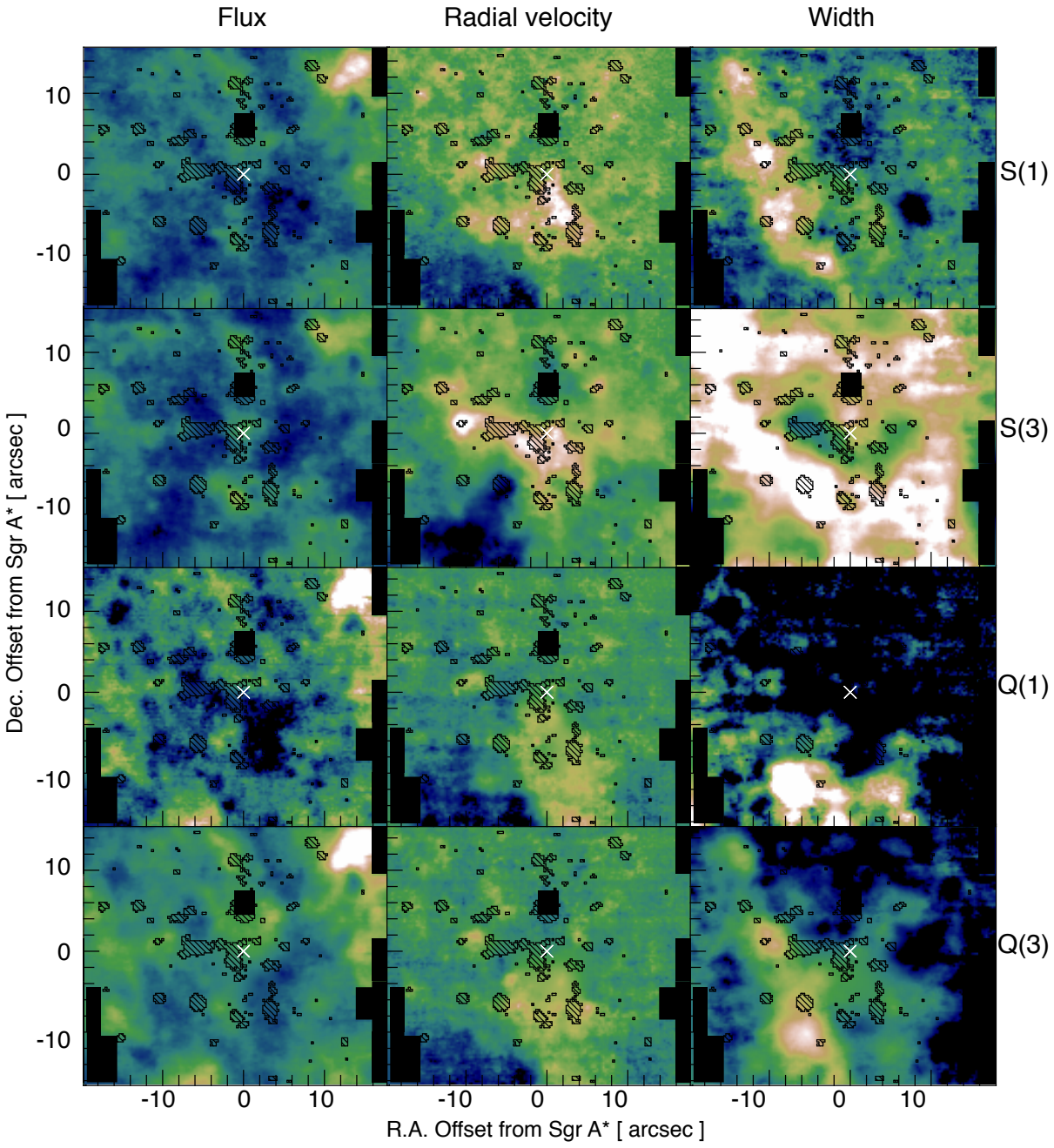

Figure 3.12: Parameter maps for each ortho line. *left to right:* line flux, velocity and width. *Top to bottom:* 1-0 S(1), S(3), Q(1) and Q(3) lines. The color-bars are the same for all lines and as in Fig. 3.1, 3.5, 3.8.

Width maps: S(3) is affected by the above mentioned, close, atmospheric line. This proximity is probably the cause of the observed higher values of the width. Nevertheless, one can still observe the features observed for S(1): the smaller width at the border the field and the strong enhancement East of the Minispiral Northern Arm. The Q(1) line is affected by the nearby CO features as previously discussed. If this feature does not seem to affect particularly the velocity map, it strongly influences the measured width and flux. Therefore it is not surprising to observe much lower values of the width where there are more stars. Nevertheless, in the east, a width increase is still visible. Q(3) is clearly less affected than Q(1) by the CO absorption feature. Even though in the southeastern corner of the map the line appears wider than 1-0 S(1), the width map structure presents the same behavior as 1-0 S(1). This map nicely confirms the previous finding of an emission coming from the Northern Arm Cloud.

In summary, taking into account the local peculiarities and spectral pollution, the parameter maps of four ortho H_2 lines are compatible. This strengthens the validity of our results, assuming the same dynamics applies for all H_2 molecules, whatever is their excitation state, as expected if all the lines are emitted by a common source.

According to this interpretation all lines could be described by 1-0 S(1) velocity and width. This is the line for which these parameters are best estimated. Hence the regularized 3D-fit procedure has been applied a second time, by imposing these conditions on the other lines (1-0 S(3), Q(1) and Q(3)). It has to be kept in mind that the S(1) velocity maps shows some artifacts (Sect. 3.1.2) and thus the corresponding areas has to be considered carefully. The corresponding new flux maps are reported in Fig. 3.13.

The new 3D-model obtained with these constraints is consistent with the raw data. The retrieved flux maps show very little variation with respect to the free-parameters fit as displayed in Fig. 3.13. This confirms the relevance of using a common width and velocity.

This assumption improves the fitting, since two of the parameters rely on the most robust line, lowering the impact of spectral environment pollution.

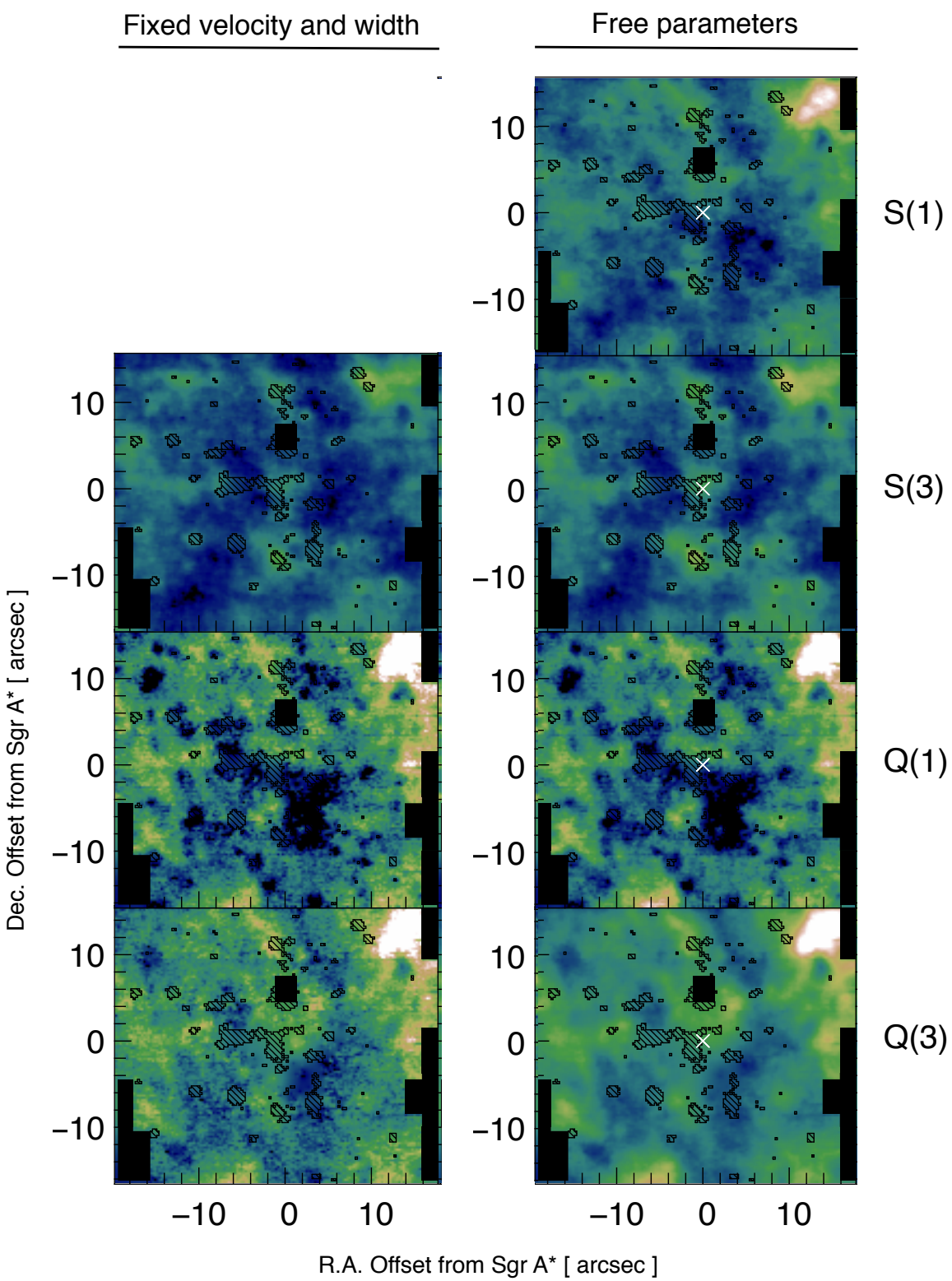

Figure 3.13: Line flux maps for each ortho line. *Left:* flux with speed and width imposed to be those of S(1) line. *Right:* free-parameters fit. *Top to bottom:* 1-0 S(1), S(3), Q(1) and Q(3) lines. The color-bar is as in Fig. 3.1.

3.2.2 Para 1-0 S(0) line

The 1-0 S(0) line is the para line with the best signal-to-noise. However, there is a Fe III line on one side of the spectrum and an absorption feature on the other. Despite these difficulties S(0) is clearly detected almost everywhere in the SPIFFI field of view. However when one tries to fit S(0), the regularized 3D-fit does not converge on a satisfactory solution. A satisfactory fit can be achieved only if the line is simultaneously fitted with 1-0 S(1). When S(0) and S(1) are fitted together, the result is much more stable and robust. Fig. 3.14 displays the parameter maps obtained for this simultaneous fit. The S(1) flux, velocity and width maps are very much alike and compatible with the previous findings. The S(0) para line is therefore well described by the same velocity and width as S(1) and others ortho lines.

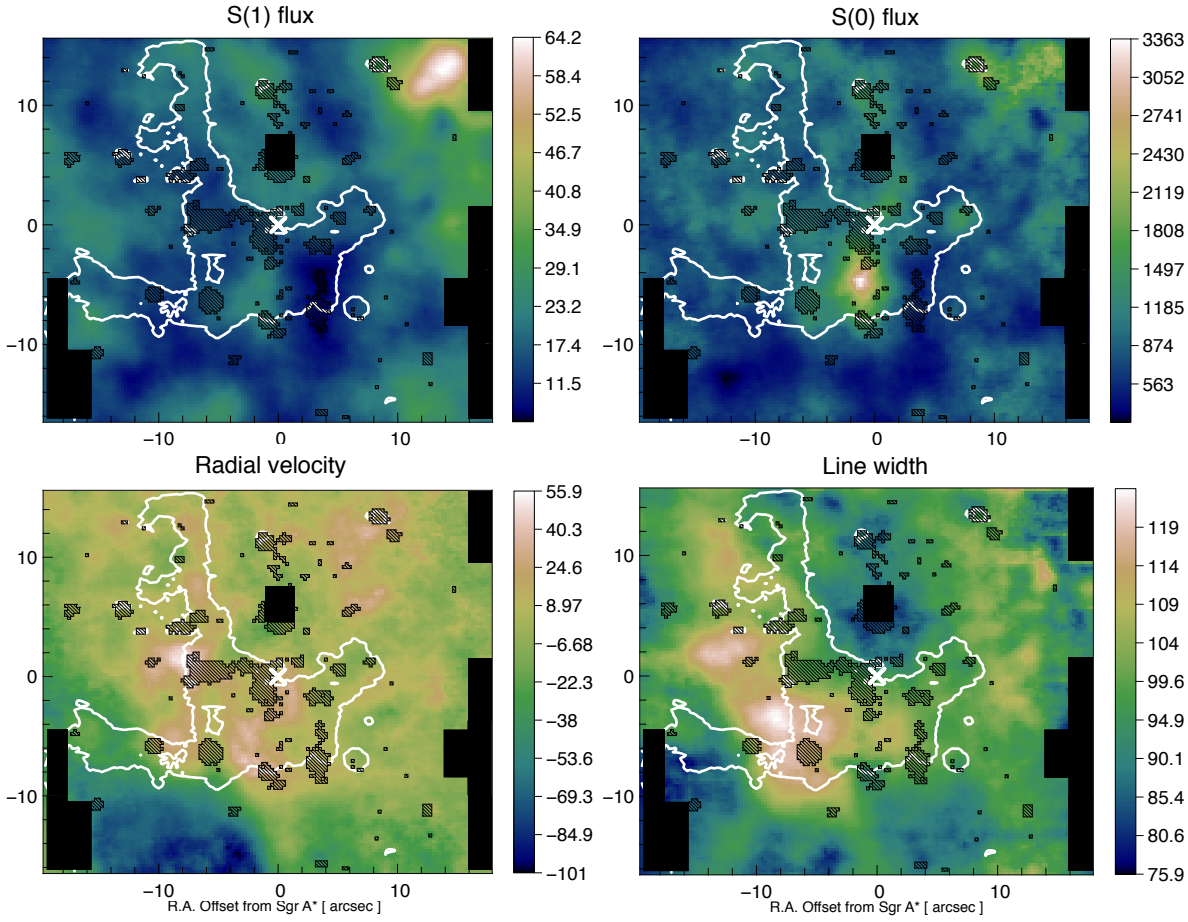

Figure 3.14: Parameters maps of the multi-line regularized 3D-fit. *From top to bottom and from left to right:* S(1) and S(0) fluxes (10^{-19} W m^{-2} arcsec^{-2}), velocity map and width map (km s^{-1}).

The S(0) flux map presents the same patterns as all previously analyzed ortho lines. The main difference with respect to other studied lines is that this transition shows a strong emission maximum few arcseconds South of Srg A*. All other lines show an emission coming from this

region but never such a strong peak as in the S(0) map. In this zone, the signal-to-noise ratio is good and the S(0) line very clearly stands out of the continuum. The nearby Fe III cannot be suspected of influencing on the S(0) line because the two are very well separated.

There is always the possibility that a different non-H_2 line, very close in wavelengths, appears in this regions and makes S(0) line look much stronger than it really is. However, looking at lines atlas no candidate lines is found and the S(0) line does really appear as a clear gaussian profile in the spectrum. Moreover the fact that this line is very well fitted by the same velocity and width as S(1) is one more indication of it as a H_2 line.

The region of strong S(0) emission happens to be located at the border of the Minicavity. The Minicavity is an U-shaped region, identified at different wavelengths. The origin of this cavity is believed to resides in the interaction of strong stellar winds with the surrounding, dense, ISM, or in a jet coming from Sgr A* itself. In any case it is a region of shock and strong radiation.

This area also happens to be at the meeting point of the Eastern and Northern Arms of the Minispiral, in projection. The Eastern Arm is believed to be in free-fall towards Sgr A* in this point (Paumard et al. 2004) and maybe in collision with the Northern Arm. This is therefore a very peculiar region where many different effects may contribute to produce the observed feature. The S(0) enhancement is presumably connected to this particular environment but it is the only of the H_2 transitions under analysis to show it. One can imagine that this enhancement is connected with a ortho-para effect, because of OPR smaller than the theoretical local thermodynamic equilibrium (LTE) value of 3 at this peculiar location (see Chapter 4, Sect. 4.3.2.1). This aspect will be investigated deeply in the next chapter, where the gas excitation is analyzed.

3.3 Extinction corrected map

Extinction correction is crucial not only for obtaining the absolute flux values but also to compare fluxes in different lines. This especially because the extinction curve is fairly steep in the NIR.

In the past decade various authors have addressed the question of the local variations of the extinction in the Galactic Center and traced the extinction map of this region. Two aspects are of fundamental importance and have to be considered: the profile of the extinction law and the local variations of the extinction coefficient (at the Galactic Center).

3.3.1 Extinction law

Dust extinction's law can be estimated comparing fluxes of two identical or equivalent sources (for instance a star or an emitting clump of ISM): one located in a dusty environment (producing at wavelength λ an observed flux $F(\lambda)$) and the other in a dust-free location ($F_0(\lambda)$). Then one can define the extinction coefficient A as follow:

$$A(\lambda) = -2.5 \cdot log \frac{F(\lambda)}{F_0(\lambda)} \tag{3.1}$$

Fritz et al. (2011) presented the extinction law toward the central 14″× 20″ of the GC (Fig. 3.15).

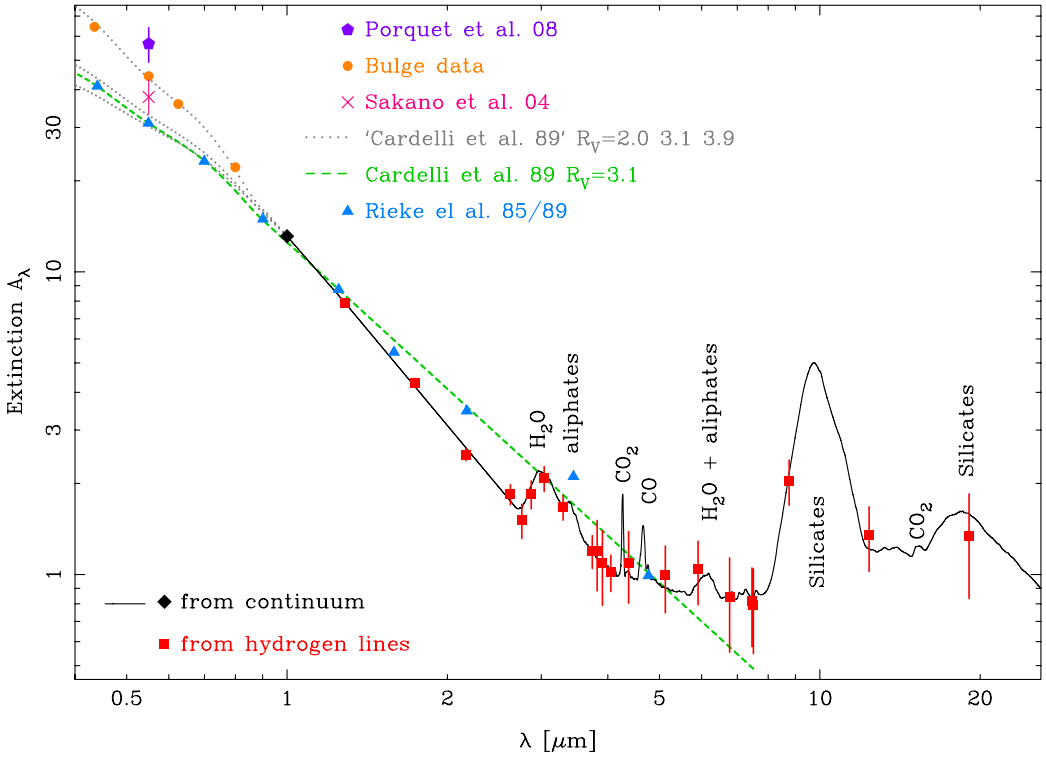

Figure 3.15: Extinction toward the central 14″×20″ of the GC by Fritz et al. (2011). The extinction in the range 1.28–18 μm (*red boxes*) is obtained through hydrogen lines. At 1 μm (*black diamond*) they used stellar colors. Data have been interpolated using the continuum emission (*black line*). Authors used other publications data to extend the extinction curve to the visible (*orange dots*). For comparison authors added values obtained in others publications (*all others lines and colors*, Fritz et al. 2011 and references therein).

For what concerns the present work, the NIR range of the extinction law is relevant. In this spectral range the extinction follows a power-law $\lambda^{-\alpha}$:

$$\frac{A_a}{A_b} = \left(\frac{\lambda_a}{\lambda_b}\right)^{-\alpha} \tag{3.2}$$

Where α takes different values in the range 1.6–2.1 as noted from different publications in the last years (Fritz et al. 2011 and references therein). Since 2005 all publications seem to agree on a steeper extinction law in the NIR than earlier articles. Fritz et al. (2011) indicate as the reason for this reevaluation the fact that, before 2005, publications used stars which are detectable in the optical and that are, mostly, closer than 3 kpc. Since 2005 large infrared surveys became available and most publications started calculating the extinction towards the Galactic disk and bulge at ∼8 kpc. Therefore the medium probed by the two series of studies (before 2005 α ∼1.75 and after α ∼2.1) is not identical. Fritz et al. (2011) suggest

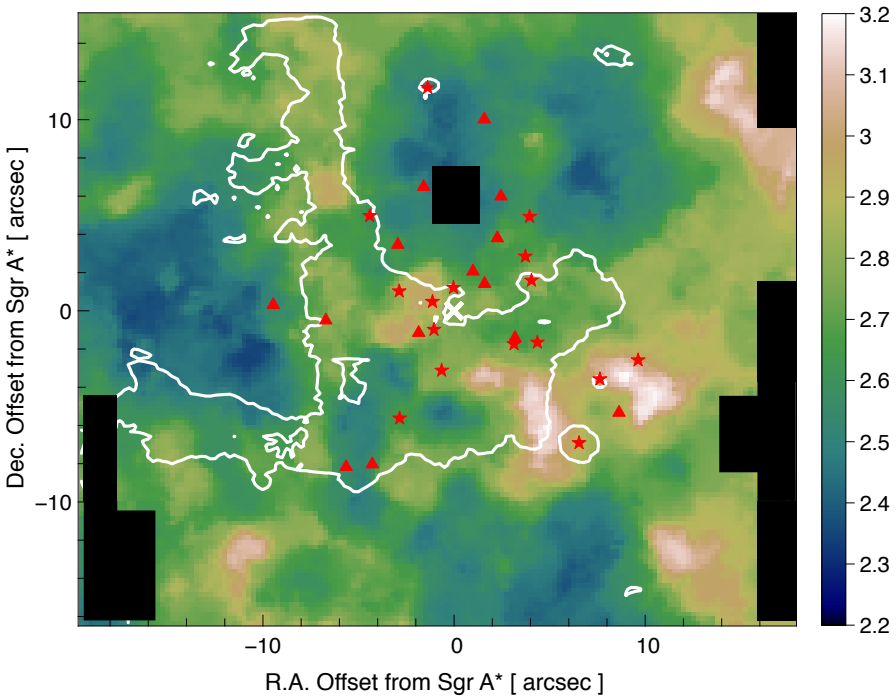

Figure 3.16: Schödel et al. (2010) map of A_{Ks} for the Galactic Center derived from H–Ks colors of all stars detected in these bands. The map is adapted to SPIFFI field of view for comparison, while the published maps is slightly bigger. The Minispiral contour and the position of WR stars (c.f. Fig. 3.1) have been superimposed on the map.

that the extinction law varies between these regions with a flatter NIR extinction in the solar neighborhood than in the inner Galaxy.

A value of $\alpha = 2.07$ is used for the present work. This is the value that Fritz et al. (2011) indicate as the average among the main publications since 2005.

3.3.2 Local extinction variations

The local variations of the extinction, introduced by the specific environment observed, are fundamental to distinguish between variations of the intrinsic source brightness and variations caused by local variations of the extinction.

Indeed, even though the bulk of extinction is foreground and amounts to A_K ~2.5 mag, most of the variation in extinction is local: up to 1 magnitude at K. For instance Paumard et al. (2004) showed that the dust contained in the Eastern Bridge of the Minispiral is responsible for 0.76 K mag extinction of the Northern Arm. Schödel et al. (2010) obtained a A_{Ks} map showing local variations of more than 1 mag as well (Fig. 3.16). Other authors have provided maps of the extinction variation towards the central parsecs (c.f. Scoville et al. 2003) showing similar results.

One must point out that extinction correction is dependent on the 3D-position of an object. Extinction maps are of a limited use by the fact that the various emitters – stars, ionized gas,

molecular gas – are not at the same 3D-position and not at the same optical depth. This is also true for any source used as a probe to evaluate the local extinction. For this reason it is fundamental to evaluate the extinction variations directly from the emitter that is being studied. In the next section, we derive an extinction map linked to H_2 in the central parsec.

3.3.3 Extinction map

For an optically thin line l one can write the observed intensity I_l (Beckwith et al. 1983) as:

$$I_l = \frac{h}{4\pi}\frac{\mathcal{A}_l}{\lambda_l} \cdot N_l \cdot 10^{-A_{\lambda_l}/2.5} \tag{3.3}$$

where $\mathcal{A}_l$ is the spontaneous decay rate in s^{-1}, h is the Planck constant, N_l the column density of population of molecules in the upper level of the the transition and A_{λ_l} the extinction at wavelength λ_l corresponding to the considered line.

This equation becomes very useful in the case of two lines arising from the same upper state. In the SPIFFI spectral range one can consider the 1-0 Q(3) and 1-0 S(1) lines for this purpose, both arising from the state $\nu_u = 1$, $J_u = 3$ (c.f. Chapter 2, Table 2.1).

Since all H_2 lines are optically thin (as shown in the Orion nebula for instance, by Gautier et al. 1976) one can write:

$$\frac{I_{Q3}}{I_{S1}} = \frac{\mathcal{A}_{Q3} \cdot \lambda_{S1}}{\mathcal{A}_{S1} \cdot \lambda_{Q3}} \cdot 10^{E/2.5} \tag{3.4}$$

where I_{Q3} and I_{S1} are the intensities of the considered lines and $E = A_{\lambda_{S1}} - A_{\lambda_{Q3}}$.

Solving Equation 3.4 for E one obtains:

$$E = 2.5 \cdot log_{10}\left(1.425 \cdot \frac{I_{Q3}}{I_{S1}}\right) \tag{3.5}$$

Where the 1.425 factor comes from the ratio of the Einstein coefficient and wavelengths of the two transitions.

This expression, using the extinction law of Equation 3.2, permits to obtain the total extinction A_λ at every wavelength.

Q(3)-S(1) ratio Considering the ratio of the observed intensities is equivalent to considering the ratio of the observed fluxes, since both lines have the same width. When considering a line ratio one has to take care of the relative error bars and the regularized 3D-fitting procedure artifacts. The best way to cope with these problems is to apply the regularized 3D-fitting directly on the ratio I_{Q3}/I_{S1} (i.e. F_{Q3}/F_{S1}), instead of fitting the two lines separately and consider the ratio afterwards. Fitting the flux ratio directly allows the result to be less affected by small-scale artifacts and local variations of any of the parameter. This approach suits well the other assumption one must make in order to consider this ratio for the extinction correction: that the two lines arise from the same gas. Therefore these lines must have the same velocity and width. For this purpose one could have considered the Q(3) flux map obtained when fixing the velocity and width with S(1) and divide it by the S(1) map itself (c.f. Sect. 3.2.1). However, as previously mentioned, this would enhance small artifacts present in

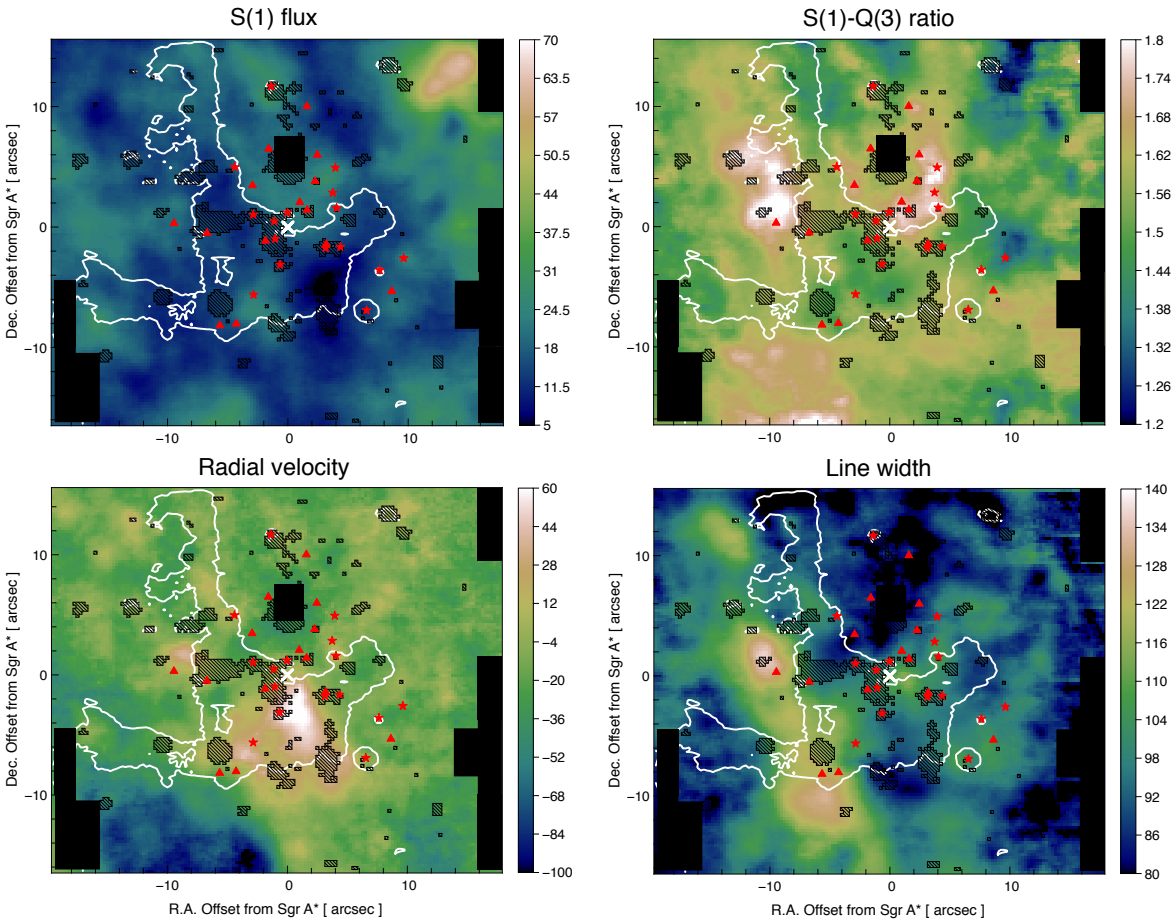

Figure 3.17: Parameters maps of the multi-line regularized 3D-fit. *From top to bottom:* S(1) flux (10^{-19} W m^{-2} arcsec^{-2}), Q(3)-S(1) flux ratio, velocity map and width map (km s^{-1}).

either the velocity or the width maps of S(1). A much safer and conservative way of obtaining that ratio is to fit it directly. To that end, both lines have been fitted simultaneously assuming they have the same velocity and width. The model fits both lines, through four parameters: S(1) flux, Q(3) flux normalized by S(1) flux – i.e. the derived ratio – velocity and width. The retrieved parameters maps are reported in Fig. 3.17. Uncertainty on every of the four parameters has been obtained in the same way as before (i.e. building 4 separate cubes and running on each the regularized 3D-fitting). The uncertainty is thus directly on the lines ratio and no error propagation is needed.

Once the line ratio is measured, E is calculated through Equation 3.5. Then E leads to A_{S1} and A_{Q3} values through the extinction law of Equation 3.2, at every pixel. Consequently, we obtain the first map of H_2 dereddened flux of the central parsec ever published (Fig. 3.18).

With Equation 3.2 one can actually obtain the absorption coefficient at every NIR wavelength. Therefore we calculated the extinction in the K short band, A_{Ks}, where $\lambda_{Ks} = 2.168$ μm as in Schödel et al. (2010). The uncertainty on A_{Ks} is calculated as the propa-

gation of the uncertainty on the line ratio.

The S(1) flux map has been calibrated as in Sect. 3.1 and therefore it suffers an additional 30% error on the the absolute values. The latter does not affect the ratio of two lines which, however, still suffers of the uncertainty of the relative calibration, which is around 8% and applies to the final A_{Ks} map values.

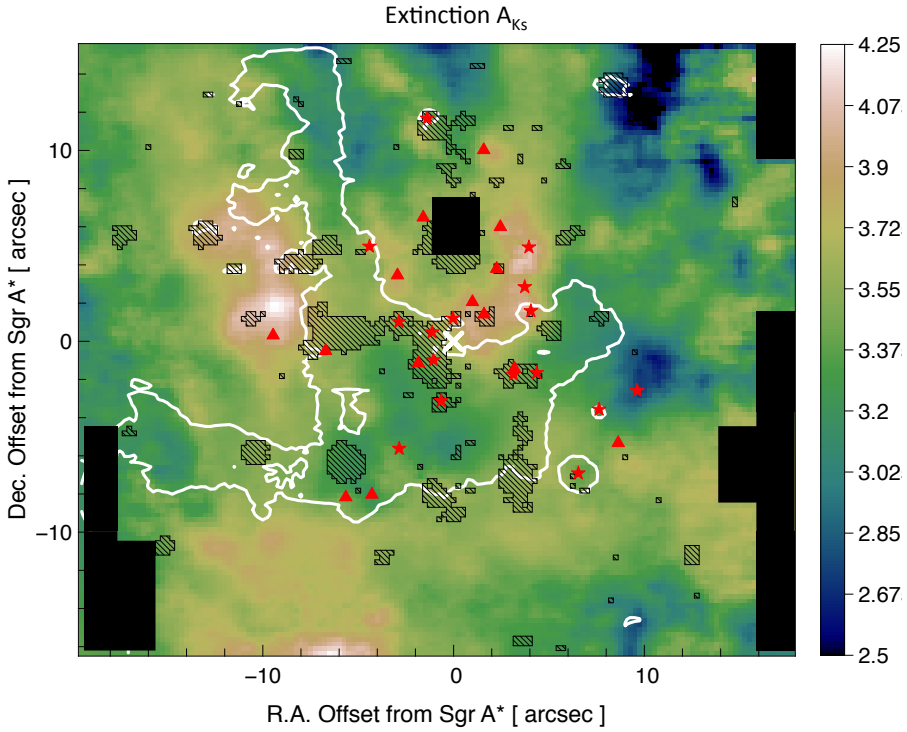

Figure 3.18: Extinction A_{Ks} map at $\lambda_{Ks} \sim 2.168$ μm, in mag, obtained from Q(3)-S(1) ratio. Symbols as in Fig. 3.1.

In order to check the obtained extinction map – as for the 1-0 S(1) maps – a multi-line 1D-fit is applied on some portions of the field (the same zones as in Chapter 2, Fig. 4.1) to obtain the Q(3)-S(1) ratio and calculate A_{Ks}. The values obtained with the two methods are compatible within the error bars which amount to ∼10–20% on average.

3.3.3.1 Comparison to previous works

The extinction map obtained here shows A_{Ks} variations in the range 2.8–4, with a mean value of A_{Ks} ∼3.4. This is almost 0.7 mag greater than what was determined by Schödel et al. (2010) (A_{Ks} ∼2.7 mag) through star color excess in the same region. The two maps show also a different gradient of extinction in the central parsec as can be seen in Fig. 3.19. For instance, Schödel et al. (2010) extinction is high in the region of the CND and the Northern Arm of the Minispiral, while the extinction is lower in the regions corresponding to the rest of the Central Cavity. The A_{Ks} map derived here shows some of the same large-scale structures in the chunk of the CND located in the South of the SPIFFI field of view, while, at the Northern Arm and

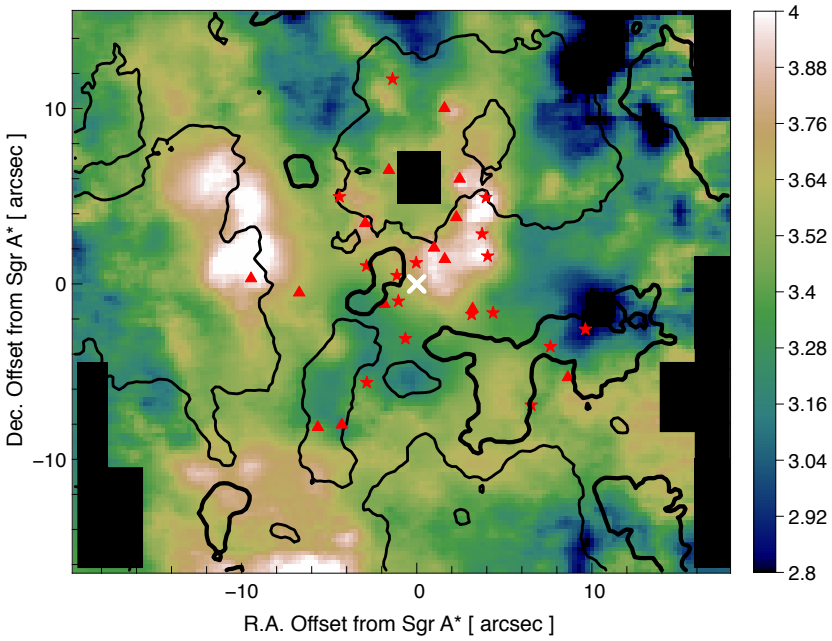

Figure 3.19: The Schödel et al. (2010) extinction is represented in contours (at 2.6, traced by the thin line, and at 2.9 mag, traced by the thick line), superimposed on the A_{Ks} map obtained through Q(3)-S(1) flux ratio. Symbols as in Fig. 3.1.

Western Arc, the extinction drops. The extinction remains high in the Northern Arm Cloud where the Schödel et al. (2010) extinction drops. There are two strong enhancements of the extinction, with respect to the Schödel et al. (2010) map: one at the border of the Northern Arm and the other South of GCIRS 7.

Fritz et al. (2011) computed the NIR part of their extinction curve towards the Galactic Center using the same SPIFFI data cube analyzed here. However they used recombination hydrogen lines to calculate the extinction. They found results in agreement with Schödel et al. (2010).

Scoville et al. (2003) observed the Paα and 6 cm radio continuum emission of the central few parsecs. The radio continuum traces the same ionized gas as Paα but it suffers no extinction. Therefore the authors used the Paα to 6 cm radio continuum ratio, together with an extinction law $\lambda^{-1.6}$ and the two ratios $A_{1.6\mu m}/A_V = 0.0176$, $A_{2.2\mu m}/A_V = 0.105$ (Rieke 1999), to derive the extinction at V, $A_V = 7.24 \cdot A_{Pa\ \alpha}$ (Fig. 3.20). Scoville et al. (2003) map is relative to A_V while here the map is relative to A_{Ks} but it is interesting to compare their shapes. In the north, low extinction values seem to trace the thicker Norther Arm Cloud and the Eastern Arm of the Minispiral. Everywhere else the extinction is higher, tracing the CND features, and it remains very high South of CGIRS 7 as well. On Scoville et al. (2003) map, lower values varies between 20–25 mag, while higher values are in the range 35–45 mag. Translating these values in A_{Ks} magnitudes it gives 2.2–2.7 mag for the low extinction and 3.8–4.9 mag for the high extinction. Scoville et al. (2003) obtained these values under the assumption of a power-law which is flatter than the one assumed here. However, changing the exponent of the

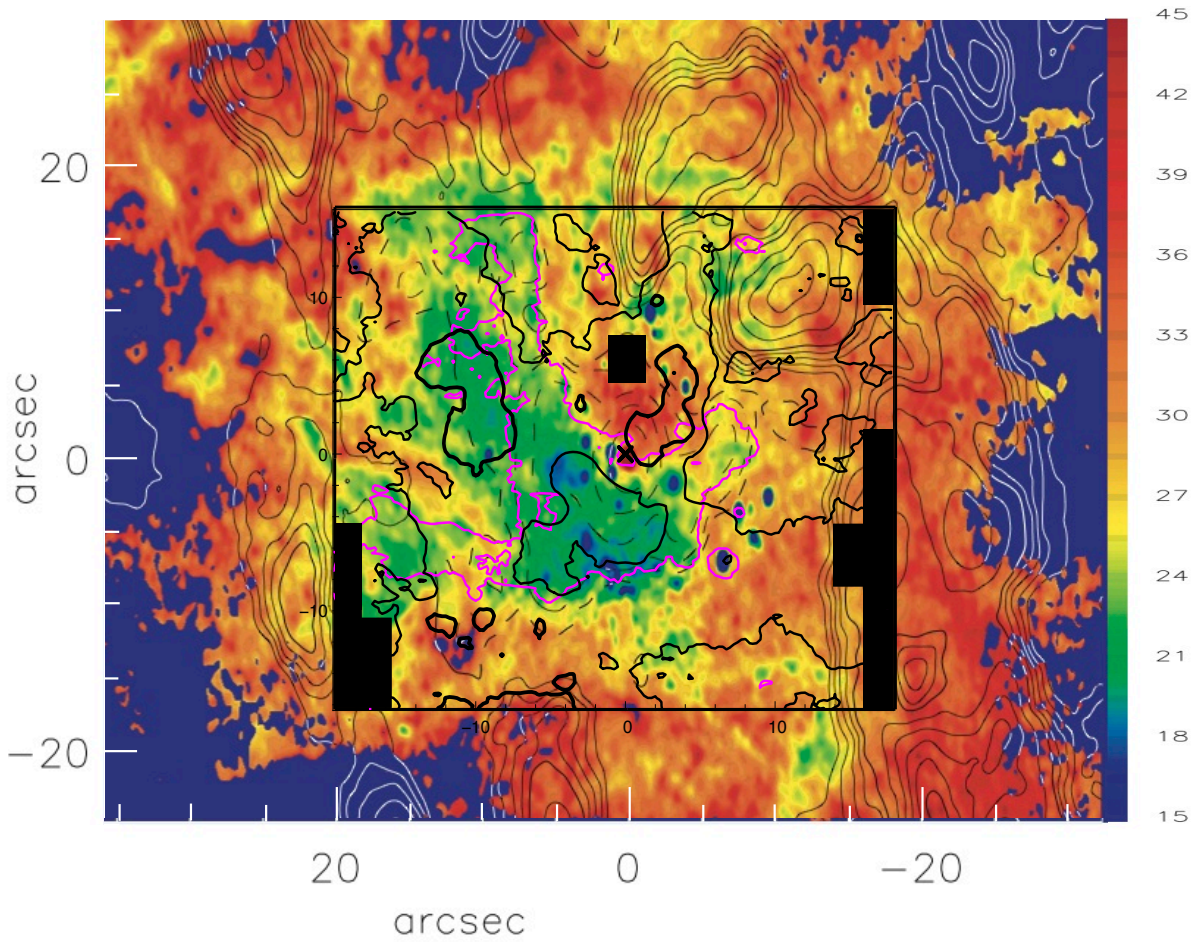

Figure 3.20: Scoville et al. (2003) A_V map (the color scale units are in A_V magnitudes). Thin contours (*gray* and *white*) trace the HCN CND emission (Sect. 3.1). The A_{Ks} map derived here is traced in black, thick, contours (at 3.4 traced by the thin line, and at 3.8 mag, traced by the thick line), together with the Brγ emission of the Minispiral (magenta).

power law leads to variations of 8% only which are of the same order as the uncertainties on the extinction. The values found here are compatible with what is obtained by Scoville et al. (2003) in the very northern end of the Northern Arm, where both maps show a low extinction, South of GSIRS 7 and in the southeastern corner of the SPIFFI field where maps exhibit very high extinction. One major difference is at the Northern Arm Cloud, where Scoville et al. (2003) found a generally low extinction, while the map derived here exhibits a sharp maximum.

The overall appearance of the three extinction maps (Scoville et al. 2003; Schödel et al. 2010 and the one obtained here) is different, however there are several common points. All maps show a drop in the extinction in the northwest, near the CND flux maximum, and an enhancement in the southeastern corner and southwestern part of the SPIFFI field of view. Scoville et al. (2003) and Q(3)-S(1) extinction map also have in common the drop in the extinction in the northern end of the Northern Arm, the Western Arc and in the central 10″ southeast of Sgr A*. Both maps also show extinction enhancement in the region South

and around GCIRS 7. In the Northern Arm Cloud both Scoville et al. (2003) and Schödel et al. (2010) results show a large drop in the extinction. This is the main difference with Q(3)-S(1) which, on the contrary, shows a strong maximum of extinction in this region.

We point out that Q(3)-S(1) derived map shows even more variations than Scoville et al. (2003). The ionized gas is sensible only to the foreground extinction while H_2 could be associated with the material of the cloud itself. Indeed the molecular gas can be located more deeply inside a clump. For instance, the H_2 – as inferred from the width map – is probably located inside the Northern Arm Cloud, behind the ionized layer. Therefore the anti-correlation between the two extinction maps in this region seems to confirm the interpretation that the H_2 emission is coming from inside that cloud, whereas the extinction inferred by Scoville et al. (2003) concerns the surface of the same cloud. The differences among maps are thus not surprising and reflect the position and environment at which each tracers is located.

Schödel et al. (2010) map, based on reddening of stars, represents an average extinction on larger areas and thus it shows less small-scale variations and it is less homogeneous than the others.

3.3.4 Dereddened 1-0 S(1) flux map

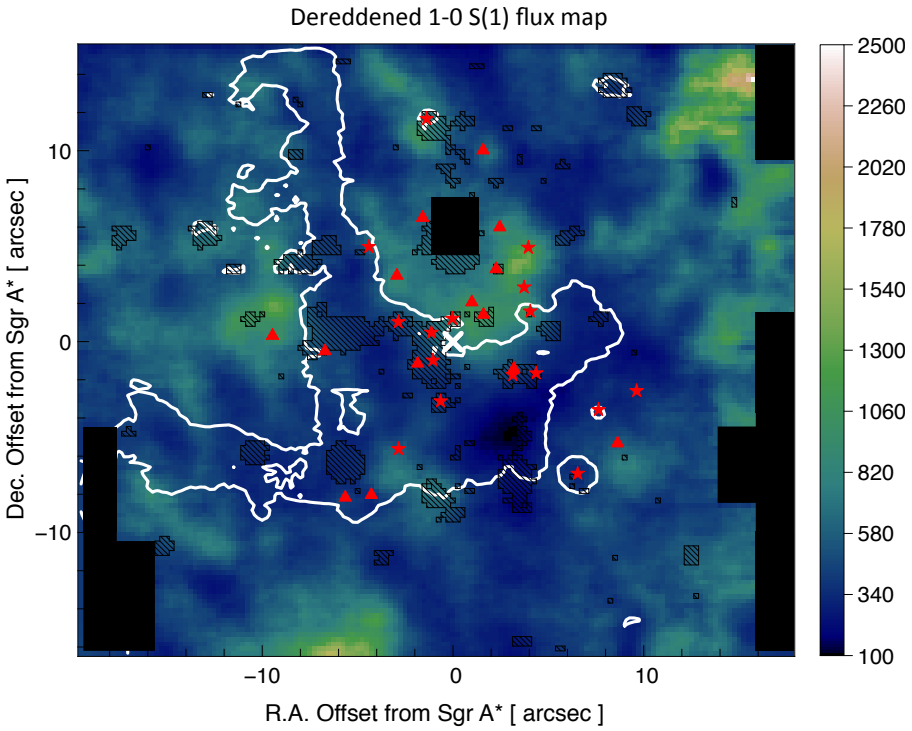

Figure 3.21: S(1) flux map, dereddened through Fig. 3.18 extinction map. The flux is in 10^{-19} W m^{-2} arcsec^{-2}. Symbols as in Fig. 3.1.

The dereddened 1-0 S(1) flux map (c.f. Fig. 3.21) shows essentially the same features as the uncorrected map.The northwestern corner shows the flux maximum related to the CND

emission already observed in the uncorrected map, as well as the emission arising from the Western Arc. The Plume feature is still visible as well, as is the northern part of the Southern Extension in the southeastern corner.

Between GCIRS 7 and the Bar of the Minispiral there is an half-moon shaped emission enhancement. This feature is also present in the uncorrected map where, however, it is less striking. At the same projected location there are several carbon-rich Wolf-Rayet stars (WC; marked by the triangles in Fig. 3.21). The environment of such stars is often dusty. Indeed, some dust has been detected by Tanner et al. (2002) and Haubois et al. (2012) at these locations, so it is natural to form H_2 on these dust grains. This H_2 emission has, however, no correspondence with the ionized gas that have been observed in the area. One possible explanation is that these stars may be located in the background and the excitation of H_2 is provided by the stars themselves. In this picture, H_2 is formed inside the carbonaceous shell of a star and heated from the interior. Indeed the observed emission presents a very well-defined rim at the border of the Minispiral. This correlation might be the sign of an emission coming from the background.

3.3.5 Dereddened 1-0 S(0) flux map

The 1-0 S(0) flux map dereddened through the A_{Ks} extinction map is displayed in Fig. 3.22.

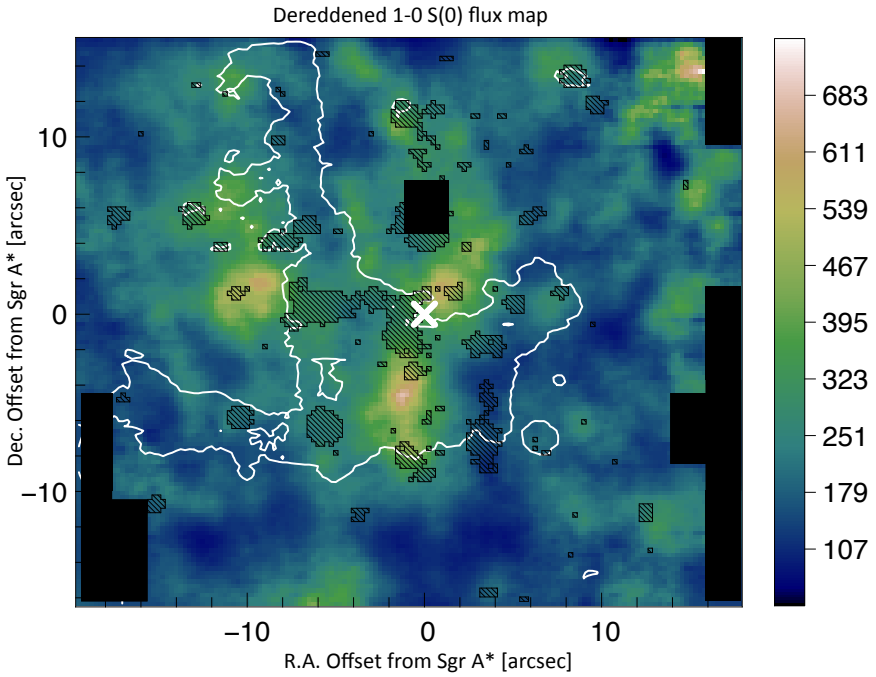

Figure 3.22: S(0) flux map, dereddened through Fig. 3.18 extinction map. The flux is in 10^{-19} W m^{-2} arcsec^{-2}. Symbols as in Fig. 3.1.

Even in the dereddened map (as in Sect. 3.2.2), the very strong maximum of emission few arcseconds South of Sgr A* remains visible. Therefore, this feature cannot be explained by a local variation of A_{Ks}. The considerations of Sect. 3.2.2 apply.

This strong flux peak is coincident with a strong peak in the Fe II line (c.f. Section 2.1.3). Due to time constraints this strong correlation has not been studied yet but a first level analysis is proposed in Appendix B and will be the object of a future work.

3.4 Flux–extinction correlation

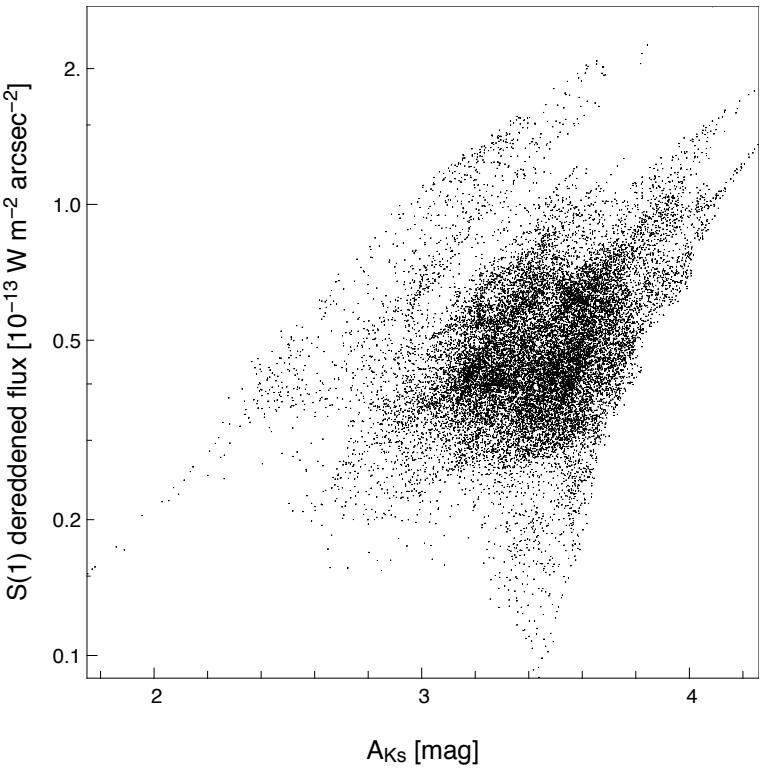

Figure 3.23: The dereddened flux of the S(1) line (dereddened through A_{Ks} obtained via the Q(3)/S(1) ratio) is plotted against A_{Ks}. There is not a plain correlation but the points seem to gather around four lines indicating four different correlations.

The dereddened flux maps and the A_{Ks} map appear correlated which could at first sight look suspicious, although we have taken great care in assuring this result. In order to study this correlation the dereddened 1-0 S(1) flux is plotted against A_{Ks} in Fig. 3.23. A correlation between flux and A_{Ks} would appear as a straight line on this plot. The plot does not show a single line, but rather several, elongated groups of data points. One can distinguish at least four sets of groups of points in the correlation plot, as if there was no global correlation, but instead several, local, correlations.

To investigate these correlations, smooth curves have been traced to characterize each set. This is done selecting manually five point on each group and drawing a smooth curve passing by them. Data points in the plot have then been selected with a distance criterium: those points closer than a chosen distance to the curve are assigned to that curve and colored with a same color. This procedure is repeated for the four observed curves and plotted in Fig. 3.24

(top).

This approach does not necessarily covers all points (some of them remain black on the plot) and depends on two arbitrary parameters:

- the correlation curve, which is drawn manually on the distribution of points on the plot;
- the maximum distance to that curve, which is chosen in order to cover a maximum of points that seem related to the curve avoiding any overlap between distinct curves.

Each colored point of the plot corresponds to a SPIFFI pixel which can be painted with the same color. The result is a map which shows where the different sets of correlation are distributed (Fig. 3.24, bottom). Interestingly, each set corresponds to a continuous area on the SPIFFI field and thus seems to strengthen the idea that the observed correlation is real.

There are two questions that arise from these observations : why is the extinction correlated with flux and why is this correlation split in several, distinct, areas.

3.4.1 Individual extinction-flux correlation

Considering just one of the colored curves obtained in the correlation plot, the problem is to understand how flux and extinction could be correlated. This positive correlation is a bit surprising at first sight since it would mean that the larger the extinction, the higher the flux. In fact it means that the emitting material (i.e. the molecular gas) is located at the same spatial location as the absorbing material (i.e. dust).

In a very clumpy environment, the molecular gas emission from one clump can be absorbed by dust in other clumps. The emission that arises from these molecules is then absorbed by dust grains on its way out of the emitting area. The emitting and the absorbing material can thus be mixed together.

When the total thickness of a clumpy material increases – i.e. when the number of clumps on the line of sight increases – the total amount of photons produced increases, but at the same time the average extinction that affects these photons increases as well. This can lead to the observed correlation.

3.4.2 Sets of correlation

The above argument apply for each correlated set of points. Separated sets correspond to distinct areas on the SPIFFI field of view. The reason for this separation might reside in the different large scale, foreground, extinction along the line of sight for each of these areas. This extinction acts as a “screen” which attenuates the photons coming from the emitting material. Each of the painted area corresponds to a medium which is submitted to a specific extinction.

3.4.3 Radiative transfer model

To investigate this correlation we propose a phenomenological model to account for both these effects. The model we built is then compared to the observed data points. In a very simplified model, one can imagine the emitting clouds as composed of homogenous medium, with a constant excitation temperature but with a variable optical depth $\tau(x) = a \cdot x$, where a is the

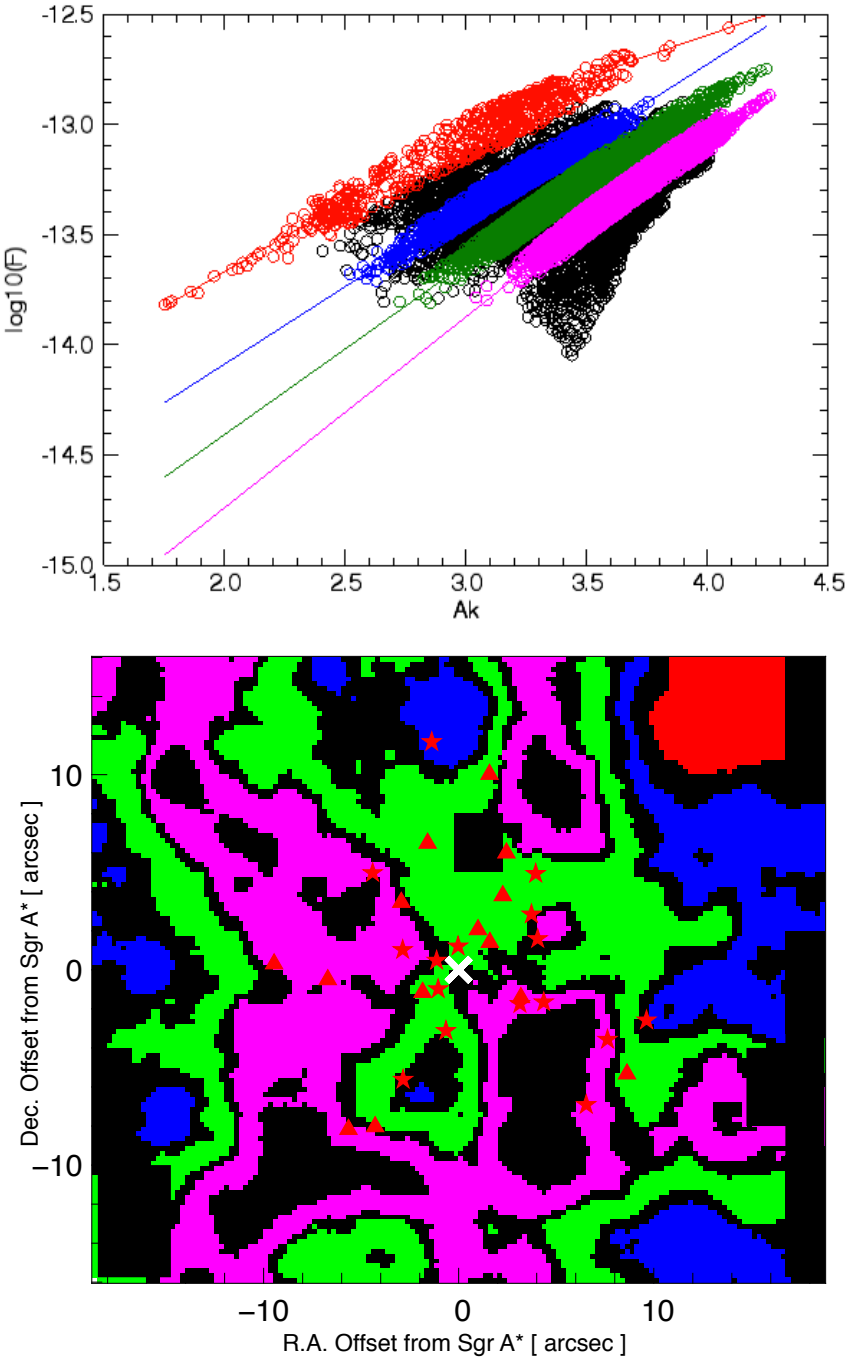

Figure 3.24: *Top:* plot of the dereddened flux of S(1) versus the extinction for every pixel of the map. Four separate sets of correlation are identified by different colors. *Bottom:* each pixel is painted according to the set it belongs to, to show that the correlations translate into continuous areas. Over each region identified by a given color, extinction and emitted flux are correlated.

absorption coefficient per unit length and x is the geometrical thickness. This extinction is entirely due to dust since no self-shielding is provided by H_2 itself (c.f. Appendix A).

In front of this cloud, a dust screen absorbs part of the cloud emission, adding an optical depth τ_0 (Fig. 3.25). Both optical depths depend on the wavelength λ.

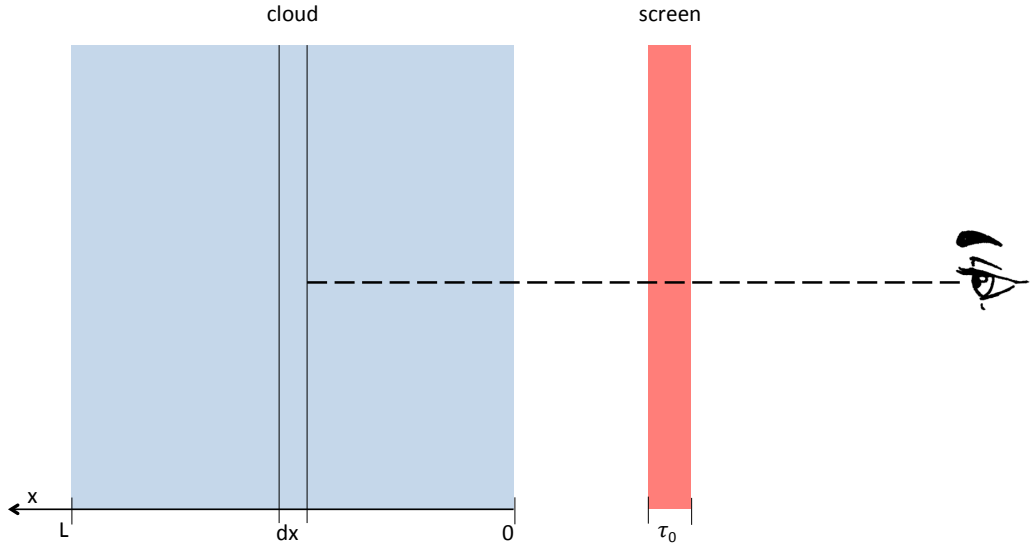

Figure 3.25: Simplified model representing the emission and extinction. The emission comes from an homogeneous cloud where the emitting material is mixed with the absorbing one. The emission is partially absorbed while traversing the cloud. An additional extinction is caused by a dust screen positioned between the emitting cloud and the observer.

In this case the flux received by the observer is determined by the radiative transfer and would be:

$$F_\lambda \propto \int_0^L I_\lambda^0 \cdot e^{-(\tau_\lambda(x)+\tau_0)}\, dx = I_\lambda^0 \frac{1-e^{-a_\lambda L}}{a_\lambda} \cdot e^{\,-a_\lambda L_0} \tag{3.6}$$

Where L is the thickness of the emitting shell and I_λ^0 is the source intensity.

Assuming the previously discussed power-law for the extinction law one can define $a = a_{Q3}/a_{S1} = A_{Q3}/A_{S1} = (\lambda_{Q3}/\lambda_{Q3})^{-\alpha}$ with $\alpha = 2.07$ (Sect. 3.3.1).

In order to obtain the extinction coefficient, the relevant quantity is F_{Q3}/F_{S1}, therefore we considered all values as relative to the S(1) line ($a_{S1} = 1 \rightarrow a_{Q3} = a$, $\tau_{S1} = \tau \rightarrow \tau_{Q3} = a \cdot \tau$). Thus:

$$F_{Q3} \propto I_{Q3}^0 \frac{1-e^{-a\tau}}{a} \cdot e^{-a\tau_0} \tag{3.7}$$

$$F_{S1} \propto I_{S1}^0 (1-e^{-\tau}) \cdot e^{-\tau_0} \tag{3.8}$$

Since Q(3) and S(1) arises from the same upper level (Sect. 3.3.1): $\frac{I_{Q3}^0}{I_{S1}^0} = \frac{\mathcal{A}_{Q3} \cdot \lambda_{S1}}{\mathcal{A}_{S1} \cdot \lambda_{Q3}}$. Calculated this way F_{Q3}/F_{S1}, Equation 3.5 and 3.2 gives the corresponding A_{Ks}:

$$A_{Ks} = \frac{\lambda_{Ks}^{-\alpha}}{\lambda_{S1}^{-\alpha} - \lambda_{Q3}^{-\alpha}} \cdot 2.5\ log_{10}\left(\frac{1 - e^{-a\tau}}{1 - e^{-\tau}} \frac{e^{1-a\tau_0}}{a}\right) \tag{3.9}$$

Once we adjusted this factor, this simplified model actually reproduces the observed correlation curves rather well, as is shown in Fig. 3.26. Is interesting to note that the slope is well reproduced.

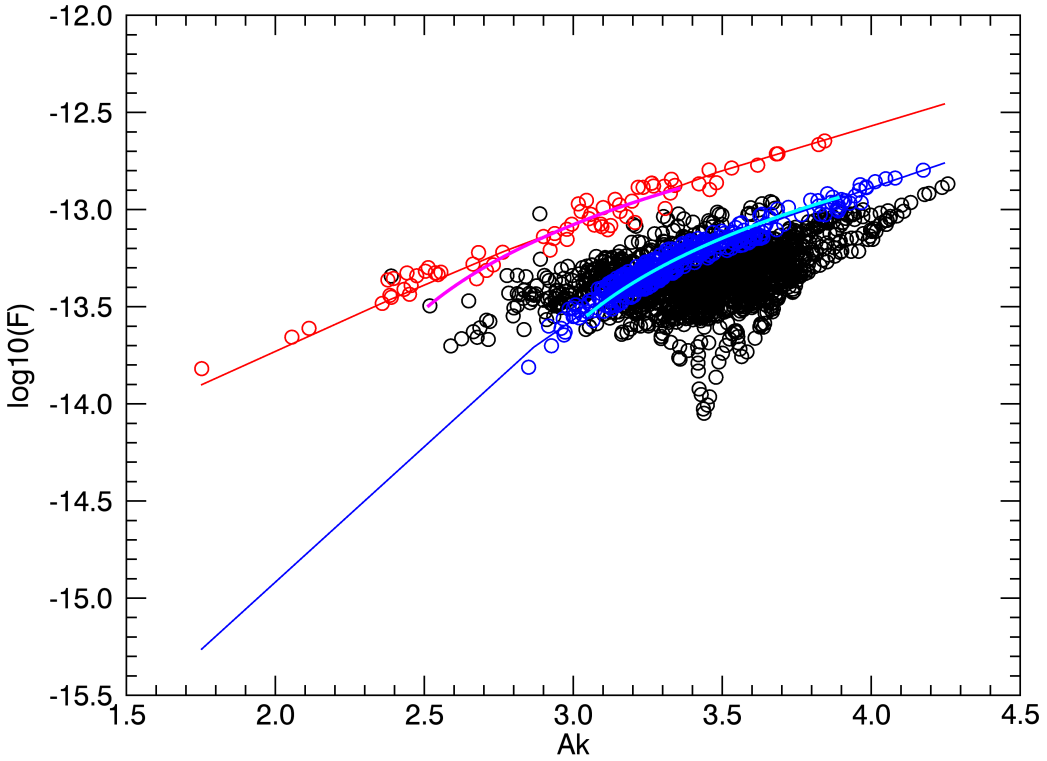

Figure 3.26: Plot of the dereddened S(1) flux versus the extinction for every pixel of the map. The point align on four curves, identified by different colors (two are show in the image). This behavior can be nicely reproduced by a simplified model (traced in *magenta* and in *cyan*).

Since the model seems to describe the observations quite well one can invert the problem and compute, for each point (i.e. for each dereddened flux and A_{Ks}), the corresponding τ and τ_0. This is done inverting Equation 3.9. The result is a value of τ and τ_0 for each point of the plot (i.e. each pixel on the 2D-plane) once given a flux factor. To compare this model to observations one has to consider a flux factor which scales the flux obtained through the model in order to take into account the actual flux measured. This arbitrary factor cannot vary over a wide range and its value ($0.75\ 10^{-13}$) has been chosen because it is the one that allows most points to converge.

The results on τ and τ_0 for each pixel are shown in Fig. 3.27 (top left and top right respectively).

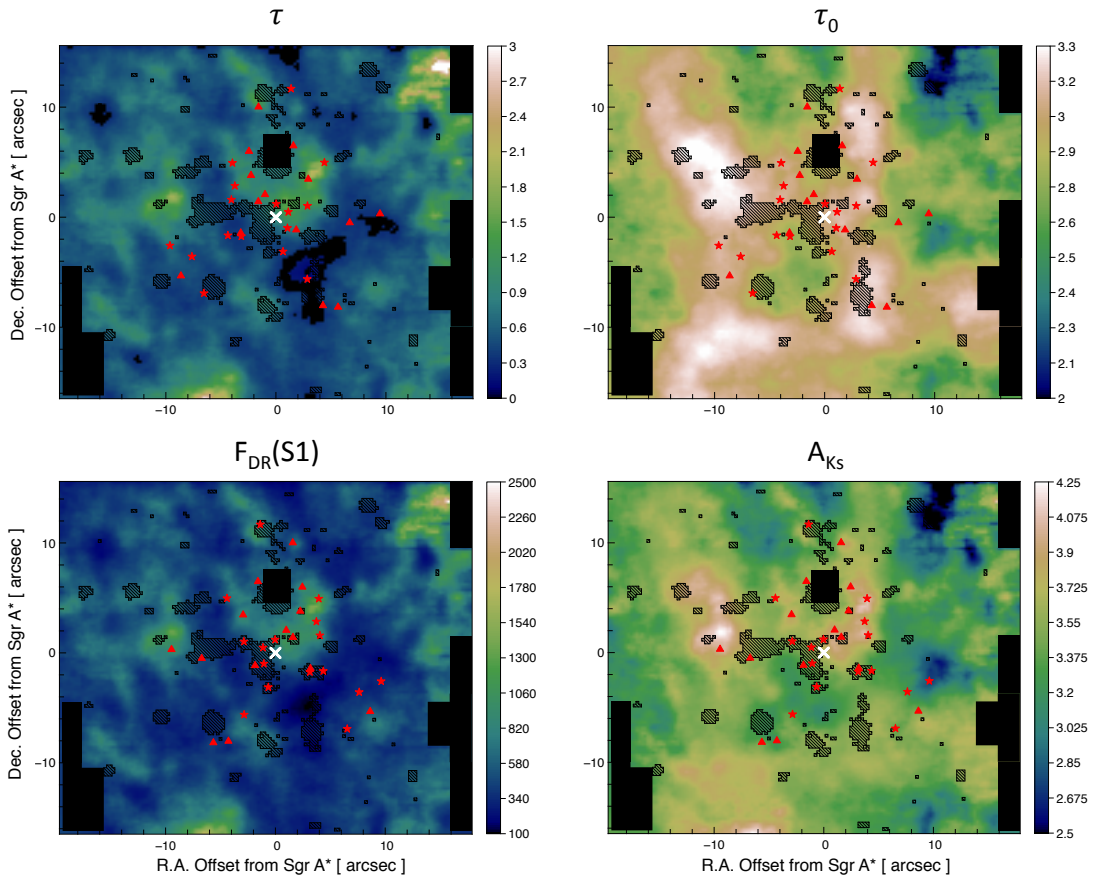

Figure 3.27: *Top:* 2D representation of the τ (cloud extinction; $left$) and τ_0 (screen extinction; $right$) obtained through the simplified model. These maps highly resembles in shape to the dereddened flux (*bottom left*) map and A_{Ks} map (*bottom right*) respectively.

The τ map very closely resembles the dereddened flux distribution. τ_0 resembles the A_{Ks} map, but it is smoother. This outcome is quite coherent since τ represents the extinction within the emitting shell and thus it is naturally correlated with the flux in this context. The fact that the model reproduces well the observed correlation between the dereddened flux and the extinction strengthens this interpretation.

3.4.4 Screen extinction τ_0

The offset of the distinct curves seems indeed to corresponds to different foreground screen optical thickness (i.e. different τ_0). In Fig. 3.24 (bottom) this translate in the various colored areas while in Fig. 3.24 (top) it represent the shift of the different curves.

The differences in the screens depth can be interpreted as the geometrical location (on the

z-axis) of the emitting medium in a uniform screen. For instance, in Fig. 3.24 (bottom) the northwestern corner corresponds to the CND (see previous sections) which is the closest object to the observer in the SPIFFI field of view. This corner corresponds to the lowest extinction among the correlation curves (Fig. 3.24 top, the red curve). The Central Cavity and the Minispiral areas correspond to the highest extinction curves in the plot (magenta and green). This result is coherent with the interpretation of the offset among curves as a difference in the location of the emitting source within a more or less uniform cold absorbing medium encompassing the whole region. Sources closer to the observer (the CND northwestern corner) present lower extinction (i.e. a lower τ_0) than sources located further away (the Minispiral), because in this case the absorbing screen is thicker geometrically and, more importantly, optically.

Therefore the interpretation of the variation of the optical depth of this screen (τ_0) as variation of the distance of the emitting source to the observer is coherent with the known 3D-distribution of the CND and Minispiral features. However, one has to keep in mind the phenomenological model used here is very simplified, even though the global consistency of the results and interpretations is reasonable.

3.4.5 Cloud extinction τ

The flux increases for increasing extinction because, as the depth increases, the corresponding shell emits more. The increase in the flux saturates when the cloud becomes optically thick.

To make the optical depth vary there are two possible scenarios (c.f. Fig. 3.28):

A) H_2 emission arises from a thin shell, at the surface of a clump, where dust is mixed with the H_2 molecules. Each clump is irradiated differently and thus each has a different optical depth of the emitting shell. For increasing optical depth, both emission and extinction are enhanced with the above described mechanism. In this case only the most external clumps can be observed, those who are not hidden behind others clouds. For a PDR in standard conditions simulations shows that the excited H_2 is confined into a very thin shell (1/1000; J. Le Bourlot, private communication, c.f. Chapter 4, Sect. 4.3.1.1). To reproduce data points as in Fig. 3.26, the τ of this emitting shell has to be of the order of 0.5–1. This interpretation implies that the τ of the whole cloud is very high (A_V=200–10 000). This is possible only for very dense clumps but, Christopher et al. (2005) and Smith & Wardle (2014) have shown that such high density are reached in the CND in many clumps. For the CND the observed densities ranges is between 0.1 10^7–4 10^7 cm^{-3}. From $n_{H_2}/A_V = 1.8\ 10^{21}$ cm^{-3} mag^{-1} (Predehl & Schmitt 1995) one derives A_V=650–2 500 which is coherent with the proposed model.

B) H_2 is produced on each clump in a more or less identical emitting shell. The H_2 emission, on its way out of the medium, is attenuated by bulk dust in other clumps but also enhanced by the emission coming from these same clumps emitting shell. For an increasing number of clumps on the line of sight both the emission and the extinction are enhanced (c.f. Fig. 3.30). The model is the same described in Equation 3.6 but, instead of an absorption coefficient varying with the thickness of the emitting shell, we considered n separated, identical clumps: $(1 - e^{-\tau}) \cdot (e^{-n\tau} + e^{-(n-1)\tau} + .. + e^{-\tau} + 1)$. The final model that reproduces the observations is the one which implied from 1 to 20 clumps on the line

of sight, each of $\tau = 0.5$. This model works, provided that the filling factor by clumps is not so high so that there is a large variation of the number of clouds on the line of sight. In this case the photons produced on a clump surface would be attenuated but would still be able to exit the cloud. This scenario applies well to the Central Cavity since there the filling factor is likely smaller than in the CND.

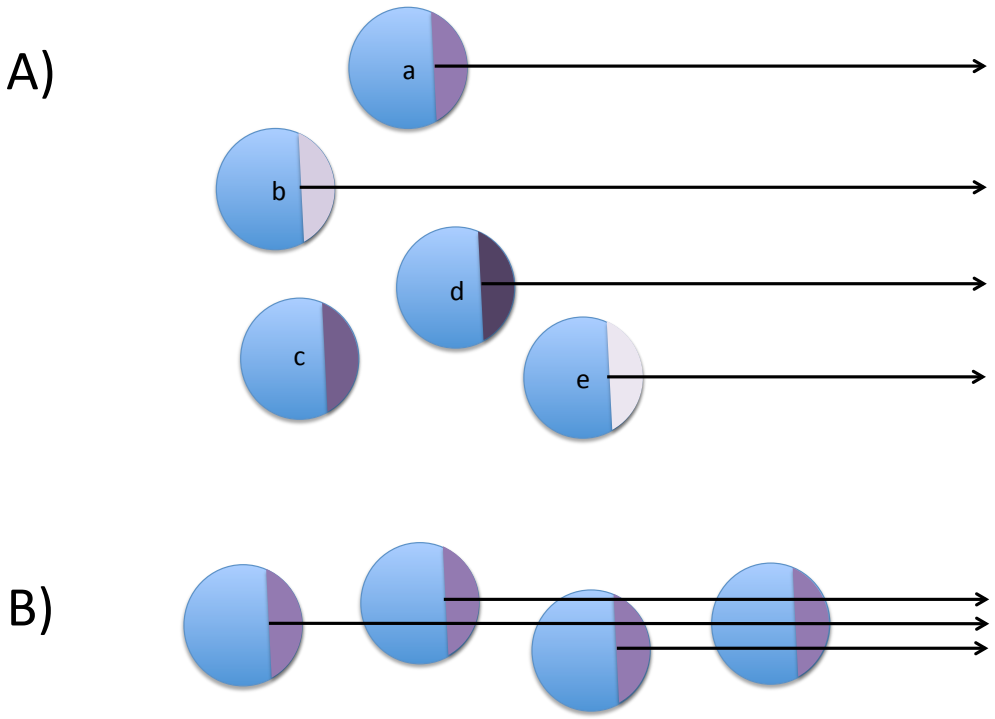

Figure 3.28: Illustrations of the two scenarios for the flux-extinction correlation. In case A, the emission arises from the thin external shell of clouds of variable optical depth. Only the most external clumps are visible (a, b, d, e but not c). In case B, the emission arises from identical external shell and it is attenuated and enhanced by clumps on the line of sight.

Both scenarios reproduce well the observed slope in the correlation plot and thus we cannot conclude on either one or the other. Scenario A seems coherent for the CND. However in the Central Cavity the high density required cannot be attained. There Scenario B seems to apply better even though it implies fairly high density as well (20 clouds of $A_K \sim 1$ are needed to reproduce the observed dynamics, i.e. $A_{K_{cloud}} \sim 20$). In practice, the two scenarios probably coexist and the final result is a superposition of the two effects.

In fact, the computed extinction is a compromise between the effect of the absorbing screen and the variation of the optical depth of the emitting clouds on the line of sight (either because of differences in the optical depth or in the number of the clumps). The second causes the

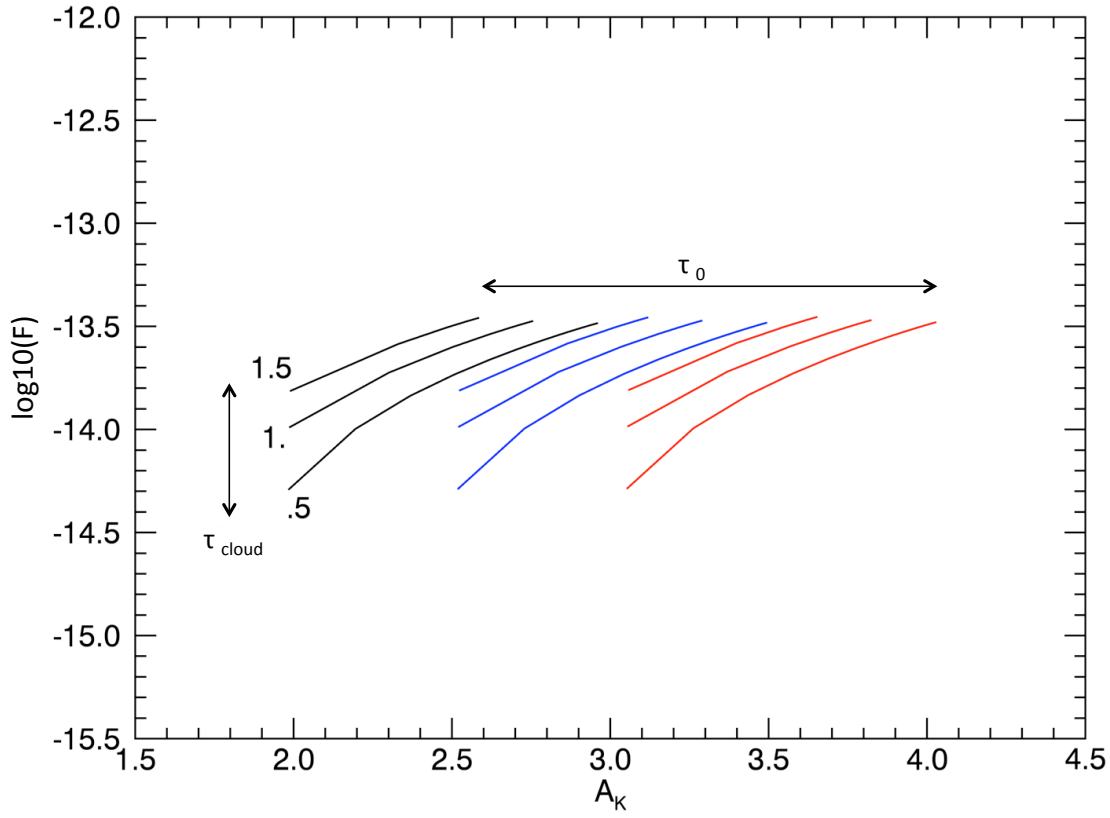

Figure 3.29: The model for a scenario B with up to 20 clouds for different values of the cloud absorption coefficient τ_{cloud} and different τ_0 of the foreground screen: τ_0=3 (*black*), 3.5 (*blue*), 4 (*red*). The variation of the absorption coefficient in clumps has the effect of expanding the dynamics covered by the model. The variation of the absorption coefficient of the screen shifts the curve to higher extinction values.

splitting in multiple curves for different optical depth of the absorbing screen while the first causes the variation of the optical depth along the line of sight and consequently the correlation between the flux and the extinction.

In summary the observed slope traces the fragmentation of the interstellar medium while the split into different groups of correlated points translates the large scale foreground extinction. The extinction measured through the Q(3)-S(1) ratio is a combination of these effects. These results underline the importance of estimating the extinction for the specific emitter under study since each source is located at a different optical depth for the observer.

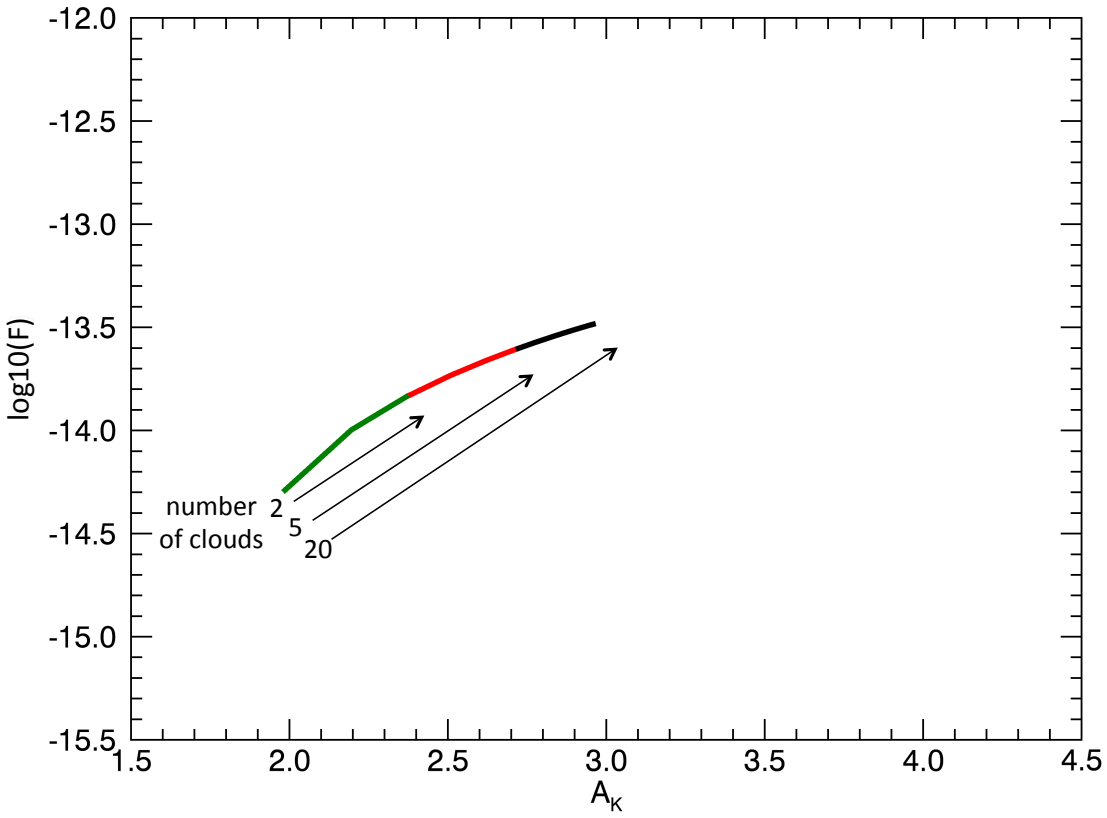

Figure 3.30: The model is traced for 20 (*black*), 5 (*red*) and 2 clumps (*green*) with τ=0.5 each. Models overlap on the plot and in fact all starts from the same value so that the 20-clumps model is the one which covers the larger dynamics. Increasing the number of clumps on the line of sight has indeed the effect of enhancing both the flux and the extinction.

Chapter 4

Physical properties of the molecular hydrogen emission

Contents

In the previous chapter, the dynamics and projected distribution of H_2 were investigated. This analysis led to the detection of two main components of the emission: one in the CND and one in the Central Cavity, at least in projection. In this chapter, the physical conditions of the emitting gas and the possible excitation mechanism are investigated.

Literature discusses two possible excitation mechanisms for the CND: collisions and fluorescence (Yusef-Zadeh et al. 2001 and references therein). Shock excitation can be provided either by the impact of stellar winds – coming from the central star cluster – on the inner rim of the CND, or by inter-clump collisions due to the random motion of clouds which have large velocities because of the central BH. Fluorescence excitation is caused by the radiative de-excitation of UV-pumped H_2, the UV field being provided, once again, by stars in the central parsec which illuminate the CND. The clumpiness of the CND implies a low volume filling factor which allows the radiation to reach deep inside the CND. It is sometimes difficult to determine which of the two competing mechanisms dominates since, if the gas density is high enough (10^5 cm^{-3}, Burton & Allen 1993), the thermal de-excitation of UV-pumped molecules produces H_2 lines typical of collisional excitation. In this case the two excitations mechanisms are difficult to distinguish, in terms of relative intensities of distinct lines and excitation temperature.

Concerning the Central Cavity, the question is to understand whether the observed H_2 emission comes from the central parsec region or from further or closer regions, through a projection effect. Given that the region encircled by the CND is quite transparent in comparison to the surrounding disk (Becklin et al. 1982), an emission coming from the background, beyond the central parsec, would not be absorbed by foreground material and would hence be seen. This idea is supported by the fact that in the dereddened flux map of H_2 lines, the shape of the Minispiral seems to stand out, with lower values. This can be interpreted as the Minispiral blocking part of the flux which is coming from behind it. If this is the case, the question is to understand how far behind the Minispiral the gas might be and if it is still in connection with the central few parsecs region or far behind. Another possible interpretation is that the gas is not behind the Minispiral but that it is all over the Central Cavity. In this case, the observed minimum in the Minispiral could just indicate that the gas there is mainly dissociated or ionized.

To answer this question, studying the physical conditions of the gas is required. In which environment is the observed emission produced: the extreme region of the central parsec or a less energetic region in the background? To do so, comparing the relative intensities of different lines is a useful tool since the excitation mechanism influences the relative populations of the various levels of energy. The relative intensities give information on the gas excitation temperature while the absolute flux values allow determining the total column density of excited H_2, as well as its mass. Therefore, the comparison of several lines can reveal different, specific processes, and give important hints on the dominating excitation mechanism.

In the first part of the next section, three additional emission lines are analyzed. Afterwards, adding the previously discussed five 1-0 transitions, all detectable H_2 lines on the SPIFFI spectral range are simultaneously analyzed. This analysis leads to the estimation of the temperature, density and mass of the observed excited H_2. In the rest of the chapter, the results of these analysis are used to trace H_2 excitation diagrams in several areas of the SPIFFI field of view and discuss the possible excitation mechanisms.

4.1 Data analysis

As previously discussed, the regularized 3D-fitting method can be applied only to five lines out of the eight detected in the SPIFFI dataset. For the other three, the signal-to-noise ratio is not high enough across the whole field. However they remains detectable in some areas. For the comparison of intensities required by the study of the H_2 physical conditions it is important to gather as much lines as possible to obtain stronger constraints on the gas properties. Therefore, even though no complete maps can be achieved for all detected lines, we select zones where H_2 conditions can be studied and used a classical 1D analysis.

4.1.1 Para 1-0 lines: S(2), Q(2)

In addition to the previously discussed ortho lines and the 1-0 S(0) para line, a few other 1-0 para lines are detectable: S(2) and Q(2) lines, respectively at 2.0338 μm and 2.4134 μm. These lines are in a more challenging spectral environment than the previously studied transitions. In particular:

- The Q(2) line is very close to a stellar CO absorption feature that strongly affects the observed intensity and width. In the northwestern corner of the field, void of bright stars, the line presents the best signal-to-noise ratio and is neatly detected. Elsewhere in the SPIFFI field, the line remains detectable but its intensity and width are biased by the above mentioned CO feature beyond usefulness.

- The S(2) line is very close to several OH sky lines which are not perfectly subtracted. These lines affect the spectral environment of S(2) degrading the continuum. As for Q(2) this effect is not an issue in the northwest corner, where almost all lines show a strong emission. Unlike Q(2), however, the S(2) line stands out of the continuum everywhere in field, except the southern region.

Because of these difficulties, it is in practice impossible to apply the regularized 3D-fitting method on these lines. The signal-to-noise ratio is quite low across the field. However the areas where they clearly stand out can be isolated and studied separately, with a classical 1D-fit (i.e. one spectrum at a time). The procedure consists in considering the average spectrum over regions of few arcseconds and fitting the observed line with a Gaussian profile to obtain the three parameters: flux, velocity and width. It was already shown in Chapter 2 that the 1D-fitting method on the average spectrum of some restricted portion of the field is consistent with the model obtained through regularized 3D-fit.

The previous chapter also proved that fitting lines simultaneously avoids problems due to artifacts and uncertainty of the fitting procedure. This is true as long as the assumption of a unique component of gas emitting all transitions is valid. Under this assumption all lines should have the same velocity and width. This has been proven for 1-0 ortho lines as well as the 1-0 S(0) line analyzed in the previous chapter. Now the assumption is extended to the others detectable lines. Moreover, the advantage of doing a simultaneous fit of the transitions is that lines with poorer signal-to-noise ratio are constrained by lines with better signal-to-noise ratio (especially S(1)).

4.1.2 2-1 S(1) line

In addition to the two previous 1-0 para transitions the 2-1 S(1) ortho line at 2.2476 μm is also detected, mainly at the borders of the field, where the CND lies. As for 1-0 S(2) and Q(2) transitions, it is hard to get complete parameter maps with the regularized 3D-fitting procedure. The spectral environment of this line is not particularly affected by nearby features but the transition is less intense than the 1-0 lines because the $v = 2$ level is less populated. However we can still apply the 1D zone analysis as for the above mentioned para lines.

The comparison between distinct vibrational levels is very precious in the understanding of the gas physical conditions. For instance, the ratio of 1-0 S(1) to 2-1 S(1) is a useful indicator of the excitation mechanism. The fact that transitions of high vibrational levels ($v > 1$) can be detected is already the indication of highly excited gas. Unfortunately no other $v > 1$ transitions has signal-to-noise ratio good enough to be included in this analysis. This represents a limitation that would be worth overcoming with data at a higher-spectral resolution, since it would permit to better separate H_2 lines from their polluting spectral environment and thus

allow a deeper study of the gas temperature and excitation. However, many conclusions can be drawn with the available lines.

The 2-1 S(1) line is therefore included in the simultaneous fit of the H_2 lines, thus assuming the same velocity and width for this line as well. This hypothesis is valid if the gas does not present different dynamical states each featuring a different state of vibrational levels populations.

4.1.3 Multiline analysis

The zones chosen for the multiline 1D analysis are displayed in Fig. 4.1. These zones have been selected because they present good signal-to-noise ratio for the studied lines and little influence from nearby spectral features. For instance, regions too close to bright stars are usually to be avoided because of the presence of stellar lines (as He I around 2.113 μm) affecting the spectral environment. Moreover, the selection of these regions tries to cover a sample of each of the main areas of interest in the field of view: the maximum of the flux in the CND northwest corner, the Northern Arm Cloud, the Minicavity.

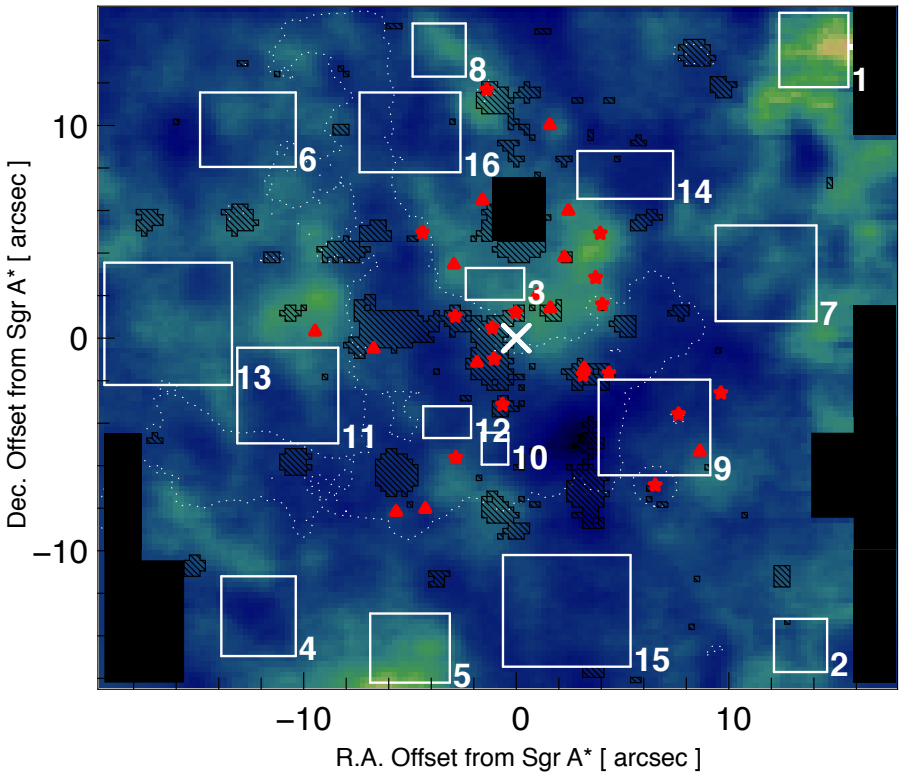

Figure 4.1: Zones considered for the multiline analysis traced on the dereddened flux map of the 1-0 S(1) line (Chapter 3, Sect. 3.3.4).

The multiline procedure, together with the related uncertainties, is discussed in more details in Chapter 2. The result is a unique model, fitting all detectable lines. The fitted parameters

are: the flux of S(1) line, the ratio of each of the other lines flux with respect to S(1), velocity and width (the same for all lines). Not every line has a good signal-to-noise ratio on each of the chosen regions. The average spectra over regions are examined one by one to identify the exploitable lines. For instance, Q(2) has a sufficient signal-to-noise ratio only in the Northwest corner where its flux is maximum. It is still detectable in many regions of the field but it is too biased by the CO absorption feature to be measurable.

The main uncertainties in this procedure come from the continuum evaluation and the relative spectral calibration (c.f. Chapter 2). Both can overestimate or underestimate line fluxes and thus affect the lines ratio. The effect of the relative calibration has been previously shown to be around 8% for lines ratios. The uncertainty on the continuum evaluation is always of the order of – or greater than – 10%. Therefore it dominates the uncertainty. The only exception is for the Northwest corner of the field. Here the really high signal-to-noise ratio leads to small uncertainties on the continuum evaluation (3 – 4%). There the uncertainty is dominated by the relative calibration and is fixed to 8%.

Once the dereddened flux of each line, in each region, has been computed, the standard approach is to plot an excitation diagram (or population diagram). It consists in plotting the column density of the upper level of each line versus its energy.

4.2 Excitation diagrams

In several astrophysical regions the emission of H_2 has been explained as coming from gas excited dynamically by shock-waves which compress and heat the gas to the temperatures and densities for which the emission becomes detectable. This applies in the Orion (Scoville et al. 2003) and in the Crab Nebulae (Loh et al. 2011). On the other hand, several of these NIR H_2-emitting regions, for instance ultra luminous IR galaxies (ULIRGs, Davies et al. 2003), are coupled to an environment filled with UV radiation which can excite the gas directly (Sternberg & Dalgarno 1989), producing Photon Dominated Regions (PDRs, c.f. Chapter 1 Sect. 1.3.5). In the central parsec region the stellar winds and high velocities of the clumps cause frequent shocks, while the intense UV radiation illuminating gas clouds produces PDRs where molecules can be either vibrationally excited by far-ultraviolet (FUV) pumping or collisionally excited in gas heated by FUV-radiation (collisional fluorescence). Therefore here both shocks and UV radiation compete to excite H_2. The excitation diagram helps distinguishing between these mechanisms.

Given the dereddened line flux f_{vj} of a line, the column density N_{vj} of molecules in state $[v, j]$ can be calculated as:

$$N_{vj} = \frac{4\pi}{\Omega} \frac{f_{vj}}{\mathcal{A}_{vj} \nu_{vj} h} \tag{4.1}$$

where $\mathcal{A}_{vj}$ the Einstein's coefficient and ν_{vj} the frequency of the considered state $[v, j]$ and Ω is the aperture solid angle (Davies et al. 2003). Each column density is normalized by 1-0 S(1).

The excitation diagram consists in plotting the column densities per statistical weight of a given transition N_{vj}/g_{vj} – where g_{vj} is the degeneracy of the state – as a function of the

energy of the upper state E_{up}. The column densities are typically represented on a semi-log scale. On this diagram the relative intensities of several lines can be easily and simultaneously compared and the physical conditions of the gas can be evaluated by comparison with straight lines that would correspond to perfectly thermalized gas.

4.2.1 Expression of the column density

For a gas in LTE all states have the same excitation temperature. The column density N_{vj} is characterized by a Boltzmann distribution:

$$\frac{N_{vj}}{N_{tot}} = \frac{g_{vj}\ e^{-E_{vj}/T_k}}{\sum_i g_i\ e^{-E_i/T_k}} \tag{4.2}$$

Where N_{tot} is the total column density, E_{vj} is the upper level energy and T_k is the kinetic temperature of the gas.

In the more general case of a molecule not in LTE, one can write:

$$\frac{N_{v_1 j_1}}{N_{v_2 j_2}} = \frac{g_{v_1 j_1}}{g_{v_2 j_2}} e^{-(E_{v_1 j_1} - E_{v_2 j_2})/T_e} \tag{4.3}$$

Where T_e is the excitation temperature that is defined by the relative column densities of any two levels $[v_1, j_1]$ and $[v_2, j_2]$.

For an arbitrary excitation mechanism, a distinct excitation temperature might characterize each level. The excitation temperature is not a physical temperature but rather a convenient parameter to characterize relative non-LTE populations. Generally, in non-LTE gas $T_e \neq T_k$, except for very dense regions. For further details see Goldsmith & Langer (1999).

4.2.2 Excitation mechanism

In the central parsec both shocks and UV-pumping can play a role in H_2 excitation and thus both mechanisms have to be considered.

Collisional excitation Collisional excitation is caused by shock waves dynamically heating and compressing the gas. At high enough density, collisional excitation and de-excitation dominates so that the gas is thermalized and the population follows the Boltzmann distribution of Equation 4.2. In this case the column densities, in the log scale, align on a straight line in the excitation diagram, if a single temperature is present, or on a smoothly decreasing curve, if a range of temperatures occurs on the line of sight (Fig.4.2). The inferred temperature is the physical temperature of the gas.

Fluorescent excitation The H_2 excitation in PDRs is well described in Sternberg & Neufeld (1999) and Le Bourlot (2008). In the case of pure fluorescent excitation the absorption of a FUV photon by the molecule is followed by radiative de-excitation. The excitation diagram would rather exhibit different excitation temperatures for distinct vibrational states (i.e. different v). Levels with large v can be populated. This is the case for instance for the reflection nebula NGC 7023 as it has been shown by Martini et al. (1997) (Fig. 4.3).

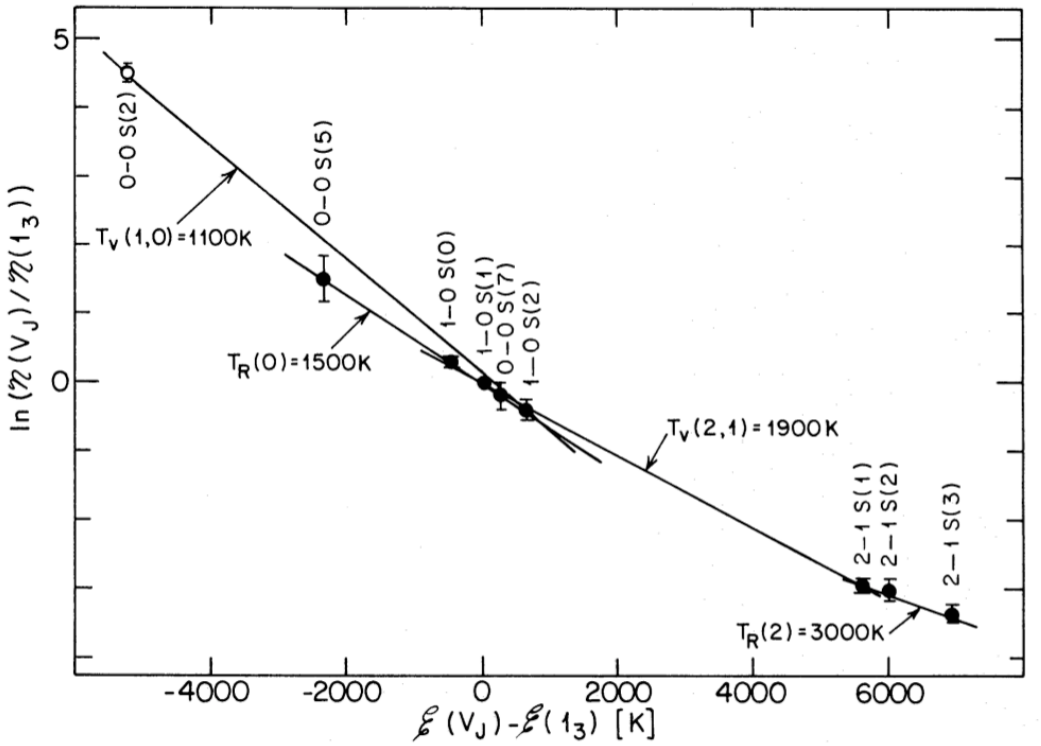

Figure 4.2: Beckwith et al. (1983) excitation diagram for the Orion molecular cloud.

For gas densities exceeding 10^5 cm^{-3} (Burton & Allen 1993), the UV-pumped molecules can be collisionally de-excited, producing collisionally excited lines whose excitation diagram appears thermalized. This collisional fluorescence is thus sometimes difficult to distinguish from collisionally excited gas since both lead to thermalized populations even though the excitation mechanism is different.

The 1-0 S(1) to 2-1 S(1) line ratio allows in principle to distinguish between FUV-pumping and collisional excitation (Shull & Hollenbach 1978). A high ratio (∼10) is the signature of shock excitation (Shull & Hollenbach 1978) while a low ratio (∼2) is indicative of pure fluorescence (Black & Dalgarno 1976). Intermediate values (∼5) are indicative of collisional fluorescence (Burton & Allen 1993).

Since observations seem to indicates different regimes for the CND and the Central Cavity, in terms of densities and UV field, the possible excitation mechanism for each is investigated separately.

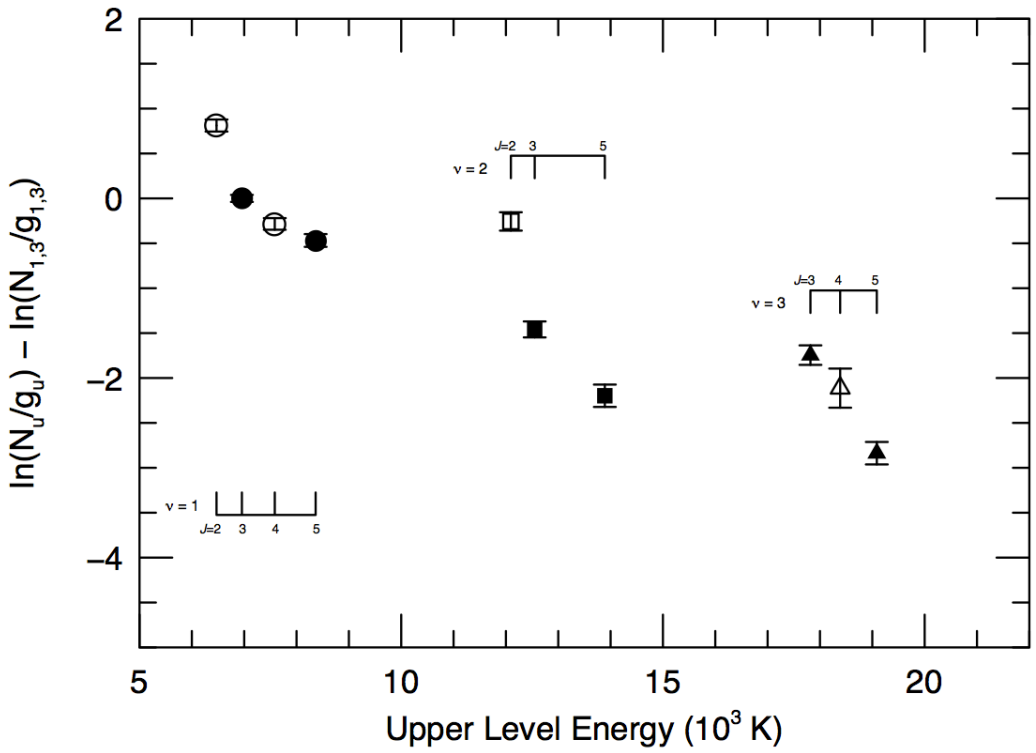

Figure 4.3: Martini et al. (1997) excitation diagram for NGC 7023. The column density of H_2 in a given state, N_u is divided by the statistical weight, g_u, and normalized to the 1-0 S(1) transition (v=1, J=3). Para (even J) rotational transitions are represented by open symbols, ortho (odd J) transitions by filled symbols.

4.2.3 Data analysis using excitation diagrams

In this section the above-discussed excitation diagram analysis is applied to the SPIFFI dataset, in particular to each individual region of Fig. 4.1. For each zone the observed fluxes of H_2 lines have to be dereddened first. The extinction correction is applied via the A_{Ks} map obtained in the previous Chapter. The A_{Ks} average value over each region is used to compute $A_\lambda = A_{Ks} \cdot (\lambda/2.168)^{2.07}$ (c.f. Chapter 3, Sect. 3.3.3) which is applied to deredden the observed fluxes. Column densities of each line are calculated as in Equation 4.1.

Each column density is divided by the level degeneracy g_{vj} and normalized by N_{13}/g_{13} (1-0 S(1) line). The excitation diagram for each zone is reported in Fig. 4.4 and 4.5. The column densities of 1-0 S(1) and 1-0 Q(3) are almost coincident in every zone, meaning that the extinction obtained with regularized 3D-fit method corrects very well the extinction for flux obtained with a 1D-fit, confirming the validity of the 3D method.

In several of the zones under study, the points align on one straight line on the excitation diagram. It is the case for instance for zones 1, 2, 4, 5, 7 (all corresponding to the CND), zone 8 (the "Plume") and 16 (the Northern Arm of the Minispiral).

In all other regions the points on the excitation diagram show a split between ortho and

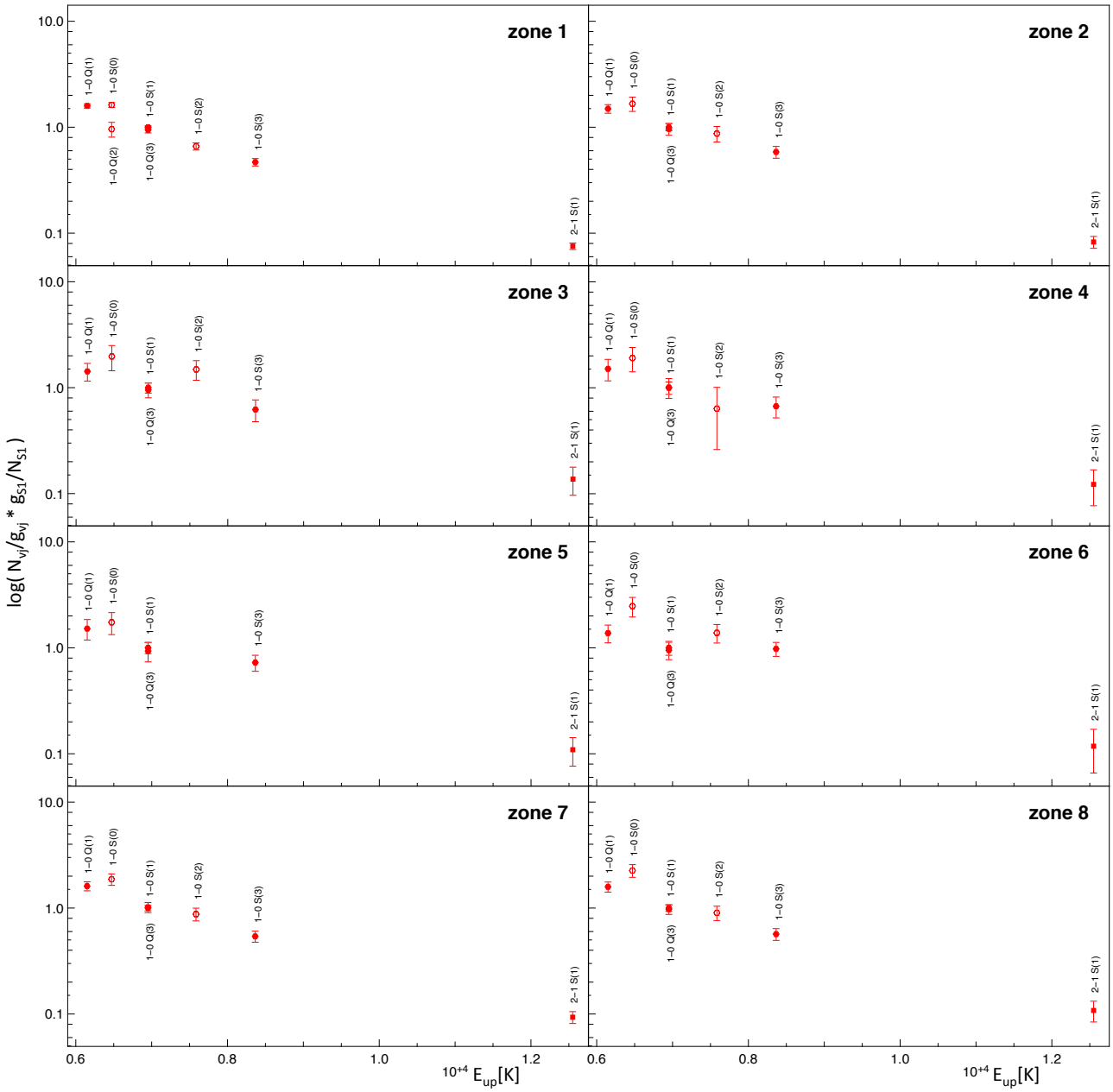

Figure 4.4: Excitation diagrams of zones 1 to 8. The column density is normalized by 1-0 S(1) and represented in the log scale: $\log(\frac{N_{vj}/g_{vj}}{N_{13}/g_{13}})$. The upper level energy expressed in K. Full symbols represent ortho transitions (odd-J), open symbols represents para transitions (even-J). The $v = 1$ levels are represented with circles, $v = 2$ with squares.

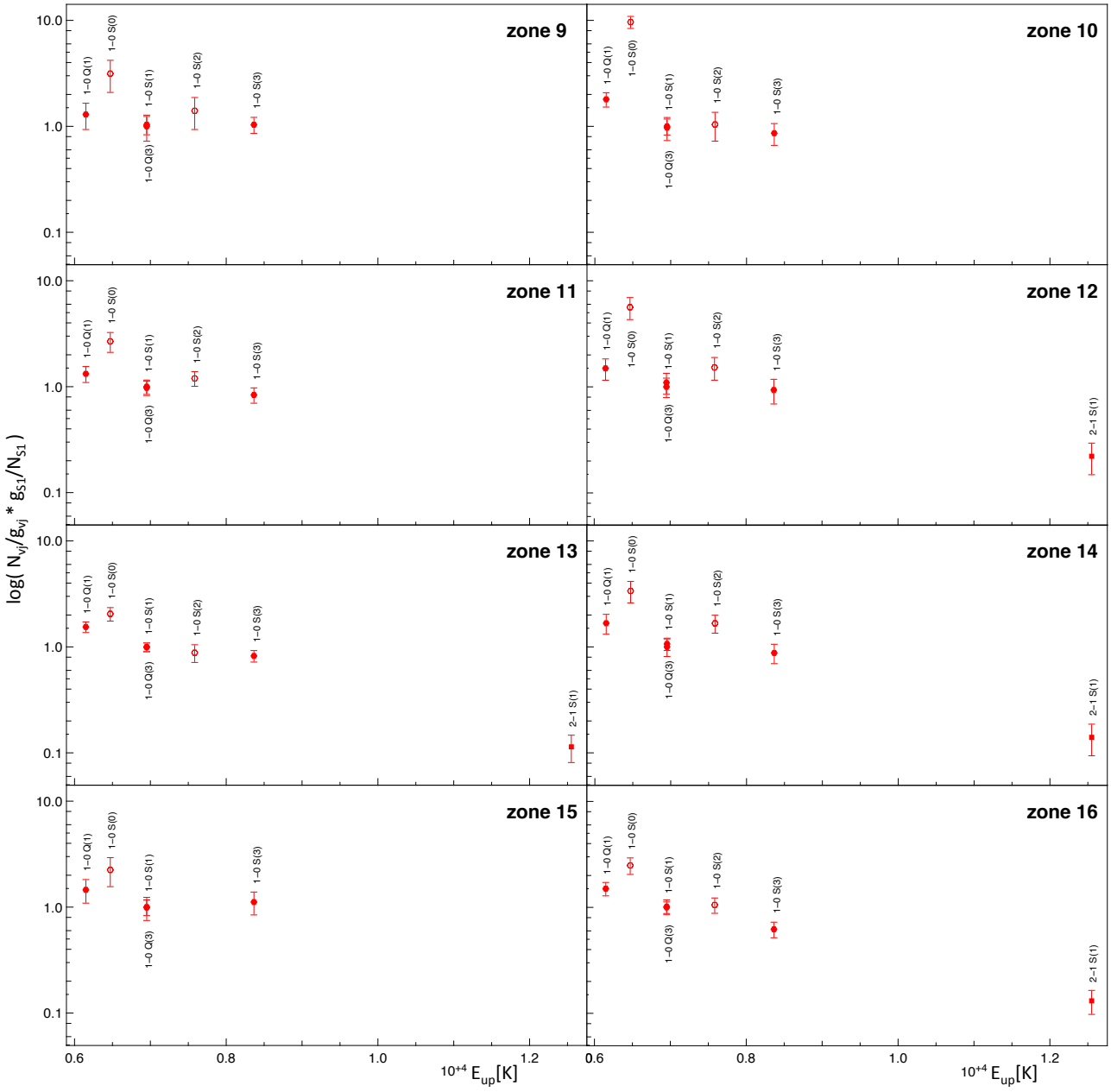

Figure 4.5: Excitation diagrams of zones 9 to 16. Continue from Fig. 4.4.

para or among transitions within different rotational levels.

To quantitatively investigate all these configurations and test the thermalization hypothesis, each excitation diagram is fitted with the function:

$$\frac{N_{vj}/g_{vj}}{N_{13}/g_{13}} = a \cdot e^{-(E_{vj}-E_{13})/T_e} \tag{4.4}$$

where T_e is a proxy for the excitation temperature and a is the y-intercept in the log space. In case the population is thermalized, the excitation temperature corresponds to the actual kinetic temperature and the a parameter is straightforwardly connected to the total column density of H_2.

The model fitting can be done using either all observed H_2 lines or the ortho lines and the para lines independently. In the first case this is equivalent to assuming that the OPR has the standard value of 3, which comes from the spin statistics in a thermalized population (see for instance Takahashi 2001). The degeneracy $g_{\nu j}$ of ortho lines takes into account the standard OPR of 3, i.e. every ortho $g_{\nu l}$ contains this factor: $g_{\nu j} = 3 \cdot (2J + 1)$ for ortho and $g_{\nu j} = (2J + 1)$ for para lines. In the second case, this allows to test whether the distribution is close from thermal for each isomer but with a non-standard OPR.

In the fitting procedure the 2-1 S(1) line is not considered because, even if the gas was thermalized, different vibrational levels can have different kinetic temperatures if the temperature varies along the line of sight. The signal-to-noise ratio does not allow the clear detection of lines with $v > 1$ other than the 2-1 S(1) line. It is therefore impossible to look for different temperatures for distinct vibrational levels. For this reason, this line is not necessarily aligned with the other and it is taken out of the fitting procedure. However, it is still interesting to study it since the 2-1 to 1-0 S(1) ratio is of great interest. It is indeed one of the parameters allowing discrimination between collisional and fluorescent excitation. If fluorescent excitation dominates, then the rotation temperature (states with same v) is lower than the vibrational temperature (states with same J) leading to small values of this ratio. The UV radiation in high density material can lead to collisional de-excitation of the UV-pumped H_2. In this case the level populations would appear thermalized as in the case of shock excitation. However, the two mechanisms can still be distinguished comparing 2-1 S(1) and 1-0 S(1) ratio.

4.2.4 Uncertainties

The uncertainties on the fitted parameters of Equation 4.4 have to be carefully considered. Many sources of errors contribute to the final uncertainty and their propagation is not straightforward. The sources of errors on the column densities are connected to the continuum evaluation and the spectral calibration. The issue is to correctly propagate these uncertainties in such a non-linear regime. Moreover, the two fitting parameters are correlated and a classical analytical propagation is not applicable. To overcome these difficulties, one solution is to consider the χ^2 map of the model.

Considering a grid of values for a and $1/T_e$ one can obtain a χ^2 maps in the $(a, 1/T_e)$-plane, i.e. the χ^2 of the model applied to the data points for each combination of a and $1/T_e$. This particular pair of parameters is adopted because it yields a linear relation in the log space. The minimum on the χ^2 map corresponds to the best estimate of a and $1/T_e$ for a given dataset.

A Monte Carlo simulation is run 10 000 times over a set of column densities, normally distributed – according to the known uncertainties – around the observed values for each line. Each simulated set is fitted with Equation 4.4 to obtain an estimate of a and $1/T_e$. The best-fit model is compared to the data points to calculate the corresponding χ^2. An example of the Monte Carlo result is plotted over the χ^2 grid obtained for zone 16 in Fig. 4.6.

Contours enclosing the 68%, 95%, and 99% of the smallest χ^2 values are traced. The [a, $1/T_e$] values corresponding to these contours are considered as the 1, 2 and 3 sigma values of the parameters distribution. The final uncertainties on the fitted parameters are calculated as the maximum and minimum values of a and $1/T_e$ corresponding to the 1σ-contour.

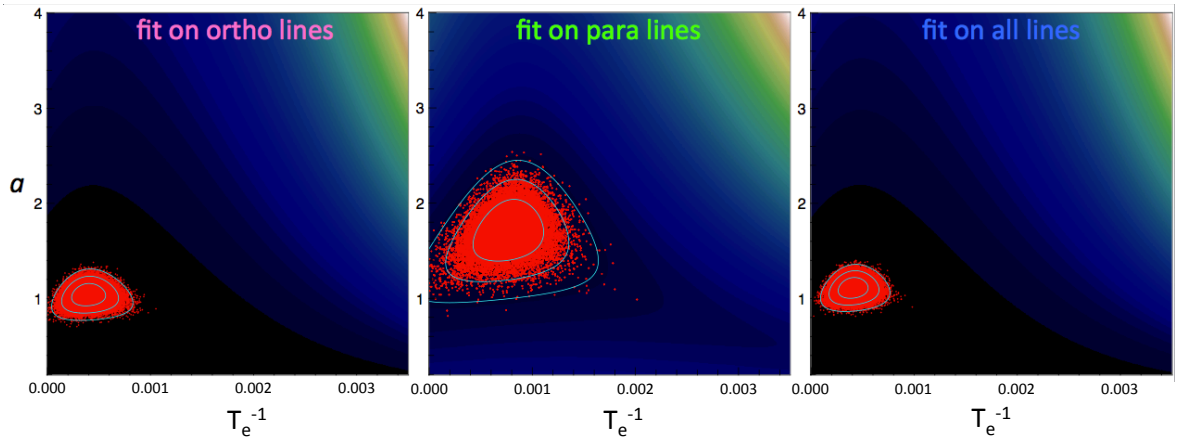

Figure 4.6: Map of the χ^2 values obtained for different combinations of a and $1/T_e$ parameters. The red point represents the χ^2 resulting from the fit of 10 000 simulated column densities. Contours trace the 1,2, and 3 sigma values. *From left to right:* χ^2 obtained fitting only ortho lines, fitting only para lines and fitting all 1-0 lines.

In Fig. 4.7 and 4.10 the best χ^2 value and the 1, 2 and 3 σ contours are represented on the left of the corresponding excitation diagram, where the thermal models are traced as solid straight lines of different colours.

4.2.5 Distinguishing thermalized from non-thermalized regions

Fig. 4.7 and 4.10 allow to compare the models obtained for different sets of lines (all 1-0 lines, ortho or para lines alone), represented in different colours and theirs uncertainties. The objective of this comparison is to infer whether, in a given zone, the gas is thermalized or not.

Looking at the excitation diagrams, some zones appear aligned on a straight line. However, the 1-0 S(0) line always shows a small offset, with respect to the other lines, toward higher values of the column density. This behavior is striking for zone 10 but it is still visible in all the zones. It can of course be a systematic effect but, at least for zone 10, this strong enhancement is visible even in the raw data and in the regularized 3D-fit map where it appears as a strong emission maximum. Therefore the strong effect of zone 10 seems real whereas elsewhere 1-0 S(0) is mostly aligned with other lines within the error bars. We therefore applied a criterium to determine whether the observed populations are thermalized or not within the uncertainties.

We considered that the population is thermalized when the all-line, ortho-lines and para-

line models are compatible within the uncertainties. This translates in having the three 1-sigma contours in the $\chi 2$ space overlapping.

The all-lines model is always dominated by the ortho lines contribution, since they are the most numerous lines. The para-lines model is always a bit steeper – tilted towards higher values of $1/T_e$ and a – with respect to the other two models, but remains compatible within 1 σ for zone 1, 2 and 4. These three zones correspond to regions in the CND.

For zones 5 and 15, not enough para lines where detected to trace a thermal para-model. In particular, almost all the central-southern part of the field presents no emission in the 1-0 S(2) line. This is either because there is no detectable emission coming from the region or because there is a spurious spectral feature of different origin preventing the detection of this line. Zone 5 corresponds to the CND Southern Extension, while zone 15 is located on the Central Cavity in projection (just South of Sgr A*). For zone 5, 1-0 S(0) is compatible with the thermalized ortho-model, we therefore considered the gas as thermalized here. This is not the case for zone 15.

For zone 3 the para- and ortho-models are compatible with parallel lines in the excitation diagram. The offset, in $log(N/g)$, of the two curves of the excitation diagram of zone 3 is 0.76. If actual, it would mean that the real OPR is 2.28, instead of the assumed value of 3. An OPR smaller that 3, with values ranging from 1.5 to 2.2 has been previously measured in PDRs, for instance like in NGC 7023 (Fuente et al. 1999). Authors interpreted the non-standard OPR as arising in shock-heated gas that has not reached the LTE yet. This interpretation implies that the OPR at time of formation of H_2 is lower than 3 and that the gas phase molecules are destroyed before attaining the equilibrium value of 3. This is quite evident for this region, but also zones 6, 14, 16 and, to some extent, 9 are compatible with this kind of behavior. However, even for zone 3, the separation of the two models (para and ortho) measured by the a parameter, is only significant to 1 σ, i.e. there is only a 68% probability that the two lines are actually separated. If significant, this particular result has to be considered at most as a hint of a possible non standard-OPR in this region. More detailed analysis, in particular with a higher signal-to-noise ratio is needed to conclude.

Finally, there is a region where the slopes of the ortho and para models are significantly different: zone 10. Here, the para-model gives lower temperatures and higher values of a, with larger uncertainties with respect to the ortho- and all-models. The para-model shows a 5-σ offset with respect to the ortho and all models. For zones 12, and 14 the ortho- and para-models show a 2 sigma separation. Even though for these zone the effect is less striking they are most probably not thermalized. All these zones are located in the Central Cavity.

For zones 7, 8, 9, 11 and 13 a tilt can be seen but not to a significant level, due to larger uncertainties. All these areas are located at the border of different specific regions, so that the observed behavior may be the result of an average between different regimes. Zones 3, 6, 9, 11, 13 and 16 are at the border of the Minispiral, zones 8 is on the tail of the Plume feature, zone 7 is at the border of the CND.

4.3 Zone analysis

In this section physical properties of H_2 are calculated from the fitted parameters of the thermalized gas case. At least two regimes are conceivable: one in the CND, thermalized, and a one in the Central Cavity, not-LTE. The possible excitation mechanism is then investigated for both the different areas.

4.3.1 Thermalized zones: the CND

For regions where thermalization applies, T_e corresponds to the kinetic temperature of the gas and the total column density of excited H_2 can be derived from the model parameters. For regions 1, 2, 4 and 5 the ortho- and para-models are both compatible with the all-lines thermal model, and the column density can be evaluated through Equation 4.2. In zone 5 not enough para-lines are available to fit a para-model. Interestingly, all these regions correspond to the CND location on the SPIFFI field of view.

4.3.1.1 Excitation temperature and total column density

Knowing a, $1/T_e$ and N_{vj} one can solve equations 4.2 and 4.4 to derive the total H_2 column density N_{tot}:

$$N_{tot} = \frac{N_{13}}{g_{13}} a \cdot e^{E_{13}/T_e} \sum_{vj} g_{vj} e^{-E_{vj}/T_e} \tag{4.5}$$

Temperatures and total column densities obtained for each thermalized zone are listed in Table 4.1.

		all lines model		ortho lines model		para lines model	
zone	1-0 S(1)/2-1 S(1)	T_e	N_{tot}	T_e	N_{tot}	T_e	N_{tot}
1	9.8	1700^{+150}_{-150}	27^{+11}_{-7}	1800^{+200}_{-150}	22^{+10}_{-6}	1400^{+280}_{-150}	53^{+66}_{-27}
2	9	2300^{+730}_{-450}	6^{+5}_{-2}	2340^{+830}_{-450}	6^{+5}_{-2}	1720^{+1940}_{-450}	15^{+90}_{-11}
4	6	2460^{+3030}_{-940}	4^{+11}_{-2}	2910^{+5010}_{-940}	3^{+8}_{-1}	1010^{+2470}_{-940}	> 1
5	6.8	3100^{+4400}_{-1220}	7^{+13}_{-1}	3560^{+7400}_{-1220}	6^{+10}_{-4}	-	-

Table 4.1: 1-0 S(1) to 2-1 S(1) ratio, excitation temperature (in K) and total column density (in $10^{22} \cdot \mathrm{m}^{-2}$) for each zone where thermalization applies. These values are estimated with a fit of all-lines, ortho-lines and para-lines (where possible) with a thermal distribution.

Excitation temperature The derived temperatures are quite high, ranging from 1 700 K to 3 100 K, but below the H_2 dissociation temperature (∼4 000–5 000 K). The values are very high with respect to previous measurements. The literature indicates values as high as 400 K (Genzel et al. 1985) for the neutral gas for the temperature of the molecular gas in the CND. A more recent measurement of the CND temperature, via NH_3, has been presented by Mills et al.

(2015) and leads to temperatures of 200–300 K. On the other hand very high temperatures have been previously observed in other analyses of NIR H_2 lines, such as in the Crab nebula where Loh et al. (2011) analyzed several H_2 lines in the range 2.02–2.33 μm, among others the 1-0 S(0), S(1), S(2) and 2-1 S(1) lines analyzed here. The inferred temperatures are in the range of 2 000–3 000 K, thus comparable to our findings.

The likely reason of the apparent discrepancy between H_2 and other molecules, such as NH_3, resides in the fact the H_2 becomes directly detectable only when highly excited (see Sect. 1.3.4). Looking at NIR H_2 lines implies selectively observing only the most excited gas, whereas NH_3 probes the dense – presumably colder – gas properties. The H_2 that is less excited is not detected. This hidden part can be probed only indirectly by CO and NH_3 but not directly by H_2 emission.

Total column density and mass Knowing the total column density given by the thermalized all-lines model and considering a distance to the Galactic Center of $D = 8$ kpc, the mass contained in a certain region can be roughly estimated as $N_{tot} D^2 S M_{H_2}/M_\odot$, where S in the solid angle covered by the region in steradians and M_{H_2} the mass of a H_2 molecule. Considering N_{tot} in zone 1, the observed column densities lead to a mass of $7^{+4}_{-3}\ 10^{-3}\ M_\odot$, over a surface of $\sim$ 13 arcsec^2. Zone 1 is the region where the highest thermalized emission from the CND arises and has to be considered as giving an upper limit of the mass. Even so the mass is much lower than previous estimates: $\sim 10^4$ $M_\odot$ for a cloud of typical diameter 0.2 pc (Christopher et al. 2005).

The above discussion on H_2 temperatures applies to the observed masses as well. The analysis of NIR H_2 lines gives access only to the most excited gas and misses the much more important fraction of colder gas. In the determination of column density, hot H_2 dominates the intensities, making the results very sensitive to thermal structures of the cloud. Just a small amount of H_2 – at high temperatures – is responsible for the observed column densities. If the portion of the CND which is covered by the SPIFFI dataset (at least the equivalent of one big cloud) had a mass of 10^4 $M_\odot$, at 400 K, it follows from Equation 4.2 that the flux of the 1-0 S(1) line would be almost 10 times weaker than the one observed. This emission from excited H_2 is likely to come from the UV illuminated skin of bigger, colder clouds in the CND. Only the H_2 located in a thin shell at the border of these clouds would be heated either by the UV from the central star cluster or by collisions, presumably from stellar winds or cloud-cloud collisions.

Simulations of the standard conditions of a PDR are coherent with this result (J. Le Bourlot, private communication). In these simulations the considered parameters are: a total optical depth $A_V = 10$, a density $=10^3$ cm^{-3}, a radiation field 100 times the interstellar radiation field and solar abundances. The result is that almost all excited gas is located in the $A_V = 0.14$ layer and 30% of the emitting gas is in the $A_V = 0.014$ layer, i.e. in 1/700 of the volume (c.f. Fig 4.11).

In Loh et al. 2011 the authors propose the same interpretation: the hotter H_2 is just a small fraction of the total cloud mass, but it is the source that dominates the intensity. They find that the H_2 traced by NIR lines is 1/1000 of the total mass. Similarly, in Orion Scoville et al. (1982) found a H_2 mass around 10^{-2} $M_\odot$, significantly lower than what is predicted by

models.

Applying the 1/700 factor to the above estimated mass of hot H_2 in the CND we find still much smaller value than what estimated by Christopher et al. (2005). The huge initial discrepancy is largely reduced, but still there is a big gap which may indicate that a large fraction of the hot gas is not seen at all because of a much larger dust opacity. Considering that the PDR conditions in the Sgr A* region are more extreme than elsewhere (Güsten 1989) with 90% of the ionizing flux coming from OB supergiants and Wolf-Rayet stars (Martins et al. 2007) and additional factor must be applied.

Hence on one hand, the cooler molecular hydrogen is missed because its too low temperature prevents its detection and on the other hand, the huge dust opacity must block most of the emission of the hot component.

4.3.1.2 Circumnuclear Disk gas excitation mechanism

The population is thermalized in the zones that are very well identified as part of the CND (zones 1, 2, 4 and 5). The high 1-0 S(1) to 2-1 S(1) ratio in zones 1 and 2 is consistent with a shock-excited gas. Even though, for dense PDRs, UV-excited H_2 can produce a ratio which resembles shock excited gas (Sternberg & Dalgarno 1989), for zone 1 and 2 our result seems fairly consistent with previous conclusion of a shock-driven excitation. Yusef-Zadeh et al. (2001) for instance argued that the emission arises from shocks deriving from random motions of clouds for a clumpy medium or of turbulence for a more homogeneous one. For zone 4 and 5 the ratio drops to values midways. Burton & Allen (1993) explain these values as indicative of collisional fluorescence. The thermalization observed for these zones can be produced by either shock or collisional fluorescence. Since these zones show 1-0 S(1) to 2-1 S(1) ratios significantly lower than 10, shock excitation seems to be ruled out leaving collisional fluorescence as the favured scenario in contrast with the opposite corner of the SPIFFI field which is more probably dominated by collisional excitation.

Given the known inclination of the CND (Fig. 4.12), and that the emission arises from the surface of the torus, it is possible that different mechanisms are involved in exciting the two distinct parts of the CND covered by SPIFFI. The southeastern corner seems more illuminated by the central cluster and is therefore consistent with a UV-dominated excitation. On the other hand the northwestern corner could be less exposed to the radiation and thus dominated by shock excitation. However, this interpretation is in contradiction with the fact that the western border of the CND is ionized (the Western Arc of the Minispiral) implying that this zone is indeed exposed to UV radiation whereas the southeastern corner shows no ionization. Nevertheless, the CND is very asymmetric and the two observed corners are not necessarily located at the same distance from the central ionizing sources. Moreover, other intervening material could prevent the UV radiation from reaching the southeastern corner. Because of the high complexity of this region, no definitive conclusion can be drawn yet.

4.3.2 Non-thermalized zones: the Central Cavity

For the zones where the para- and ortho-model are not compatible with a common thermalized model (zone 10, 12 and 14), no kinetic temperature and total column density can be

determined straightforwardly. Nevertheless the fitting parameters are reported in Table 4.2 for completeness and to compare the results obtained for the distinct sets of lines. Therefore, when looking at the Central Cavity, these values have to be interpreted as indicators of a trend of temperature and column density and they have to be considered cautiously. Often the parameters uncertainty allows putting only a lower or upper limit on the value.

		all lines model		ortho lines model		para lines model	
zone	1-0 S(1)/2-1 S(1)	T_e	N_{tot}	T_e	N_{tot}	T_e	N_{tot}
3	5.6	> 3333	< 13	> 1630	< 17	> 3280	< 58
6	6.3	> 3390	< 5	> 6440	< 10	< 8910	< 168
7	7.9	1980^{+480}_{-340}	7^{+7}_{-3}	2040^{+560}_{-340}	6^{+6}_{-3}	1470^{+870}_{-340}	22^{+94}_{-17}
8	6.8	2070^{+620}_{-390}	8^{+8}_{-4}	2190^{+780}_{-390}	7^{+8}_{-3}	1210^{+620}_{-390}	71^{+414}_{-59}
9	-	> 3960	< 19	> 30000	< 32	< 140000	> 12
10	-	2340^{+2940}_{-910}	5^{+21}_{-3}	2740^{+6760}_{-910}	4^{+18}_{-0}	< 620	> 8640
11	-	> 2850	< 5	3050	< 5	< 3030	> 4
12	3.3	> 2230	< 7	> 2040	< 9	< 1440	> 25
13	6.5	3240^{+2460}_{-1010}	4^{+3}_{-1}	3960^{+4430}_{-1010}	3^{+2}_{-1}	1320^{+940}_{-1010}	38^{+341}_{-32}
14	5.3	4460^{+43070}_{-2260}	2^{+3}_{-16}	$4320^{+138250}_{-2260}$	2^{+5}_{-30}	1580^{+3700}_{-2260}	21^{+276}_{-18}
15	-	> 2130	< 6	> 13000	< 19	-	-
16	5.6	2500^{+1250}_{-670}	3^{+5}_{-1}	2550^{+1650}_{-670}	3^{+5}_{-1}	1300^{+1040}_{-670}	32^{+265}_{-28}

Table 4.2: 1-0 S(1) to 2-1 S(1) ratio for each zone where 2-1 S(1) is detected. Best fit parameters obtained when considering a thermal distribution on all-, ortho- and para-lines are added for each zone. These values are valid under the assumption of thermalized populations, which does not apply on these regions. They therefore have to be considered with caution as indicators of a trend of temperature and column density. Apparent T_e is in K, apparent N_{tot} is in $10^{22} \cdot \mathrm{m}^{-2}$.

As for thermalized zone, the observed H_2 represents only the most excited fraction. However, in the Central Cavity, the density drops by one order of magnitude (Jackson et al. 1993; Davidson et al. 1992, among others) and the interpretation of the emitting gas as a thin layer at the border of clouds does not necessarily apply. For instance the 1-0 S(1) width map and the extinction map indicate that part of the emission comes from inside the Northern Arm Cloud.

The different excitation (non-thermalized gas) seems to indicate different conditions of UV irradiation compared to those of the CND. In particular, the UV density must be much larger, as testified by the streamers of ionized gas (the Minispiral). Because of the lower density and clumpiness, the UV radiation penetrates more deeply inside.

This explains why one can detect H_2 emission from inside the Northern Arm Cloud but not from inside CND's clouds. In the CND the emission remains confined at the surface because

of the higher density that allows an efficient self-shielding. On the contrary, the clumpier environment of the Northern Arm Cloud and the stronger UV field allow the radiation to penetrate deeper inside the cloud.

In the rest of the Central Cavity the gas might be even more diffuse and distributed in bigger volumes. In this case the observed intensities might represent a larger fraction of the total gas mass.

4.3.2.1 Central Cavity gas excitation mechanism

The population in the inner cavity is not thermalized which rules out shock excitation.

The tilt between the ortho and para lines observed in the excitation diagram of regions 10, 12 and 14 suggests an OPR smaller than 3. As pointed out by Sternberg & Dalgarno (1989) the OPR of FUV-pumped vibrationally excited states is not the standard OPR. The authors argue that FUV-pumping is realized through the Lyman and Werner band absorption lines which are expected to become optically thick in PDRs. When this happens H_2 becomes self-shielded. Therefore, the observed tilt between ortho and para lines could be a consequence of the greater optical depth of ortho transitions which become self-shielded before the para H_2, reducing the ortho pumping rate. In this case, the observed OPR is $\sqrt{3} \sim 1.7$, significantly smaller than the standard value (Sternberg & Dalgarno 1989). The apparent low OPR can thus be falsely introduced as a consequence of the more efficient self-shielding of ortho-lines with respect to para-lines. In this case the observed OPR would not reflect the real OPR. The problem with this explanation is that the model shows this effect only for weak PDR, i.e. low UV radiation, whereas the central parsec is a very strong PDR because the UV-radiation is stronger than elsewhere in the Galaxy. We note that the tilt between the ortho and para models is mainly due to the high value of 1-0 S(0).

Zone 10 is the region that corresponds to the strong flux enhancement of the para 1-0 S(0) line seen in its flux map (c.f. Fig. 3.14, Chapter 3). This zone is particularly challenging to explain. In this region all 1-0 lines align quite well on a straight line while S(0) strongly deviates on the excitation diagram, with much higher values of the column density. The strong emission from the 1-0 S(0) line in region 10 is already visible in raw SPIFFI data and thus a systematic error seems very unlikely. An pollution by a line of different origin (stellar, atmospheric, etc.) could introduce a spurious enhancement of the line. However S(0) is very well fitted by the same velocity and width as S(1), and no other candidate has been identified. It is thus very unlikely that the observed profile does not correspond to a H_2 line.

To better understand the observed excitation diagram a collaboration with experts of H_2 in PDRs (J. Le Bourlot, F. Le Petit and E. Bron, LUTH, Observatoire de Paris) has been started. The model they have developed since several years computes the structure of ISM clouds illuminated by UV radiation, solving numerically the radiative transfer. The "Meudon PDR code"[1] (Le Bourlot et al. 1993; Le Petit et al. 2006) they developed can in particular reproduce the H_2 conditions in PDRs.

The shape of the excitation diagram is well reproduced by a UV-driven excitation, especially the bump of the 1-0 S(0) line. However, one notes that the same model predicts also an enhancement of the para 1-0 S(2) line, albeit less pronounced, that is not observed (c.f.

[1] http://pdr.obspm.fr/PDRcode.html

Fig 4.13). The specific mechanism that enhances the S(0) line (and not S(2)) is still unclear and is part of the perspectives of this work.

The problem of this model is also that it fails to reproduce the observed intensities by a factor of 30. In Fig. 4.14, several PDR simulations, for a grid of gas pressure and UV-radiation values, are plotted. I thank E. Bron who ran these simulations and computed the excitation diagrams expected for various pairs of pressure and incident radiation. The UV-field required to reach the observed values would heat the gas to the limit where it is sufficiently hot for collisions to become efficient and the excitation diagram takes a flatter form. Either the relative distribution or the absolute values of the column densities can be reproduced but not at the same time.

This analysis is still at a preliminary stage. The heating mechanism plays a key role for the model and has to be carefully considered. Moreover, the code has never been tested before in extreme conditions such as those of the Galactic Center. The UV radiation field is around $10^{6.5}$ time the ISRF (Lutz 1999) which is at the edge of the "Meudon PDR code" grid of values. In any case different mechanisms, or the combination of several mechanisms, must be considered.

For instance, zone 10 happens to be located in a very peculiar region in the central parsec. This region is at the border of the Minicavity. This feature is believed to originate in the interaction between a strong stellar wind and the dense ISM (Lutz et al. 1993), or from a jet coming from Sgr A* (Eckart et al. 1992). The SPIFFI spectral range covers also a few ionized lines. In Annex B the regularized 3D-fitting is applied to Fe II, Fe III and Brγ to obtain maps of the Gaussian parameters, as it has been done in the previous Chapter 3 with H_2 line. Interestingly, Fe II shows a pronounced maximum in the flux map at the same location as S(0) (zone 10). This is another indication that the observed enhancement of S(0) could be associated with peculiar conditions in this area, rather than a systematic error. A possible explanation of the discrepancy between the prediction and the observations might be found in the time scale of the H_2 formation and destruction process. The tentative explanation proposed is the following:

a) in the Central Cavity, there is a high density of UV photons and cosmic rays;

b) in such an energetic region, H_2 molecules are more rapidly destroyed and have thus a shorter mean-life during which thermalization cannot fully occur;

c) we would thus mostly observe recently formed H_2 molecules that may form mainly as the para isomer and did not yet reach the equilibrium where OPR=3 ;

d) in addition it is possible for molecular hydrogen to be formed in a state where peculiar energetic states are favored, such as S(0).

Indeed, with increasing depth of the cloud, the dominant mechanism passes from photodissociation to H_2 formation, while the FUV is attenuated. A H_2 formation happens every 9 FUV-pumping (Sternberg & Neufeld 1999) but it can dominate the excitation of a specific state $[v, j]$ if this one is not directly populated by FUV-pumping. Of course, this hypothesis would require a realistic modeling to be supported in a more precise way and a work has been started in this direction.

In general, the Central Cavity environment is complex and many mechanisms may contribute to excite the gas. Probably, different interpretations apply to the Northern Arm cloud emission, the GCIRS 7 – Bar emission and the Minicavity emission. A model involving UV-pumping seems very promising to explain the behavior of some of the excitation diagrams such as the Northern Arm cloud (zone 6), but fails to reproduce the observed intensities. This excitation mechanism does not explain as well the peculiar behavior of the Minicavity emission. The GCIRS 7 – Bar emission might present a different excitation and physical conditions which possibly reveals an OPR truly different from 3. A more detailed study of this region will be the object of a future research.

This preliminary analysis shows that, in a volume as small as the zone inside the rim of the CND, there are different areas, each featuring some very peculiar conditions, which can be attained only in an extreme environment such as the central parsec. This argument supports the idea that the Central Cavity emission comes from the central parsec itself and not from further in the background.

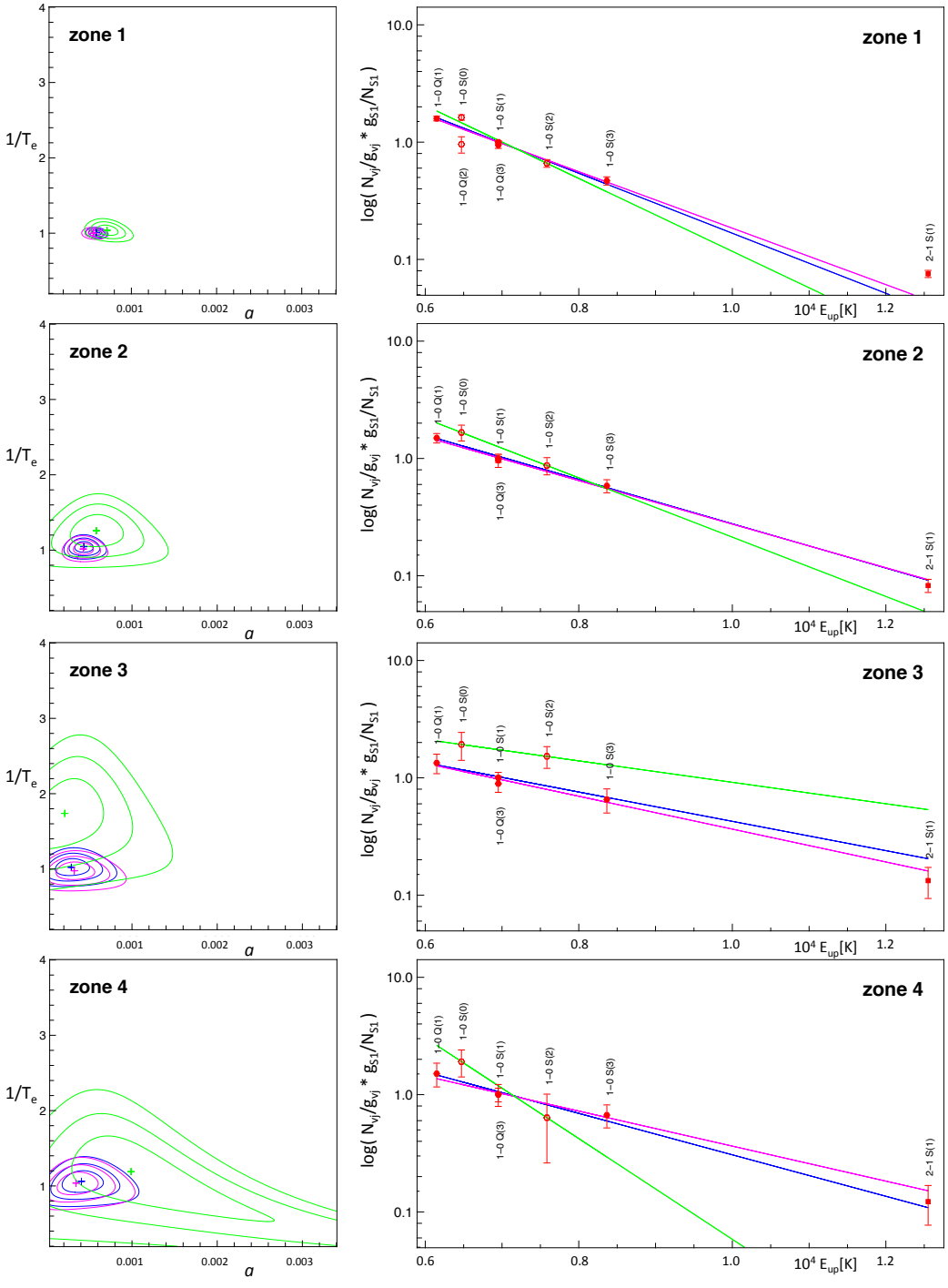

Figure 4.7: *Left:* χ^2 contours maps in the $[a,\ 1/T_e]$-plane of 1,2 and 3 σ for all-lines (*blue*), ortho-lines (*magenta*) and para-lines models (*green*). The cross indicates the minimum χ^2. *Right:* thermal model corresponding to each fit.

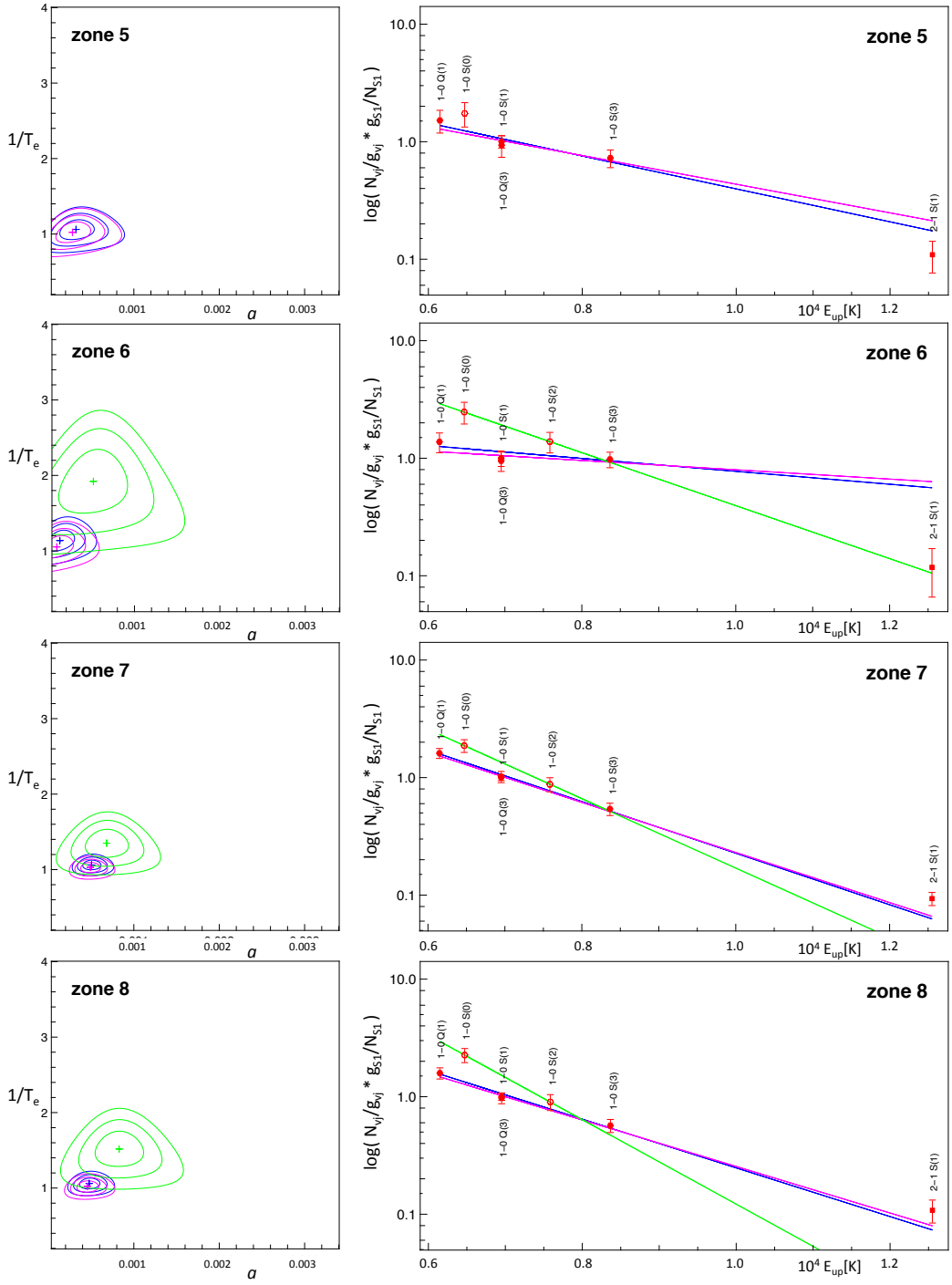

Figure 4.8: Follow from Fig. 4.7.

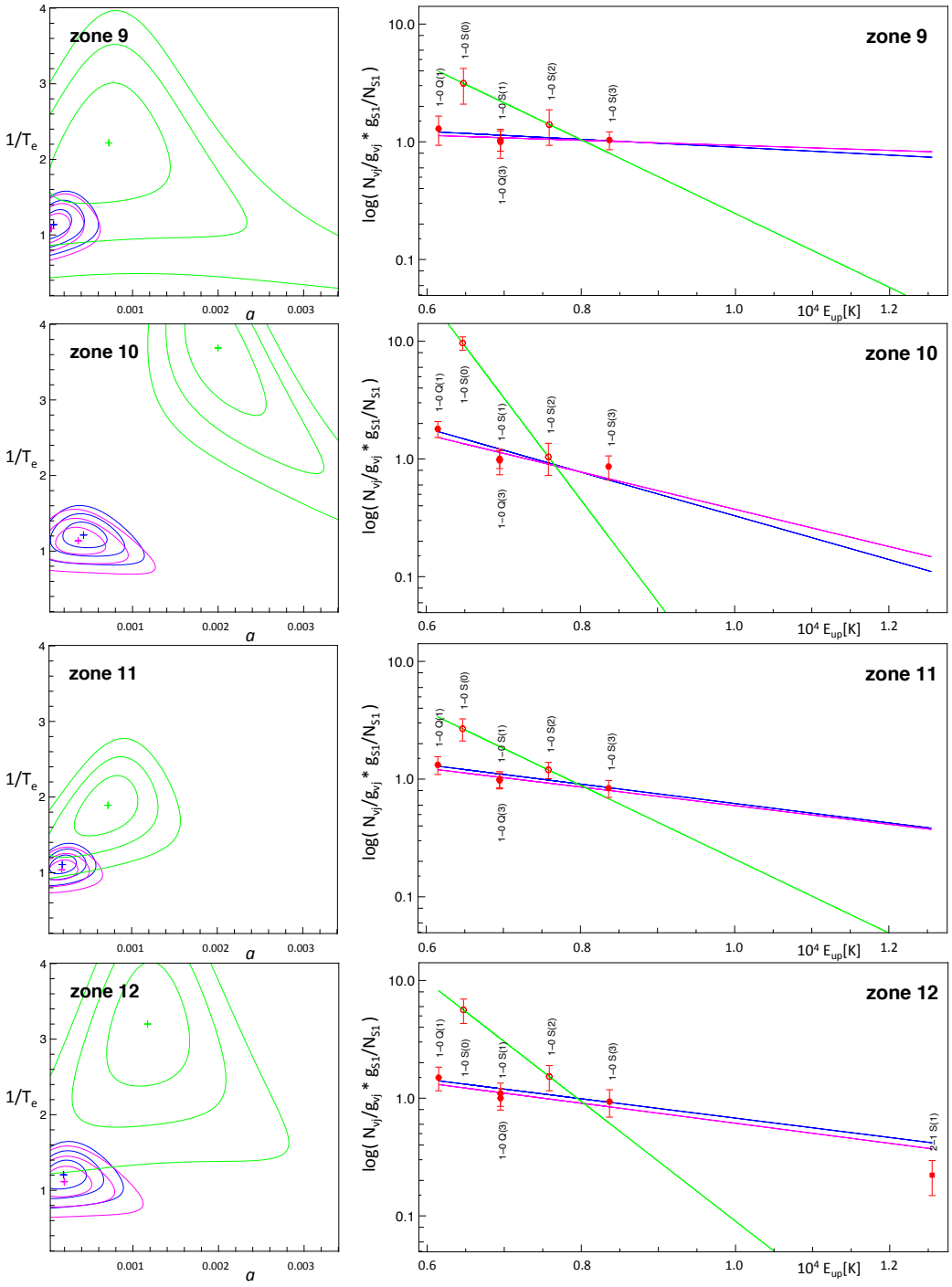

Figure 4.9: Follow from Fig. 4.7.

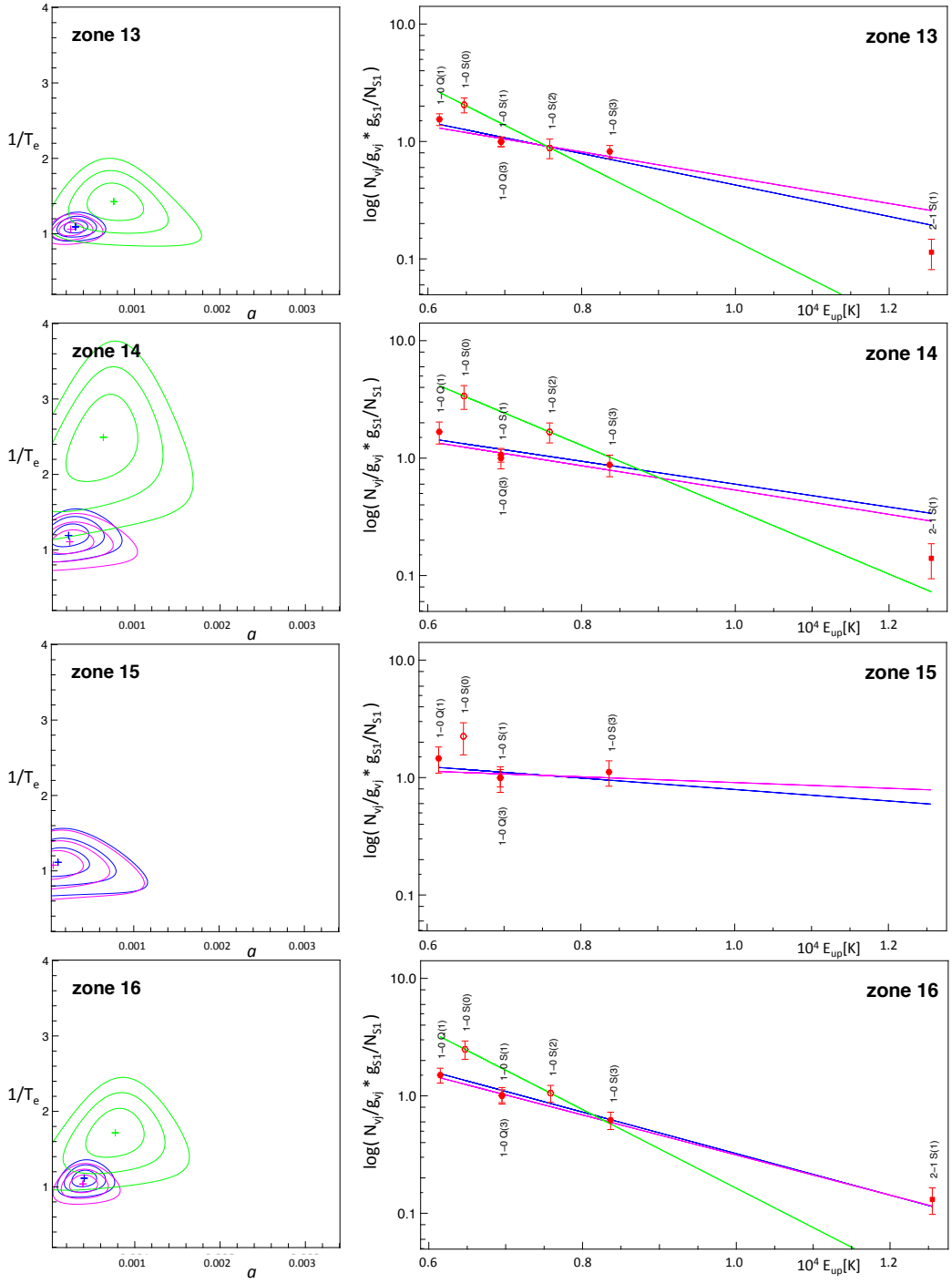

Figure 4.10: Follow from Fig. 4.7.

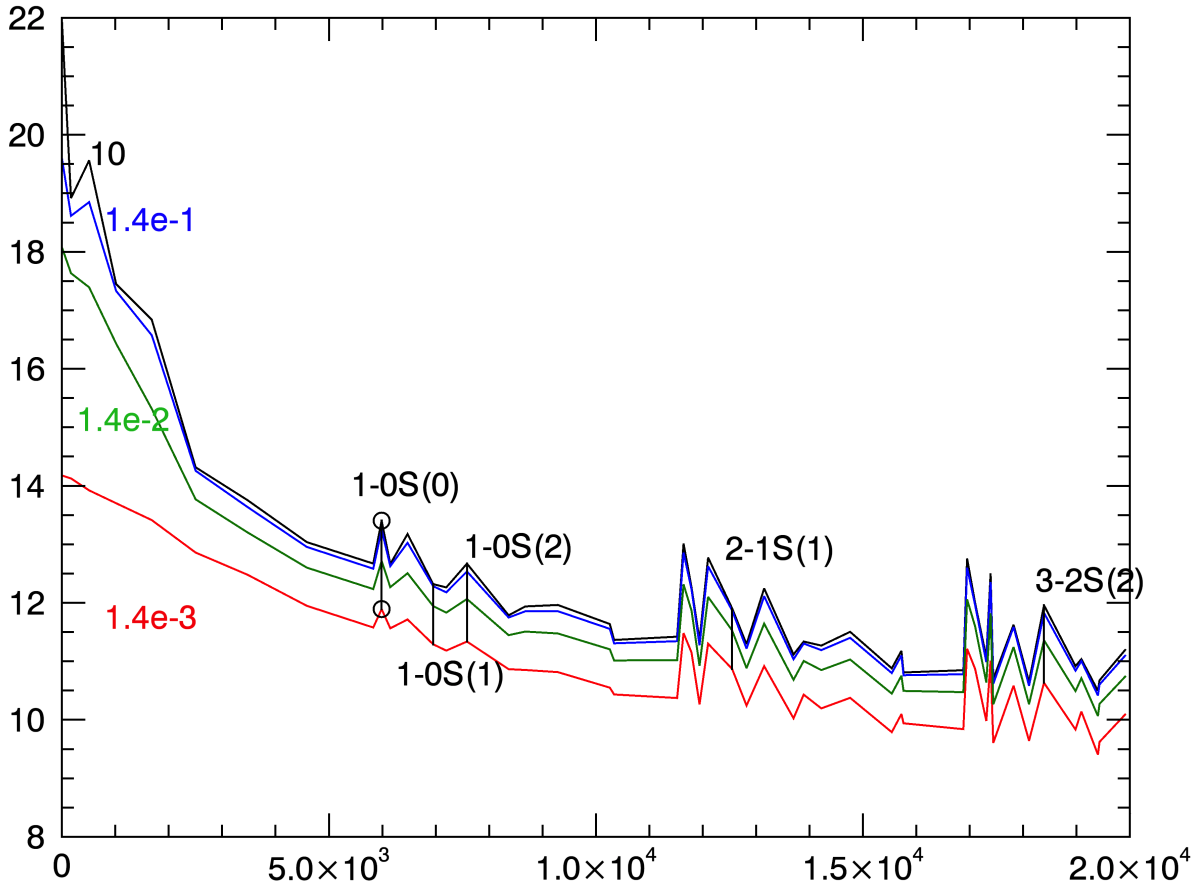

Figure 4.11: Excitation diagram illustrating results of simulations of standard conditions in a PDR (J. Le Bourlot private communication). It shows that almost all the excited gas, except the pure rotational levels (v=0, j=0,1,2), is located within Av = 0.14, corresponding to 1/70 of the volume. 30% of the gas is located within Av = 0.014, i.e. into 1/700 of the volume.

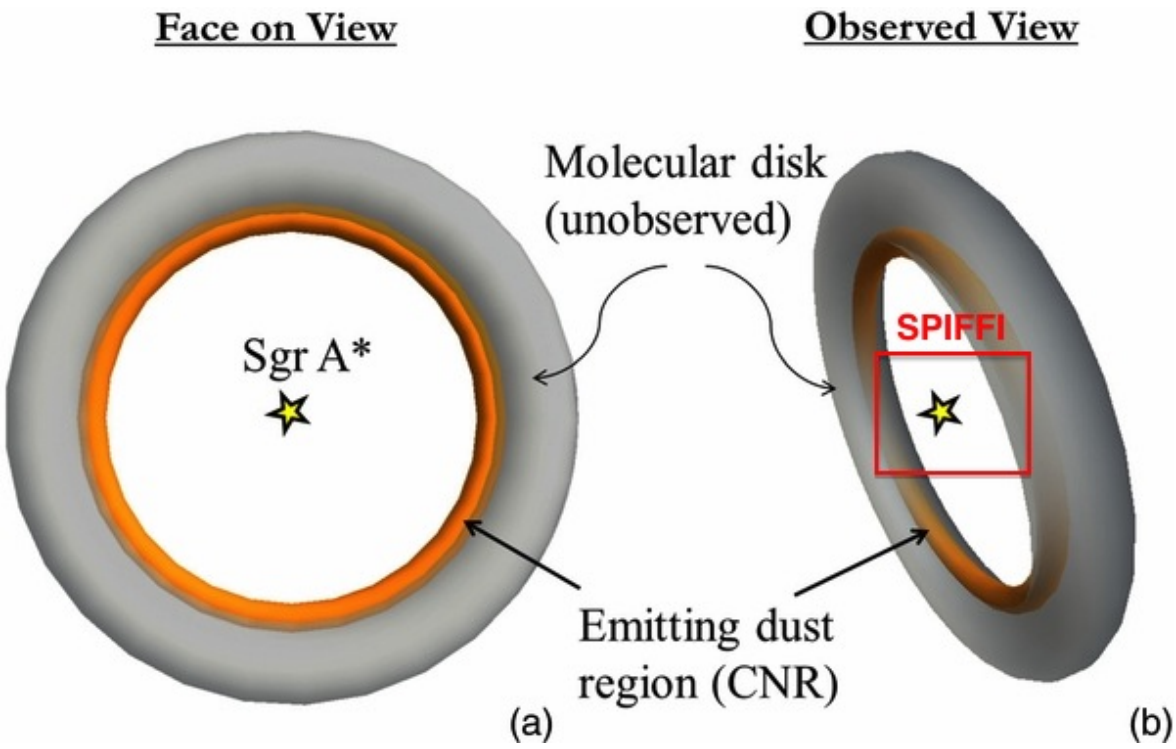

Figure 4.12: Representation of the CND inclination with respect to the line of sight. In the SPIFFI field of view only the northwestern and southeastern part of the ring are visible. The northwestern side lies closer to the observer and its observable surface, in this simplified picture, seems less exposed to the central UV radiation than the observable southeastern part corresponding to the inner rim of the CND. Credit: Lau et al. (2013).

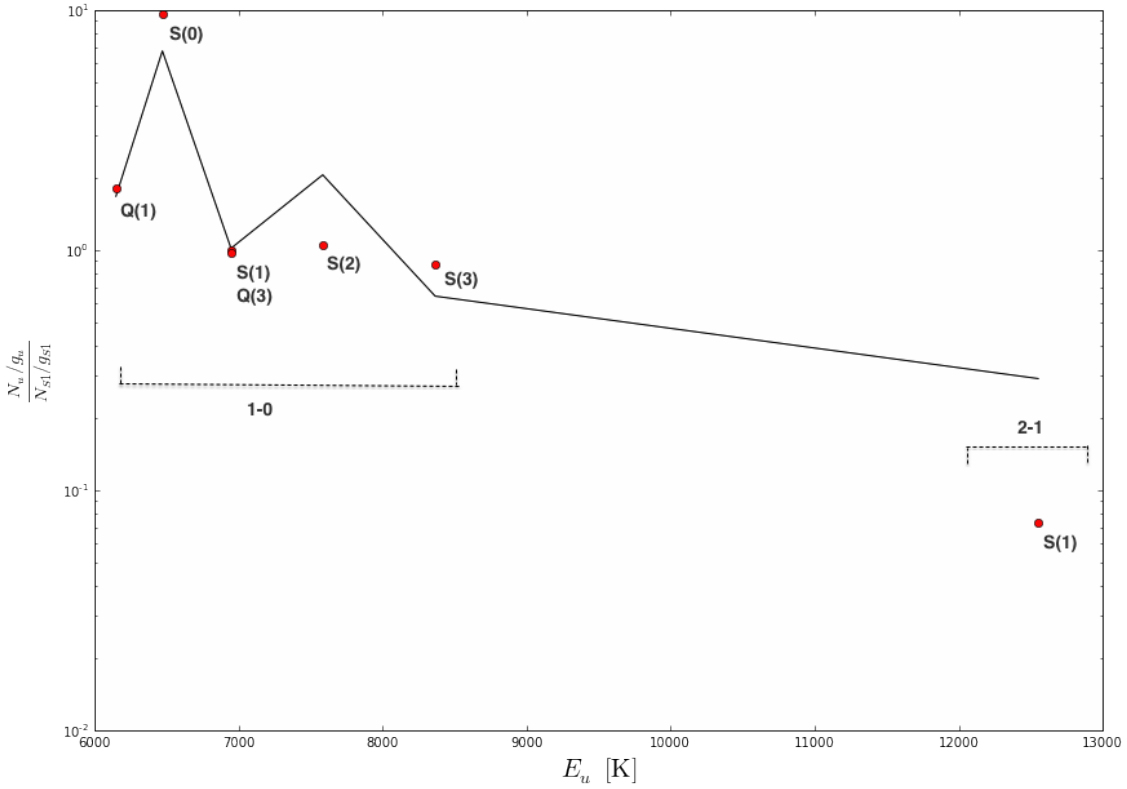

Figure 4.13: Comparison between the column densities of zones 10 (red dots) and the PDR model for a gas pressure of 10^3 K cm^{-3} and UV radiation of 10^5 times the ISRF (solid black line). Credits: Emeric Bron.

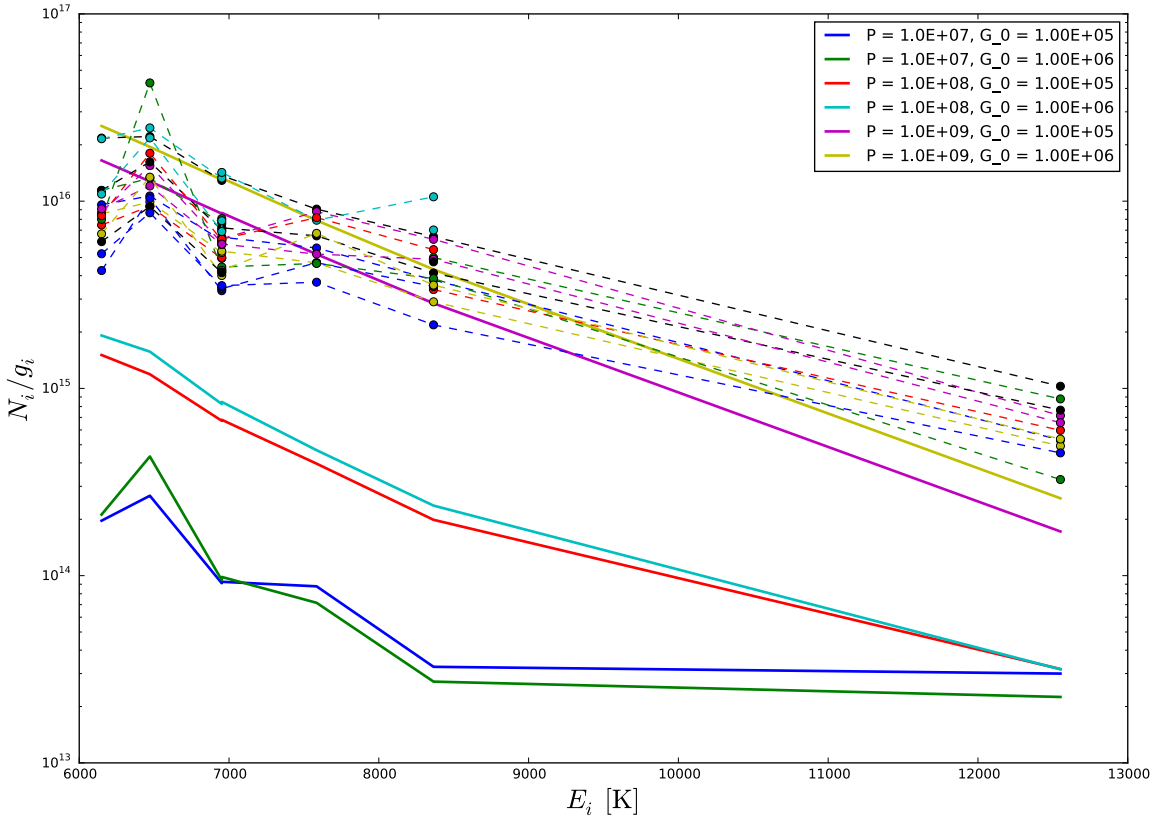

Figure 4.14: The excitation diagrams for each zone (points and dashed lines of different colours) are displayed on the same plot and compared to several models (solid lines of different colours) predicted by the "Meudon PDR code" for different pressure P (K cm^{-3}) and incident radiation G_0 (in terms of ISRF). The column densities are not normalized to show that the absolute column densities are difficult to reproduce conserving the right relative intensities. Credits: Emeric Bron.

Chapter 5

Conclusions and perspectives

The study of the ISM in the central parsec of the Galaxy interested me to contribute to disentangling the structure of this complex environment, whose stellar population, dynamics and energetics are governed ultimately by the presence of a black hole of 4 10^6 $M_\odot$. On the other hand the central parsec presents an unique chance to investigate the ISM behavior in such an energetic environment.

In particular, I focused on the inner part of the CND and the Central Cavity it encloses, where the ionized Minispiral lies. The aim of this work was to characterize the distribution and dynamics of the molecular phase of the ISM, and investigate whether the observed emission is actually formed in this region of strong radiation field. To this end, I have applied a novel regularized 3D-fitting method to extract several H_2 emission lines from a spectro-imaging dataset covering the entire central parsec.

The analysis of several NIR emission lines of the molecular hydrogen through spectro-imaging at good angular resolution allowed to identify and characterize H_2 emission arising from the entire central parsec region. The analysis is divided into two main parts:

- In the first part I studied the gas distribution and dynamics: thanks to the new regularized 3D-fitting method of data analysis, I was able to probe the morphology and dynamics of the ortho 1-0 S(1), S(3), Q(1), Q(3) lines and the para 1-0 S(0), providing high-resolution maps of the fit parameters – flux, velocity and width – for each line. This required a careful tuning of the hyper-parameters to be injected in the method. The obtained results are checked via the comparison to a more classical 1D fit. A separate procedure is developed to estimate the statistical uncertainties due to the regularized 3D-fitting method, involving the creation of four independent cubes to evaluate the significance of the observed spatial gradients. For the first time, the extinction map is computed directly from the comparison of two of those lines S(1) and Q(3) and the interesting outcomes are modeled.

- In the second part several peculiar regions are selected to include the 1-0 S(2), Q(2) and 2-1 S(1) lines in a more classical 1D part of the analysis. On these zones a simultaneous fit of all detectable lines leads to excitation diagrams allowing to characterize the gas excitation.

5.1 Conclusions

The new regularized 3D-fitting method allowed me to detect H_2 emission all over the central parsec. Both from the morphological and dynamical points of view, there are several components identified in this emission with distinct physical properties.

CND: In the part of the CND covered by our dataset, the observed H_2 emission is intense in all lines, but its width is weaker than elsewhere in the analyzed field. This suggests that the emission is confined in a thinner emitting region. The excitation diagrams of regions associated with the CND show energy levels populations compatible with a thermalized distribution and lead to very high excitation temperatures (1 700–3 000 K) and very low masses for individual clouds (0.07 $M_\odot$) when compared to previous measurements obtained through other tracers ($>10^3$ $M_\odot$ at 400 K, Christopher et al. 2005; Genzel et al. 1985). However, H_2 emission is only detectable when highly excited. Therefore, observing NIR lines of H_2 implies selectively observing only the most excited component, missing the bulk of the gas which is not sufficiently excited to be detected. Indeed the observed emission represents only a small fraction of the total volume: the very thin layer of hot H_2, at the surface of denser clouds, which is sufficiently excited by shocks or UV radiation to be detectable. This result is similar to findings in the Orion nebula (Scoville et al. 1982) and the Crab nebula (Loh et al. 2011). The high dust opacity also plays a role in the small fraction detected. The portion of the CND which is the closest to the observer – in the northwestern part of the field – is compatible with a shock-driven excitation, as proposed by previous publications. These shocks are either due to clump–clump collisions at their interfaces (Yusef-Zadeh et al. 2001) or to the strong stellar winds coming from the central stellar cluster (Gatley et al. 1984). The emission arising from the opposite, southeastern corner of the field likely arises from the collisional de-excitation of UV-pumped molecules.

Central Cavity: H_2 emission is detected everywhere in the central region encircled by the CND, in accordance with findings by Yusef-Zadeh et al. (2001) on the 1-0 S(1) line. I have detected the same emission in several H_2 lines. The gas in the Central Cavity is not thermalized and the observed emission lines have larger widths than in the CND. Three distinct regimes are identified.

- There is a strong width enhancement in the region East of the Northern Arm of the Minispiral (the Northern Arm Cloud). This increase in the line width is the signature of turbulence deep inside this cloud, integrated over the geometrical thickness of the cloud. This cloud has likely been drawn to the centre by tidal forces that have also probably stretched it (Ekers et al. 1983). Although this should be backed up by a physical modeling, it is reasonable to assume that this stretching has lowered the filling factor of the small-scale clumps inside this cloud. This allows the incoming UV radiation to reach far inside, with moderate attenuation, and the outgoing IR emission to escape, with moderate additional extinction. The CND is also very clumpy but probably has a higher filling factor. This explains why in its case the emission more likely arises from the surface of the structure. Inside the Northern Arm Cloud the gas can probably survive dissociation, since the UV radiation is attenuated behind the ionization front. Another explanation, suggestied by the presence of Fe II in the depth of the Northern Arm Cloud (Fig. B.1 and B.2), is turbulent shock emission presumably caused by tidal shearing. The observation of this protected H_2 confirms the previous works inferring that the Minispiral Northern Arm is the ionized border of a more extended cloud (Davidson et al. 1992; Telesco et al. 1996). Therefore the nature of the cloud associated with the

Minispiral and the CND is very alike, but the density of the material and the strength of the UV field differ. The gas observed in this area is, as for the CND, only the most excited, small, fraction.

- The rest of the Central Cavity is usually perceived by infra-red astronomers as being empty of any ISM material. However, our findings show that this volume contains very hot, non-thermalized, likely short-lived H_2. These observations and the extinction map study imply that a population of dust grains (presumably with very low density) occupy this volume. H_2 is formed quite naturally at the surface of these grains, and is destroyed very rapidly by the strong UV field pervading in the region. X-ray data have already demonstrated that this "empty" volume is actually filled with a hot plasma (Muno et al. 2003). This matter can come from the mass loss of stars showed by Cuadra et al. (2005). The central cavity is therefore far from being empty. The region between the Bar and GCIRS 7 shows both a strong emission and extinction which can be interpreted as produced in the shells of the numerous evolved stars, located in this particular area: this could be a peculiar case where the H_2 in these shells is heated from the inside by the central star.

- A very peculiar zone is detected at the border of the Minicavity. Here I observed a very strong enhancement of 1-0 S(0) with respect to the other lines. This line unambiguously deviates from the alignment of the other lines on the excitation diagram. A very strong enhancement of this line is directly visible in its flux map, obtained with the regularized 3D-fit as well as in the raw data. In the Minicavity region, several processes may occur and H_2 has a short mean-life. Tentatively, we suggest that the quick processes of destruction and formation of new, very hot, H_2 molecules could favor S(0) with respect to the others lines. This enhancement is also strongly correlated with a Fe II emission peak (Fig. B.1 and B.2). In this particular zone some very peculiar conditions apply. They could be connected, for instance, with very strong shocks, with the presence of a young star or some other local phenomenon.

Thanks to the large number of lines available and to the capabilities of the regularized 3D-fitting method, I derived the extinction map from the ratio of two of the observed H_2 lines directly. The computed extinction appears locally correlated with the flux maps in several distinct regions. The correlation can seem surprising, but we propose two models that successfully reproduce the observation. In these models the correlation is due to the fact that the local emitting H_2 is mixed everywhere with dust, either in a thin emitting shell at the surface of extended clumps or on small-scale clumps where the emission from one clump is obscured by the dust of another clump. This has the effect of enhancing both the emission and the extinction while integrating over the line of sight. In both models, the densities required are very high. The fact of observing correlation only locally is due to a second component of the extinction as a result of the foreground material. Both effects are important to probe: from one side the local structure of the medium and from the other side the foreground extinction to which our specific emitter is subjected.

5.2 Perspectives

Thanks to the unique combination of sensitivity, large spectral coverage, good spectral and angular resolution as well as the new regularized 3D-fitting data analysis method, the present work brings new important elements on the distribution and physical conditions of the molecular gas and dust both in the CND and in the Central Cavity. Nevertheless some points would need further investigation.

For instance, the analysis of the extinction map derived here leads to the conclusion that dust and H_2 are present everywhere. Actually the existence of very hot plasma in this region has already been pointed out by X-ray observations (Muno et al. 2003). One possible interpretation, backed up by simulations by Cuadra et al. (2005), is that the combined wind from the many mass-loosing stars in the central parsec provide the material and energy to build up this plasma, as well the dust grains that are necessary to explain our observations. This hypothesis would need a more detailed study.

The excitation of the molecular gas in the central cavity has to be more deeply investigated, especially in the region where the S(0) enhancement is the strongest and correlated to Fe II. The models produced with the Meudon PDR code can reproduce either the observed intensities or the excitation diagram distribution, but fail to reproduce both at once. Some further investigation on the excitation mechanism, especially on dust heating, is necessary. Together with the datacube used in this work, another SPIFFI data cube of the central $10''$ was acquired at higher spatial and spectral resolution. This is a good starting point for a more detailed analysis of this area, allowing to better separate the contribution of the studied lines (including Fe II) from polluting features and to isolate in a better way the stars on the field. Afterwards it would be interesting to expand this analysis to the other regions of the Central Cavity where this enhancement is observed at a lower level. This can lead to important information on the local conditions of the medium filling the Central Cavity, in particular heating of dust grains and the H_2 formation processes in such an extreme environment. This analysis has already been started as part of the collaboration with J. Le Bourlot, F. Le Petit and E. Bron.

The SPIFFI spectral range also offers the possibility to expand the analysis to other lines with the regularized 3D-fitting. In particular comparing in details the H_2 and ionized gas maps. This has not been done in the present work due to time constraints, even though maps of Brγ, Fe II and Fe III obtained with the regularized 3D-fitting are provided in Appendix B. The regularized 3D-fit could also be applied to other Fe lines to provide a more detailed description on this emission.

On a longer term, it would be interesting to compute a global 3D radiative transfer model for the whole central parsec region. In particular taking into account the position of stars and giving a more comprehensive look on the Central Cavity medium and its conditions. This would help understanding the effect of these stars on the surrounding medium in a region dominated by the central supermassive black hole.

Moreover, the type of analysis that we have developed here can be applied to other galactic nuclei or other PDRs. This can probe the distribution and excitation of H_2 (or other molecules) as well as of the dust (through the powerful S(1)-Q(3) ratio) and the ionized lines (including the one tracing very hard radiation, e.g. Fe II, Fe III) in spatially extended regions. The regularized 3D-fitting procedure is indeed very well suited to analyze any spectro-imaging

datacube, especially when the signal-to-noise ratio per pixel is of the order of 1 or slightly below, and there is a need to conserve spatial resolution.

Appendix A

Estimation of the line absorption coefficient in radiative excitation

For a transition from the upper (i) to the lower (j) level the absorption coefficient α_{ji} can be calculated as:

$$\alpha_{ji} = \frac{h\ \nu_{ji}}{4\pi}\ n_j\ B_{ji}\ \phi_{ji} \tag{A.1}$$

where ν_{ji} is the line frequency and n_j the column density (in m^{-3}). The Einstein coefficient B_{ji} is given by:

$$B_{ji} = B_{ij}\frac{g_i}{g_j} = A_{ij}\frac{c^2}{2h\nu^3}\frac{g_i}{g_j} \tag{A.2}$$

ϕ_{ji} is the line profile, with $\int \phi_{ji}\ d\nu = 1$, and it is given by:

$$\phi_{ij} = \frac{1}{\Delta\nu} = \frac{c}{\nu\Delta v} = \frac{\lambda_{ij}}{\Delta v} \tag{A.3}$$

where λ_{ij} is the line wavelength and Δv the line width. One can thus write:

$$\alpha_{ij} = n_j\frac{\lambda_{ij}^3}{8\pi}A_{ij}\frac{g_i}{g_j}\frac{1}{\Delta v} \tag{A.4}$$

The column density can be expressed as $n_j = n_{H_2}\cdot f_j$, where f_j is the relative population of the j-level and is given by:

$$f_j = \frac{e^{-E_j/kT}}{\sum e^{-E_k/kT}} \tag{A.5}$$

For 1-0 S(1) ($J = 3 \rightarrow 1$, $v = 1 \rightarrow 0$) at $\lambda = 2.12$ μm: $A_{ij} = 3.48\ 10^{-7}$ s^{-1}, $g_i = 21$, $g_j = 9$ and $E_j = 6.952\ 10^3$ K.

For a PDR such as the central parsec $\Delta v \sim 100$ km s^{-1} (Sect. 3.1.2), $n_{H_2} = 10^{-5}$ cm^{-3} (Smith & Wardle 2014) and T=1 200 K as estimated for Orion in Beckwith et al. (1983). Therefore one finds $\alpha_{ij} \sim 2.7\ 10^{-22}$ m^{-1}.

Since $\tau_{ij} = \alpha_{ij}\cdot L$ and typical cloud has a diameter $L = 0.2$ pc (Christopher et al. 2005) one finds $\tau_{ij} = 1.6\ 10^{-6}$. This value has to be compared to $A_V = n_{H_2}\cdot L/1.8\ 10^{21}$ (Predehl & Schmitt 1995). For $n_{H_2} = 10^5$ cm^{-3} it gives $\tau_{ij}/A_V = 5\ 10^{-8}$ which translates to $\tau_{ij}/A_K \sim 5\ 10^{-7}$. Therefore, the H_2 line is optically thin and there is no self-shielding. The extinction is thus completely due to the dust component of clouds.

Appendix B

Regularized 3D-fit on recombination lines

In addition to the H_2 lines (discussed in the main body), we also started to analyze a few recombination lines: Fe II, Fe III and Brγ. The regularized 3D-fitting has been applied to these lines, leading to maps of flux, radial velocity and width for each. We calibrated every flux map with the procedure described in Chapter 2, Sect. 2.2.

Due to time constraints these maps have not been included in the discussion, but their parameter maps are reported below for the sake of completeness (Fig. B.1, Fig. B.3 and Fig. B.4) together with a brief discussion. Future research will focus on studying these lines in details, comparing the results with those obtained for H_2 and previous findings from the literature.

Fe II: Fe II (at 1.643 μm) emission has been previously identified by Depoy (1992) in the central parsec region. They have identified a peak of emission coming from a region 10″ South of GCIRS 7 and an overall distribution similar to the Brγ distribution. The flux map obtained here (Fig. B.1) confirms the strong peak of emission, well identified in the map, as a strong enhancement $\sim 5''$ South and $\sim 1-2''$ East of Sgr A*. Interestingly, Fig. B.2 shows that it is the same location where the 1-0 S(0) H_2 line shows a strong enhancement – higher than all the other H_2 lines detected in this work – as well. This enhancement has been tentatively associated with the quick processes of formation and destruction of H_2 molecules. The detection of Fe II at the exact same location is one more indication that in this zone some very peculiar conditions must apply. Depoy (1992) point out that Fe II is often indicative of very strong shocks(McKee et al. 1984) and it is often mixed with large amounts of neutral hydrogen. This likely is a region of strong shock, since it is about the location where the Eastern Arm enters in collision with the Northern Arm (Paumard et al. 2004). A young star could also be located in this region and contribute to the observed conditions. This interesting correlation surely can help putting constraints on physical conditions in this peculiar zone. In the rest of the field of view the Fe II emission is well correlated with the Eastern Arm and the Bar of the Minispiral. Concerning the Northern Arm, the Fe II seems well correlated with the neutral Northern Arm Cloud more than with its ionized border.

Fe III: Fe III (at 2.2178 μm) has been previously analyzed by Lutz et al. (1993). The map we obtained obtained shows the same U-shaped feature observed by Lutz et al. (1993) that identifies the Minicavity. Lutz et al. (1993) described it as an expanding bubble, driven by winds originating either in jet from Sgr A* or fro He I stars. In this picture the Fe III originates in the shocks at the interface between the expanding bubble and the surrounding medium. The

velocity map obtained here shows a motion very close to the one obtained for Brγ, indicating that it mainly follows the orbital motion of the Northern Arm.

Brγ Brγ recombination line at 2.166 μm traces the ionized gas of the Minispiral. In the flux map obtained through the regularized 3D-fitting the ionized gas seems to partially extend on the Northern Arm Cloud, confirming what previously was put in evidence in Paumard et al. (2004). The line width remains narrow on the entire structure coherently with an emission coming from a geometrically thin region: the surface of the more extended clouds illuminated by the central UV radiation. The Eastern Arm shows a positive velocity, while the Bars seems to be moving towards the observer. Refer to Paumard et al. (2004) for a detailed, high spectral resolution study of the Brγ emission.

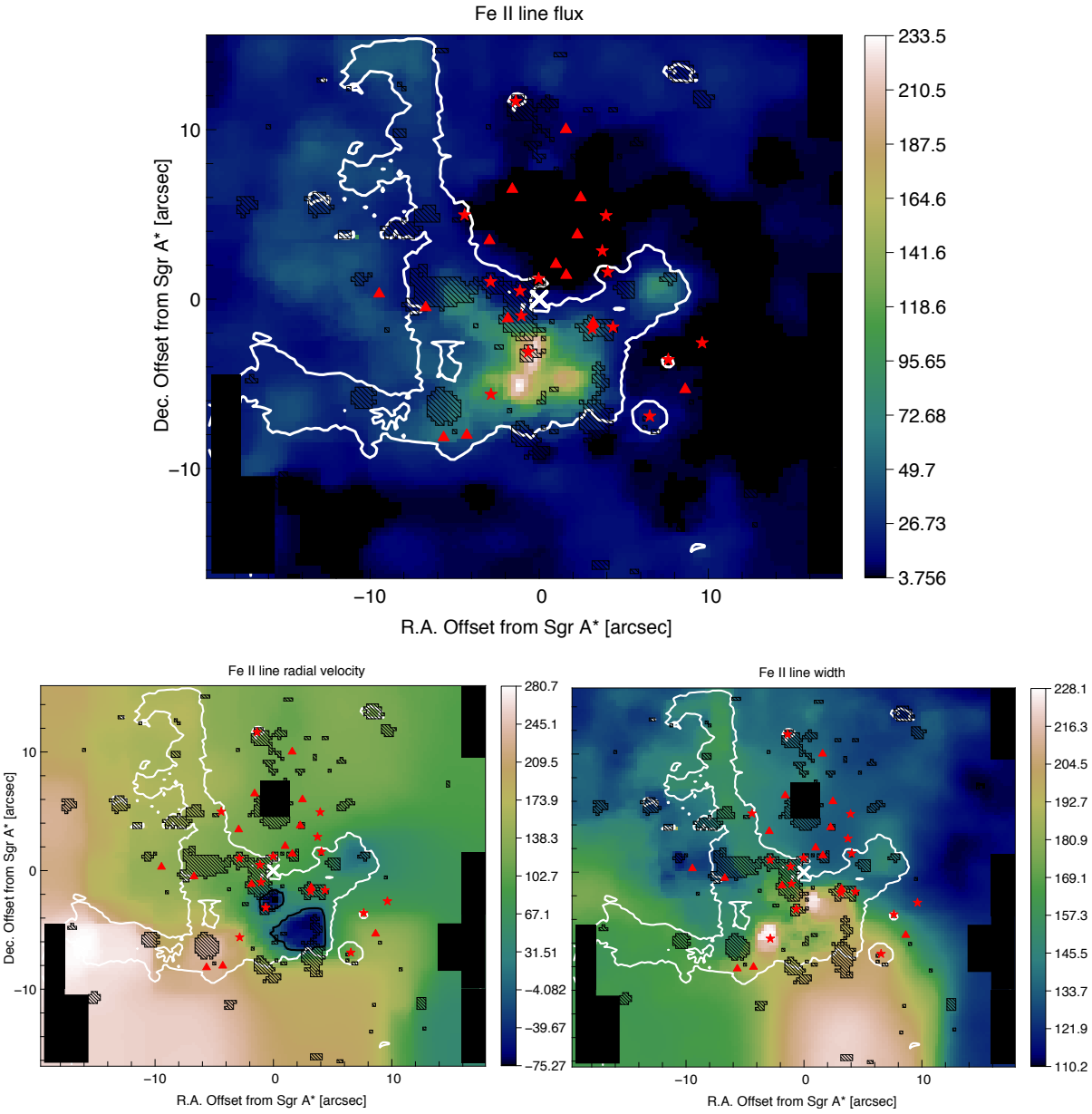

Figure B.1: *Top:* Flux map of the Fe II line in 10^{-19} W m^{-2} arcsec^{-2}. *Bottom left:* velocity map is in km s^{-1}. The solid black line indicates points at zero velocity. Negative velocities (*blue*) correspond to approaching emissions. *Bottom right:* width map in km s^{-1}. Symbols as in Fig. 3.1, Chapter 3.

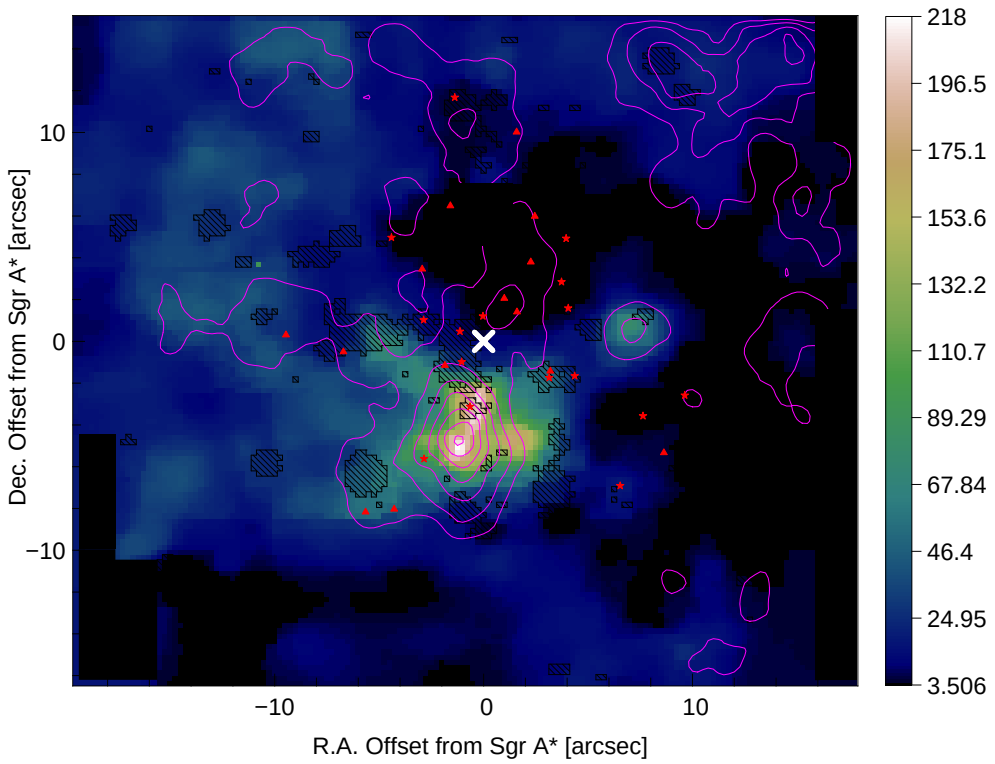

Figure B.2: 1-0 S(0) line flux contours (starting at 12 10^{-19} W m^{-2} arcsec^{-2}, with steps of 4 10^{-19} W m^{-2} arcsec^{-2}) are superimposed on Fe II line flux map (in 10^{-19} W m^{-2} arcsec^{-2}). The strong enhancement observed in 1-0 S(0) flux map corresponds to the Fe II line flux maximum. Symbols as in Fig. 3.1, Chapter 3.

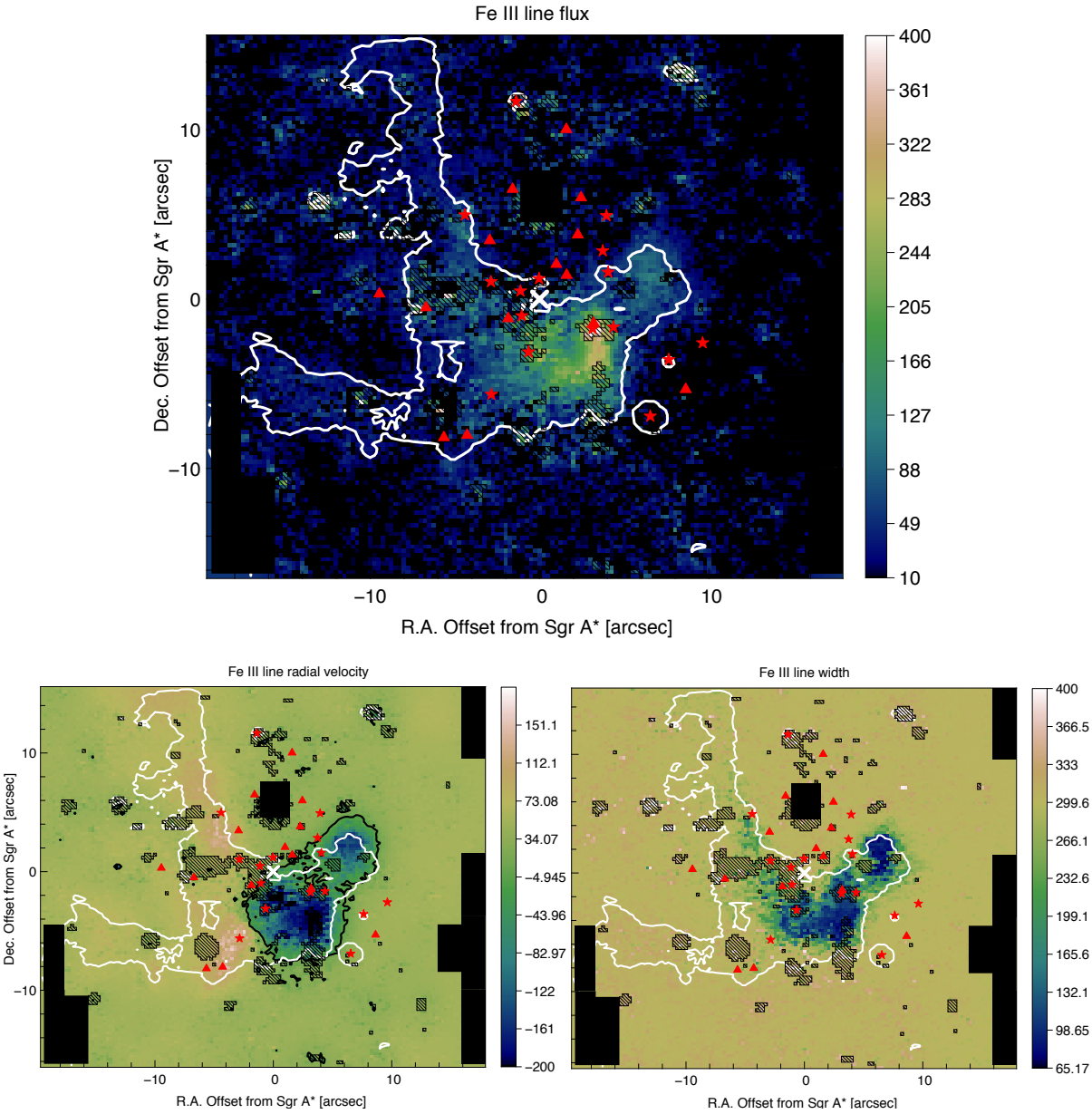

Figure B.3: *Top:* Flux map of the Fe III line in 10^{-19} W m^{-2} arcsec^{-2}. *Bottom left:* velocity map is in km s^{-1}. The solid black line indicates points at zero velocity. Negative velocities (*blue*) correspond to approaching emission. *Bottom right:* width map in km s^{-1}. Symbols as in Fig. 3.1, Chapter 3.

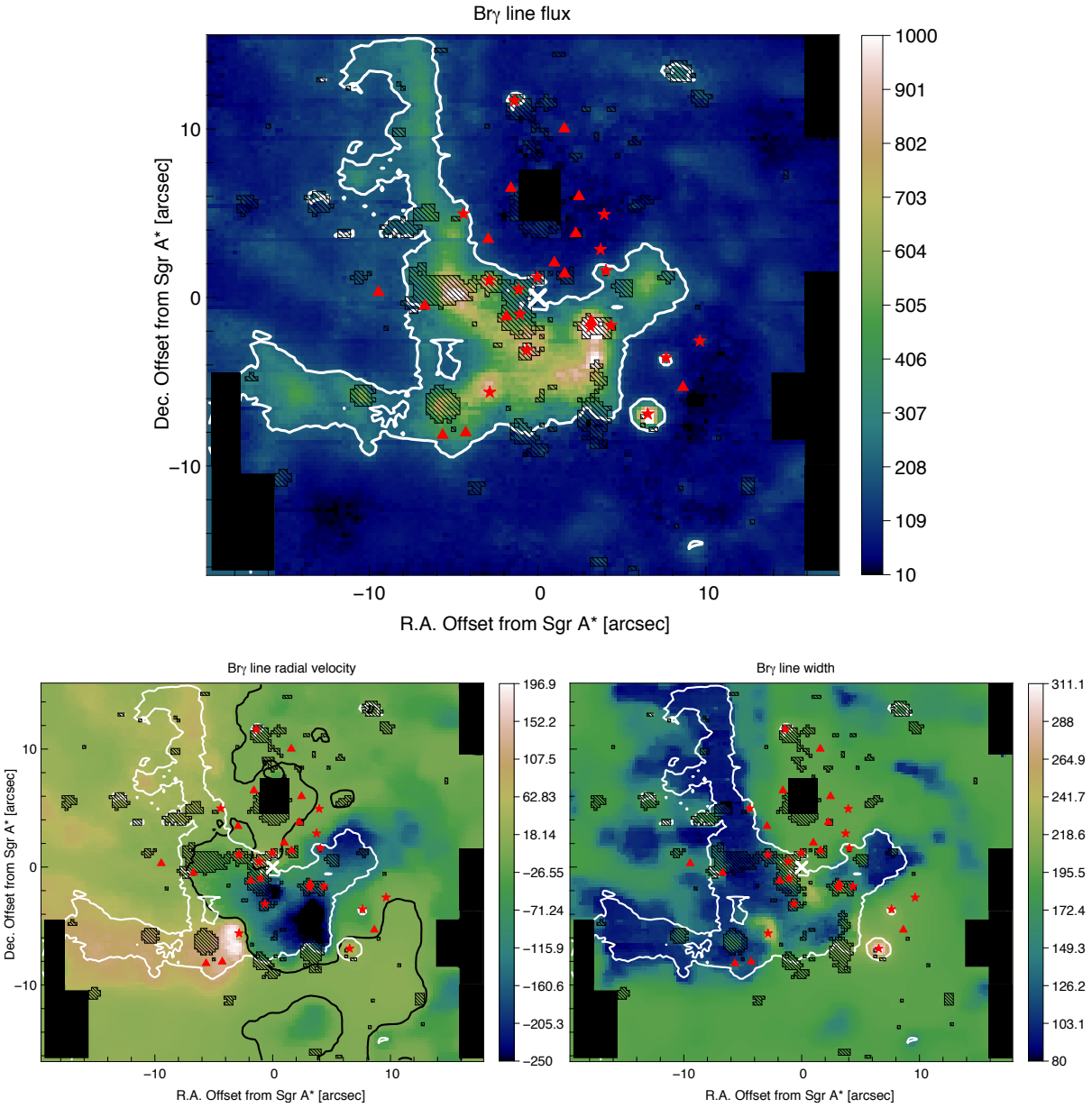

Figure B.4: *Top:* Flux map of the Brγ line in 10^{-19} W m^{-2} arcsec^{-2}. *Bottom left:* velocity map is in km s^{-1}. The solid black line indicates points at zero velocity. Negative velocities (*blue*) correspond to approaching emissions. *Bottom right:* width map in km s^{-1}. Symbols as in Fig. 3.1, Chapter 3.

Appendix C

Study of the molecular gas in the central parsec of the Galaxy through regularized 3D spectroscopy

---

The Galactic Center: Feeding and Feedback in a Normal Galactic Nucleus
Proceedings IAU Symposium No. 303

The Galactic Center: Feeding and Feedback in a Normal Galactic Nucleus
Proceedings IAU Symposium No. 303,
A.C. Editor, B.D. Editor & C.E. Editor, eds.

DOI: 00.0000/X000000000000000X

Study of the molecular gas in the central parsec of the Galaxy through regularized 3D spectroscopy

A. Ciurlo[1], T. Paumard[1], D. Rouan[1] and Y. Clénet[1]

[1]LESIA, Observatoire de Paris, CNRS, UPMC, Université Paris-Diderot
5 place Jules Janssen, 92195 Meudon, France
email: anna.ciurlo@obspm.fr, thibaut.paumard@obspm.fr

Abstract. The cool gas in the central parsec of the Galaxy is organized in the surrounding Circumnuclear Disc, made of neutral gas, and the internal Minispiral, composed of dust and ionized gas. In order to study the transition between them we have investigated the presence of H_2 neutral gas in this area, through NIR spectro-imaging data observed with SPIFFI. To preserve the spatial resolution we implemented a new method consisting of a regularized 3D fit. We concentrated on the supposedly fully ionized central cavity and the very inner edge of the CND. H_2 is detected everywhere: at the boundary of the CND and in the central cavity, where it seems to split in two components, one in the background of the Minispiral and one inside the Northern Arm.

Keywords. central parsec: molecular gas, methods: data analysis, techniques: spectroscopic

1. Introduction

In the central parsec of the Galaxy the cool gas is organized into two major structures: the Circumnuclear Disc (CND), which is molecular, and the Minispiral, atomic and ionized. These are morphologically different but both are of the same clumpy nature and present a spatial coincidence. To understand the origin and dynamics of these structures, in particular the transition between them, we have investigated the presence of molecular gas H_2 in the inner part of the CND, where the ionized Minispiral lies.

2. Observations and data processing

We are provided with NIR spectro-imagery data set taken by SPIFFI, the near-infrared integral field spectrograph on the VLT, already published in Eisenhauer *et al.* 2003. We are grateful to S. Gillessen of the MPE for giving us access to these data. The observed field of view is 36" x 29" and the spectral resolution $R = 1500$. The spectral range covers, in particular, two H_2 lines (2.122 μm and 2.223 μm) and the Brγ line (2.166 μm). There are other molecular or ionized lines, e.g. FeIII, which will be presented in further study. The analysis consists in creating maps of three physical parameters: line intensity, radial velocity and width. Usually the approach is to fit the spectrum of each spatial pixel, but, if the signal-to-noise is not good enough the risk is to fit a wrong spectral feature because of a noise spike. Instead we implemented a new method which consists in a regularized three-dimensional fit, for further information see Paumard *et al.*, these proceedings. Stars could locally bias results, due to increased photon noise and spectral features near the H_2 lines; our regularized fit provides for interpolation over these regions.

3. Preliminary Results

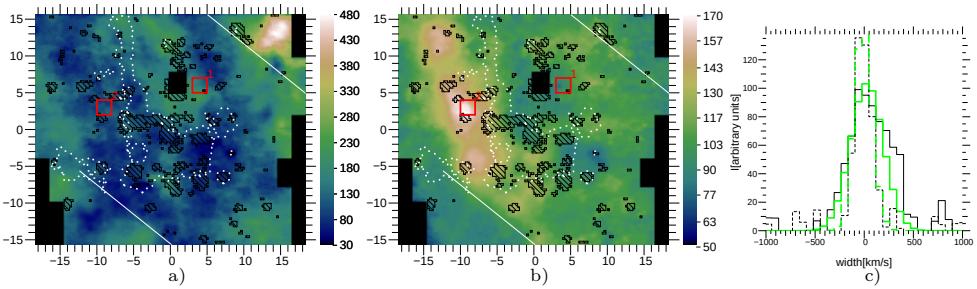

Figure 1. H_2 line a) intensity (arbitrary units) and b) velocity (km/s) maps. These images are centered on Sgr A* and displayed in arc-seconds. The meshes indicates the interpolated areas. The dotted line traces the contours of the Brγ emission and the solid lines delimit the CND emission. The two squared frames correspond to spectra showed in c), where data (dark lines) are displayed with model (light lines) for zone 1 (solid line) and 2 (dashed line).

We obtained the regularized line flux and line velocity maps shown in Fig.1; the velocity map is not reported because it doesn't add any further relevant information, because of insufficient signal-to-noise. We are confident the obtained results are reliable despite the difficulty to estimate error bars with this method, since we have checked on several individual spectra that the model accurately reproduces data. In particular width variations are significant.

The H_2 intensity map shows that the molecular gas is detected everywhere. In the South-East and North-West corners there are respectively a weak and a strong emission most probably dominated by CND molecular gas which is located there. This interpretation agrees with the known inclination of the CND (Liszt 2003) showing a stronger emission for the closer side. It is interesting to notice that the H_2 emission remains fairly strong into the inner cavity, close to the center, where it should be more unlikely for the molecular gas to resist dissociation. The shape of the Minispiral seems to stand out where the emission values are lower, in particular there is a well defined boundary West of the vertical Brγ emission.

The H_2 width map presents some bright features (i.e. large width) slightly shifted (East) with respect to the Northern Arm boundary of the Minispiral. This arm is in fact a thick cloud (Jackson *et al.* 1993), whose Eastern boundary is traced by the vertical Brγ emission. The width map features correspond, in projection, to this clump suggesting that the H_2 emission could come from inside this cloud, protected by an ionization front. Even though this interpretation is tempting, this structure is morphologically visible only on width map. As for the intensity map the emission seems to come from the background of the Minispiral and the extinction due to its dust could be hiding the H_2 structures. Our interpretation is that we are observing three dinstinct H_2 components: one associated with the CND, one in the background (intense and narrow line) and one into the Northern Arm (less intense and wide). To confirm this interpretation we will investigate the apparent anti-correlation between the intensity and width maps, derive uncertainties and compare with other species.

References

Eisenhauer, F., Tecza, M., Thatte, N. *et al.* 2003, *The Messenger*, 113, 17
Jackson, J. M., Geis, N., Genzel, R. *et al.* 1993, *ApJ*, 402, 173
Liszt, H. S. 2003, *A&A*, 408, 1009

Appendix D

Hot molecular hydrogen in the central parsec of the Galaxy through near-infrared 3D-spectroscopy

---

Accepted by A&A

Astronomy & Astrophysics manuscript no. 27173_ap
May 20, 2016

Hot molecular hydrogen in the central parsec of the Galaxy through near-infrared 3D fitting

A. Ciurlo, T. Paumard, D. Rouan and Y. Clénet

LESIA, Observatoire de Paris, PSL Research University, CNRS, Sorbonne Universités, Univ. Paris Diderot, UPMC Univ. Paris 06, Sorbonne Paris Cité, 5 place Jules Janssen, 92195 Meudon, France
e-mail: anna.ciurlo@obspm.fr; thibaut.paumard@obspm.fr; daniel.rouan@obspm.fr; yann.clenet@obspm.fr

ABSTRACT

Aims. We have investigated neutral gas in the central cavity of the circumnuclear disk (CND) at the Galactic Center, where the ionized minispiral lies, to describe the H_2 distribution and properties in this ionized environment.
Methods. This study was carried out through a spectro-imaging data cube of the central cavity obtained with SPIFFI on the VLT. The observed field of view is $36'' \times 29''$, with a spectral resolution $R = 1\,300$ in the near-infrared. These observations cover several H_2 lines. To preserve the spatial resolution and avoid edge effects, we applied a new line-fitting method that consists of a regularized 3D fit. We also applied a more classical 1D fitting to compare the relative strength of the H_2 lines.
Results. We present high spatial and spectral resolution maps of the intensity, velocity, and width of five H_2 lines and an extinction map derived from H_2. Molecular gas is detected everywhere in the field. In particular, we detected an emission from the Northern Arm cloud in addition to the known CND features. It is emitted from a region between GCIRS 7 and the Bar and from the minicavity. The excitation diagrams allow us to estimate the temperature, mass, and density of these features.
Conclusions. We interpret the CND emission as coming from a hot, thermalized, thin layer at the surface of the clouds that corresponds only to a small fraction of the total H_2 mass. The emission remains fairly strong in the central region, but it is not thermalized. A strong deviation from thermal equilibrium is detected near the minicavity. We suggest that this emission is caused by constantly forming H_2 that is destroyed again before it reaches ortho/para equilibrium.

Key words. Galaxy: center – Infrared: ISM – Galaxies: ISM – ISM: molecules – Techniques: imaging spectroscopy

1. Introduction

In the central few parsecs of the Galaxy the gas is organized into two main structures: the circumnuclear disk (CND) and Sgr A West (the minispiral). The CND is an asymmetric and very clumpy gas ring on a scale of 2–5 pc, composed of molecular clouds (Gatley et al. 1986, Guesten et al. 1987a, Yusef-Zadeh et al. 2001). At first approximation, it is in circular rotation around the radio source Srg A* at about 100 km s^{-1} (Jackson et al. 1993a). The CND inner cavity – also referred to as the central cavity – is ionized and encloses the minispiral.

Sgr A West is composed of clouds of atomic and ionized gas (Lo & Claussen 1983). It consists of the ionized surface layers of larger neutral clouds that are drawn by tidal force toward the Galactic Center (Paumard et al. 2004). The spiral aspect is caused by the projection in which we see these surface layers on the plane of the sky. More precisely, the Northern Arm of the minispiral is probably located at the surface of a cloud that falling toward the center and is exposed to intense UV radiation.

The central cavity is known to be embedded in a strong radiation field because a central cluster of young stars provides ionization for both the CND inner cavity and the minispiral (Martins et al. 2007). The CND and the minispiral are strongly connected (Ekers et al. 1983): the western arc of Sgr A West is an ionized layer at the surface of the inner edge of the CND (Guesten et al. 1987b). The CND is believed to be fueled by infall from dense molecular clouds 10 pc away. The CND, in turn, releases material into the central cavity. Here, illuminated by the UV field, it is at the origin of the observed minispiral (Güsten 1989). This suggests that the two structures have common or related origins.

We have investigated molecular hydrogen, H_2, in the ionized central cavity that is delineated by the CND, where the minispiral lies. In this environment the strong ultraviolet (UV) radiation is expected to destroy H_2. However, in principle, hydrogen molecules could be found within the neutral clouds whose ionized borders delineate the arms of the minispiral. Here they could be shielded from the radiation by an ionization front and thus survive dissociation. H_2 could also be found in the transition zone between the CND and the minispiral or on the line of sight.

H_2 emission has previously been detected inside the central cavity by Gatley et al. (1986). Jackson et al. (1993a) analyzed HCN and O I lines, which led to the detection of a large amount of neutral (300 $M_\odot$) gas associated with the streamers of the minispiral. It also showed several dense and distinct streamers at the edge of the CND. Marr et al. (1992) revealed molecules in the bar of the minispiral that are shielded by dust in the ionized features. Yusef-Zadeh et al. (2001) clearly detected H_2 in the central cavity and showed that its kinematics is inconsistent with the CND direction of rotation.

Our goal is to extend the search and study of H_2 in the central parsec by characterizing the gas distribution, dynamics, and excitation. This study is carried out by analyzing a SPIFFI (Tecza et al. 2000; Eisenhauer et al. 2003) spectroimaging dataset in the H and K bands that covers several H_2 lines.

In Sect. 2 we present these observations together with the calibration we applied. The analysis was made in two steps. In

the first part (Sect. 3), the gas morphology and dynamics were analyzed. We applied an original line-fitting method to handle the noise and conserve good angular resolution: a global regularized 3D fitting (Paumard et al. 2014, 2016 in prep.). We eventually obtained high-resolution maps of the gas flux, velocity, and line width. The comparison of two H_2 lines (1-0 S(1) and Q(3)) allowed us to correct the extinction effect. In the second part of the analysis (Sect. 4), we studied the possible excitation mechanism through the simultaneous analysis of eight H_2 lines to which we applied a more classical 1D spectroscopic model fitting. The derived flux allows tracing the excitation diagrams of several areas on the field of view and computing the relative excitation temperature and mass.

We conclude on molecular gas morphology and the variety of emission processes in Sect. 5.

2. Observations and dataset reduction

2.1. Dataset

The dataset consists of a near-infrared (NIR) spectroimaging cube with two spatial dimensions and a wavelength dimension. It has been obtained with the Spectrometer for Infrared Faint Imaging (SPIFFI), a NIR integral field spectrograph installed on the VLT (Tecza et al. 2000). This cube was acquired during the first observing runs as a guest instrument at the VLT in March and April 2003. After these observations SPIFFI was equipped with adaptive optics and became SINFONI. The same dataset has already been used for another program about stellar populations (Eisenhauer et al. 2003; Horrobin et al. 2004; Paumard et al. 2006, among others). The central parsec has been observed for two nights for one hour each, resulting in the a mosaic of $\sim 35'' \times 35''$. The southwestern (from 20″ east to 15″ south of Sgr A*) and northwestern (from 15″ north to 15″ west of Sgr A*) corners as well as the west side (from 12″ West of Sgr A*) of the SPIFFI field of view cover part of the CND (as can be inferred by comparing to Liszt 2003; Christopher et al. 2005). The rest is occupied by the central cavity.

The observations are seeing-limited (FWHM 0.75″) with a 0.25″ pixel sampling and a spectral resolution $R = 1\,300$ in the combined H+K mode.

This spectral range includes many H_2 lines. The lines we were able to detect in our dataset are reported in Table 1.

Transition	Wavelength [μm]	avg S/N	max S/N
1-0 S(3)	1.9575	2.6	9.1
1-0 S(2)	2.0337	1.1	6.4
1-0 S(1)	2.1217	5.3	30.8
1-0 S(0)	2.2232	1.9	8.0
2-1 S(1)	2.2476	1.0	3.2
1-0 Q(1)	2.4065	3.9	23.9
1-0 Q(2)	2.4133	0.9	4.9
1-0 Q(3)	2.4236	4.4	22.3

Table 1. Transition name, wavelength, and average and maximum signal-to-noise (S/N) over the field for H_2 lines covered by the SPIFFI spectral range.

The H_2 molecule has two spin states: the ortho, triplet, with parallel nuclear spins, and the para, singlet, with antiparallel nuclear spins. Odd-numbered transition lines correspond to ortho states, even-numbered match para states. In our dataset, most para lines and 2-1 S(1) have a low signal-to-noise ratio (S/N), which makes the analysis of these lines possible only in the zones of highest intensity.

The spectrum also contains recombination lines such as Brγ, Fe III, and Fe II, which will be the object of another study.

The observations where processed using the SPIFFI pipeline (Modigliani et al. 2007); the reduced data-cube is the same as in Eisenhauer et al. (2003).

2.2. Calibration

To compare different lines, the flux has to be dereddened and calibrated in photometry. The data that we obtained were already reduced and partially calibrated to remove the atmospheric absorption feature between the H and K bands. We have completed the calibration using stars in the field chosen from the catalogs of Paumard et al. (2006), Blum et al. (2003), and Bartko et al. (2009). The calibration was done in two steps: the first step was to correct the slope of all spectra (relative calibration, Sect. 2.2.1), the second step was to convert the analog-to-digital unit into physical flux units (photometric calibration, Sect. 2.2.2).

2.2.1. Relative calibration

The relative calibration consists of dividing the datacube by the observed spectrum of a standard spectrometric calibrator and multiplying it by the intrinsic – or expected – spectrum of this calibrator.

At this stage, we only considered the shape of the spectra. The absolute flux calibration comes at a later stage. To measure the observed spectrum of each calibrator, we integrated over a diamond-shaped aperture of 5 pixel width and height (13 spatial pixels). For background estimation and subtraction, we used a 5-pixel-wide square aperture minus the diamond-shaped aperture used to estimate the stellar spectrum itself.

The intrinsic spectral shape of each star was estimated using a blackbody curve, at the effective temperature of the star. For high temperatures, the H- and K-band emission is in the Rayleigh-Jeans tail of the blackbody, where the shape of the curve does not change with temperature. Therefore, we considered the same temperature ($T = 35\,000$ K) for every calibration star. This blackbody was reddened using a power-law extinction curve for the NIR: $A_\lambda \sim \lambda^{-\alpha}$, where $\alpha \sim 2.07$ (Fritz et al. 2011). The local extinction is different for each star and was taken from the extinction map in Schödel et al. (2010).

2.2.2. Photometric calibration

From the resulting data cube we extracted the spectrum of cool stars of known magnitude for the absolute calibration. We considered the same diamond-shaped aperture as before. The measured flux, integrated over the K band, was compared to the expected one (computed from the known star magnitude). This comparison was made taking into account that for our aperture, the enclosed energy is estimated to be ~25% of the total. To calculate this factor, stars of the field are not well-suited since they are not isolated. Therefore we created a synthetic point spread function (PSF) of the same width as the stars on the field (1.5±0.2 pixels, computed from the fit of a2D Gaussian over few stars). The enclosed energy in the aperture was then evaluated from this synthetic PSF.

2.2.3. Final calibration factor and uncertainty

Three stars were used as relative calibrators: GCIRS 16NW, GCIRS 16C, and GCIRS 16NE from Paumard et al. (2006). Seven stars were used as photometric calibrators: stars 19, 28, 84, 91, 102, and 105 from Blum et al. 2003 and star 68 from Bartko et al. 2009.

We obtained a correction curve, that is, a correction factor for each wavelength, for each combination of relative and absolute calibration stars. The average value of the eighteen curves was considered as the final relative correction. The uncertainty was evaluated as the dispersion of the curves of the different calibrators. It amounts to ∼35%. This rather high value is dominated by the uncertainty on the stellar magnitudes and the exact stellar location within the aperture. When considering the ratio of two spectral lines, the uncertainty due to the photometric calibration is no longer relevant because this error is common to all lines. In this case, the uncertainty is only due to the dispersion of the slopes of the relative calibrators and amounts to 8%.

To study the absolute flux and especially its spatial variations, the flux has to be corrected for extinction. To do so, we could consider values retrieved from the map of Schödel et al. (2010) (or other available extinction maps), but this extinction map is obtained from stellar color excess. The molecular gas is not necessarily situated at the same optical depth as these stars. To properly correct the gradient of the extinction in the inner parsec, it is better to apply a method that is based on the dataset itself: considering the 1-0 Q(3) over 1-0 S(1) ratio. This is detailed in Sect. 3.3.

3. Morphology and dynamics of the molecular hydrogen

Our analysis is based on a fit of each spectrum with a Gaussian function. In this way we obtain three parameters for each spatial pixel: the line flux, radial velocity, and width. We decided to search for line flux instead of the line intensity: line flux is more reliable than intensity because it does not depend on the instrumental resolution. After we obtained the three parameters for every pixel, we created for each parameter a map of its variations across the field.

3.1. Method

3.1.1. Regularized 3D fitting

The most common approach is to fit the spectrum of each spatial pixel individually. The maps resulting from this approach are noisy. Because the S/N in the SPIFFI dataset is not consistently high throughout the field of view, spatial smoothing has the effect of degrading the spatial resolution everywhere, whic increases the correlation between neighboring pixels and introduces edge effects.

To overcome these problems we applied a new method (Paumard et al. 2014): a regularized 3D fitting. We describe this method briefly, but more details will be given in Paumard et al. (2016, in prep.).

The method consists of minimizing an estimator, ε, which is the sum of χ^2 and a regularization term:

$$\varepsilon(F, v, \sigma) = \sum_{\alpha,\delta,\lambda} [(D - M) \cdot W]^2 + \sum_{a_i=F,v,\sigma} R_i(a_i), \quad (1)$$

where the first term is the χ^2 term (difference between the 3D dataset D and the model M). The elements of the cube are indicated by the spatial coordinates α and δ and by the wavelength coordinate λ. W is the weighting function that takes the S/N into account. $R_i(a_i)$ is the regularization term for the a_i-fitting parameter (flux F, velocity v, and width σ).

The regularization is an L1–L2 algorithm borrowed from the deconvolution context, developed in Green (1990), S. Brette (1996), and Mugnier et al. (2001) and generalized in Mugnier et al. (2004) and coded in Yoda software by D. Gratadour[1]. The expression of this term for every parameter map is

$$R_i(a_i) = \mu_i \sum_{u=\alpha,\delta} \left[\frac{\Delta O(u)_{a_i}}{\delta_i} - ln\left(1 + \frac{\Delta O(u)_{a_i}}{\delta_i}\right)\right]. \quad (2)$$

Here $\Delta O(u)_{a_i}$ is the spatial gradient of the a_i-parameter. For weak gradients (small $\Delta O(u)$), the logarithmic term of L1–L2 dominates and the terms become a quadratic criterion, which penalizes gradients and smooths the map. In contrast, when $\Delta O(u)$ is large, strong gradients are restored. The transition from one regime to the other is adjusted through the δ_i and μ_i hyperparameters.

This algorithm is very well suited to treat objects with strong and spatially correlated gradients such as sharp edges (e.g., planetary surfaces) or, in our case, ridges and streamers. The algorithm disfavors random variations on the maps (strong gradients between pixels, which are noise) but still allows quick and coherent variations. The fit over pixels with a low S/N is highly improved since the procedure uses neighboring points to adjust the solution. This prevents overfitting of noise spikes.

However, there is one main inconvenience in this method: the necessary tuning of hyperparameters δ_i and μ_i for each parameter map (intensity, velocity, and width). Six hyperparameters were therefore chosen. They are not independent of one another, which complicates finding the solution.

μ_i regulates the smoothness of each parameter map. An increase of μ_i has the immediate effect of smoothing the image, but it also has the secondary effect of limiting the variation range of the parameters. Relative values of $1/\delta_i$ rescale each parameter to cause them to vary around the same numerical order of magnitude. A decrease of $1/\delta_i$ leads to stronger variations of the parameter across the field, but it also has the effect of lowering the weight of the regularizing term and to amplify the noise. The challenge is to balance the six hyperparameters to gain sufficiently smooth maps while keeping fine spatial structures. The aim is to obtain maps that appear smooth at a scale most possibly close to the spatial resolution. The procedure was run several times with different combinations of hyperparameters to determine the best strategy for identifying a good hyperparameters combination.

The tuning of the hyperparameters is an iterative process. We describe below how we proceeded to determine good hyperparameters: first, we chose the initial guess as a set of constant maps. The constant for each parameter is representative of the average value of each parameter over the area. Second, we selected three values of $1/\delta_i$ so that all three parameters varied in the same range. The starting values of these hyperparameters was the order of magnitude of each parameter (for instance, 100 for a line width that is expected to be around 120 km/s). $1/\delta_i$ were then more finely tuned, trying to allow each map to cover as much of the selected range of variations as possible. When these ranges were well covered, the resulting maps were often noisy. The next step was therefore to enhance the smoothing (through μ_i) to avoid noise amplification. The equilibrium between the six hyperparameters is delicate and needs several iterations.

[1] https://github.com/dgratadour/Yoda

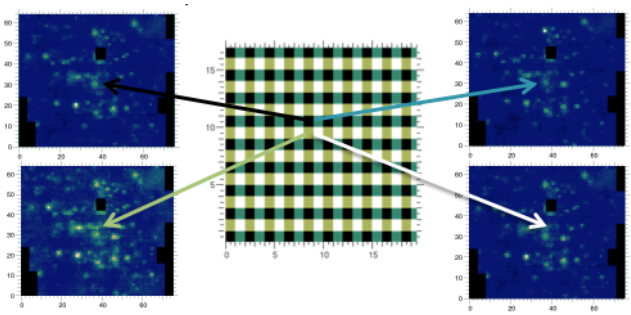

Fig. 1. Four data cubes are created from dataset, taking one pixel out of four and interpolating over the holes. The first cube comes from black pixels, the second from blue pixels, while the third and fourth cubes come from white and green pixels.

Stars in the field might locally bias results by increased photon noise and because of some spectral features. Therefore the stars were masked. The mask was built considering the root-mean-square (RMS) variation over the spectral direction at the location of each pixel (on spectral ranges free of features, especially stellar features). Pixels that showed an RMS higher than a certain threshold were masked. This threshold was chosen by comparing the resulting mask to the known position of stars (for instance, Paumard et al. 2006) to cover the main bright stars of the region. Our regularized 3D fitting allows interpolating over these masked regions.

We currently do not have an objective and absolute criterion to select the best hyperparameters combination. The reduced χ^2 of the fit gives some indications, but is not enough to distinguish among distinct results that could have very close values of reduced χ^2 (see, for instance, Fig. 3, where two models with close χ^2 are compared to raw data).

However, we have objective criteria that allow us to judge the result a posteriori, for instance, comparing the 3D model obtained with raw data. Another strong objective a posteriori criterion to assess the method is given by comparing the 3D model with a classical 1D model. Individual spectra in several zones can be extracted and fitted with a classical 1D model. The regularized 3D fit model, averaged over the same zones, can then be compared to the classical 1D model, as shown in Sect. 3.2.1. One final, stronger a posteriori criterion is to compare the regularized 3D-fit results for distinct H_2 lines. In Sect. 3.2.2 we show that 1-0 S(1), S(3), Q(1), Q(3), and S(0) all show the same large-scale structures in each parameter map.

3.1.2. Uncertainties

Since the method does not provide a direct estimate of the uncertainties, we developed a separate technique to evaluate them.

We split the SPIFFI cube into four subcubes. To do so, we selected only the odd columns and odd rows in the first cube, only the even columns and odd rows in the second cube, only the odd columns and even rows in the third cube and only the even columns and even rows in the fourth cube. We built four new cubes in this way, with the same size as the original data cube, by interpolating among the chosen points.

We ran the regularized 3D fitting method on each of these new data cubes and obtained four maps for each Gaussian parameter. We calculated the resulting standard deviation and divided it by 2 (because the information was now four times less significant). The result is a map of uncertainty for each Gaussian fitting parameter.

In addition to the above described statistical errors, some systematic errors are attached.

- The decision of which hyperparameters to inject into the algorithm as well as the initial guess for the fit procedure influences the resulting maps, especially where the S/N is poor. When the method works properly, parameter maps are smooth and show significant spatial variations. This means that the model resembles the observations. In this case, small variations of hyperparameters lead to variations in the parameter maps, which remain within the previously discussed error bars. Moreover, changes occur more frequently in the values (with a global scaling factor) than in the shapes, which are stable. When the criterion reaches an absolute minimum, the result becomes stable. This source of error is therefore not significant compared to the statistical uncertainties.
- Another source of error is the continuum estimation. Continuum is not the same everywhere and is evaluated on some portions of the spectrum that are free of any gaseous or stellar line. However, some H_2 lines lie very close to stellar lines. Continuum subtraction is estimated by a polynomial fit before the regularized 3D fitting algorithm is applied. Because of poor S/N, it is sometimes difficult to determine where the continuum is standing. This uncertainty does not affect the parameter maps we built for each line too much. However, the relative strength of the different lines can be affected, and this problem is taken into account in Sect. 4.1.
- As previously discussed, the absolute flux map has one additional source of error that comes from the photometric calibration (Sect. 2.2.2).

3.2. Regularized 3D fit maps

We started our analysis with the H_2 1-0 S(1) transition line at 2.1218 μm, which has the best S/N. As previously mentioned, a pixel-by-pixel fit (1D fit) was performed on some zones of the field to be compared with the regularized 3D fit and verify the method.

3.2.1. 1-0 S(1) line

The retrieved maps of line flux, radial velocity, and width are reported in Fig. 2 with the respective error maps.

Flux map

The flux map shows that the molecular gas is detected in the whole FOV. Some of the most prominent features are

- a bright emission at the CND position in the northwestern corner;
- a weak emission situated between two stronger emissions in the southeastern corner, where the CND lies as well;
- a plume-like feature in the north near GCIRS 7 to the right of the minispiral northern arm;
- in the southeastern corner we recognize a feature known as the southern extension (Christopher et al. 2005).

Velocity map

The velocity map presents a well-pronounced blueshift in the southeastern corner, which is consistent with the CND motion toward the observer. The remaining velocity map has

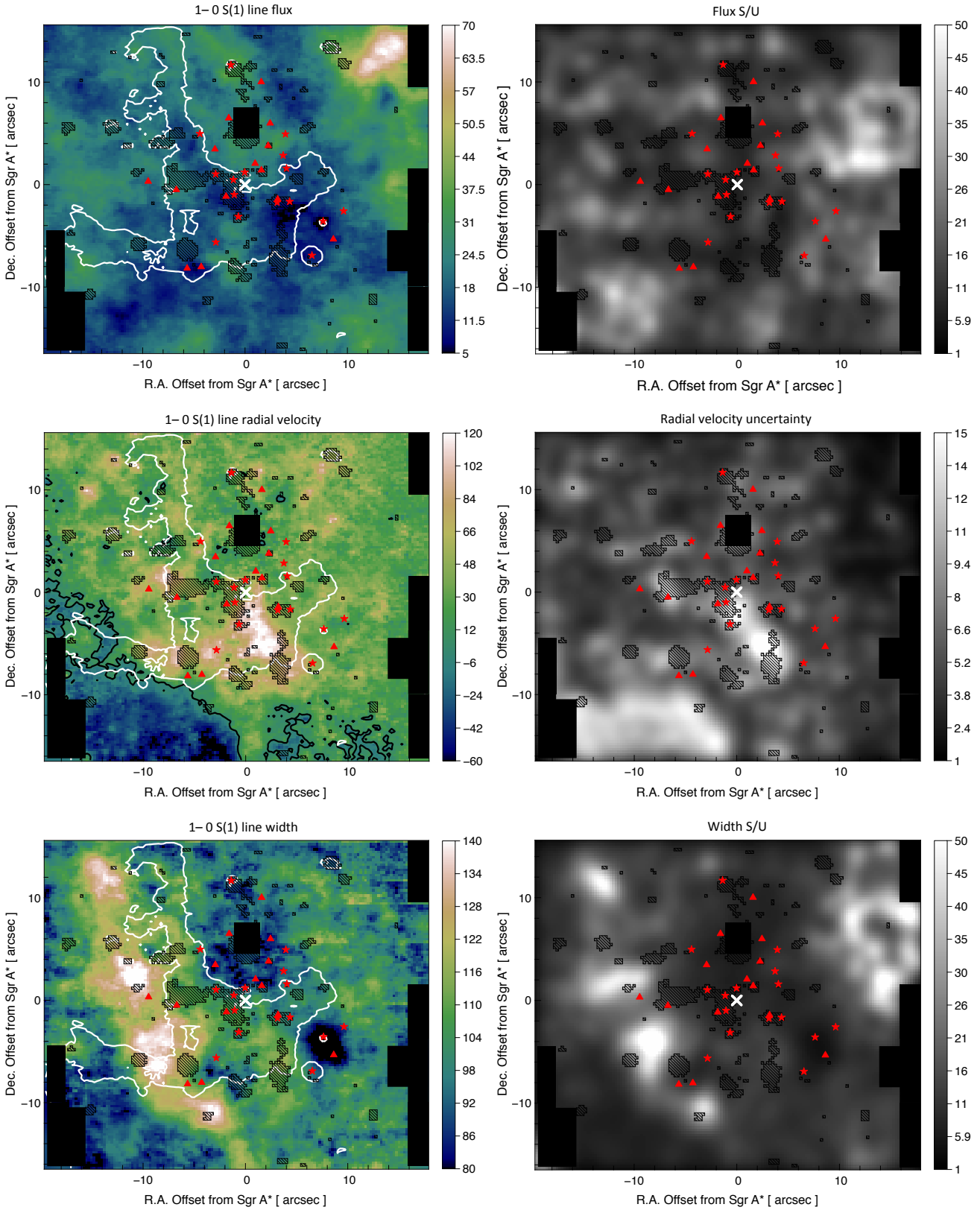

Fig. 2. *Left:* Parameter maps of the 1-0 S(1) line obtained through regularized 3D fitting. Sgr A* is indicated by the cross. The line flux color bar is in 10^{-19} W m^{-2} arcsec^{-2}. Velocity and width color bars are in km s^{-1}. The white contour traces the Brγ emission of the minispiral at $2{\cdot}10^{-16}$ W m^{-2} arcsec^{-2}. The dashed areas cover stars zones that have been interpolated. Red dots indicate the position of a Wolf-Rayet star: a star shows type WN and triangles type WC (Paumard et al. 2006 catalog). The solid black areas indicate regions of which we lack observations. GCIRS 7 is covered by the central black square. The solid black line in the velocity maps indicates points at zero velocity. *Right:* signal-to-uncertainty ratio (S/U) maps for flux and width maps, uncertainty map for velocity.

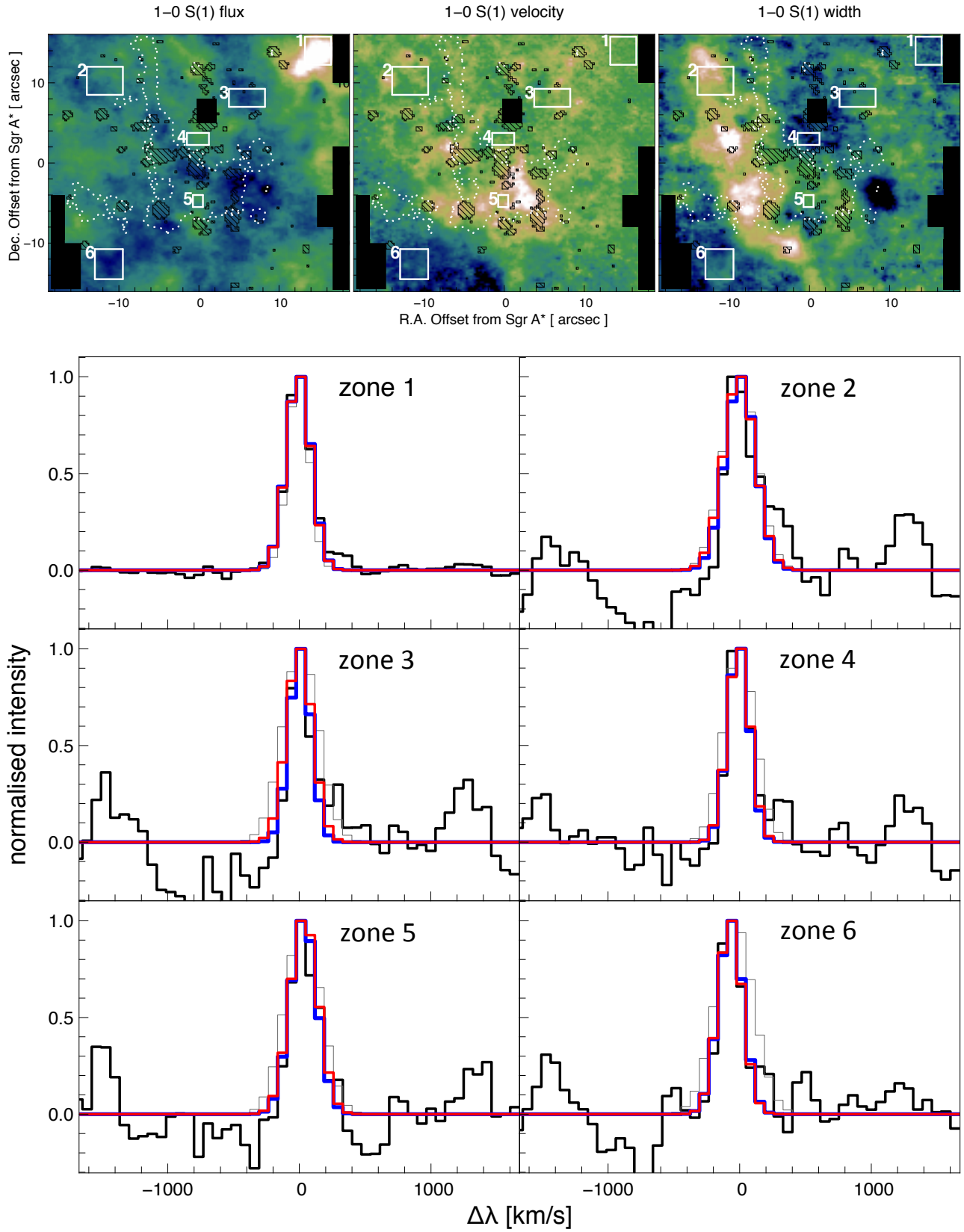

Fig. 3. *Top:* Zones where individual spectra of S(1) line, have been extracted, superimposed on parameters maps (the same as in Fig. 2). *Bottom:* for each zone the normalized average spectrum (black) is superimposed on the respective pixel by pixel model (solid blue) and regularized 3D model (solid red). The gray line reproduces another solution of the regularized 3D fitting. Both solution have close values of $\chi 2$ (1.15 and 1.49, respectively), but the red model fits the observations much better.

a uniform global pattern (moving at around 30-50 km s^{-1}) and several small-scale structures. They mostly correspond to bright stars. These features can be artifacts created by the stellar pollution, but they may also be associated with gas ejected by the stars themselves. The velocity at the center of the map is strongly affected by nearby stars. Here the S/N is low (1 or 2). However, this location is very close to the minicavity, a shell of $\sim$ 5″ that is probably created by the interaction between the stellar and the interstellar medium (Eckart et al. 1992). It is a region of shock. The high velocity we observe here may be related to this shock. A more detailed analysis of this area will be covered in future works with a second dataset that has a better spatial resolution.

Width map

The H_2 1-0 S(1) width map presents some enhancements (i.e., large width) along a ridge that is slightly shifted to the east of the northern arm. This arm is a thick cloud (hereafter the northern arm cloud; Jackson et al. 1993a; Paumard et al. 2004) whose eastern boundary is ionized and traced by the north-south Br γ emission. The width map features correspond in projection to the denser part of this cloud, suggesting that the H_2 gas inside is more turbulent. The H_2 1-0 S(1) line looks narrower in the southeastern and northwestern corners, at positions associated with the CND. The line is wider in the central cavity, with a few exceptions (the area around GCIRS 7 and a region 8″ west and 4″ south of Sgr A*). We would like to point out that the line width we give represents the fitted measured width, which is the quadratic sum of intrinsic and instrumental width.

To assess these results, we extracted individual spectra in sixteen zones and fit them with a classical 1D model. In the remaining paper we concentrate on six of the zones that are most representative of peculiar areas (CND, minispiral, central cavity, and minicavity). The detailed information on the other zones is given in Appendix A. We compared this model to the result of the regularized 3D fit (Fig.3). The two models can hardly be distinguished, which shows that when it is integrated over an aperture, our 3D method is equivalent to classical data analysis.

3.2.2. Other 1-0 ortho lines: S(3), Q(1), and Q(3)

We have applied the fitting method to the other ortho lines available in our dataset. The transitions with a sufficient S/N are 1-0 S(3), 1-0 Q(1), and 1-0 Q(3) at 1.9575 μm, 2.4066 μm, and 2.4237 μm.

These lines lie in a more complex spectral environment than the S(1) line. S(3) is near the atmospherically absorbed range between the H and K band. Q(1) and Q(3) are close to CO stellar photospheric absorption features (see Fig. 7). The retrieved maps for each of these lines are displayed in Fig. 4 (second, third, and fourth columns).

Even though the fitting procedure is more challenging than for 1-0 S(1) maps, the three ortho line maps are fairly similar to those of 1-0 S(1). The flux maps in particular show the same patterns. The velocity maps also have the same gradient shape. For the width maps we note the following.

- For 1-0 Q(3) the width map confirms the previous finding of an emission from the northern arm cloud, at least in projection. In the southeastern corner of the map the line appears wider than 1-0 S(1). However, the width map structure globally presents the same peculiarities as 1-0 S(1).
- 1-0 S(3) is affected by a close atmospheric line. This probably causes the higher values of the width, but the overall shape of the width map is compatible with the one obtained with S(1).
- The Q(1) line is affected by the nearby CO features. This absorption probably reduces the measured flux and explains the lower values of the width.

In summary, when the local peculiarities and spectral pollution are taken into account, the parameter maps of these four ortho H_2 lines are compatible. This strengthens the validity of our results, assuming the same dynamics applies for all H_2 molecules, regardless of their excitation state, as expected if all the lines were emitted by a common source.

According to this interpretation, all lines can be fit using the velocity and width obtained for 1-0 S(1). These parameters are best estimated for this line. Hence we applied the regularized 3D fit procedure a second time by imposing these conditions on the other lines (1-0 S(3), Q(1) and Q(3)). We obtained new flux maps (Fig. 4, first column). These flux maps with an imposed velocity and width are very similar to the fit where all parameters were let free to vary. This confirms the relevance of using a common width and velocity. This assumption improves the fitting, since two of the parameters rely on the most reliable line, which decreases the effect of spectral environment pollution.

3.2.3. Para 1-0 S(0) line

The 1-0 S(0) line is the para line with the best S/N. However, there is a Fe III line on one side of the H_2 line and an absorption feature on the other. Despite these difficulties, S(0) is clearly detected almost everywhere in the SPIFFI field of view. However, when we tried to fit S(0), the regularized 3D fit did not converge on a satisfactory solution. A satisfactory fit can be achieved only if the line is simultaneously fit with 1-0 S(1). In this case, the model fits both lines through four parameters: S(1) flux, Q(3) flux normalized by S(1) flux (i.e., the derived ratio), velocity, and width.

Figure 4 displays the parameter maps obtained for this simultaneous fit. The S(1) flux, velocity, and width maps are compatible with the previous findings. The S(0) para line is therefore well described by the same velocity and width as S(1) and other ortho lines. The main difference with respect to other studied lines is that this transition shows a strong emission maximum a few arcseconds south of Srg A*. In this zone, the S/N is good and the S(0) line very clearly stands out from the continuum. This peak of 1-0 S(0) emission is discussed in detail in Sect. 4.

3.3. Extinction-corrected map

Extinction correction is crucial not only to obtain the absolute flux values, but also to compare fluxes in different lines (Sect. 4).

We considered the 1-0 Q(3) to 1-0 S(1) flux ratio for the extinction evaluation because these two lines correspond to the same upper level. The ratio was fit using the regularized 3D fitting procedure directly on the line ratios instead of fitting the two lines separately and considering the ratio afterward, as for the S(0)-S(1) ratio (Sect 3.2.3). Fitting the flux ratio directly allows the result to be less affected by small-scale artifacts and local variations of any of the parameters.

Since the H_2 lines are optically thin (as shown in the Orion nebula, for instance, Gautier et al. 1976) we can write

$$\frac{I_{Q3}}{I_{S1}} = \frac{(\mathcal{A}_{Q3} \cdot \nu_{Q3})}{(\mathcal{A}_{S1} \cdot \nu_{S1})} \cdot 10^{E/2.5}, \quad (3)$$

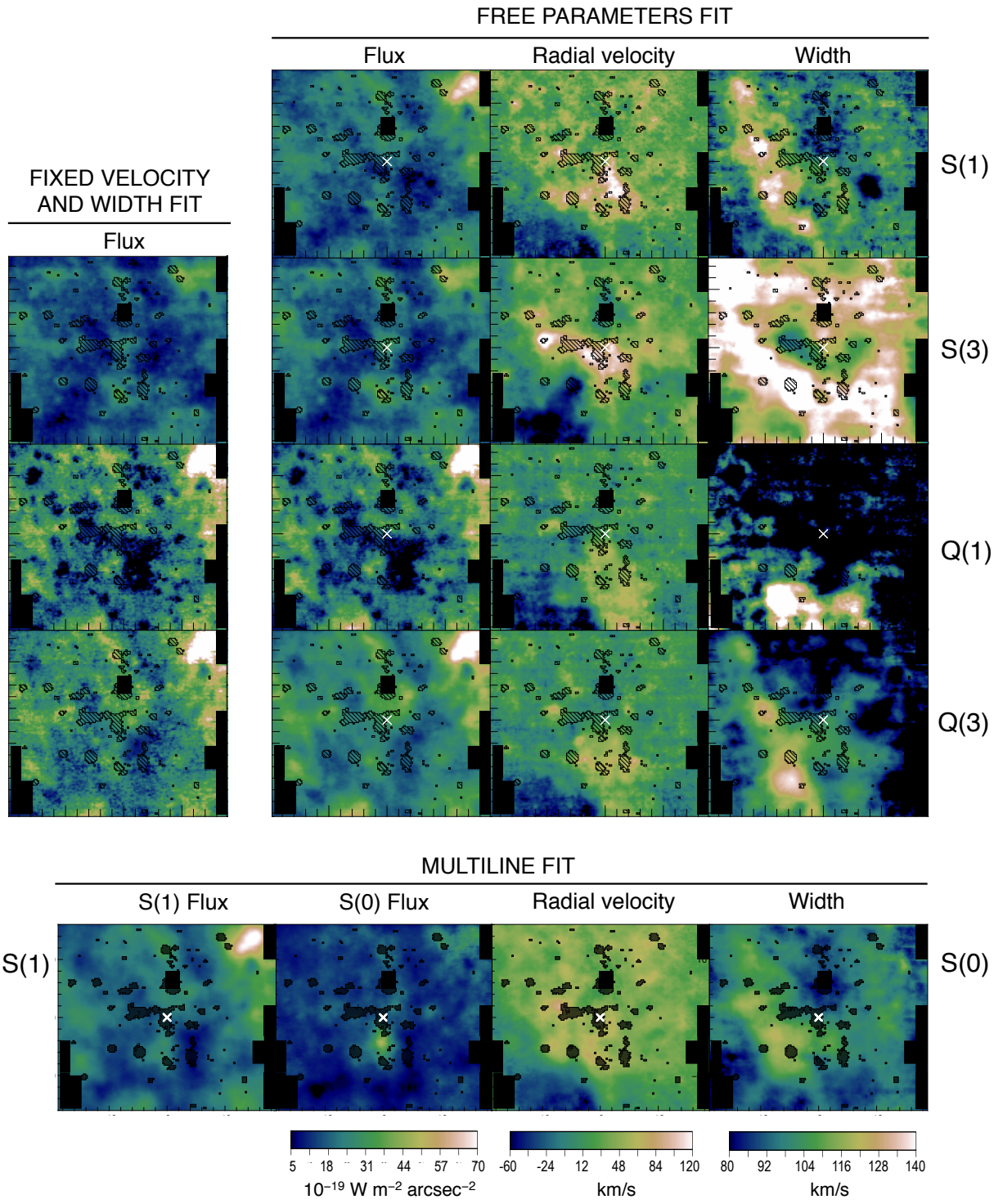

Fig. 4. Parameter maps for each ortho line. *left to right:* flux with speed and width imposed to be those of S(1) line. Line flux, speed, and width with free parameters. *Top to bottom:* 1-0 S(1), S(3), Q(1), and Q(3) lines plus the 1-0 S(0) line maps obtained with the multiline fit. Maps are centered on Srg A*. The color bars are the same for all lines and as in Fig.2. Symbols as in Fig. 2.

where I_{Q3}/I_{S1} is the intensities ratio (i.e., the flux ratio), $\mathcal{A}$ is the Einstein coefficient and ν the frequency. Considering $E = A_{\lambda_{S1}} - A_{\lambda_{Q3}}$, we have

$$E = 2.5 \cdot log\left(1.425 \cdot \frac{I_{Q3}}{I_{S1}}\right). \quad (4)$$

The 1.425 factor in Eq. 4 comes from the ratio of the Einstein coefficient of the two transitions. Assuming an extinction law, we can obtain the total extinction A_λ at every wavelength and correct every line at every pixel for reddening. We assumed a power-law in the NIR as in Sect. 2.2.1. In particular, we obtain a map for the extinction at Ks through the equation $A_a/A_b = (\lambda_a/\lambda_b)^{-\alpha}$ (with

α = 2.07 from Fritz et al. 2011), where λ_{Ks} = 2.168 μm as in Schödel et al. (2010).

The A_{Ks} map, together with the corrected flux map of S(1), is reported in Fig.5. We computed the uncertainty on the extinction from the propagation of S(1)-Q(3) ratio uncertainty, obtained as explained in Sect. 3.1.2. The histogram of the resulting statistical error is reported in Fig. 6. To this value a systematic error of 10% needs to be added because of the calibration.

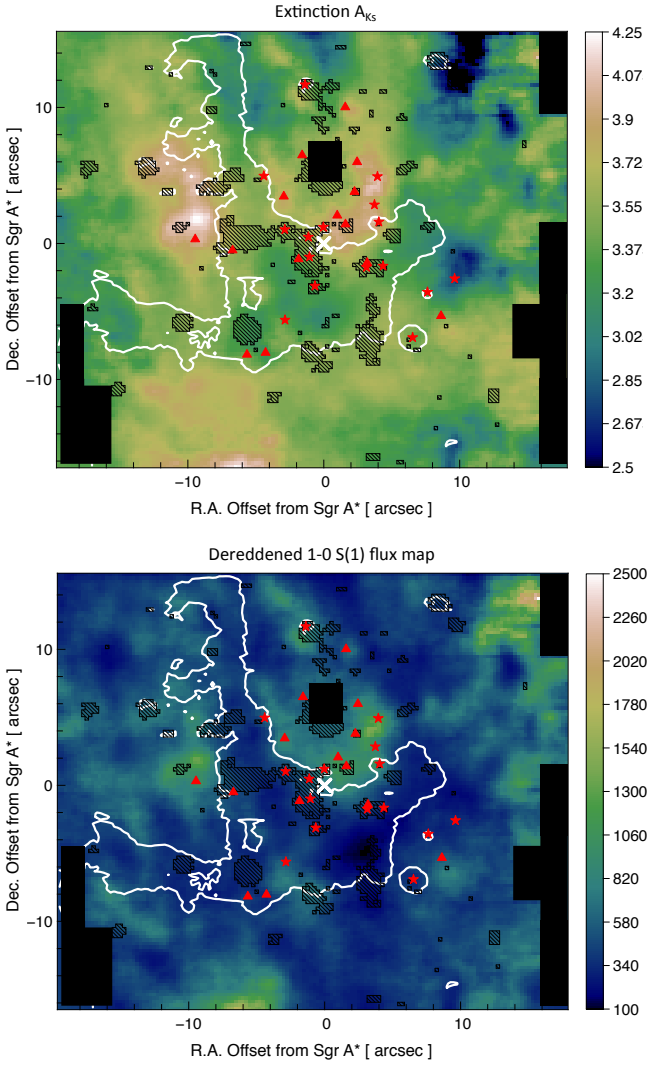

Fig. 5. *Top:* extinction A_{Ks} map at λ_{Ks} ~ 2.168 μm in mag obtained from Q(3)/S(1). *Bottom* : S(1) flux map, dereddened through this extinction map. Symbols as in Fig. 2.

The average value of A_Ks is ≃3.4. The extinction map shows significant variations, well above 1 mag.

The dereddened 1-0 S(1) flux map shows essentially the same global features as the uncorrected map. However, the western arc and the southern extension emissions are enhanced. The emission is also enhanced between GCIRS 7 and the bar of the minispiral. This feature is also present, albeit less strikingly, in the uncorrected map (Fig. 4).

The dereddened flux map appears partially correlated with the extinction map: the flux is high where the extinction is high as well. A more detailed analysis of this correlation is the object of another paper (Ciurlo 2015 and Ciurlo *et al.* 2016, in prep), where this effect modeled.

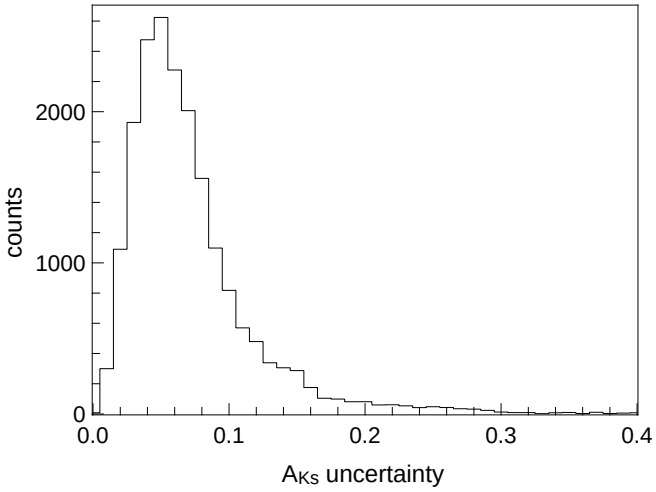

Fig. 6. Histogram showing the distribution of the statistical uncertainty of A_{Ks}.

3.4. Discussion

3.4.1. CND emission

The emission observed in the northwestern and southeastern corners of the SPIFFI field of view is most probably dominated by CND molecular gas that is located there (flux map of Fig. 2). Because the CND is inclined with respect to the plane of the sky (Liszt 2003), the CND western border in the northwest of the SPIFFI field is closer to the observer. This is coherent with a stronger emission from the closest, and thus less extinct, side (the northwestern corner).

The flux map we obtain shows the same features as the 1-0 S(1) map obtained by Yusef-Zadeh et al. (2001). For instance, both maps show the bright emission in the northwestern corner and the weak emission in the opposite corner (with the same structure of a gap between two brighter features) as well as the plume (which is probably not associated with the CND, however). The flux associated with these regions is also compatible with the values obtained by Yusef-Zadeh et al. (2001). For instance, in the northwestern corner we found an undereddened flux of ~ 60±10 10^{-16} erg s^{-1} cm^{-2} arcsec^{-2}, while Yusef-Zadeh et al. (2001) found ~ 50 10^{-16} erg s^{-1} cm^{-2} arcsec^{-2} with an uncertainty of 30%. We consider this agreement as another confirmation of the validity of our method.

Some features are also compatible with the HCN distribution obtained by Christopher et al. (2005). HCN clearly traces the densest clumps in the CND. The southern extension is particularly evident. The northwestern corner and western border also coincide with the HCN distribution. This is another strong indication that all these emissions come from the CND itself.

3.4.2. Central cavity emission

It is interesting to note that the H_2 emission remains fairly strong inside the CND borders. This emission could arise either from the background or from the central cavity itself, close to the center. In the central cavity H_2 is thought to resist dissociation with a

far lower probability. However, in the following sections we provide indications that this emission is indeed in the central parsec.

We note that the 1-0 S(0) line exhibits a strong maximum near Srg A*, at the entrance of the minicavity. This feature could result from a shock, which is not unusual in this region, as previously discussed, or from some particular environmental conditions. This point is discussed in more detail in Sect. 4.

Another flux enhancement is visible between the minispiral bar and GCIRS 7. This flux feature is very well correlated with the position of some Wolf-Rayet stars of type WC (shown by the triangles in Fig. 5). The environment of these stars is often dusty. Some dust has been detected by Tanner et al. (2002) and Haubois et al. (2012) at these locations, which means that forming H_2 is expected. These stars may be located in the background, farther from the central cluster than the northern arm. This would explain why the outer layer of these dust shells is not ionized and consequently not observed in the ionized gas maps. The emission in the remaining central cavity is weaker but still clearly detectable.

3.4.3. Gas dynamics

The velocity map we obtained shows that the northwestern corner and western border are moving at ∼30 – 50 km s−1. These values are well compatible with the HCN observations: Christopher et al. (2005) found ∼ 50 km s^{-1} and 50 – 60 s^{-1} , respectively. The velocity corresponding to the above-mentioned southern extension is around -40 km s^{-1}.

We observe no large-scale motion of H_2 associated with the minispiral arms. Even though at least part of the emission seems to be connected to the minispiral (the northern arm cloud), we see no evidence of a transport of matter along its arms.

The western part of the field that corresponds to the CND border looks smoother in velocity than the central cavity. The reason is that the central cavity has more inhomogeneous dynamics than the CND.

The spatial distribution of the width is very different from the flux map. Almost throughout the central cavity, the width map shows a wider but weaker line emission, with a particularly strong width enhancement corresponding to the northern arm cloud.
In summary, there seem to be at least two different emission components:

- one associated with the CND (northwestern and southeastern corners mainly) that presents a narrow and intense emission line, and
- one inside the central cavity (at least in projection) that is generally characterized by a wider but weaker line emission than the other component.

In the CND the line is narrower than in the remaining field probably because its clumps are more dense, which prevents the line from integrating deep into them. On the other hand, the gas is less dense in the central cavity. Here, the observed widening of the line translates the dispersion in velocity along the line of sight. This effect is particularly strong inside the thick northern arm cloud.

3.4.4. Extinction map

The average extinction we derive is almost 1 mag greater than that determined by Schödel et al. (2010) through star color excess in the same region. Fritz et al. (2011) computed the extinction curve toward the Galactic Center using the same SPIFFI data cube we analyzed and found results in agreement with Schödel et al. (2010). However, they used ionized hydrogen lines to calculate the extinction. These differences are therefore expected. The bulk of extinction is in the foreground and amounts to ∼2.5 K mag, but most of the variation in extinction is local: up to 1 additional magnitude at K. For instance, Paumard et al. (2004) showed that the dust contained in the eastern bridge is responsible for the 0.76 mag extinction of the northern arm at K. The Schödel et al. (2010) A_{Ks} map shows local variations of more than 1 mag as well. However, our map shows even more variations than were reported by Scoville et al. (2003).

The maps also shows different features. The extinction map built by Scoville et al. (2003) exhibits a minimum along the northern arm cloud. In contrast, the extinction map we obtain shows a maximum corresponding to the same cloud. An anticorrelation seems to lead to the interpretation that we are indeed observing an emission from inside the cloud, whereas the extinction inferred by Scoville et al. (2003) concerns the surface of the same cloud.

Our interpretation is that the ionized gas is essentially sensitive to the foreground extinction because it is situated at the surface of clouds, while molecular gas is located more deeply inside a clump. Therefore H_2 emission is more strongly affected by the local variable extinction. Extinction estimation depends on the 3D position of the object that is used as a probe. Extinction maps may differ because the various tracers, stars, ionized gas, and molecular gas, are at different 3D positions and different optical depths.

4. Excitation of the molecular hydrogen

We now investigate the physical properties of the observed H_2 emission in the central parsec. The relative line intensities give information on the gas excitation temperature, while the absolute flux values allow determining the total column density as well as the mass of excited H_2 . Therefore, the comparison of several lines can reveal different specific processes and give important indications on the dominating excitation mechanism. For the comparison of intensities required by the study of the H_2 physical conditions, it is important to gather as many lines as possible to obtain stronger constraints on the gas properties.

In addition to the previously discussed lines, some other lines are detectable: the 1-0 S(2), S(0), Q(2), and 2-1 S(1) lines at 2.0338 μm, 2.2233 μm, 2.4134 μm, and 2.2476 μm.

- The Q(2) line is strongly affected by CO features and it is safely detected only in the northwestern corner, where the CND lies and where all detected lines show a maximum.
- The S(2) line is probably polluted by one or more nearby OH sky lines that are not perfectly subtracted. However, it is detectable in the northwestern half of the field.
- The 2-1 S(1) line is weaker and therefore the S/N is low. This transition is detected mainly at the border of the field, where the CND lies.

These lines are difficult to analyze with the regularized 3D fitting because of the low S/N and nearby atmospheric and stellar features on the spectra (see Fig. 7). No complete maps can be achieved for all detected lines. However, H_2 conditions can be studied through a classical 1D analysis on some regions of the field, where lines are distinctly detectable.

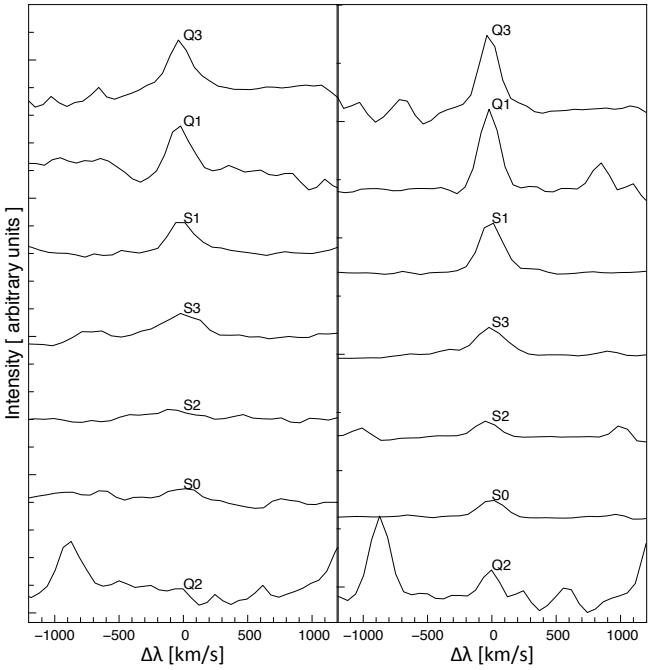

Fig. 7. Ortho (*top*) and para (*bottom*) uncalibrated spectra, arbitrarily shifted along the y-axis for the sake of comparison, averaged across the whole field (*left*) and only over the CND zone 1 (*right*).

4.1. Method

The best choice to correctly compare intensities is to simultaneously fit all the H_2 lines under study. This allows all lines to have the same velocity and width and avoids adding further uncertainties.

4.1.1. Multiline 1D analysis

We considered a spectral window of about 10 000 km s^{-1} around each detectable line and subtracted the continuum. We extracted average spectra over the zones displayed in Fig. 3. The zones were selected with the objective of having as much H_2 lines as possible. However, not all the same H_2 lines are detectable every region. Therefore not all zones present the same number of H_2 lines finally included in the analysis.

For each zone, the set of selected lines was fit with a multiple Gaussian profile function. The parameters of this function are the principal line flux (here 1-0 S(1) because it has the best S/N), the flux ratio of every other line to the principal line, the common velocity, and the width. The retrieved fluxes were dereddened through the A_{Ks} values computed from local average spectrum.

4.1.2. Uncertainties

The statistical errors, given by the fitting procedure, are small (few percents) and do not reflect the true uncertainties. The main source of error is the continuum evaluation, which over- or underestimates the intensity of a given line. This can affect the relative strength of lines and thus the quantities we wish to estimate. The line width and velocity are not much affected: thanks to the simultaneous fit, they are evaluated through many lines at the same time. To evaluate the effect on the line intensity, we considered for each spectral window the difference between the model and the spectrum subtracted from the continuum and computed the interquartile range of this difference. Half of the interquartile range provides the error estimate on the chosen continuum, thus on the intensity. We fit the flux that is related to intensity (I) and width (σ) through $F = I \cdot \sigma \cdot \sqrt{2\pi}$. Therefore the final uncertainty on flux is $\sqrt{2\pi} \cdot (I \cdot \Delta\sigma + \sigma \cdot \Delta I)$, where $\Delta\sigma$ is the statistical uncertainty on the width and ΔI the uncertainty on intensity, estimated through the interquartile range.

4.1.3. Fit of excitation diagrams

Given the dereddened line flux f of a line, the column density of molecules in state $[v, j]$ is $N_{vj} = 4\pi f g_{vj}/(\mathcal{A}_{vj}\Omega)$, where g_{vj} is the degeneracy of the considered state and Ω is the aperture solid angle. The excitation diagram shows N_{vj}/g_{vj} versus the energy of the upper level.

For thermalized populations, N_{vj} is characterized by a Boltzmann distribution:

$$\frac{N_{vj}}{N_{tot}} = \frac{g_{vj} e^{-E_{vj}/T_e}}{\sum_i g_i e^{-E_i/T_e}}, \tag{5}$$

where N_{tot} is the total column density, E_{vj} is the upper level energy, and T_e is the excitation temperature. For an arbitrary excitation mechanism, a distinct excitation temperature might characterize each level. The excitation temperature is representative of the kinetic temperature only in LTE. For more details see Goldsmith & Langer (1999).

We fit a thermal distribution to the observed points,

$$\frac{N_{vj}/g_{vj}}{N_{13}/g_{13}} = a \cdot e^{-(E_{vj}-E_{13})/T_e}, \tag{6}$$

where T_e is the excitation temperature and a is the y-intercept in the log space. The model can be fit using either all observed H_2 lines or the ortho and para lines independently. The first case is equivalent to assuming that the ortho-para ratio (OPR) has the standard the value of 3, which comes from spin statistics. The second case allows testing whether the distribution is thermal, but with a non-standard OPR. Each series of lines could then appear to be well fit by two parallel straight lines. In this case, the offset would correspond to the actual OPR.

The uncertainties on the fit parameters of Eq. 6 have to be carefully considered. Many sources of errors contribute to the final uncertainty, and their propagation is not straightforward. Moreover, the two fitting parameters are correlated, and a classical analytical propagation is not applicable. To overcome these difficulties, we considered the χ^2 map in the $(a, 1/T_e)$ plane. This particular pair of parameters was adopted because it yields the most linear relation in the log space.

The minimum on the χ^2 map corresponds to the best estimates of a and $1/T_e$ parameters. The thermal model corresponding to these best estimates is traced on the excitation diagrams. The associated uncertainties can be estimated through the χ^2 maps. To do so, we ran a Monte Carlo simulation of 10 000 sets of column densities, normally distributed, according to the known uncertainties. Then we fit each simulated set to obtain an estimate of a and $1/T_e$. We calculated the χ^2 value of this best-fit model when compared to the measured column densities. With these 10 000 χ^2 values we traced the contours that enclose the 68%, 95%, and 99% (respectively 1, 2, and 3-σ) of the smallest χ^2 obtained. We calculated the final uncertainties on the fit parameters, considering the highest and lowest values of a and $1/T_e$ that correspond to the 1-σ contour.

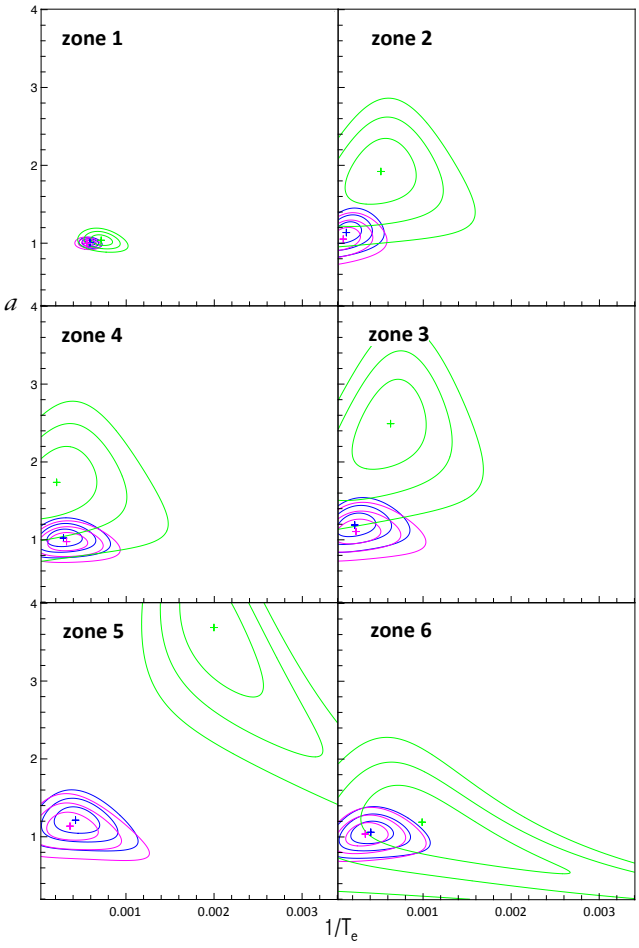

Fig. 8. χ^2 maps in the [$1/T_e$, a] plane for each zone when adjusting a thermal distribution to the data points. The cross indicates the minimum of the χ^2. Contours indicate χ^2 values corresponding to 1, 2, and 3 σ for the all-lines (*blue*), ortho-lines (*magenta*), and para-lines model (*green*).

4.2. Results of the excitation diagram analysis

Figures 8 and 9 compare for the six selected zones the $\chi 2$ maps and the excitation diagrams fit obtained for different sets of lines (all 1-0 lines, ortho or para lines alone), represented in different colors. The objective of this comparison is to infer whether in a given zone the gas is thermalized. Again only six zones are displayed, but the detailed information on the other zones is given in Appendix A.

We considered that the population is thermalized when the all-lines, ortho-lines, and para-lines models are compatible within the uncertainties. This translates into overlapping three 1-sigma contours in the $\chi 2$ space.

The all-lines model is always dominated by the ortho-lines contribution because the ortho lines are the most numerous. The para-lines model is always slightly steeper, tilted toward higher values of $1/T_e$ and a with respect to the other two models, but it remains compatible within 1 σ for zones 1 and 6. These zones correspond to regions in the CND.

In zone 5 the ortho and para models are significantly different by well above three σ. Here, the para-lines model gives lower temperatures and higher values of a, with larger uncertainties than the ortho- and all-lines models. The para-lines model exhibits a 5-σ offset on the $\chi 2$ map with respect to the ortho- and all-lines models. For zones 3 the ortho- and para-lines models show a 2-σ offset. Even though for this zone the effect is less striking, they are most probably not thermalized.

For the other zones (4 and 2) a tilt can be seen but not to a significant level. These areas are located at the border of different specific regions, so that the observed behavior may be the result of an average between different regimes.

Table 2 gives our estimate of the excitation temperature for the zones that are compatible with thermal equilibrium.

4.3. Discussion

4.3.1. Thermalized zones: the CND

For regions where thermalization applies, T_e corresponds to the kinetic temperature of the gas, and the total column density of excited H_2 can be derived from the model parameters:

$$N_{tot} = \frac{N_{13}}{g_{13}} a \cdot e^{E_{13}/T_e} \sum_{vj} g_{vj} e^{-E_{vj}/T_e}. \quad (7)$$

Excitation temperature and column density

The derived temperatures are quite high, ranging from 1 700 K to 3 100 K, but below the H_2 dissociation temperature ($\sim$ 4 000–5 000 K). The values are very high with respect to previous measurements (400 K in Genzel et al. 1985, 200–300 K in Mills et al. 2015 in the CND). On the other hand, very high temperatures have previously been observed in other analyses of NIR H_2 lines, such as in the Crab nebula, where Loh et al. (2011) found temperatures in the range of 2 000–3 000 K using several H_2 lines in the range 2.02–2.33 μm (among others the 1-0 S(0), S(1), S(2)).

Knowing the total column density can be roughly estimated as $N_{tot} D^2 S M_{H_2}/M_\odot$, where S in the solid angle covered by the region in steradians and M_{H_2} the mass of a single H_2 molecule. For instance, we considered the thermalized all-lines model of zone 1 across a surface of $\sim$ 13 arcsec^2 and a distance to the Galactic Center of D = 8 kpc. The mass of excited H_2 contained in zone 1 is 7^{+4}_{-3} 10^{-3} $M_\odot$. Christopher et al. (2005) studied the HCN emission in the CND and obtained a typical mass per cloud of 2–3 10^4 $M_\odot$ and a total gas mass of 10^6 $M_\odot$.

In summary, the analysis of H_2 lines shows that the inferred temperatures are much higher and the masses apparently much lower than is estimated with observations of other molecules (CO, NH_3). This is clearly because the molecular hydrogen detected through those infrared lines is only the most excited one. In the determination of the column density, hot H_2 dominates the intensity, making the results very sensitive to the thermal structure of the cloud. Only a small fraction of H_2 , but at high temperature, is responsible for the observed column densities. If the portion of the CND that is covered by the SPIFFI dataset (at least the equivalent of one extended cloud) had a mass of 10^4 M⊙ , at 400 K, it follows from Eq. 5 that the flux of the 1-0 S(1) line would be almost 10 times weaker than observed. The emission from excited H_2 is likely to come from the UV illuminated skin of the clouds that form the CND. Only the H_2 located in a thin shell at the surface of these clouds would be heated by either the UV field or by collisions, presumably from stellar winds or cloud-cloud collisions.

Simulation made with the Meudon code (Le Petit et al. 2006) of the standard conditions of a PDR are coherent with this result (J. Le Bourlot, private communication). In these simulations the considered parameters are a total optical depth A_V = 10, density

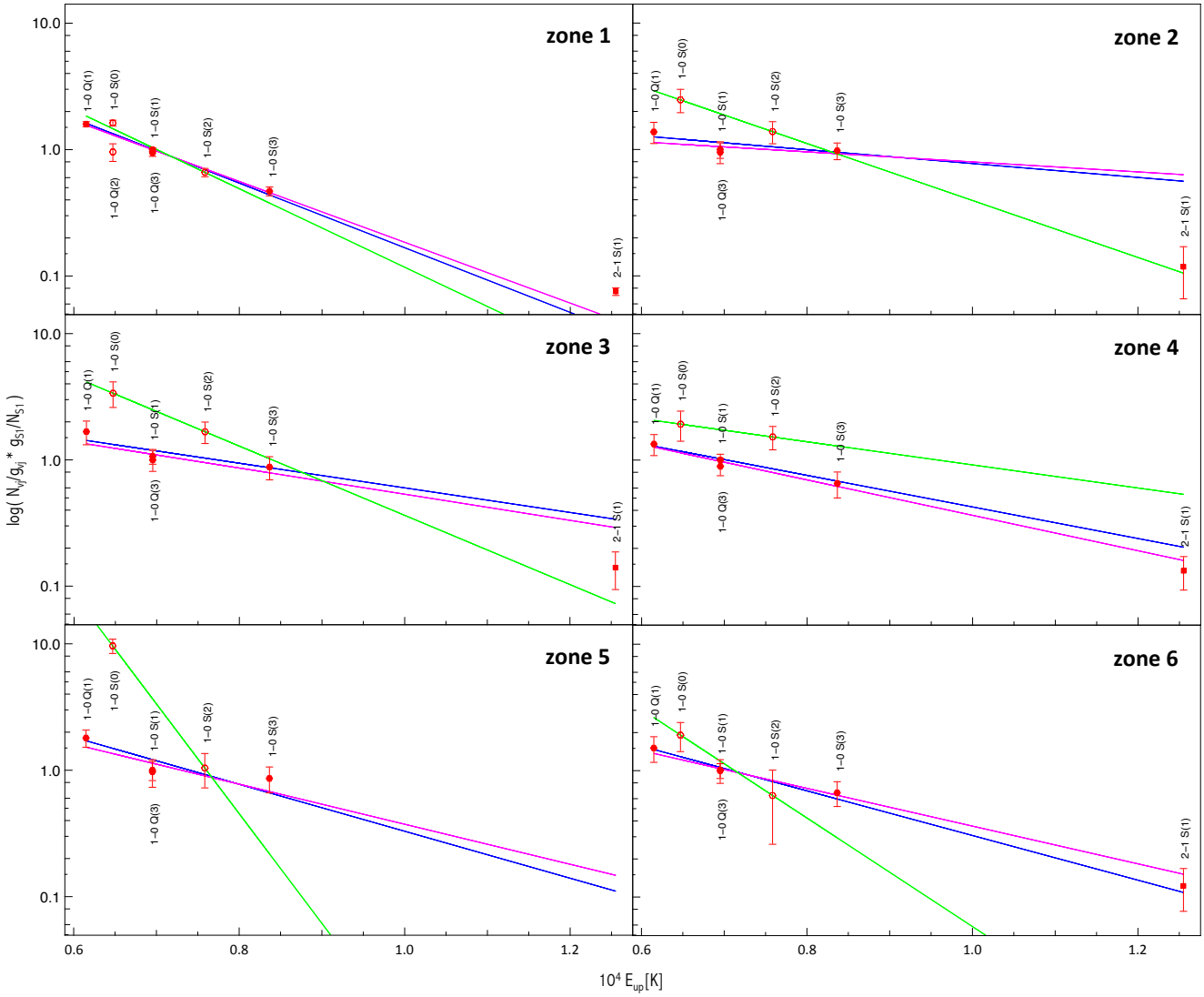

Fig. 9. Excitation diagram of column densities ($log(\frac{N_{vj}/g_{vj}}{N_{13}/g_{13}})$ versus upper level energy expressed in K) for each zone. Colored straight lines correspond to the best thermal model for all-lines (*blue*), ortho-lines (*magenta*), and para-lines (*green*).

		all-lines model		ortho-lines model		para-lines model	
zone	1-0 S(1)/2-1 S(1)	T_e	N_{tot}	T_e	N_{tot}	T_e	N_{tot}
1	9.8	1700^{+150}_{-150}	27^{+11}_{-7}	1800^{+200}_{-150}	22^{+10}_{-6}	1400^{+280}_{-150}	53^{+66}_{-27}
6	6	2460^{+3030}_{-940}	4^{+11}_{-2}	2910^{+5010}_{-940}	3^{+8}_{-1}	1010^{+2470}_{-940}	> 1

Table 2. 1-0 S(1) to 2-1 S(1) ratio, excitation temperature (in K), and total column density (in 10^{22}·m^{-2}) for zones where thermalization applies. These values are estimated with a fit of all-lines, ortho-lines and para-lines (where possible) with a thermal distribution.

$=10^3$ cm^{-3}, 100 times the interstellar radiation field, and solar abundances. The result is that almost all excited gas is located in the $A_V = 0.14$ layer and 30% of the emitting gas is in the $A_V = 0.014$ layer, that is, in 1/700 of the volume.

The huge initial discrepancy with the results of Christopher et al. (2005) is largely reduced, but still there is a large gap, which may indicate that a high percentage of the hot gas is not seen at all because of a high dust opacity. Considering that the PDR conditions in the Sgr A* region are more extreme than elsewhere (Güsten 1989), with 90% of the ionizing flux coming from OB supergiants and Wolf-Rayet stars (Martins et al. 2007), an additional factor could be applied.

This result is consistent with previous results from Loh et al. 2011 for the Crab nebula and Scoville et al. (1982) for Orion, for example. Loh et al. 2011 proposed the same interpretation: the hotter H_2 is only a small fraction of the total cloud mass,

but this source dominates the intensity. They found that the H_2 traced by NIR lines is 1/1000 of the total mass. Similarly, in Orion Scoville et al. (1982) found a H_2 mass around 10^{-2} M⊙, significantly lower than predicted by models. Hence on one hand, the cooler molecular hydrogen is missed because its too low temperature prevents its detection, and on the other hand, the huge dust opacity must block most of the emission of the hot component.

Excitation mechanism

The two main mechanisms that can excite the molecular hydrogen are UV pumping and shocks. The 1-0 S(1) to 2-1 S(1) ratio (Shull & Hollenbach 1978), is a useful tool in principle for distinguishing between these two possibilities.

The high 1-0 S(1) to 2-1 S(1) ratio in zone 1 is consistent with a shock-excited gas. Even though for dense PDRs, UV-excited H_2 can produce a ratio that resembles shock-excited gas (Sternberg & Dalgarno 1989), for zone 1 our result seems fairly consistent with previous conclusions of a shock-driven excitation. Yusef-Zadeh et al. (2001), for instance, argued that the emission arises from shocks deriving from random motions of clouds for a clumpy medium or of turbulence for a more homogeneous one.

For zone 6 the ratio drops to values midway between 10 and 1. The thermalization observed for these zones can be produced by either shock or collisional fluorescence. Since these zones show 1-0 S(1) to 2-1 S(1) ratios significantly lower than 10, shock excitation seems to be ruled out, which leaves collisional fluorescence as the favored scenario. This is in contrast with the opposite corner of the SPIFFI field, which is more probably dominated by collisional excitation. Moreover, Burton & Allen (1993) interpreted these values as indicative of collisional fluorescence.

4.3.2. Nonthermalized zones: the central cavity

The population in the central cavity is almost certainly not thermalized. No kinetic temperature and total column density can be determined straightforwardly. Nevertheless, the fitting parameters are reported in the appendix for completeness and to compare the results obtained for the distinct sets of lines. These values have to be interpreted as indicators of a trend of temperature and column density, and they have to be considered cautiously.

Again, the observed H_2 only represents the most excited fraction. However, the density in the central cavity drops by one order of magnitude (Jackson et al. 1993b; Davidson et al. 1992, among others) and the interpretation of the emitting gas as a thin layer at the border of clouds does not necessarily apply. For instance, the 1-0 S(1) width map and the extinction map indicate that part of the emission comes from inside the northern arm cloud. This might explain that the H_2 emission is detected from inside the northern arm cloud, but not from inside the CND. In the CND clouds the emission remains confined at the surface because of the higher density, which allows an efficient self-shielding. The clumpy environment of the northern arm cloud and the stronger UV field in contrast allow the radiation to penetrate deeper inside the cloud.

Elsewhere in the central cavity, the gas might be more diffuse and distributed in larger volumes. In this case, the observed intensities might represent a higher percentage of the total gas mass.

Excitation mechanism

The excitation diagram shape, which indicates that it is caused by nonthermalized gas, suggests that the excitation is provided by other sources than shock, such as UV or X-rays. The UV density must be much higher, as testified by the streamers of ionized gas.

The shape of the excitation diagram can be reproduced by a UV-pumped mechanism (E. Bron private communication). However, this model fails to reproduce the high intensities we observe. The central cavity environment is very complex, and several mechanisms may contribute to excite the gas. Different interpretations probably apply to the northern arm cloud emission, the region south of GCIRS 7 and the minicavity (zone 5).

In particular, zone 5 is the region that corresponds to the strong flux enhancement of the para line 1-0 S(0) seen in its flux map (cf. Fig. 4, Sect. 3.2.2). This zone is particularly challenging to explain. In this region all 1-0 lines align quite well on a straight line and only S(0) strongly deviates in the excitation diagram. We note that the other para line (1-0 S(2)) does not deviate, which excludes an OPR effect. A possible explanation of this discrepancy might be found in the timescale of the H_2 formation and destruction process. The tentative explanation that we propose is that

a) the central cavity has a higher density of UV photons and cosmic rays;
b) in an energetic region like this, H_2 molecules are more rapidly destroyed and therefore have a shorter mean lifetime, during which thermalization cannot fully occur;
c) if this holds true, we would mostly observe recently formed H_2 molecules that may form mainly as the para isomer and did not yet reach the equilibrium where OPR=3 ;
d) in addition, it is possible for molecular hydrogen to be formed in a state where peculiar energetic states are favored, such as the upper level of S(0), for instance.

Of course this hypothesis requires a realistic modeling to be supported in a more precise way, and work has been started in this direction. Finally, a modeling involving UV pumping seems very promising to explain the minicavity emission. A more detailed study of this region will be the object of a future research.

5. Conclusions

We have studied the NIR H_2 emission in the central parsec of the Galaxy. Our analysis was divided into two main parts.

In the first part (Sect. 3) we studied the gas distribution and dynamics. Thanks to the new regularized 3D fitting, we were able to probe the morphology of H_2 in the central cavity. We provided a high-resolution map of the 1-0 S(1) line emission together with its velocity and width maps. The same was done for the other detectable ortho lines. The flux maps are compatible with previous studies, and the velocity is consistent with the dynamics of the CND. The new method allowed us to build an extinction map for the molecular gas as well. The shapes of the flux and of the width maps together suggest that there are two main components of the emission. In addition to the CND emission, a second component corresponds to the central cavity and it might be situated in the background, that is, behind the minispiral or in the central parsec itself.

This ambiguity was clearly solved in the second part of our study (Sect. 4) through the multiline analysis. The comparison between the fluxes of each of the detectable lines allowed us to

draw the excitation diagrams of the gas in several zones of the field. For the CND we found very high temperatures and very low masses compared to estimates obtained through CO observations. The reason is that the lines we observe trace only the very hot gas. This gas is a small fraction of the total amount, a thin layer at the surface of cooler clouds. In addition, we had to invoke high dust opacities to explain the huge discrepancy. The observation of the emission from the northern arm cloud confirms the close relationship between the CND and the minispiral. In the rest of the central cavity we observed a very high emission of S(0), especially in the zone close to the entrance of the mini-cavity. Here H_2 probably has a short mean lifetime because of the strong UV radiation. We tentatively proposed that the quick processes of destruction and formation of new H_2 molecules favors S(0) over other lines. This preliminary analysis shows that there are several different areas in a volume as small as the zone inside the rim of the CND. Each feature shows some very peculiar conditions that can be attained only in an extreme environment such as the central parsec.

Since we did not observe evidence of a motion of H_2 from the CND toward the central cavity, this molecular gas might be thought to be produced locally, but the mechanism is still unclear. One possible interpretation, supported by simulations by Cuadra et al. (2005), is that the combined wind from the many mass-loosing stars in the central parsec provides the material and energy to build a plasma, as well the dust grains on which H_2 forms. If this were found to be true, it would explain our observations. On the other hand, the observed emission might arise from H_2 produced in denser regions and then brought into the central cavity by small-scale inward-motions that are able to escape detection in the velocity map. Additional studies are needed to conclude on one or the other hypothesis.

Acknowledgements. We would like to thank the infrared group at the Max Planck Institute for Extraterrestrial Physics (MPE), who built the SPIFFI instrument, carried out the observations, and provided the data. We thank E. Bron, J. Le Bourlot and F. Le Petit for the simulations of H_2 in PDR and useful discussions. We are also grateful to N. Scoville for his comments and suggestions. This work is partially supported by the OPTICON project (EC FP7 grant agreement 312430) in "Image reconstruction in optical interferometry" WP4.

References

Bartko, H., Martins, F., Fritz, T. K., et al. 2009, ApJ, 697, 1741
Blum, R. D., Ramirez, S. V., Sellgren, K., & Olsen, K. 2003
Burton, M. & Allen, D. 1993, in Astronomical Society of the Pacific Conference Series, Vol. 41, Astronomical Infrared Spectroscopy: Future Observational Directions, ed. S. Kwok, 289
Christopher, M. H., Scoville, N. Z., Stolovy, S. R., & Yun, M. S. 2005, ApJ, 622, 346
Ciurlo, A. 2015, PhD thesis, Université Paris Diderot – Paris 7, Sorbonne Paris Cité, ED 127
Cuadra, J., Nayakshin, S., Springel, V., & Di Matteo, T. 2005, Monthly Notices of the Royal Astronomical Society: Letters, 360, L55
Davidson, J. A., Werner, M. W., Wu, X., et al. 1992, ApJ, 387, 189
Eckart, A., Genzel, R., Krabbe, A., et al. 1992, Nature, 355, 526
Eisenhauer, F., Tecza, M., Thatte, N., et al. 2003, The Messenger, 113, 17
Ekers, R. D., van Gorkom, J. H., Schwarz, U. J., & Goss, W. M. 1983, A&A, 122, 143
Fritz, T. K., Gillessen, S., Dodds-Eden, K., et al. 2011, ApJ, 737, 73
Gatley, I., Jones, T. J., Hyland, A. R., et al. 1986, MNRAS, 222, 299
Gautier, III, T. N., Fink, U., Larson, H. P., & Treffers, R. R. 1976, ApJ, 207, L129
Genzel, R., Crawford, M. K., Townes, C. H., & Watson, D. M. 1985, ApJ, 297, 766
Goldsmith, P. F. & Langer, W. D. 1999, ApJ, 517, 209
Green, P. 1990, Medical Imaging, IEEE Transactions, Volume:9, 84
Guesten, R., Genzel, R., Wright, M. C. H., et al. 1987a, ApJ, 318, 124
Guesten, R., Genzel, R., Wright, M. C. H., et al. 1987b, ApJ
Güsten, R. 1989, in IAU Symposium, Vol. 136, The Center of the Galaxy, ed. M. Morris, 89
Haubois, X., Dodds-Eden, K., Weiss, A., et al. 2012, A&A, 540, A41
Horrobin, M., Eisenhauer, F., Tecza, M., et al. 2004, Astronomische Nachrichten, 325, 88
Jackson, J. M., Geis, N., Genzel, R., et al. 1993a, ApJ, 402, 173
Jackson, J. M., Geis, N., Genzel, R., et al. 1993b, ApJ, 402, 173
Le Petit, F., Nehmé, C., Le Bourlot, J., & Roueff, E. 2006, ApJS, 164, 506
Liszt, H. S. 2003, A&A, 408, 1009
Lo, K. Y. & Claussen, M. J. 1983, Nature, 306, 647
Loh, E. D., Baldwin, J. A., Ferland, G. J., et al. 2011, Monthly Notices of the Royal Astronomical Society, 421
Marr, J. M., Rudolph, A. L., Pauls, T. A., Wright, M. C. H., & Backer, D. C. 1992, ApJ, 400, L29
Martins, F., Genzel, R., Eisenhauer, F., et al. 2007, Highlights of Astronomy, 14, 207
Mills, E. A. C., Sun, B., Liu, H. B., et al. 2015, in American Astronomical Society Meeting Abstracts, Vol. 225, American Astronomical Society Meeting Abstracts, 142
Modigliani, A., Hummel, W., Abuter, R., et al. 2007
Mugnier, L. M., Fusco, T., & Conan, J.-M. 2004, J. Opt. Soc. Am. A, 21, 1841
Mugnier, L. M., Robert, C., Conan, J.-M., Michau, V., & Salem, S. 2001, J. Opt. Soc. Am. A, 18, 862
Paumard, T., Genzel, R., Martins, F., et al. 2006, Journal of Physics Conference Series, 54, 199
Paumard, T., Maillard, J.-P., & Morris, M. 2004, A&A, 426, 81
Paumard, T., Morris, M. R., Do, T., & Ghez, A. 2014, in IAU Symposium, Vol. 303, IAU Symposium, ed. L. O. Sjouwerman, C. C. Lang, & J. Ott, 109–113
S. Brette, J. I. 1996, Proceedings of the International Conference on Image Processing
Schödel, R., Najarro, F., Muzic, K., & Eckart, A. 2010, A&A, 511, A18
Scoville, N. Z., Hall, D. N. B., Ridgway, S. T., & Kleinmann, S. G. 1982, ApJ, 253, 136
Scoville, N. Z., Stolovy, S. R., Rieke, M., Christopher, M., & Yusef-Zadeh, F. 2003, ApJ, 594, 294
Shull, J. M. & Hollenbach, D. J. 1978, ApJ, 220, 525
Sternberg, A. & Dalgarno, A. 1989, ApJ, 338, 197
Tanner, A., Ghez, A. M., Morris, M., et al. 2002, ApJ, 575, 860
Tecza, M., Thatte, N., Eisenhauer, F., et al. 2000
Yusef-Zadeh, F., Stolovy, S. R., Burton, M., Wardle, M., & Ashley, M. C. B. 2001, ApJ, 560, 749

Appendix A: Plots and tables for all sixteen zones

		all-lines model		ortho-lines model		para-lines model	
zone	1-0 S(1)/2-1 S(1)	T_e	N_{tot}	T_e	N_{tot}	T_e	N_{tot}
1	9.8	1700^{+150}_{-150}	27^{+11}_{-7}	1800^{+200}_{-150}	22^{+10}_{-6}	1400^{+280}_{-150}	53^{+66}_{-27}
6	6	2460^{+3030}_{-940}	4^{+11}_{-2}	2910^{+5010}_{-940}	3^{+8}_{-1}	1010^{+2470}_{-940}	> 1
7	6.8	3100^{+4400}_{-1220}	7^{+13}_{-1}	3560^{+7400}_{-1220}	6^{+10}_{-4}	-	-
9	9	2300^{+730}_{-450}	6^{+5}_{-2}	2340^{+830}_{-450}	6^{+5}_{-2}	1720^{+1940}_{-450}	15^{+90}_{-11}

Table A.1. Top : 1-0 S(1) to 2-1 S(1) ratio, excitation temperature (in K), and total column density (in $10^{22}\cdot m^{-2}$) for each zone where thermalization applies. These values are estimated with a fit of all-lines, ortho-lines, and para-lines models (where possible) with a thermal distribution.

		all-lines model		ortho-lines model		para-lines model	
zone	1-0 S(1)/2-1 S(1)	T_e	N_{tot}	T_e	N_{tot}	T_e	N_{tot}
2	6.3	> 3390	< 5	> 6440	< 10	< 8910	< 168
3	5.3	4460^{+43070}_{-2260}	2^{+3}_{-16}	$4320^{+138250}_{-2260}$	2^{+5}_{-30}	1580^{+3700}_{-2260}	21^{+276}_{-18}
4	5.6	> 3333	< 13	> 1630	< 17	> 3280	< 58
5	-	2340^{+2940}_{-910}	5^{+21}_{-3}	2740^{+6760}_{-910}	4^{+18}_{-0}	< 620	> 8640
8	-	> 2130	< 6	> 13000	< 19	-	-
10	6.5	3240^{+2460}_{-1010}	4^{+3}_{-1}	3960^{+4430}_{-1010}	3^{+2}_{-1}	1320^{+940}_{-1010}	38^{+341}_{-32}
11	-	> 2850	< 5	3050	< 5	< 3030	> 4
12	3.3	> 2230	< 7	> 2040	< 9	< 1440	> 25
13	-	> 3960	< 19	> 30000	< 32	< 140000	> 12
14	5.6	2500^{+1250}_{-670}	3^{+5}_{-1}	2550^{+1650}_{-670}	3^{+5}_{-1}	1300^{+1040}_{-670}	32^{+265}_{-28}
15	6.8	2070^{+620}_{-390}	8^{+8}_{-4}	2190^{+780}_{-390}	7^{+8}_{-3}	1210^{+620}_{-390}	71^{+414}_{-59}
16	7.9	1980^{+480}_{-340}	7^{+7}_{-3}	2040^{+560}_{-340}	6^{+6}_{-3}	1470^{+870}_{-340}	22^{+94}_{-17}

Table A.2. Best-fit parameters obtained when considering a thermal distribution on all-, ortho-, and para-lines models are added for each zone. These values are valid under the assumption of thermalized populations, which does not apply to these regions. They therefore have to be considered with caution as indicators of a trend of temperature and column density. Apparent T_e is in K, apparent N_{tot} is in $10^{22}\cdot m^{-2}$.

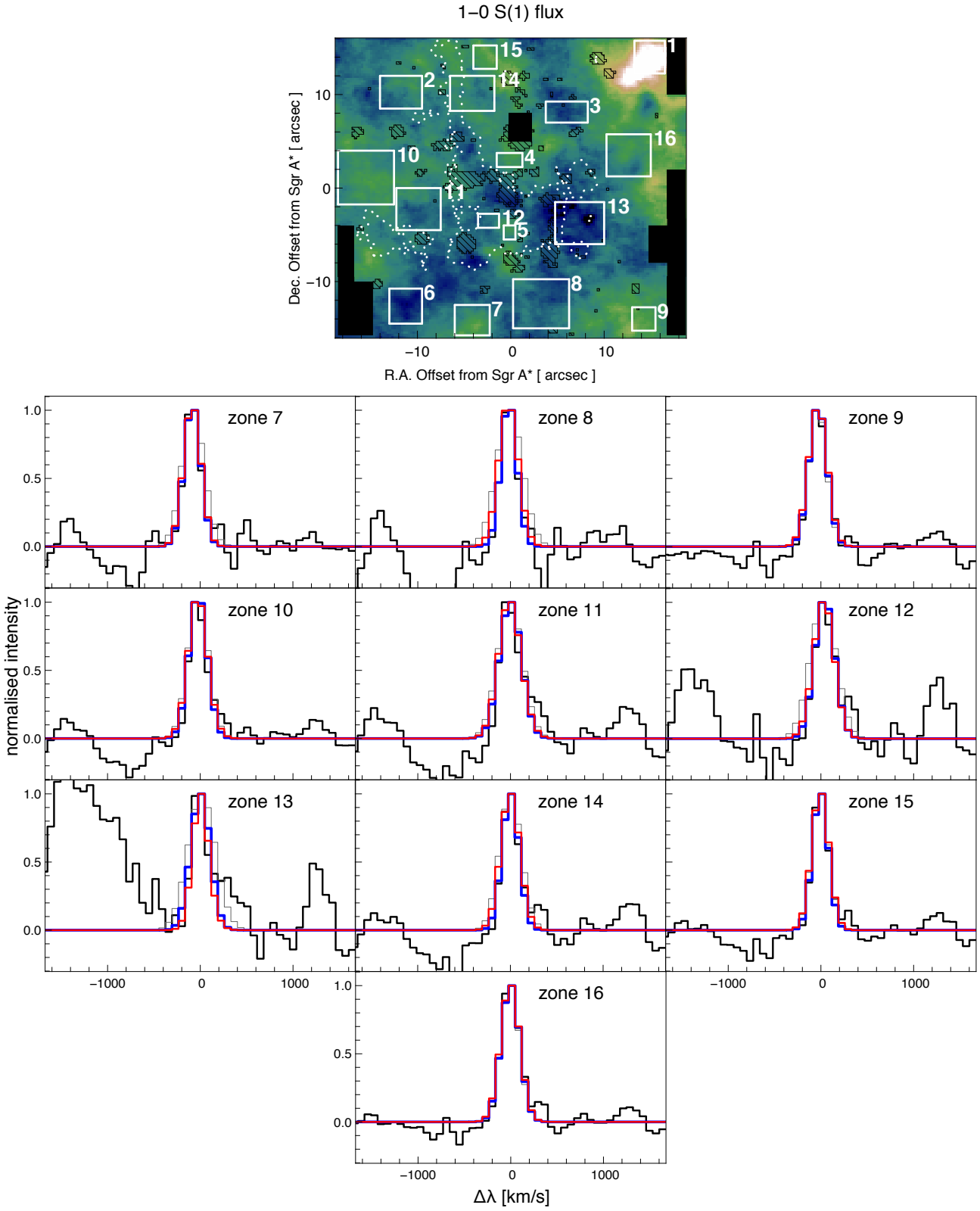

Fig. A.1. *Top left:* Zones where individual spectra of S(1) line have been extracted, superimposed on the flux map. *Bottom:* for each zone we plot the normalized average spectrum (black) superimposed with the respective pixel by pixel model (solid blue) and regularized 3D model (solid red). The gray line reproduces another solution of the regularized 3D fitting. Both solutions have similar values of $\chi 2$ (1.15 and 1.49, respectively), but the red model fits the observations much better.

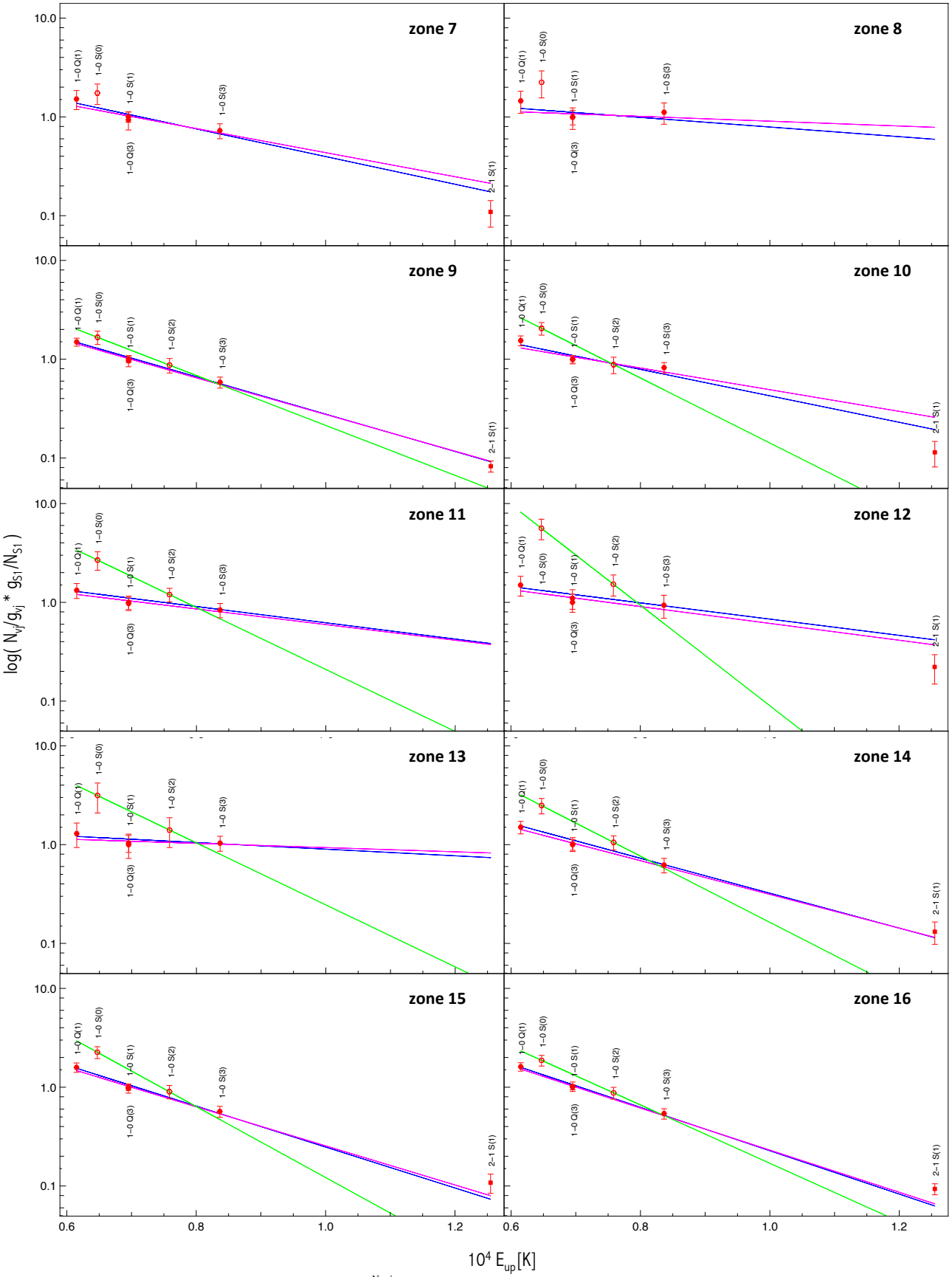

Fig. A.2. Excitation diagram of column densities ($log(\frac{N_{vj}/g_{vj}}{N_{13}/g_{13}})$ versus upper level energy expressed in K) for each zone. Colored straight lines correspond to the best thermal model for all-lines (*blue*), ortho-lines (*magenta*), and para-lines (*green*) models.

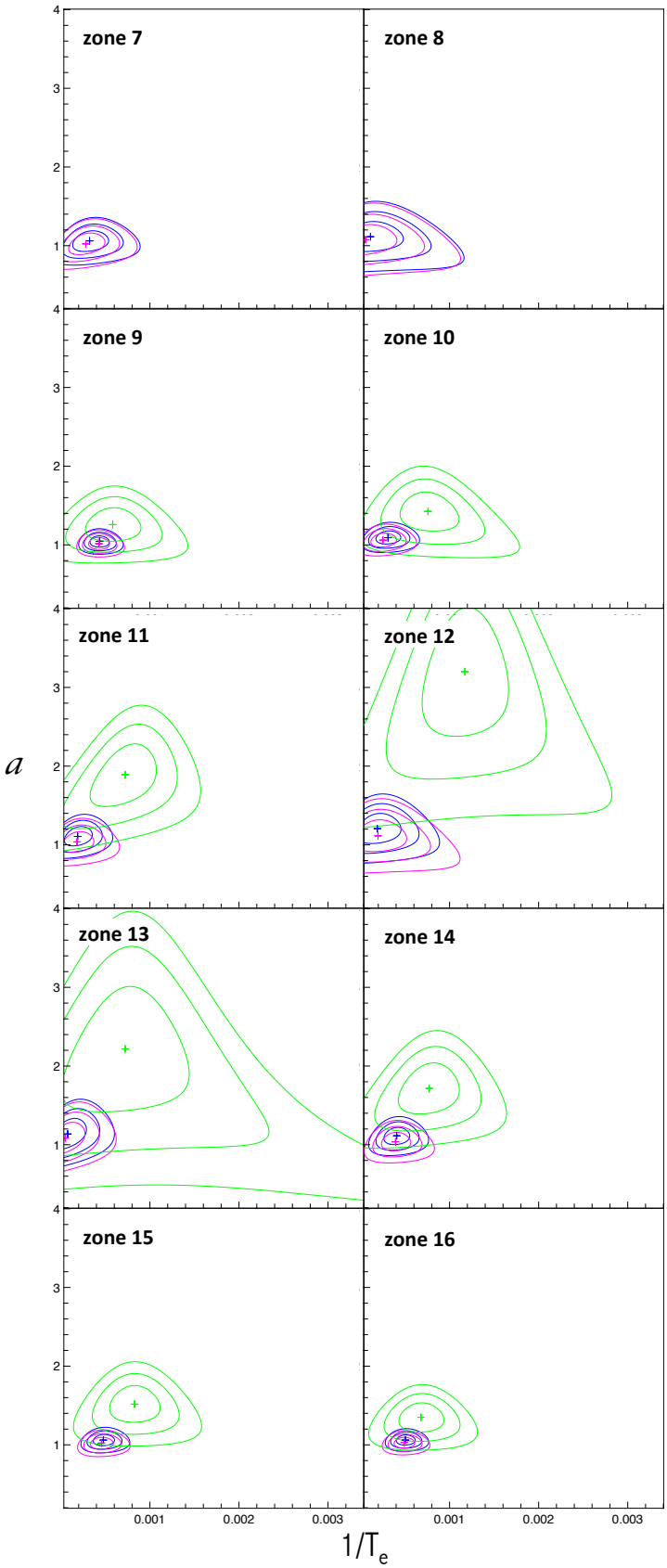

Fig. A.3. χ^2 maps for each zone. The cross indicates the minimum of the χ^2. Contours indicates the χ^2 values corresponding to 1, 2, and 3 σ. On the same map the all-lines (*blue*), ortho-lines (*magenta*), and para-lines model (*green*) are superimposed.

Bibliography

Allen, D. A., Hyland, A. R., & Hillier, D. J. 1990, MNRAS, 244, 706 (cited on page 10)

Baganoff, F. K., Maeda, Y., Morris, M., et al. 2003, ApJ, 591, 891 (cited on pages 2, 5 and 7)

Balick, B. & Brown, R. L. 1974, ApJ, 194, 265 (cited on page 11)

Bally, J., Stark, A. A., Wilson, R. W., & Henkel, C. 1988, ApJ, 324, 223 (cited on page 4)

Bartko, H., Martins, F., Fritz, T. K., et al. 2009, ApJ, 697, 1741 (cited on pages 10, 30, 32, 33, 34, 35, 36 and V)

Beckert, T., Duschl, W. J., Mezger, P. G., & Zylka, R. 1996, A&A, 307, 450 (cited on page 11)

Becklin, E. E., Gatley, I., & Werner, M. W. 1982, ApJ, 258, 135 (cited on pages 4, 6, 98 and I)

Becklin, E. E. & Neugebauer, G. 1968, ApJ, 151, 145 (cited on pages 9 and 10)

Beckwith, S., Evans, II, N. J., Gatley, I., Gull, G., & Russell, R. W. 1983, ApJ, 264, 152 (cited on pages 79, 103 and 131)

Binney, J., Gerhard, O. E., Stark, A. A., Bally, J., & Uchida, K. I. 1991, MNRAS, 252, 210 (cited on page 4)

Black, J. H. & Dalgarno, A. 1976, ApJ, 203, 132 (cited on pages 103 and XIII)

Blum, R. D., Ramirez, S. V., Sellgren, K., & Olsen, K. 2003 (cited on pages 10, 30, 32, 33, 34, 35, 36 and V)

Brown, R. L. & Johnston, K. J. 1983, ApJ, 268, L85 (cited on page 9)

Burton, M. & Allen, D. 1993, in Astronomical Society of the Pacific Conference Series, Vol. 41, Astronomical Infrared Spectroscopy: Future Observational Directions, ed. S. Kwok, 289 (cited on pages 9, 97, 103, 112 and XIII)

Catchpole, R. M., Whitelock, P. A., & Glass, I. S. 1990, MNRAS, 247, 479 (cited on page 9)

Christopher, M. H., Scoville, N. Z., Stolovy, S. R., & Yun, M. S. 2005, ApJ, 622, 346 (cited on pages 6, 61, 62, 63, 66, 92, 111, 112, 126, 131, I, II and IX)

Combes, F. & Pineau Des Forets, G., eds. 2000, Molecular Hydrogen in Space (cited on page 15)

Cuadra, J., Nayakshin, S., Springel, V., & Di Matteo, T. 2005, Monthly Notices of the Royal Astronomical Society: Letters, 360, L55 (cited on pages 127 and 128)

Dalgarno, A. 2000, in Molecular Hydrogen in Space, ed. F. Combes & G. Pineau Des Forets, 3–12 (cited on page 13)

Davidson, J. A., Werner, M. W., Wu, X., et al. 1992, ApJ, 387, 189 (cited on pages 7, 9, 113, 126 and II)

Davies, R. I., Sternberg, A., Lehnert, M., & Tacconi-Garman, L. E. 2003, ApJ, 597, 907 (cited on page 101)

Depoy, D. L. 1992, ApJ, 398, 512 (cited on pages 9, 28 and 133)

Depoy, D. L., Gatley, I., & McLean, I. S. 1989, in IAU Symposium, Vol. 136, The Center of the Galaxy, ed. M. Morris, 411 (cited on page 9)

Downes, D. & Martin, A. H. M. 1971, Nature, 233, 112 (cited on pages 4 and I)

Draine, B. T. & McKee, C. F. 1993, ARA&A, 31, 373 (cited on pages 18 and III)

Eckart, A. & Genzel, R. 1997, MNRAS, 284, 576 (cited on page 11)

Eckart, A., Genzel, R., Krabbe, A., et al. 1992, Nature, 355, 526 (cited on pages 9, 65, 115 and XV)

Eckart, A., Genzel, R., Ott, T., & Schödel, R. 2002, MNRAS, 331, 917 (cited on page 11)

Eisenhauer, F., Perrin, G., Brandner, W., et al. 2008, in Society of Photo-Optical Instrumentation Engineers (SPIE) Conference Series, Vol. 7013, Society of Photo-Optical Instrumentation Engineers (SPIE) Conference Series, 2 (cited on page 18)

Eisenhauer, F., Tecza, M., Mengel, S., et al. 2000, in Society of Photo-Optical Instrumentation Engineers (SPIE) Conference Series, Vol. 4008, Optical and IR Telescope Instrumentation and Detectors, ed. M. Iye & A. F. Moorwood, 289–297 (cited on pages 22, 23 and V)

Eisenhauer, F., Tecza, M., Thatte, N., et al. 2003, The Messenger, 113, 17 (cited on pages 26 and V)

Ekers, R. D., van Gorkom, J. H., Schwarz, U. J., & Goss, W. M. 1983, A&A, 122, 143 (cited on pages 9, 126 and II)

Ferrière, K. 2009, A&A, 505, 1183 (cited on page 4)

Fritz, T. K., Gillessen, S., Dodds-Eden, K., et al. 2011, ApJ, 737, 73 (cited on pages 26, 32, 76, 77, 78, 82, V and X)

Frogel, J. A. 1988, in Astrophysics and Space Science Library, Vol. 141, Towards Understanding Galaxies at Large Redshift, ed. R. G. Kron & A. Renzini, 1–14 (cited on page 3)

Fuente, A., Martín-Pintado, J., Rodríguez-Fernández, N. J., et al. 1999, ApJ, 518, L45 (cited on pages 16 and 109)

Gatley, I., Beattie, D. H., Lee, T. J., Jones, T. J., & Hyland, A. R. 1984, MNRAS, 210, 565 (cited on pages 7 and 126)

Gatley, I., Jones, T. J., Hyland, A. R., et al. 1986, MNRAS, 222, 299 (cited on pages 7, 19 and IV)

Gautier, III, T. N., Fink, U., Larson, H. P., & Treffers, R. R. 1976, ApJ, 207, L129 (cited on pages 79 and IX)

Genzel, R., Crawford, M. K., Townes, C. H., & Watson, D. M. 1985, ApJ, 297, 766 (cited on pages 110 and 126)

Genzel, R., Eisenhauer, F., & Gillessen, S. 2010, Reviews of Modern Physics, 82, 3121 (cited on pages 3 and I)

Genzel, R., Hollenbach, D., & Townes, C. H. 1994, Reports on Progress in Physics, 57, 417 (cited on pages 3, 6, 9, 12 and I)

Genzel, R., Pichon, C., Eckart, A., Gerhard, O. E., & Ott, T. 2000, MNRAS, 317, 348 (cited on page 10)

Genzel, R., Schödel, R., Ott, T., et al. 2003a, Nature, 425, 934 (cited on page 2)

Genzel, R., Schödel, R., Ott, T., et al. 2003b, ApJ, 594, 812 (cited on page 10)

Gezari, D. and Dwek, E. and Varosi F. 2003, Astronomische Nachrichten Supplement, 324, 573 (cited on page 7)

Ghez, A. M., Duchêne, G., Matthews, K., et al. 2003, ApJ, 586, L127 (cited on page 10)

Ghez, A. M., Klein, B. L., Morris, M., & Becklin, E. E. 1998, ApJ, 509, 678 (cited on pages 10 and 11)

Ghez, A. M., Morris, M., Becklin, E. E., Tanner, A., & Kremenek, T. 2000, Nature, 407, 349 (cited on page 11)

Ghez, A. M., Salim, S., Hornstein, S. D., et al. 2005, ApJ, 620, 744 (cited on pages 1 and I)

Gillessen, S., Eisenhauer, F., Perrin, G., et al. 2010, in Society of Photo-Optical Instrumentation Engineers (SPIE) Conference Series, Vol. 7734, Society of Photo-Optical Instrumentation Engineers (SPIE) Conference Series, 0 (cited on page 18)

Ginsburg, A., Henkel, C., Ao, Y., et al. 2015, ArXiv e-prints (cited on page 3)

Goldsmith, P. F. & Langer, W. D. 1999, ApJ, 517, 209 (cited on page 102)

Green, P. 1990, Medical Imaging, IEEE Transactions, Volume:9, 84 (cited on page 39)

Guesten, R. & Downes, D. 1980, in Astron. Soc. Inform., 76–79 (cited on page 3)

Guesten, R., Genzel, R., Wright, M. C. H., et al. 1987, ApJ, 318, 124 (cited on pages 6, 7 and I)

Güsten, R. 1989, in IAU Symposium, Vol. 136, The Center of the Galaxy, ed. M. Morris, 89 (cited on pages 2, 3, 9, 112, II and III)

Habart, E., Walmsley, M., Verstraete, L., et al. 2005, Space Sci. Rev., 119, 71 (cited on page 13)

Harvey, P. M., Campbell, M. F., & Hoffmann, W. F. 1976, ApJ, 205, L69 (cited on page 4)

Haubois, X., Dodds-Eden, K., Weiss, A., et al. 2012, A&A, 540, A41 (cited on page 85)

Hollenbach, D. J. & Tielens, A. G. G. M. 1997, ARA&A, 35, 179 (cited on pages 18 and III)

Hollenbach, D. J. & Tielens, A. G. G. M. 1999, Reviews of Modern Physics, 71, 173 (cited on pages 17 and III)

Horrobin, M., Eisenhauer, F., Tecza, M., et al. 2004, Astronomische Nachrichten, 325, 88 (cited on pages 23, 26 and V)

Jackson, J. M., Geis, N., Genzel, R., et al. 1993, ApJ, 402, 173 (cited on pages 6, 7, 19, 67, 113 and II)

Koyama, K., Maeda, Y., Sonobe, T., & Tanaka, Y. 1996, in Roentgenstrahlung from the Universe, ed. H. U. Zimmermann, J. Trümper, & H. Yorke, 315–318 (cited on page 4)

Krabbe, A., Genzel, R., Eckart, A., et al. 1995, ApJ, 447, L95 (cited on page 10)

Lau, R. M., Herter, T. L., Morris, M. R., Becklin, E. E., & Adams, J. D. 2013, ApJ, 775, 37 (cited on page 122)

Le Bourlot, J. 2000, A&A, 360, 656 (cited on page 16)

Le Bourlot, J. 2008, in EAS Publications Series, Vol. 31, EAS Publications Series, ed. C. Kramer, S. Aalto, & R. Simon, 29–34 (cited on page 102)

Le Bourlot, J., Pineau Des Forets, G., Roueff, E., & Flower, D. R. 1993, A&A, 267, 233 (cited on pages 114 and XV)

Le Petit, F., Nehmé, C., Le Bourlot, J., & Roueff, E. 2006, ApJS, 164, 506 (cited on pages 114 and XV)

Levin, Y. & Beloborodov, A. M. 2003, ApJ, 590, L33 (cited on page 10)

Liszt, H. S. 2003, A&A, 408, 1009 (cited on page 59)

Lo, K. Y. 1985, in European Southern Observatory Conference and Workshop Proceedings, Vol. 22, European Southern Observatory Conference and Workshop Proceedings, ed. P. A. Shaver & K. Kjar, 273–281 (cited on page 11)

Lo, K. Y. & Claussen, M. J. 1983, Nature, 306, 647 (cited on pages 2 and 9)

Loh, E. D., Baldwin, J. A., Ferland, G. J., et al. 2011, Monthly Notices of the Royal Astronomical Society, 421 (cited on pages 101, 111, 126, XIII and XV)

Lu, J. R., Ghez, A. M., Hornstein, S. D., et al. 2009, ApJ, 690, 1463 (cited on page 10)

Lutz, D. 1999, in ESA Special Publication, Vol. 427, The Universe as Seen by ISO, ed. P. Cox & M. Kessler, 623 (cited on page 115)

Lutz, D., Feuchtgruber, H., Genzel, R., et al. 1996, A&A, 315, L269 (cited on page 9)

Lutz, D., Krabbe, A., & Genzel, R. 1993, ApJ, 418, 244 (cited on pages 9, 28, 65, 115, 133, II and XV)

Lynden-Bell, D. 1969, Nature, 223, 690 (cited on page 2)

Lynden-Bell, D. & Rees, M. J. 1971, MNRAS, 152, 461 (cited on pages 1, 11 and I)

Markevitch, M., Sunyaev, R. A., & Pavlinsky, M. 1993, Nature, 364, 40 (cited on page 4)

Martini, P., Sellgren, K., & Hora, J. L. 1997, ApJ, 484, 296 (cited on pages 102 and 104)

Martins, F., Genzel, R., Eisenhauer, F., et al. 2007, Highlights of Astronomy, 14, 207 (cited on pages 7, 9 and 112)

McGee, R. X. & Bolton, J. G. 1954, Nature, 173, 985 (cited on pages 4 and I)

McKee, C. F., Chernoff, D. F., & Hollenbach, D. J. 1984, in Astrophysics and Space Science Library, Vol. 108, Galactic and Extragalactic Infrared Spectroscopy, ed. M. F. Kessler & J. P. Phillips, 103–131 (cited on page 133)

Mezger, P. G., Duschl, W. J., & Zylka, R. 1996, A&A Rev., 7, 289 (cited on pages 3, 6 and I)

Mezger, P. G., Zylka, R., Salter, C. J., et al. 1989, in IAU Symposium, Vol. 136, The Center of the Galaxy, ed. M. Morris, 357 (cited on page 6)

Mills, E. A. C., Sun, B., Liu, H. B., et al. 2015, in American Astronomical Society Meeting Abstracts, Vol. 225, American Astronomical Society Meeting Abstracts, 142 (cited on page 110)

Morris, M. & Serabyn, E. 1996, ARA&A, 34, 645 (cited on pages 2, 3, 4, 7, 9, 12, I and II)

Morris, M. R., Meyer, L., & Ghez, A. M. 2012, Research in Astronomy and Astrophysics, 12, 995 (cited on pages 3 and I)

Mugnier, L. M., Fusco, T., & Conan, J.-M. 2004, J. Opt. Soc. Am. A, 21, 1841 (cited on page 39)

Mugnier, L. M., Robert, C., Conan, J.-M., Michau, V., & Salem, S. 2001, J. Opt. Soc. Am. A, 18, 862 (cited on page 39)

Muno, M., Morris, M., & Baganoff, F. 2004, in Bulletin of the American Astronomical Society, Vol. 36, American Astronomical Society Meeting Abstracts, 1399 (cited on page 7)

Muno, M. P., Morris, M. R., Baganoff, F. K., et al. 2003, in Bulletin of the American Astronomical Society, Vol. 35, American Astronomical Society Meeting Abstracts, 110.03 (cited on pages 127 and 128)

Narayan, R., Mahadevan, R., Grindlay, J. E., Popham, R. G., & Gammie, C. 1998, ApJ, 492, 554 (cited on page 2)

Nottingham, M. R., Skinner, G. K., Willmore, A. P., et al. 1993, A&AS, 97, 165 (cited on page 4)

Pak, S., Jaffe, D. T., & Keller, L. D. 1996, in Astronomical Society of the Pacific Conference Series, Vol. 102, The Galactic Center, ed. R. Gredel, 28 (cited on page 7)

Pasquali, A., Schmutz, W., Leitherer, C., et al. 1996, in Science with the Hubble Space Telescope - II, ed. P. Benvenuti, F. D. Macchetto, & E. J. Schreier, 386 (cited on page 32)

Paumard, T. 2003, PhD thesis, Institut d'astrophysique de Paris / Université Pierre & Marie Curie (Paris VI (cited on page 30)

Paumard, T., Genzel, R., Martins, F., et al. 2006, Journal of Physics Conference Series, 54, 199 (cited on pages 10, 26, 30, 33, 35, 36, 60, 62, 65, V and VIII)

Paumard, T., Maillard, J.-P., & Morris, M. 2004, A&A, 426, 81 (cited on pages 9, 10, 58, 67, 76, 78, 133, 134, II and IX)

Paumard, T., Morris, M. R., Do, T., & Ghez, A. 2014a, in IAU Symposium, Vol. 303, IAU Symposium, ed. L. O. Sjouwerman, C. C. Lang, & J. Ott, 109–113 (cited on pages 39 and VI)

Paumard, T., Pfuhl, O., Martins, F., et al. 2014b, A&A, 568, A85 (cited on pages 10 and 22)

Piddington, J. H. & Minnett, H. C. 1951, Australian Journal of Scientific Research A Physical Sciences, 4, 459 (cited on pages 4 and I)

Predehl, P. & Schmitt, J. H. M. M. 1995, A&A, 293, 889 (cited on pages 92 and 131)

Ricarte, A. & Dexter, J. 2015, MNRAS, 446, 1973 (cited on page 18)

Rieke, G. H. & Lebofsky, M. J. 1982, in American Institute of Physics Conference Series, Vol. 83, The Galactic Center, ed. G. R. Riegler & R. D. Blandford, 194–203 (cited on page 10)

Rieke, M. J. 1999, in Astronomical Society of the Pacific Conference Series, Vol. 186, The Central Parsecs of the Galaxy, ed. H. Falcke, A. Cotera, W. J. Duschl, F. Melia, & M. J. Rieke, 32 (cited on page 82)

Rosenthal, D., Bertoldi, F., & Drapatz, S. 2000, A&A, 356, 705 (cited on pages 18 and III)

S. Brette, J. I. 1996, Proceedings of the International Conference on Image Processing (cited on page 39)

Schödel, R., Najarro, F., Muzic, K., & Eckart, A. 2010, A&A, 511, A18 (cited on pages 32, 78, 80, 81, 82, 83, 84 and X)

Schödel, R., Ott, T., Genzel, R., et al. 2002, Nature, 419, 694 (cited on pages 1, 11 and I)

Schreiber, J., Thatte, N., Eisenhauer, F., et al. 2004, in Astronomical Society of the Pacific Conference Series, Vol. 314, Astronomical Data Analysis Software and Systems (ADASS) XIII, ed. F. Ochsenbein, M. G. Allen, & D. Egret, 380 (cited on pages 25, 26 and V)

Scoville, N. Z., Hall, D. N. B., Ridgway, S. T., & Kleinmann, S. G. 1982, ApJ, 253, 136 (cited on pages 111, 126 and XIII)

Scoville, N. Z., Stolovy, S. R., Rieke, M., Christopher, M., & Yusef-Zadeh, F. 2003, ApJ, 594, 294 (cited on pages 78, 82, 83, 84 and 101)

Shull, J. M. & Hollenbach, D. J. 1978, ApJ, 220, 525 (cited on pages 103 and XIII)

Sjouwerman, L. O., Lang, C. C., & Ott, J., eds. 2014, IAU Symposium, Vol. 303, The Galactic Center: Feeding and Feedback in a Normal Galactic Nucleus (cited on pages 3 and I)

Smith, I. L. & Wardle, M. 2014, MNRAS, 437, 3159 (cited on pages 6, 92, 131 and II)

Sternberg, A. & Dalgarno, A. 1989, ApJ, 338, 197 (cited on pages 101, 112 and 114)

Sternberg, A. & Neufeld, D. A. 1999, ApJ, 516, 371 (cited on pages 16, 102 and 115)

Takahashi, J. 2001, ApJ, 561, 254 (cited on page 107)

Tanner, A., Ghez, A. M., Morris, M., et al. 2002, ApJ, 575, 860 (cited on page 85)

Tecza, M., Thatte, N., Eisenhauer, F., et al. 2000 (cited on pages 23 and 25)

Telesco, C. M., Davidson, J. A., & Werner, M. W. 1996, ApJ, 456, 541 (cited on pages 9, 126 and II)

Thiebaut, E. 2002, in Society of Photo-Optical Instrumentation Engineers (SPIE) Conference Series, Vol. 4847, Astronomical Data Analysis II, ed. J.-L. Starck & F. D. Murtagh, 174–183 (cited on page 40)

Tielens, A. G. G. M. 2010, The Physics and Chemistry of the Interstellar Medium (cited on page 13)

von Linden, S., Lesch, H., & Combes, F. 1996, in Astrophysics and Space Science Library, Vol. 209, New Extragalactic Perspectives in the New South Africa, ed. D. L. Block & J. M. Greenberg, 570 (cited on page 2)

Westmoquette, M. S., Exter, K. M., Christensen, L., et al. 2009, ArXiv e-prints (cited on page 26)

Woltjer, L. 1959, ApJ, 130, 38 (cited on page 2)

Yusef-Zadeh, F. 1994, in NATO Advanced Science Institutes (ASI) Series C, Vol. 445, NATO Advanced Science Institutes (ASI) Series C, ed. R. Genzel & A. I. Harris, 355 (cited on page 7)

Yusef-Zadeh, F., Morris, M., & Ekers, R. 1989, in IAU Symposium, Vol. 136, The Center of the Galaxy, ed. M. Morris, 443 (cited on page 65)

Yusef-Zadeh, F., Morris, M., Slee, O. B., & Nelson, G. J. 1986, ApJ, 310, 689 (cited on page 11)

Yusef-Zadeh, F., Stolovy, S. R., Burton, M., Wardle, M., & Ashley, M. C. B. 2001, ApJ, 560, 749 (cited on pages 6, 7, 19, 27, 58, 59, 61, 62, 63, 97, 112, 126, II, IV, V, IX and XV)

Zhao, J.-H., Morris, M. R., Goss, W. M., & An, T. 2009, ApJ, 699, 186 (cited on page 9)

Zylka, R., Mezger, P. G., & Wink, J. E. 1990, A&A, 234, 133 (cited on page 6)

Résumé

Introduction

Les phénomènes énergétiques qui ont lieu au centre des galaxies sont fondamentaux pour caractériser la formation et l'évolution des galaxies. La proximité du Centre Galactique de la Voie lactée en fait un endroit unique pour l'étude des phénomènes liés à l'activité des noyaux galactiques. Le Centre de la Voie Lactée est généralement considéré comme non-actif. Cependant, des cycles d'activité plus élevée pourraient avoir eu lieu dans le passé et pourraient avoir lieu dans le futur.

Le Centre de la galaxie contient une masse d'environ 4 10^6 $M_\odot$ dans un volume de 0,1 pc (Schödel et al. 2002; Ghez et al. 2005). On pense que la plupart des galaxies contiennent des objets compacts supermassifs dans leur centre (Lynden-Bell & Rees 1971). Le Centre Galactique, situé a 8 kpc de la Terre, est donc un laboratoire unique pour étudier les trous noirs supermassifs et pour explorer leur impact sur leur environnement stellaire et interstellaire.

L'objectif de ce travail est d'étudier la phase moléculaire du milieu interstellaire (MIS) dans le parsec central de la Galaxie, pour caractériser ses conditions physiques et dynamiques. Plus particulièrement, ce travail consiste en l'analyse de plusieurs raies de H_2 dans l'infrarouge proche, à l'aide d'un cube de données de spectro-imagerie obtenues avec l'instrument SPIFFI au Very Large Telescope.

Structure du Centre Galactique

La notion de Centre Galactique (Morris & Serabyn 1996; Genzel et al. 1994; Mezger et al. 1996; Genzel et al. 2010; Morris et al. 2012; Sjouwerman et al. 2014) fait référence à une large gamme d'échelles de longueurs : depuis plusieurs milliers de parsecs jusqu'à l'environnement immédiat du trou noir central.

Le 30 pc centraux sont occupés par plusieurs structures, dénommées à partir de la source radio Sgr A (Piddington & Minnett 1951; McGee & Bolton 1954; Downes & Martin 1971) :

- Sgr A Est, une source étendue de radiation synchrotron ;
- Sgr A West, une zone d'émission de H II en forme de spirale à trois bras aussi connue sous le nom de Minispirale ;
- Sgr A *, une source compacte d'émission radio située à proximité du centre dynamique de la Galaxie, qui a été identifiée comme un trou noir supermassif (Schödel et al. 2002; Ghez et al. 2005).

A l'échelle de 10 pc se trouve le Disque Circumnucléaire (*Circumnuclear Disc*, CND, Becklin et al. 1982). Il s'agit un anneau compact et asymétrique, composé de poussière et de gaz moléculaire (HCN, Guesten et al. 1987; Christopher et al. 2005, CO, Guesten et al. 1987 et H_2,

Yusef-Zadeh et al. 2001). Il est en rotation quasi-circulaire autour de Sgr A*, dans le même sens que la rotation galactique (Jackson et al. 1993). Le CND est fragmenté en de nombreux nuages massifs, très denses ($\sim 10^{6-8}$ cm^{-3}; Christopher et al. 2005; Smith & Wardle 2014), qui présentent de grandes dispersions de vitesse ($\sim$17 km s^{-1}). Le bord interne du CND est bien défini et est ionisé par le rayonnement provenant de l'amas d'étoiles central. La plupart des estimations de masse et densité du CND sont inférieures à la densité critique nécessaire pour assurer la stabilité vis-à-vis des forces de marée, ce qui implique que cette structure est de courte durée de vie. Cependant, Christopher et al. (2005) trouvent des densités plus élevées et proposent une durée de vie plus longue pour cette structure. Il y a deux hypothèses sur l'origine du CND : la capture et la fragmentation d'un nuage moléculaire géant passant trop près du Centre ou la destruction d'un disque stable préexistant.

Dans la Cavité Centrale du CND, à une distance de Sgr A* en deçà de 1,7 pc, la densité du gaz diminue d'un ou deux ordres de grandeur par rapport à celle du CND. Dans cette région s'étale la Minispirale, une structure de gaz ionisé d'environ 2 pc×3 pc. C'est une région H II, optiquement mince, plus filamentaire que le CND et qui se trouve autour de ce dernier. La Minispirale est composée d'un Bras Nord, d'un Bras Est, d'une Barre et d'un Arc West. L'Arc West est en fait la frontière ionisée du CND. Le Bras Nord est la couche photoionisée à la surface d'un nuage neutre (le Nuage du Bras Nord), en chute vers le Centre (Davidson et al. 1992; Telesco et al. 1996). La Bras Nord contient la Minicavité : une boule presque circulaire de 2ãrcsec, située 3.5 ″au sud-ouest de Sgr A* (Lutz et al. 1993). Le gaz ionisé apparaît, en projection, en forme de spirale. Cependant, les bras de la Minispirale ne se trouvent pas tous dans le même plan (Paumard et al. 2004). Cette structure s'est probablement formée lors de la chute d'un nuage moléculaire dans la Cavité Centrale. Le nuage a été étiré par les forces de marée et sa surface a été ionisée par le rayonnement intense provenant de l'amas d'étoiles central (Ekers et al. 1983; Paumard et al. 2004).

Il existe un mouvement global du milieu interstellaire, de l'extérieur vers le parsec central. Les nuages moléculaires massifs, en orbite dans la zone moléculaire centrale, ont un mouvement non-circulaire en raison de la présence d'une barre d'étoiles. Le gaz neutre peut donc se déplacer vers l'intérieur et alimenter le CND. Depuis le CND, le matériel peut tomber vers la Cavité Centrale et être illuminé par le rayonnement UV, ce qui expliquerait la structure observée de la Minispirale (Güsten 1989; Morris & Serabyn 1996; Paumard et al. 2004).

Le milieu interstellaire au Centre Galactique

Dans cette thèse nous nous sommes concentrés sur la molécule la plus abondante du MIS : H_2. L'hydrogène moléculaire joue un rôle important dans les processus régissant la formation des étoiles et l'évolution des galaxies. De nombreux mécanismes concurrents pourraient contribuer à son excitation et il peut donc sonder une large variété d'environnements distincts. La détection et l'étude dans l'infrarouge proche de l'émission de H_2 dans le parsec central est le sujet principal de ce travail.

H_2 peut se former principalement sur les grains de poussière et est généralement détruit par le rayonnement UV. Pour que H_2 puisse exister il doit y avoir une assez grand opacité le protégeant des photons UV ($A_V \sim$ 0,01 – 0,1 mag). Pour que le H_2 excité soit détectable, la température d'excitation doit être supérieure à $1000K$. Les molécules sont principalement

excitées par :

- les collisions, dans ce cas le gaz est chauffé par des chocs ;
- la fluorescence UV, où l'absorption d'un photon UV entraîne un pompage de la population suivi par une désexcitation radiative .

Les régions dominées par les photons (*photon dominated regions*, PDR) sont la source la plus importante d'émission H_2 (Hollenbach & Tielens 1999). Dans une PDR, le champ de rayonnement UV éclaire la surface chaude et partiellement ionisée des nuages moléculaires. Par conséquent, les PDRs séparent le gaz froid des nuages moléculaires du gaz chaud, ionisé.

Les régions de choc sont aussi des sources importantes d'émission H_2. Parmi les causes de chocs, on peut trouver les jets, les supernovae et l'expansion des régions H II (Draine & McKee 1993; Hollenbach & Tielens 1997). L'énergie mécanique du choc chauffe le gaz. Les températures typiques sont de 2000 – 3000 K. Orion OMC-1 (Rosenthal et al. 2000) est un exemple d'émission H_2 excitée par choc.

Objectifs de la thèse

Dans le Centre Galactique, les températures, les densités et la dispersion de vitesse sont plus élevées que dans le reste de la Galaxie (Güsten 1989). De puissants chocs à grande échelle sont impliqués dans l'excitation du MIS. La nature très différente du MIS dense dans le Centre de la Galaxie le rend utile non seulement pour prouver les théories sur l'interaction avec les étoiles dans les noyaux des autres galaxies, mais aussi comme laboratoire pour l'étude des effets physiques sur le MIS dans des conditions extrêmes de champ UV et chocs.

De plus le Centre Galactique présente de nombreuses questions sans réponse, comme le "paradoxe de la jeunesse" des étoiles "S". En effet, la formation des étoiles dans cet environnement extrême doit être inhibée par le champ magnétique intense et par gravité. Pourtant, beaucoup de jeunes étoiles sont observées dans cette région. Le problème du bas taux d'accrétion sur le trou noir central n'est pas expliqué non plus. Une autre question ouverte est le mouvement du gaz d'une échelle à l'autre. Le problème ici est de comprendre le mécanisme qui cause la perte de moment angulaire et, par conséquent, provoque la chute du gaz vers l'intérieur.

Dans ce contexte, le rôle du MIS et son interaction avec l'environnement extrême du parsec central, est important pour caractériser ce milieu complexe.

L'objectif de ce travail est d'étudier la phase moléculaire du MIS (H_2) dans une zone où le CND neutre laisse la place à la Minispirale ionisée. Même si le fort champ UV est censé dissocier les molécules de H_2, celles-ci peuvent cependant survivre si elles sont efficacement protégées. Cela peut être assuré soit par des PDRs, soit par la poussière ou par l'auto-écrantage, à condition que la densité de colonne soit suffisamment élevée. Les photons UV, atténués par l'un de ces mécanismes, peuvent alors fournir l'excitation nécessaire pour que H_2 devienne détectable. Le gaz moléculaire dans les parsecs centraux a précédemment été étudié à travers l'analyse de raies de CO, qui est le traceur principal des nuages moléculaires denses et froids. Ces analyses tracent par exemple les nuages denses et froids du CND, mais elles ne peuvent pas détecter le gaz moléculaire chaud qui pourrait se trouver dans la Cavité Centrale. En

effet, l'émission du gaz moléculaire à l'intérieur de la Cavité Centrale a été détectée par Gatley et al. (1986). Yusef-Zadeh et al. (2001) qui ont détecté de l'hydrogène moléculaire dans le bord interne du CND. Ces auteurs se sont concentrée sur la raie 1-0 S(1) à 2,1218 μm. D'autres raies de H_2 sont observables autour de 2 μm, mais elles sont moins intenses ou à proximité de fortes raies stellaires ou interstellaires, ce qui rend difficile de les mesurer avec précision. Ici, nous avons appliqué une nouvelle méthode, développée par T. Paumard, qui peut surmonter certains de ces problèmes, même dans les régions où le signal sur bruit est bas et qui n'auraient pas été accessibles avec des techniques classiques. De plus, la carte obtenue par Yusef-Zadeh et al. (2001) n'est pas corrigée de l'extinction. L'extinction varie considérablement, localement, dans le parsec central. La connaissance de l'extinction locale est donc cruciale pour séparer les variations d'intensité dues à l'extinction de celles qui sont dues aux fluctuations intrinsèques de luminosité.

L'objectif de ce travail est d'aller plus loin et d'étendre la recherche et l'étude du H_2 dans le parsec central, caractérisant sa distribution, sa dynamique et son excitation avec une meilleure résolution angulaire. Une demi-douzaine de raies sont analyses, inter-comparées, et l'extinction est directement calculée à partir des raies observées. L'analyse des raies d'émission est utile non seulement pour étudier la distribution du gaz dans le champ, mais aussi sa vitesse radiale et la largeur de raies. La comparaison de plusieurs raies peut révéler différents processus spécifiques et donner des indications importantes sur le mécanisme d'excitation dominant.

Observer le MIS dans le Centre Galactique est rendu compliqué par l'importante extinction interstellaire et le grand nombre d'étoiles brillantes dans le champ. Une haute résolution spectrale et spatiale est nécessaire pour démêler les composantes stellaires et interstellaires. Un jeu de données de spectro-imagerie est donc bien adapté pour l'étude du MIS. Ceci permet d'accéder à l'information spectrale détaillée d'une source spatialement étendue (comme le MIS). En outre, en raison de la grande extinction due à 8 kpc de poussière, le Centre Galactique est observable seulement à des longueurs d'onde plus longues (infrarouge et radio) ou plus courtes (rayons X durs et γ) que le domaine visible. Nous avons donc analysé des données spectro-imagerie dans le proche infrarouge, obtenues par le spectrographe intégral de champ SPIFFI. Cela nous permet de séparer l'émission du gaz des sources discrètes et d'étudier la distribution spatiale, la dynamique et l'excitation du gaz moléculaire.

Observations et méthodes appliquées

SPIFFI

SPIFFI (*Spectrometer for Infrared Faint Field Imaging*) est le spectrographe intégral de champ de l'instrument SINFONI sur le VLT.

La spectroscopie intégrale de champ (*integral field spectroscopy*, IFS) pallie les inconvénients de la spectroscopie d'image traditionnelle puisque les spectres de tous les pixels d'un champ 2D peuvent être obtenus simultanément. Tous les spectres prélevés par un IFS sont affectés par l'atmosphère de façon égale, ce qui entraîne un étalonnage relatif nettement amélioré. Avec le ISF le temps d'intégration est beaucoup plus réduit aussi. L'inconvénient est que les deux résolutions – spatiales et spectrales – doivent être l'objet d'un compromis dans la combinaison des deux types de données.

Dans SPIFFI, le champ 2D observé par le télescope est séparé en plusieurs tranches par un découpeur d'image pour former une pseudo-fente qui est ensuite amenée à un spectrographe, pour disperser tous les pixels observés en même temps. Le format final des données est celui d'un cube de données, avec deux dimensions spatiales et une dimension spectrale. Cela signifie qu'à chaque pixel spatial du champ 2D observé, correspond un spectre.

Données

Les données ont été acquises au cours des premiers essais d'observation de SPIFFI (Eisenhauer et al. 2000) au VLT en Mars et Avril 2003. Le parsec central de la Galaxie a été observé pendant une heure, ce qui a conduit à la construction d'une mosaïque de $\sim 35 \times 35''$. Les observations ont été utilisées dans plusieurs publications qui s'intéressaient essentiellement à la population stellaire (Eisenhauer et al. 2003; Horrobin et al. 2004; Paumard et al. 2006; Fritz et al. 2011, entre autres). Les observations sont limitées par le *seeing* (FWHM 0,75 ″), elles ont un échantillonnage des pixels de 0,25 ″ et une résolution spectrale $R = 1\,300$ dans le mode combiné H + K. Les observations ont été traitées par le *pipeline* de SPIFFI (Schreiber et al. 2004). Le cube de données réduit est le même que dans Eisenhauer et al. (2003) et Horrobin et al. (2004). Le cube de données est corrigé du fond atmosphérique mais aucun étalonnage en flux est appliqué aux intensités qui sont laissées en ADU (*analog to digital unit*).

En raison de la large gamme spectrale couverte, les données comprennent des nombreuses raies de H_2. La raie 1-0 S(1) a été détectée auparavant dans le parsec central par Yusef-Zadeh et al. (2001) et est clairement visible aussi dans le cube de SPIFFI. C'est la raie avec le meilleur rapport de signal sur bruit dans le spectre moyen du cube, suivie par 1-0 Q (3) et 1-0 Q (1). 1-0 S (3) et 1-0 S (0) ont un rapport signal sur bruit plus faible, mais elles sont encore assez bien détectables dans le spectre moyen. D'autre part, 1-0 S (2) et 1-0 Q (2) sont impossibles à distinguer du bruit sur le spectre moyen. Cependant, elles sont détectables dans plusieurs régions du champ.

L'analyse de ces raies – tant dans le champ entier que dans certaines zones choisies pour les raies non détectables partout – constitue la coeur de ce travail.

Calibration

Les observations que nous avons utilisées ont déjà été réduites et partiellement calibrées. Cependant l'ensemble de données n'est pas étalonné en flux et un étalonnage photométrique est nécessaire. Pour déterminer cet étalonnage, nous avons choisi plusieurs étoiles dans le champ à partir de catalogues de Paumard et al. (2006), Blum et al. (2003) et Bartko et al. (2009). L'étalonnage a été fait en deux étapes : la première étape consiste à corriger la pente de tous les spectres (étalonnage relatif), la deuxième étape consiste à convertir les ADU en unités de flux physiques (étalonnage photométrique).

Le spectre de ces calibrateurs est extrait en additionnant des pixels au sein d'une ouverture en forme de losange. La calibration relative consiste à diviser tous les spectre du cube par le spectre observé d'un calibrateur et multiplier par la le spectre théorique de ce calibrateur. Le flux observé dans l'ouverture est comparé au flux attendu – calculé à partir la magnitude, connue, de l'étoile – pour obtenir le facteur de conversion d'unités. Ceci est fait pour plusieurs

calibrateurs conduisant à une incertitude sur le flux de $\sim 35\%$.

Ajustement 3D Régularisé

Une raie spécifique de H_2 peut être étudiée avec un ajustement gaussien. Cet ajustement se fait sur chaque spectre du cube et donne donc les valeurs de flux, vitesse et largeur de la raie pour chaque pixel. Il est alors possible de construire des cartes, en deux dimensions, des paramètres de l'ajustement (le flux, la vitesse et la largeur) pour une H_2 donnée. Le résultat de cette analyse est donc une carte pour le flux, une pour la vitesse et une pour la largeur de la raie.

L'approche classique pour ce type d'analyse est de considérer chaque spectre individuellement et d'ajuster un profil gaussien sur chaque spectre, pixel par pixel. Il en résulte des cartes bruitées, rendant souvent nécessaire un lissage spatial. Cependant, dans le cube de SPIFFI, le rapport signal sur bruit des raies de H_2 n'est pas bon partout dans le champ, en particulier en correspondance des étoiles, où il y a du bruit de photons supplémentaire. Dans ce cas, le lissage spatial a pour effet de dégrader la résolution spatiale partout. En outre, cette opération augmente la corrélation entre les pixels voisins et introduit des effets de bord sur les côtés du champ et dans les zones de données manquantes.

Pour surmonter les problèmes ci-dessus une nouvelle approche est utilisée, développée par Paumard et al. (2014a): un ajustement 3D régularisé. Cette méthode, au lieu de considérer chaque spectre individuellement, effectue un ajustement global sur le cube 3D (Paumard et al. 2016, in prep.). Cet ajustement global sur le champ se fait en tenant compte du fait que les pixels voisins doivent être corrélés. L'ajustement 3D régularisé puise son inspiration du contexte de déconvolution et consiste à minimiser un estimateur, ε, qui est la somme pondérée d'un terme de χ^2 et d'un terme de régularisation :

$$\varepsilon(F, v, \sigma) = \sum_{x,y,\lambda} [(DM) \cdot W]^2 + \sum_{a_i=F,v,\sigma} R_i(a_i) \tag{D.1}$$

La régularisation a le rôle d'injecter autant d'information *a priori* que possible. A cet effet, une régularisation quadratique linéaire est utilisée. Cette régularisation est appelée L1–L2. Pour chaque paramètre de l'ajustement gaussien $a_i = F, v, \sigma$ le terme de regularisation s'écrit :

$$R_i(a_i) = \mu_i \sum_{u=x,y} \left[\frac{\Delta O(u)_{a_i}}{delta_i} - ln\left(1 + \frac{\Delta O(u)_{a_i}}{\delta_i}\right)\right] \tag{D.2}$$

où $\Delta O(u)_{a_i}$ est le gradient spatial du paramètre gaussien a_i. Pour des faibles gradients (petits $\Delta O(u)$) le terme logarithmique de L1–L2 domine et devient un critère quadratique qui pénalise les gradients et lisse la carte. Au contraire, quand $\Delta O(u)$ est grand, les forts gradients sont restaurés. La transition d'un régime à l'autre est réglée par les hyper-paramètres δ_i et μ_i. Cet algorithme est très bien adapté au traitement d'objets avec de forts gradients, spatialement corrélés, tels que des bords nets (par exemple des surfaces planétaires) ou, dans notre cas, des crêtes et des frontiers. Grace à cette méthode l'effet de pixels à faible signal sur bruit est minimisé, la résolution est conservée et il n'y a pas d'effets bords.

Cependant il y a un inconvénient majeur dans cette méthode 3D : le réglage nécessaire des hyper-paramètres δ_i et μ_i, pour chaque carte de paramètre (flux, vitesse et largeur), soit six

hyper-paramètres. Ils ne sont en fait pas indépendants les uns des autres et cela complique la recherche d'un bon équilibre entre eux. Le but du réglage des l'hyper-paramètres est de mener la procédure d'ajustement vers le minimum absolu du critère ε. Pour atteindre ce minimum il est nécessaire de régler finement chacun des six hyper-paramètres. L'objectif est d'obtenir des cartes de flux, vitesse et largeur qui apparaissent lisses à une échelle aussi proche que possible de la résolution spatiale. Le résultat final doit être tel que le modèle 3D obtenu soit équivalent à ce que l'on obtiendrait avec un ajustement classique 1D sur une certaine ouverture. Le défi consiste trouver l'équilibre entre les six hyper-paramètres afin d'avoir des cartes suffisamment lisses, tout en conservant les structures spatiales fines. La procédure a été exécutée plusieurs fois avec différentes combinaisons d'hyper-paramètres, pour trouver la meilleure stratégie pour identifier la bonne combinaison des hyper-paramètres.

Une fois que l'on trouve une combinaison d'hyper-paramètres satisfaisant, un bon critère pour évaluer *a posteriori* le résultat est de le comparer à un modèle 1D classique. Cela se fait à travers l'extraction des spectres individuels sur une ouverture variable sur le champ et l'ajustement avec un modèle 1D classique. Le résultat de l'ajustement 3D peut ainsi être comparé aux données brutes et au modèle 1D. Un autre critère *a posteriori* fort pour tester le résultat est de regarder le résultat de l'application de l'ajustement 3D régularisé pour raies de H_2différentes mais physiquement liées.

La méthode ne fournit pas une estimation directe des incertitudes statistiques. Nous avons donc développé une technique distincte pour les évaluer.

Le cube SPIFFI est divisé en quatre sous-cubes en gardant dans du cube initial un pixel sur quatre et interpolant les points manquants. On crée ainsi quatre nouveaux cubes de données indépendantes. Chaque cube est en suite analysé avec l'ajustement 3D régularisé. L'incertitude est donnée par l'écart-type des quatre solutions obtenues, divisée par 2 (parce qu'il y a quatre fois moins d'information puisqu'un seul pixel sur quatre provient du cube d'origine).

Méthode 1D

En plus de cette méthode, une analyse plus classique 1D est appliquée sur certaines régions choisies pour les raies qui ne présentent pas un signal sur bruit assez élevé sur tout le champ. Pour chaque zone sélectionnée le spectre moyen est ajusté par un profil gaussien.

Résultats

Morphologie et dynamique du gaz

1-0 S (1) est la première raies que nous avons analysé, puisque c'est celle qui présente le plus haut signal sur bruit (Fig. D.1). La carte de flux de cette raie montre que l'émission du gaz moléculaire provient de tout le champ observé par SPIFFI. Dans le coin nord-ouest il y a un pic d'émission très lumineux. La carte de vitesse présente un décalage vers le bleu bien prononcé dans le coin sud-est. Le reste de la carte de vitesse paraît plus uniforme mis à part plusieurs structures à petite échelle. Ces structures correspondent – la plupart du temps – à des étoiles brillantes. Même s'il peut s'agir d'artefacts, créés par la pollution des étoiles, ces structures peuvent également être associées au gaz éjecté par les étoiles elles-mêmes. La carte de largeur

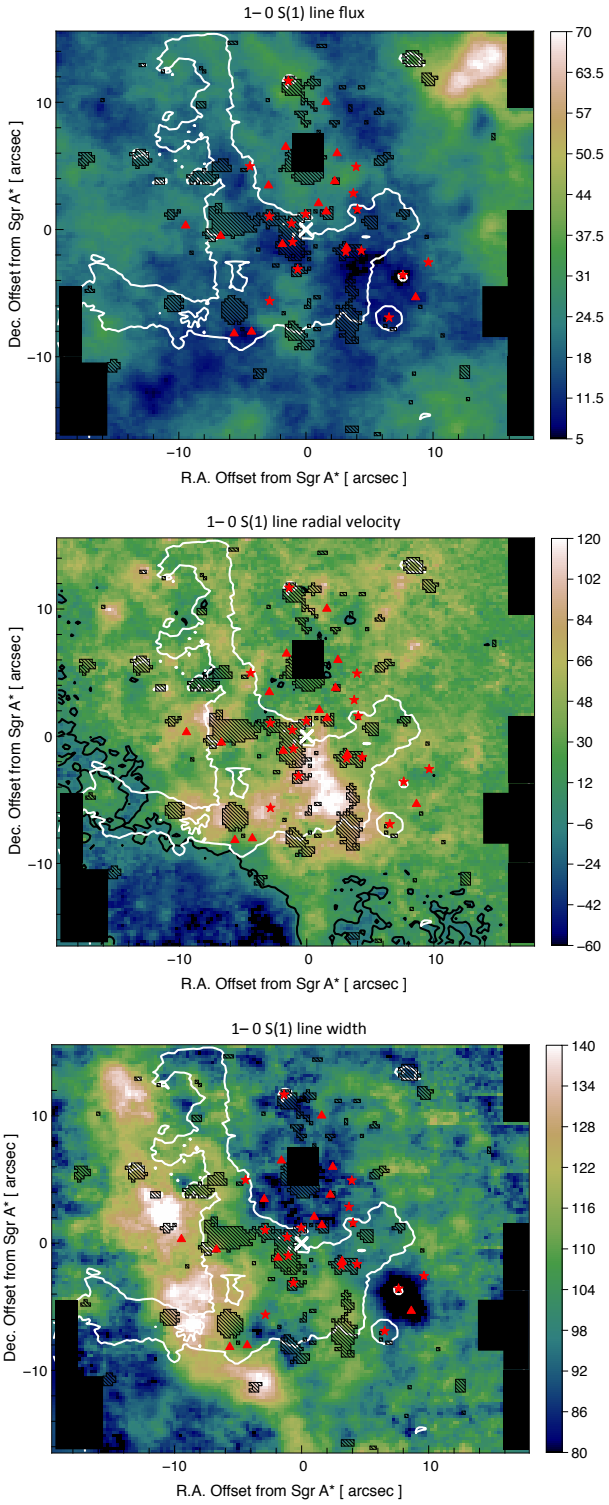

Figure D.1: Résultats de l'Ajustement 3D Régularisé pour 1-0 S(1). *Haut :* carte de flux en 10^{-19} W m^{-2} arcsec^{-2}. *Milieu :* carte de vitesse radiale en km s^{-1}. La ligne noire indique les contour à vélocité nulle. *Bas :* carte de largeur de raie en km s^{-1}. Les décalages spatiaux son relatifs à Sgr A* (marqué par la croix). Le contour blanc trace l'émission Brγ de la Minispirale à $2 \cdot 10^{-16}$ W m^{-2} arcsec^{-2}. Les régions rayées interpolées pour éviter la pollution due aux raies stellaires. Les symboles rouges marquent la position des étoiles Wolf-Rayet (Paumard et al. 2006). Les zones noires couvrent des zones où il n'y a pas de données.

présente des valeurs particulièrement élevées le long d'une crête légèrement décalée vers l'est du Bras du Nord. Ce bras est en fait la frontière d'un nuage épais (le Nuage du Bras Nord; Paumard et al. 2004). La grande largeur de raie observée correspond, en projection, à la partie plus dense de ce nuage, ce qui suggère que le H_2 se trouve à l'intérieur du nuage et qu'il serait plus turbulent.

Nous avons appliqué l'Ajustement 3D Régularisé à d'autres raies disponibles dans notre jeu de données. Les transitions avec un signal sur bruit suffisant sont : 1-0 S (3), 1-0 Q (1), 1-0 Q (3) et 1-0 S (0) à 1,9575 μm, 2,4066 μm, 2.4237 μm et 2.2232 μm. Même si l'ajustement est plus difficile que pour 1-0 S (1), compte tenu des particularités locales et de la pollution spectrale, les cartes de paramètres de ces raies sont compatibles avec celles de 1-0 S(1). Cela renforce la validité de nos résultats. 1-0 S(0) est la seule raie de type para analysée mais elle est bien décrite par la même vitesse et largeur que les autres. La principale différence par rapport aux autres raies étudiées est que cette transition montre une émission très forte quelques secondes d'angle au sud de Sgr A*.

L'émission observée dans les coins nord-ouest et sud-est du champ de SPIFFI est très probablement dominée par le gaz moléculaire du CND. La carte de vitesse dans ces deux coins est compatible avec le mouvement connu du CND. La carte de flux présente globalement les mêmes caractéristiques que la carte de 1-0 S(1) obtenue par Yusef-Zadeh et al. (2001). Certaines structures en correspondance du CND sont également compatibles avec la distribution de HCN obtenu par Christopher et al. (2005). Cette molécule trace clairement les nuages du CND les plus denses. La carte de vitesse montre que l'émission dans le coin nord-ouest et sud-est se déplace à des vitesses compatibles avec les observations de HCN. Ce qui est intéressant est que l'émission de H_2 reste assez forte aussi à l'intérieur de la Cavité Centrale.

Il semble y avoir au moins deux composantes de l'émission :

- une associée au CND (coins nord-ouest et sud-est principalement) qui présente une raie d'émission étroite et intense ;
- une à l'intérieur de la Cavité Centrale, généralement caractérisée par une raie d'émission plus large, mais moins intense par rapport à l'autre composante.

Dans le CND la raie apparait plus étroite que dans le reste du champ probablement à cause de la densité plus élevée de ses nuages qui ne permettent pas d'intégrer en profondeur. D'autre part, dans la Cavité Centrale le gaz est moins dense. Ici, l'élargissement observé traduit donc la dispersion de vitesse le long de la ligne de visée. Cet effet est particulièrement fort à l'intérieur du Nuage du Bras Nord.

Extinction

Les cartes de flux obtenues doivent être corrigées de l'effet de l'extinction. Nous pouvons considérer le rapport de flux de 1-0 Q(3)/1-0 S(1) pour cette évaluation puisque ces deux transitions correspondent au même niveau supérieur d'énergie de la molécule.

Comme les raies de H_2 sont optiquement minces (comme le montre dans la nébuleuse d'Orion Gautier et al. 1976) on peut écrire :

$$\frac{I_{Q3}}{I_{S1}} = \frac{(\mathcal{A}_{Q3} \cdot \nu_{Q3})}{(\mathcal{A}_{S1} \cdot \nu_{S1})} \cdot 10^{E/2.5} \tag{D.3}$$

où I_{Q3}/I_{S1} est le rapport des intensités (i.e. le rapport de flux), $\mathcal{A}$ est le coefficient d'Einstein et ν la fréquence. Considérant $E = A_{\lambda_{S1}} - A_{\lambda_{Q3}}$, nous avons :

$$E = 2,5 \cdot log\left(1.425 \cdot \frac{I_{Q3}}{I_S 1}\right) \tag{D.4}$$

En se donnant une loi d'extinction, on peut obtenir l'extinction totale A_λ pour chaque longueur d'onde et corriger de l'extinction chaque pixel. Nous avons supposé comme loi d'extinction une loi de puissance dans l'infrarouge proche. En particulier $A_a/A_b = (\lambda_a/\lambda_b)^{-\ alpha}$ (avec $\alpha = 2,07$ de Fritz et al. 2011). Nous avons donc obtenu une carte pour l'extinction en bande Ks, en considérant sa longueur d'onde centrale $\lambda_{Ks} = 2.168$ μm comme dans Schödel et al. (2010).

En moyenne nous obtenons une extinction presque 1 mag supérieure à celle déterminée dans la même région par Schödel et al. (2010) au moyen de l'excès de couleur d'étoiles. Ces différences ne sont pas surprenantes : en effet la majeure partie de l'extinction est de premier plan et vaut $\sim$ 2.5 K mag. Cependant, la plupart de la variation d'extinction est locale : jusqu'à 1 magnitude supplémentaire en K. L'estimation de l'extinction dépend de la position 3D de l'émetteur utilisé comme sonde. Les cartes d'extinction peuvent donc différer parce que les différents traceurs – étoiles, gaz ionisé, gaz moléculaire – ne sont pas à la même position dans l'espace 3D et pas à la même profondeur optique.

Corrélation flux-extinction

La carte de flux dérougi apparaît partiellement corrélée avec la carte d'extinction : le flux est élevé là où l'extinction est élevée aussi.

Afin d'étudier cette corrélation nous traçons un graphe du flux dérougi de 1-0 S(1) en fonction de A_{Ks}. Une corrélation entre le flux et l'extinction apparaîtrait comme une ligne droite sur ce graphe. En fait dans le graphe on n'observe pas un alignement de points sur une unique droite. Par contre on peut distinguer au moins quatre ensembles allongés de points, comme s'il n'y avait pas une corrélation globale, mais plusieurs corrélations locales.

Nous avons sélectionné ces ensembles et attribué une couleur à chacun. Chaque point du graphe correspond à un pixel de SPIFFI. Si l'on assigne à chaque pixel du champ 2D la couleur correspondante du graphe on observe qu'à chaque ensemble de points correspond à une zone continue sur le champ de SPIFFI. Cela semble donc renforcer l'idée que la corrélation observée est réelle. Il y a deux questions qui se posent à l'examen de ces observations : pourquoi l'extinction est elle corrélée avec le flux ? et pourquoi cette corrélation apparaît-elle séparément en plusieurs zones distinctes ?

Pour étudier cette corrélation et tenir compte de ces deux effets, nous proposons le modèle phénoménologique suivant. On peut imaginer un nuage d'émission comme étant composé d'un milieu homogène, avec une température d'excitation constante, mais avec une profondeur optique variable $\tau(x) = a \cdot x$, où a est le coefficient d'absorption par unité de longueur et x

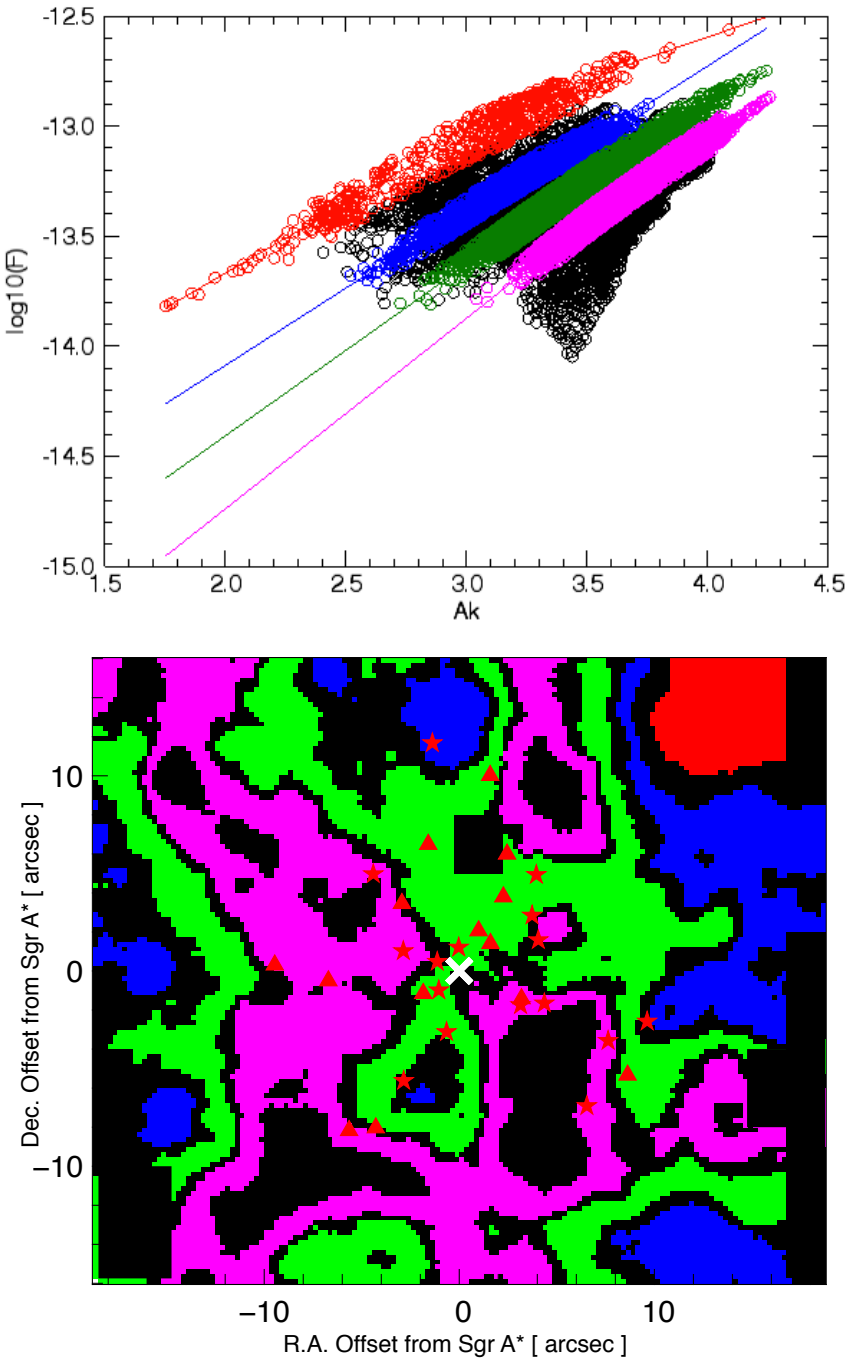

Figure D.2: *Haut :* graphe du flux dérougi de 1-0 S(1) en fonction de l'extinction. Quatre groupes de points corrélés apparaissent et sont marquées dans le graphe avec des couleurs différentes. *Bas :* chaque pixel dans le champs de SPIFFI est coloré selon le groupe auquel il appartient.

est l'épaisseur géométrique. En face de ce nuage, un écran de poussière absorbe une partie de l'émission de nuages, ajoutant une profondeur optique τ_0.

$\tau(x)$ représente le fait que le matériau émetteur (le gaz moléculaire) se trouve au même endroit que le matériau absorbant (par exemple la poussière). Par exemple, dans un environnement très grumeleux, l'on peut imaginer que l'émission du gaz moléculaire d'un grumeau soit absorbée par la poussière dans d'autres grumeaux. L'émission qui provient de ces molécules est alors absorbée par les grains de poussière sur son chemin vers l'extérieur de la zone d'émission. L'émetteur et l'absorbant peuvent ainsi se retrouver mélangés.

L'argument ci-dessus s'applique à chaque ensemble de points corrélés. Les ensembles observés correspondent chacun à des zones distinctes sur le champ de SPIFFI. La raison de cette séparation pourrait s'expliquer par la différence d'extinction en avant plan, le long de la ligne de visée pour chacun de ces ensembles, i.e. par des différentes valeurs de τ_0. Cette extinction agit comme un "écran" qui atténue les photons provenant du matériel émetteur. Chacune des zones identifiées correspond à un milieu qui est soumis à une extinction spécifique τ_0. Le décalage des courbes sur le graphe de corrélation correspond donc à une épaisseur optique différente de cet écran de premier plan. Les différences de profondeur des écrans eux mêmes peuvent traduire l'emplacement géométrique du milieu émetteur le long de la ligne de visée : un nuage au premier plan sera soumis à une extinction mineure par rapport à un nuage en arrière plan puisqu'il se trouve à une distance inférieure de l'observateur (donc l'écran de poussière à traverser est plus fin). Ceci est cohérent avec les points identifiés sur le graphe de corrélation. Par exemple le coin nord-ouest du champ SPIFFI correspond l'extinction la plus basse parmi les courbes de corrélation. En effet le coin du CND est le plus proche de l'observateur dans le champ. Lors qu'on rentre dans la Cavité Centrale on s'éloigne de l'observateur et à ces zones correspondent des courbes d'extinction de plus en plus élevées.

En fait, l'extinction calculée est une conjugaison de la variation de profondeur optique dans les nuages émetteurs et de l'effet de l'écran absorbant. Le premier effet est responsable de la corrélation entre le flux et l'extinction. Le deuxième effet provoque la scission en plusieurs courbes pour différentes profondeurs optiques. En résumé, la pente observée trace la fragmentation du milieu interstellaire alors que la division en différents groupes de points corrélés traduit l'extinction en avant plan.

Ces résultats soulignent l'importance de l'estimation de l'extinction à partir de l'émetteur spécifique étudié, puisque chaque source est située à une profondeur optique différente pour l'observateur et donc soumise à une éxtinction différente.

Excitation du H_2

La comparaison des plusieurs raies donne accès à des informations sur l'excitation du gaz.

En plus des raies discutées précédemment, les autres raies détectables sont 1-0 S(2) et 1-0 Q(2), respectivement à 2,0338 μm et 2,4134 μm ainsi que la raie 2-1 S (1) à 2,2476 μm. Ces raies sont dans un environnement spectral plus difficile que les précédentes et le rapport signal sur bruit est plus faible en moyenne. Cependant, les raies se distinguent nettement dans certaines zones. Ces régions peuvent être isolées et étudiées séparément, avec un ajustement 1D classique (considérant un spectre moyen sur la zone). Dans la suite nous avons donc considéré plusieurs zones particulièrement intéressantes dans le champ (le CND, la Cavité Centrale, le

Nuage du Bras Nord, la Minicavité) et poursuivi l'analyse sur ces régions spécifiques.

Un fois calculé le flux dérougi de chaque raie f_{vj}, la densité de colonne de N_{vj} des molécules dans l'état $[v, j]$ peut être calculée comme :

$$N_{vj} = \frac{4\pi}{\Omega} \frac{f_{vj}}{\mathcal{A}_{vj}\nu_{vj}h} \tag{D.5}$$

On peut ainsi considérer le diagramme d'excitation qui consiste à tracer les densités de colonne (normalisées par la dégénérescence) g_{vj}) N_{vj}/g_{vj} en fonction de l'énergie du niveau supérieur E_{up}. Les densités de colonne sont généralement représentées dans une échelle semi-log. Sur ce diagramme, les intensités relatives de plusieurs raies peuvent être facilement et simultanément comparées. Les conditions physiques du gaz peuvent être évaluées par comparaison avec des lignes droites qui correspondraient à un gaz parfaitement thermalisé.

Dans le parsec central les chocs et le pompage UV peuvent jouer un rôle dans l'excitation de H_2 et donc les deux mécanismes doivent être pris en considération :

- Collisions : la population est thermalisée et suit la distribution de Boltzmann. Dans ce cas, les densités de colonne s'alignent sur une ligne droite dans le diagramme d'excitation représentée en échelle semi-log et la température d'excitation peut être évaluée par un ajustement.

- Fluorescence: une température unique ne décrit pas la distribution sur le diagramme d'excitation. Pour des densités de gaz supérieures à 10^5 cm^{-3} (Burton & Allen 1993), les états pompés par UV peuvent se désexciter par collisions, produisant des raies qui apparaissent thermalisées. Cette fluorescence collisionnelle est donc parfois difficile à distinguer de l'excitation par chocs.

Le rapport 1-0 S(1)/2-1 S(1) permet, en principe, de distinguer entre le pompage UV et l'excitation collisionnelle (Shull & Hollenbach 1978). Un rapport élevé ($\sim$ 10) est indicatif d'une excitation par choc (Shull & Hollenbach 1978) tandis qu'un rapport faible ($\sim$ 2) est la signature de la pure fluorescence (Black & Dalgarno 1976). Les valeurs intermédiaires ($\sim$ 5) indiquent la fluorescence collisionnelle (Burton & Allen 1993).

Zones thermalisées : le CND

Pour les régions où la thermalisation s'applique, la température d'excitation T_e correspond à la température cinétique du gaz et la densité de la colonne totale de H_2 excité peut être calculée. La thermalisation s'applique à des régions qui correspondent au CND dans le champ.

L'analyse montre que les températures calculées pour le CND sont beaucoup plus élevés et les masses beaucoup plus faibles par rapport à que ce qui a été estimé avant avec d'autres molécules (CO, NH_3). Cette différence est due au fait que le gaz détecté représente seulement la partie la plus excitée. Ceci est cohérent avec les résultats obtenus par Loh et al. 2011 dans la nébuleuse du Crabe et par Scoville et al. (1982) pour Orion, par exemple. Dans la détermination de la densité de la colonne, le H_2 chaud domine les intensités, ce qui rend les résultats très sensibles aux structures thermiques du nuage. Cette émission provient d'une couche mince du nuage, illuminée par les UV. Le reste du nuage (qui constitue la grande partie de sa masse) reste

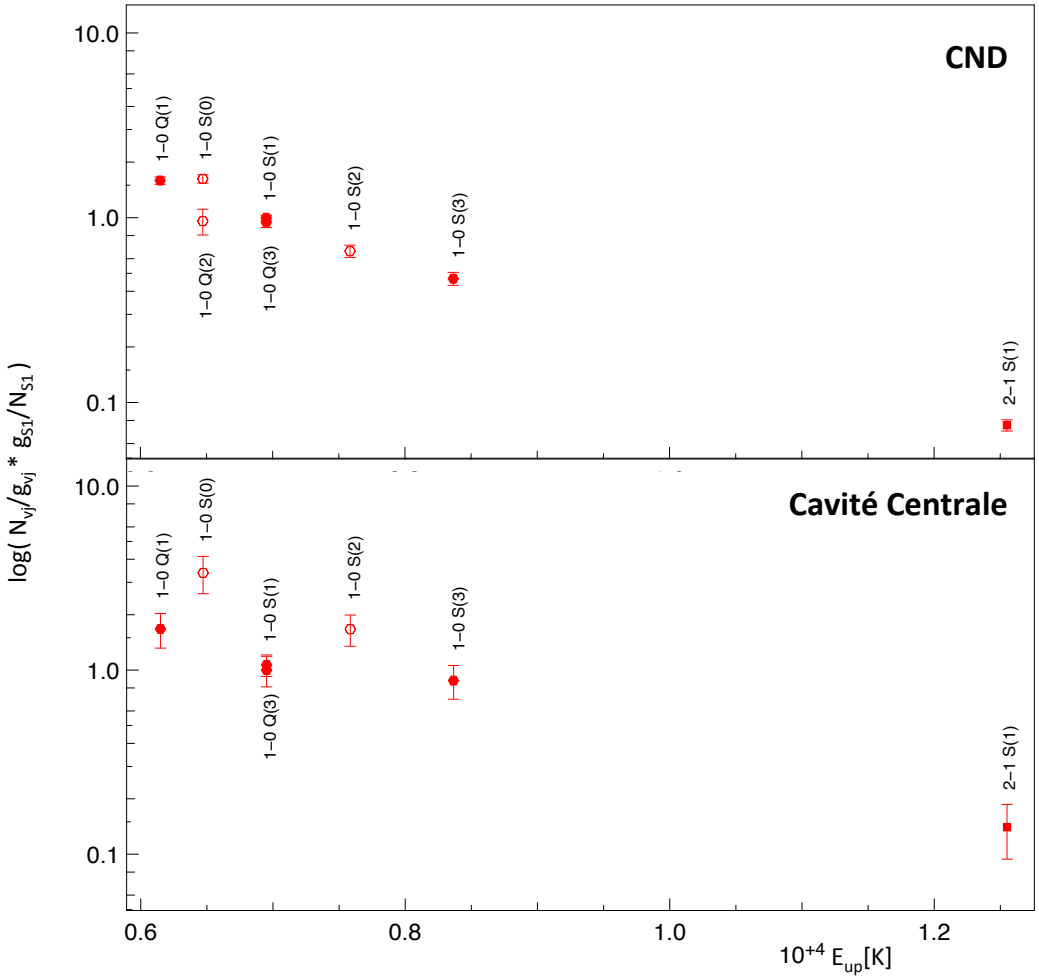

Figure D.3: Diagrammes d'éxcitation de H_2pour dix zones du champ de SPIFFI. *Haut :* diagramme du coin nord-ouest du CND. *Bas :* diagramme de la Cavité Centrale (quelque second d'angle ouest de GCIRS 7 (le carré noir au centre du champ dans Fig. D.1).

plus froid. Seulement le H_2 situé dans la couche mince à la frontière de ces nuages (chauffé soit par les UV provenant de l'amas central ou par collision) est responsable des densités de colonne observées. Dans Loh et al. 2011 les auteurs proposent la même interprétation : le H_2 le plus chaud représente juste une petite fraction de la masse totale mais il domine l'intensité.

Pour ce qui concerne le mécanisme d'excitation, dans le coin nord-ouest du CND le rapport 1-0 S (1)/2-1 S(1) semble assez cohérent avec une excitation par choc. Cela est en accord avec ce qui est proposé par Yusef-Zadeh et al. (2001), qui suggère que l'émission est engendrée par des chocs dus aux mouvements aléatoires de nuages dans un milieu grumeleux ou par la turbulence dans un milieu plus homogène. Pour le coin sud-est du CND le rapport montre des valeurs intermédiaires. Donc l'excitation par choc semble être exclue, laissant la fluorescence collisionnelle comme le scénario favori en contraste avec le coin opposé. Compte tenu de l'inclinaison connue du CND, et de ce que l'émission provient de la surface de ce tore, il est possible que des mécanismes d'excitation différents s'appliquent aux parties distinctes du CND couvertes par le champ de SPIFFI.

Zones non-thermalisées : la Cavité Centrale

Dans la Cavité Centrale l'émission n'est pas thermalisée. Ici, la densité des UV doit être beaucoup plus élevée. En raison de la plus faible densité et de la composition en grumeaux, le rayonnement UV pénètre plus profondément dans la Cavité que dans le CND où il reste confiné à la surface. Cela expliquerait pourquoi on peut détecter de l'émission qui semble provenir de l'intérieur du Bras Nord (probablement étiré par les forces de marée) mais pas d'émission à l'intérieur des nuages CND où elle reste confinée à la surface.

Pour mieux comprendre le mécanisme d'excitation dans cette région nous avons entamé une collaboration avec des experts de H_2 dans les PDR (J. Le Bourlot, F. Le Petit et E. Bron, LUTH, Observatoire de Paris). Le "code de PDR de Meudon" [1] (Le Bourlot et al. 1993; Le Petit et al. 2006) qu'ils ont développé calcule la structure des nuages du MIS éclairés par les UV, en résolvant numériquement le transfert radiatif. Nous avons comparé aux observations les simulations construites à l'aide du "code de Meudon" (E. Bron) pour une gamme de paramètres (densité, UV, flux, etc.). La forme du diagramme d'excitation est bien reproduite. Le problème est que le modèle ne parvient pas à reproduire les fortes intensités observées. Le champ UV nécessaire pour atteindre les valeurs observées pourrait chauffer le gaz jusqu'à la limite où l'excitation par collisions devient efficace et le diagramme d'excitation prend une forme plate. [pas clair !] Cette analyse est encore à un stade préliminaire. Le mécanisme de chauffage des poussières pourrait jouer un rôle clé dans le modèle et doit être examiné plus en détail. En outre, le code n'a jamais été testé auparavant dans des conditions extrêmes telles que celles du Centre Galactique.

La zone correspondant au maximum du flux observé dans la raie 1 - 0 S(0) est particulièrement difficile à expliquer. Dans cette région, toutes les raies correspondant aux transitions vibrationnelles 1-0 s'alignent assez bien sur une droite, tandis que seule 1-0 S(0) dévie fortement vers des valeurs beaucoup plus élevées de densité de colonne. Cette région est à la frontière de la Minicavité. Cette structure est probablement due à l'interaction entre un fort vent stellaire et le MIS dense (Lutz et al. 1993) ou d'un jet provenant de Sgr A* (Eckart

[1] http://pdr.obspm.fr/PDRcode.html

et al. 1992). La fort intensité de 1-0 S(0) par rapport aux autre raies pourrait être liée à une constante de temps courte des processus rapide de destruction et formation des molécules : en effet si la formation se faisait dans un état énergétique particulier, c'est lui qui dominerait l'émission, avant que l'équilibre entre niveaux peuplés ne soit atteint, comme cela se passé dans les autres regions. Cette hypothèse nécessite un étude plus détaillé.

Perspectives

Cette analyse montre que dans un volume aussi petit que le parsec central, il existe des zones très différentes, chacune présentant des conditions très particulières, qui ne peuvent être atteintes que dans un environnement extrême, comme celui du Centre Galactique.

Quelques questions restent ouvertes et nécessitent une analyse plus approfondie, comme par exemple l'origine du H_2 et de la poussière dans la Cavité Centrale. Le vent combiné des nombreuses étoiles dans le parsec central pourrait être la source de la matière et de l'énergie pour produire les grains de poussière. L'origine de l'excitation du gaz moléculaire dans la Cavité Centrale n'est pas toujours claire, en particulier dans la région où 1-0 S(0) est très intense et montre une forte corrélation avec le Fe II. L'étude poussée de cette zone et des autres régions de la Cavité Centrale peut conduire à des informations importantes sur les conditions locales du milieu dans le parsec central. A plus long terme, il serait intéressant de construire un modèle de transfert radiatif global pour toute la région du parsec central, en particulier, en tenant compte de la position 3D des étoiles. Cela permettrait de comprendre l'effet de ces étoiles sur le milieu environnant dans une région dominée par le trou noir supermassif central.